USAAVLABS TECHNICAL REPORT 68-3

AN EXPERIMENTAL STUDY OF THE PERFORMANCE AND STRUCTURAL LOADS OF A FULL-SCALE ROTOR AT EXTREME OPERATING CONDITIONS
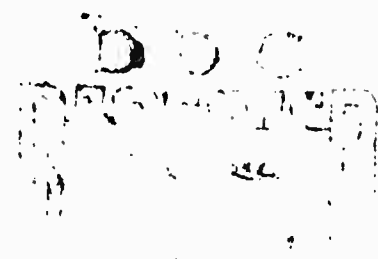
By

Vincent M. Paglino

Andrew H. Logan

July 1968

U. S. ARMY AVIATION MATERIEL LABORATORIES FORT EUSTIS, VIRGINIA

DISCLAIMER NOTICE

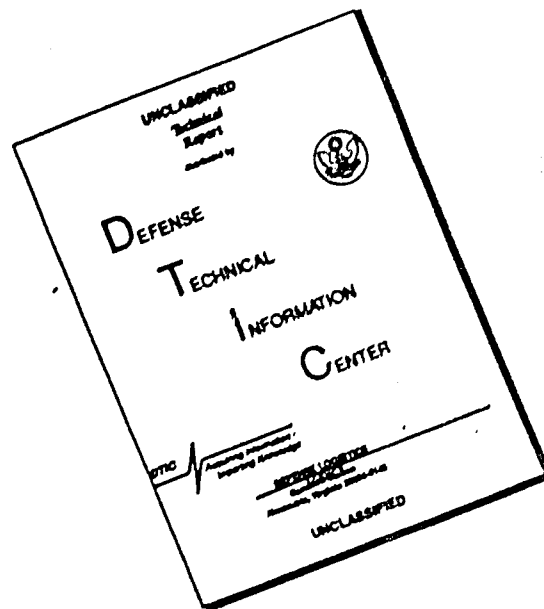THIS DOCUMENT IS BEST QUALITY AVAILABLE. THE COPY FURNISHED TO DTIC CONTAINED A SIGNIFICANT NUMBER OF PAGES WHICH DO NOT REPRODUCE LEGIBLY.

Disclaimers

This report has been reviewed by the U. S. Army Aviation
Materiel Laboratories and is considered to be technically
sound. The report is published for the exchange of infor-
mation and the stimulation of ideas.

AN EXPERIMENTAL STUDY OF
THE PERFORMANCE AND STRUCTURAL LOADS OF A
FULL-SCALE ROTOR AT EXTREME OPERATING CONDITIONS

SER-50505

by

Vincent M. Paglino
Andrew H. Logan

Prepared by

United Aircraft Corporation
Sikorsky Aircraft Division
Stratford, Connecticut

for

U. S. ARMY AVIATION MATERIEL LABORATORIES
FORT EUSTIS, VIRGINIA

SUMMARY

Two sets of strain-gage instrumented full-scale rotor blades were tested in the NASA/Ames Research Center 40' x 80' Wind Tunnel. One of the blade sets was a standard Sikorsky CH-34 rotor system with -8 degrees of twist, while the other set was structurally identical but had zero twist. Advance ratios up to 1.05 and tip Mach numbers to 0.93 were tested over a wide range of collective pitch and shaft angle of attack. Included in the analysis are the effects of blade twist, Mach number advance ratio, and shaft angle on both blade vibratory stress and performance. Correlation of measured and predicted performance is also examined.

The negative twist blades improved performance in all propulsive force operating regimes. A reduction in twist was generally found desirable for reducing blade stresses, and the twist reduction caused little or no performance penalty when the rotor lift and propulsive force requirements were decreased.

The measured and predicted values of power required at high Mach number were in good agreement, but the predicted power rate of increase with Mach number was somewhat greater than measured in the rotor propulsive mode.

Reductions in power loading and disc loading optimized rotor lift-drag ratio at high advance ratios. This trend was predicted by theory, although rotor drag calculations were low by 1 to 2 square feet of parasite area at advance ratios between 0.5 and 1.0. High-advance-ratio operation caused blade stress increases primarily in the flapwise vibratory mode.

The measured onset of rotor stall is more gradual than predicted by the theory, and the inclusion of induced, boundary layer, and unsteady effects appears desirable for improved prediction of helicopter performance.

FOREWORD

Mr. Alfred A. Lizak of the Sikorsky Aircraft Advanced Research Section supervised the development of the test article and shared the responsibility for the conduct of the wind tunnel tests. Mr. Robert Piper and Mr. John Yeates monitored this program for the U. S. Army Aviation Materiel Laboratories, and the NASA/Ames Project Engineer for the tunnel testing was Mr. John McCloud, III. Mr. Lawrence Doyle of the Sikorsky Measurements Instrumentation Section was the principal instrumentation engineer and wrote the instrumentation section of the report. The contribution of each towards the success of the program is gratefully acknowledged. The many helpful suggestions of Mr. John P. Rabbott, Jr., Supervisor of Sikorsky's Aircraft Advanced Research Section, are also gratefully acknowledged.

TABLE OF CONTENTS

LIST OF ILLUSTRATIONS

ix

x

xi

xii

xiii

xiv

xvi

xvii

xviii

LIST OF SYMBOLS

B_{1S}	longitudinal cyclic pitch, positive when pitch of advancing blade is reduced, degrees
b	number of blades
C_D/σ	rotor drag coefficient-solidity ratio, $D/\sigma \pi R^2 \rho\, (\Omega R)^2$
C_L/σ	rotor lift coefficient-solidity ratio, $L/\sigma \pi R^2 \rho\, (\Omega R)^2$
C_Q/σ	rotor torque coefficient-solidity ratio, $Q/\sigma \pi R^3 \rho\, (\Omega R)^2$
C_{Q_D}	single blade torque coefficient due to profile drag, $Q_D/\pi R^3 \rho\, (\Omega R)^2$
C_{d_o}	blade section drag coefficient at zero lift
C_N	Nth chordwise bending mode of blade
c	blade chord, feet
D	rotor drag, pounds
F_N	Nth flapwise bending mode of blade
f	equivalent parasite area, D/q, square feet
HP	rotor shaft horsepower
L	rotor lift, pounds
$M_{(1 0,90)}$	advancing blade tip Mach number $(\frac{r}{R} = 1.0, 90^\circ$ azimuth$)$
Q	rotor shaft torque, foot-pounds
Q_D	single blade torque due to profile drag, foot-pounds
q	free-stream dynamic pressure, $\frac{1}{2} \rho V^2$, pounds per square foot

xx

R	blade radius, feet
r	distance from center of rotation to blade radial station, feet
T_N	Nth torsional bending mode of blade
V	forward velocity, feet per second or knots, as indicated
α_C	rotor angle of attack, $\alpha_S - B_{1S}$, degrees
α_S	rotor shaft angle of attack, negative when shaft is tilted forward, degrees
θ_C	blade collective pitch at 0.75R, positive when leading edge is up, average value, degrees
θ_1	blade twist, negative when tip pitch is less than root pitch, degrees
μ	advance ratio, $V/\Omega R$
ρ	air density, slugs per cubic foot
σ	rotor solidity, $bc/\pi R$
Ω	rotor angular velocity, radians per second

SUBSCRIPTS

N	bending mode order, N = 1, 2, 3....

INTRODUCTION

As a result of the increasing desirability of high-speed VTOL aircraft for both military and commercial application, much attention has been focused on extending the speed capability and range of the helicopter without sacrificing its low-speed and hover capabilities. Studies such as that presented in Reference 1 indicated that the rotor was far from being utilized to its full capability. However, additional full-scale structural, aerodynamic, and performance data were needed as an aid in developing more sophisticated analytical techniques for design work. The extensive flight test results presented in Reference 2 provided much useful aerodynamic and structural data, though necessarily limited to normal helicopter speeds. In late 1964, to extend the range of available data of this type, the pressure and strain-gage instrumented Sikorsky CH-34 full-scale rotor system, used in the study of Reference 2, was tested in the NASA/Ames full-scale wind tunnel at speeds up to 175 knots. The results of that test as well as a comparison of the results with those predicted by modern analytical techniques are presented in Reference 3.

One purpose of the present investigation was to test the CH-34 rotor system under even more demanding conditions of forward speed, tip Mach number, and advance ratio, and to correlate the performance results with an existing rapid prediction method. The other objective of the study was to investigate the behavior of blade vibratory stresses and control loads at these extreme conditions and to determine their sensitivity to a number of parameters, including blade twist.

To achieve these objectives, two sets of strain-gage instrumented full-scale rotor blades were tested in the NASA/Ames Research Center 40' x 80' Wind Tunnel. One of the blade sets was a standard Sikorsky CH-34 rotor system with -8 degrees of twist, while the other set was structurally identical but had zero twist. Advance ratios up to 1.05 and tip Mach numbers to 0.93 were tested over a wide range of collective pitch and shaft angle of attack. Included in the analysis are the effects of blade twist, Mach Number, advance ratio, and shaft angle on both blade vibratory stress and performance. Correlation of measured and predicted performance is also examined.

This program was jointly sponsored by the United States Army Aviation Materiel Laboratories and Sikorsky Aircraft, and the test was conducted by the Ames Research Center of the National Aeronautics and Space Administration.

DESCRIPTION OF FACILITIES AND EQUIPMENT

WIND TUNNEL

The full-scale wind tunnel located at the NASA/Ames Research Center is of the closed-throat, closed-return type, with a test section 40 feet high and 80 feet wide. This tunnel has a nominal maximum speed capability of 200 knots and is powered by six 6000-horsepower electric motors. Model forces and moments are measured by a six-component mechanical balance, with the readings punched directly on IBM cards for processing.

ROTOR DRIVE AND CONTROL SYSTEM

The faired rotor drive and control system is shown as installed in the wind tunnel in Figure 1. The fully articulated rotor is mounted on a standard CH-34 transmission powered by a NASA 1500-horsepower variable-speed electric motor. The four-bladed hub is equipped with coincident flapping and lagging hinges located one foot from the center of rotation. Lagging motion is restrained by standard production hydraulic dampers. A terminal plate is mounted on the rotor head to accommodate instrumentation leads from the rotating system through the slip rings to the fixed system. All components are mounted on a triangular I-beam frame, and the complete assembly is enclosed in a streamlined fairing. The model was supported on the tunnel balance by means of two faired forward struts and one faired, telescoping tail strut. A self-centering, hydraulic vibration isolation system was installed at each strut attachment point to diminish the in-plane forces transmitted by the model to the balance frame. The rotor head, at zero angle of attack, was positioned approximately one foot above the tunnel center line.

Certain modifications to the CH-34 control system were made to minimize pitch-lag coupling and to provide for adequate strength to react the anticipated control loads which, at the high speeds and advance ratios possible in the wind tunnel, were expected to be in excess of the CH-34 design loads. The swash plate, scissors, and control horn were redesigned. The CH-34 pushrods and primary control servos were replaced by units standard on the Sikorsky S-61 helicopter. The usual aircraft collective and cyclic pitch control sticks were replaced by three remotely operated electromechanical actuators which controlled rotor blade pitch through the standard aircraft linkage.

2

ROTOR BLADES

The test was conducted using both a standard four-bladed CH-34 main rotor as well as an untwisted blade set. One blade of each rotor was modified only to the extent required for the necessary instrumentation. The remaining blades were balanced to match the instrumented blade. Rotor radius is 28 feet, and the standard blades are of -8 degrees aerodynamic twist with a blade chord of 16.4 inches. Blades of the second set have zero twist but are otherwise identical to the standard rotor blades. Airfoil contour is that of an NACA 0012, based on a chord of 16.0 inches modified by a 0.4-inch trailing edge extension of 0.096-inch thickness. A comparison of the basic airfoil shape, the tip cap region at 99 percent radius, and the inboard blade spar is shown in Figure 2. The blade's physical properties are given in Figure 3; the blade frequency diagram is shown in Figure 4.

INSTRUMENTATION AND DATA ACQUISITION SYSTEM

One rotor blade of each set was strain-gaged to measure five flapwise, four chordwise, and three torsion stresses. As a safety precaution, five total stress gages were also provided and continuously monitored during testing. The radial locations of the gages are shown schematically in Figure 5. Three stationary and two rotating star loads were also recorded.

A master control console was used to provide rotor control and monitoring functions. The panel display consisted primarily of a rotor tachometer, gearbox oil pressure and temperature indicators, two dials for the resolved flapping angle, and three dial indicators for the control inputs. Three-position toggle switches controlled servo actuators, and a servo position indicator system was utilized to set test conditions.

Blade flap angles were measured by Baldwin-Lima-Hamilton angulators installed on the rotor head. A flapping resolver system was used to derive the first harmonic sine and cosine components electrically from the output of one of two flapping transducers. These flapping components were displayed on the control console for use in setting trim conditions during testing.

Rotor power was derived from torsion strain gages located on the rotor shaft. Pretest calibrations showed that there was no measureable interaction of rotor shaft torque with either shaft bending or shaft thrust. Electrical signals were transmitted from the rotating to the non-rotating system through a 160-channel slip-ring assembly. Photoelectronic

3

pickups were used to sense blade azimuth position. Time-averaged six-component rotor performance data were recorded by the wind tunnel balance and processed by NASA/Ames wind tunnel equipment.

In order to utilize automated electronic data processing techniques, the recording medium selected for all dynamic measurements was magnetic tape. A block diagram of the instrumentation is shown in Figure 6. The principal acquisition device was an Ampex Model 800B Magnetic Tape Recorder which has a capacity of 14 tracks of information.

The recording system was a narrow-band FM multiplex using standard IRIG subcarrier oscillators. Eight channels of information, IRIG bands 9 through 16, were recorded on individual tape tracks. Four direct record tracks were used for dynamic data. In addition, one track was used for audio comments, one other was used for main rotor azimuth reference information, and a final track contained a data run command to be used in processing. All dynamic measurements were recorded simultaneously to provide proper time correlation of the data.

The strain-gage instrumentation channels were conditioned by B & F Bridge Balance Units. The resulting output signals were then supplied to the subcarrier oscillators.

In order to provide for on-line monitoring of test conditions, a patch panel and an 18-channel CEC Datarite Oscillograph were provided. It was also necessary to observe specific signals continually during the entire test program. For this purpose, a 17-inch oscilloscope and a four-trace electronic switch were supplied and patched into the appropriate channels.

Operation of the recording system was accomplished by use of a single control unit. Features included selectable time duration data bursts and an automatic calibration sequence using standard shunt resistance techniques.

DATA PROCESSING SYSTEM

The dynamic test data were processed at Sikorsky Aircraft by means of the technique block-diagrammed in Figure 7. A single tape track, which contained a maximum of eight measurements in an FM multiplex, was played back into a bank of narrow-band FM discriminators (Model GFD-7, Data Controls Systems, Inc.). The discriminator outputs were then fed into normalizing amplifiers that scaled all measurements to a common signal level (10 volts=full scale). These data were presented to a

4

solid-state multiplex with sample and hold amplifiers. The sampling rate of the multiplexer was controlled by special Sikorsky-designed hardware that utilized control signals from the analog tape. The control signals, 72 azimuth pulses per rotor revolution, and a data run command were combined to generate 720 data sampling pulses for 10 data cycles within a given data burst. The multiplexer output was digitized by a nine-bit (eight bits plus sign) analog to digital converter and put into format on digital tape through a Scientific Data Systems Computer, Model 910. This digital tape was then processed in final form by a UNIVAC 1108 computer, with calibration constants incorporated in the digital computations.

ANALYTICAL METHOD, TEST PROCEDURE,
AND DATA REPEATABILITY

The theory used for correlation with the performance results is the
Sikorsky Generalized Rotor Performance Method which is described in
Reference 4. Briefly, the method assumes hinged, rigid blades sub-
jected to uniform momentum inflow. The blades are mathematically
divided into a number of segments, each of which is assumed to behave
as if immersed in a two-dimensional flow field, including the effects of
stall and compressibility. Although more sophisticated analytical
techniques such as those described in Reference 3 are currently in use
for detailed rotor design studies, the Generalized Performance Method
is used here to investigate its range of applicability as a rapid
performance prediction technique.

Prior to installation of the rotor blades on the test article, the model
(including the rotor head) was tested at various combinations of
rotational speed, forward speed, and shaft angle of attack to determine
its lift, drag, and moment characteristics. The tare values thus
obtained were represented by a mathematical curve fit and used in the
NASA/Ames performance data reduction program. The performance
data thus reflect only the forces generated by the rotor. The rotor
blades, however, have an attachment fitting or "cuff" which is not
accounted for either in the tares or in the theory. At zero shaft angle
of attack and maximum tunnel speed of approximately 195 knots,
corresponding to a q of 110 pounds per square foot, the maximum error
in tare lift or drag introduced by the curve fit process was less than 3
percent of the over-all tare lift and drag of 1500 and 2100 pounds,
respectively (at this speed and shaft angle of attack). The static system
amplitude accuracy for strain gage measurements is 2.2 percent of full
scale, as reported in Reference 3.

The testing procedure used was to set a desired tip speed, shaft angle of
attack, forward speed, and collective pitch such as to obtain a near-zero
rotor lift. Collective pitch was then increased by increments not
exceeding 2 degrees, with each collective setting representing a data
recording point. Longitudinal and lateral cyclic pitch were adjusted at
each point to provide zero (± 0.2 degree) first harmonic flapping with
respect to the shaft. Fifteen different combinations of tip speed and
forward speed were tested and are listed in the table on the following
page along with advance ratio, air density, and advancing tip Mach
number. * Conditions 16 and 17 are reruns of conditions 1 and 2. The

---

* The range of test conditions is shown graphically in Figure 8.

6

AVERAGE VALUES OF TEST CONDITIONS

Condition	Forward Velocity (Knots)	Advance Ratio	Blade Twist (Deg)	Advancing Tip Mach Number	Tip Speed (Ft/Sec)	Air Density (Slugs/Ft^3)
1	117	0.30	-8	0.74	650	0.002203
2	161	0.40	-8	0.82	680	0.002114
3	177	0.46	-8	0.82	651	0.002112
4	116	0.30	0	0.74	646	0.002213
5	162	0.40	0	0.83	683	0.002167
6	178	0.46	0	0.82	654	0.002113
7	132	0.40	0	0.67	555	0.002159
8	174	0.41	0	0.87	720	0.002063
9	175	0.39	0	0.89	750	0.002039
10	180	0.39	0	0.93	775	0.002121
11	194	0.50	0	0.83	651	0.002036
12	194	0.62	0	0.73	528	0.002061
13	193	0.71	0	0.68	460	0.002083
14	195	0.82	0	0.62	399	0.002029
15	197	1.05	0	0.54	315	0.001963
16*	117	0.30	-8	0.74	650	0.002190
17*	163	0.40	-8	0.82	679	0.002108

* Conditions 16 and 17 are reruns of conditions 1 and 2, respectively.

stress data presented later in the report reflect the values recorded during these reruns.

All quantities shown in the table represent the average of all those recorded during each condition (approximately 25 data bursts). It may be noted that the average velocity, when converted to feet per second and divided by the average tip speed, does not necessarily yield the average value of advance ratio since, mathematically, it may be easily computed for a simple case that the quotient of the average values need not equal the average of the quotients. These values are therefore not meant to imply the accuracy of measurement but merely represent the prevailing conditions, and are listed on appropriate figures throughout the report. For the purposes of subsequent discussion, however, it will be assumed that two conditions are essentially the same if the average tunnel speed, tip speed, and advance ratio listed in the table differ by only a few units in the last place. This assumption is justified based on the fact that the mean deviations of tunnel velocity and tip speed from the average values shown are ± 1 percent and ± 0.5 percent, respectively.

A sample of performance data repeatability is shown in Figure 9, which compares the results of conditions 2 and 17. Since the results are in cross-plotted form for ease of comparison, the symbols do not represent test points but are used to show the points of line definition. Excellent repeatability is noted even though the data were recorded approximately one week apart.

Another example of longer term data repeatability is presented in Figure 10, showing actual performance data points acquired during the 1964 tests of Reference 3 and those of the present study on a dimensional basis. Even though the tunnel velocities are not identical, good correlation is evidenced for lift, drag, and torque. Some isolated point discrepancies are noted, but they may be caused by differences in tunnel speed and air density between tests. A sample comparison of vibratory stress results obtained during the two separate tests is given in Figure 11. Again, good agreement is noted, with only slight differences appearing in the chordwise bending mode.

As a further check on the validity of the wind tunnel stress results, a comparison of the present results with the free-flight data of Reference 2 is given in Figure 12. Since identical conditions could not be found, two radial distributions of the wind tunnel stress results are presented. These distributions are enclosed by the shaded area, whose upper boundary corresponds to a lift coefficient-solidity ratio of 0.096 and a drag coefficient-solidity ratio of -0.0095. The lower boundary is defined by 0.078 and -0.0064, lift and drag, respectively. The symbols represent flight data at lift coefficient-solidity ratios between 0.087 and

8

0.092, with a drag coefficient-solidity ratio of approximately -0.0099. The comparison of the present tunnel data and the flight data is good in all the bending modes except chordwise. The chordwise discrepancies are probably due, for the most part, to differences in the lag damper setting, but these minor differences do not detract from the validity of the results. An evaluation of the magnitude of the influence of the tunnel walls on rotor angle of attack was made based on the analysis of Reference 5. The results indicated that a maximum error of less than 0.5 degree would be expected throughout the range of test parameters, so that no wind tunnel wall correction was applied to the data.

DISCUSSION OF MEASURED AND CALCULATED
PERFORMANCE RESULTS

BASIC PERFORMANCE DATA

Complete nondimensional performance data (lift, drag, power) obtained
in these tests are presented in Figures 13 through 27, as a function of
rotor angle of attack. Lines of constant collective pitch and shaft angle
of attack are indicated on each figure to completely define the longitudinal
control inputs. All data points shown were obtained with first harmonic
flapping with respect to the shaft trimmed to essentially zero.

Figures 13 through 15 represent conditions of increasing forward speed
employing blades twisted -8 degrees. Figures 16 through 18 repeat these
same conditions with zero-degree twist blades. Figures 19 through 22
are conditions of constant advance ratio and increasing tip Mach number,
while Figures 23 through 27 are conditions of approximately constant
free-stream velocity and increasing advance ratio. Thus, these data
define a wide spectrum of full-scale rotor operating conditions, ranging
in advance ratio from 0.30 to 1.05 and ranging in tip Mach number from
0.67 to 0.93. More detailed information concerning the average
operating conditions may be obtained from the table on page 7. There
are data points at each condition well beyond theoretical stall and others
extending into autorotation. The data exhibit much the same
characteristics as small-scale test results such as those in Reference 6.
These characteristics will be examined separately in subsequent sections
of this report.

EFFECT OF SHAFT ANGLE OF ATTACK ON PERFORMANCE

Figures 28 through 30 illustrate the manner in which rotor drag and torque
coefficient are affected when subjected to a change in shaft angle of attack
while keeping first harmonic flapping with respect to the shaft trimmed to
zero and lift constant. It should be remembered that the important
physical parameter is tip path plane inclination and that shaft angle of
attack is identical to tip path plane angle of attack since first harmonic
flapping is trimmed to zero. Figures 28 and 29 represent conditions with
the same rotor tip speed and differing forward velocities, while Figures
29 and 30 have the same forward velocity but differing tip speeds. This
gives a range of advance ratios of 0.30 to 0.62. In order to make the
presentation comparable to aircraft flight conditions, the results are
shown at constant disc loading rather than at constant lift coefficient.

10

A high and a low disc loading are plotted for each condition, the high one reflecting the maximum loading at which data were available over a sufficient range of shaft angles. The low disc loading was kept at 2 pounds per square foot for each condition. As an aid to the reader, a line on each graph indicates the dimensional equivalent of the ordinate scale.

At the lowest advance ratio ($\mu = 0.30$, Figure 28), an increase in shaft angle at constant disc loading (and therefore constant lift) is seen to cause a very nearly linear increase in drag and a decrease in power. However, as advance ratio increases ($\mu = 0.50$ and 0.62, Figures 29 and 30), nonlinearities become more marked, probably because of increases in stall and reverse flow areas. The theoretical calculations are able to qualitatively predict the effect of shaft angle (that is, tip path plane angle) on rotor drag and torque, although quantitative agreement is notably better for the low advance ratio condition. General correlation of theory and experiment will be discussed in detail in a separate section of this report. For the present, it is sufficient to note that at the two higher advance ratios ($\mu = 0.50$ and 0.62, Figures 29 and 30), the prediction of drag is optimistic at both high and low disc loadings. Power calculations for these same two advance ratios are conservative at the high (theoretically stalled) disc loading but reasonably good at the 2-pound-per-square-foot disc loading (which is theoretically unstalled). The autorotative angle of attack (zero-torque point) is also predicted to within one-half a degree for these cases.

As might be expected, the principal effect of a decreased disc loading is a decreased sensitivity of drag and torque to shaft angle of attack. How these sensitivities are affected by advance ratio at constant lift is illustrated by Figure 31. The advance ratio change between 0.30 and 0.50 is accomplished through a change in forward velocity, while the advance ratio change between 0.50 and 0.62 is the result of a rotor tip speed change. In general, drag response to shaft angle decreases while power sensitivity increases in magnitude. The curves represent data obtained at moderate values of advancing tip Mach Number (0.73 to 0.83), and some vertical displacement in the curves would be expected if Mach number were to change markedly. For example, theoretical calculations at an advance ratio of 0.40 indicate that if advancing tip Mach number is increased from 0.67 to 0.93, the drag sensitivity changes from approximately 90 pounds per degree to 100 pounds per degree. The power sensitivity also increases in magnitude from -35 to -65 horsepower per degree over this same Mach number range. At advance ratios higher than those shown, it was not possible to obtain data at this disc loading of 2 pounds per square foot because of high vibratory blade structural loads. The data obtained at lower lifts and higher advance ratios do not lend themselves to this type of presentation, since the manner in which

11

power and drag vary with shaft angle is dependent upon the assumed disc loading. Of more practical interest at higher advance ratios are the shaft angle of attack and the collective pitch required to maintain optimum rotor lift and rotor power. If the desired rotor loading and power are known, the required shaft angle of attack and collective pitch may be found from the basic performance data (Figures 13 through 27). Determination of optimum rotor loading and power is discussed in the section entitled "Effect of Advance Ratio on Performance".

EFFECT OF BLADE TWIST ON PERFORMANCE

Negatively twisted blades have long been used on helicopter rotors as a means of increasing both hovering and cruise efficiency. Reference 1 has shown that significant delays in calculated stall onset are achieved with blade twist, but at the cost of increased blade stresses. One of the purposes of the present study was to compare the results from an untwisted and a -8-degree linearly twisted blade set over a substantial range of rotor drag, lift, and advance ratio, to determine the effect of twist on both performance and blade stress. The results of the blade stress study are discussed in a later section. From a performance standpoint, model tests such as those described in Reference 7 indicated that increasing blade twist from -4 degrees to -8 degrees was beneficial, for the conditions tested, at higher propulsive forces but detrimental at low or negative propulsive force (drag force). Theoretical calculations of Reference 7 also indicated that, for a given lift and advance ratio, the optimum blade twist was dependent on the required operating rotor drag or propulsive force. These previous conclusions are substantiated by the experimental and calculated results of the present study, as depicted by Figures 32 through 34. The theory shows good qualitative agreement with test results but tends to predict too great a power reduction with the twisted blades at high lift because of pessimistic stall prediction, which will be discussed in a later section. At lower lifts, the test results show slightly greater power savings than calculated (or less power loss as in the case of higher advance ratios and rotor drags). Overall, the test data substantiate the predicted and model rotor test effects of blade twist and lend additional credence to theoretical optimum twist curves such as those presented in Reference 7.

The measured torque coefficient reduction induced by twisting the blades -8 degrees is summarized in Figure 35. It is seen that a linear blade twist of -8 degrees provides a power savings over zero-twist blades in all pure helicopter operating regimes, and that twist effectiveness decreases with decreasing lift and propulsive force. For the higher

advance ratios shown (0.40 and 0.40), the result is in fact a slight increase in torque due to twist at low rotor lift and positive rotor drag. As will be shown in a later section, a reduction in blade twist is sometimes desirable for a reduction of blade stress, especially at higher advance ratios. Thus, the present results indicate that in high-speed helicopter configurations such as the compound, where the rotor is partially or fully unloaded and producing little or negative propulsive force (positive drag), a reduced twist blade for purposes of stress alleviation would incur little performance penalty and perhaps a benefit.

EFFECT OF MACH NUMBER ON PERFORMANCE

Reference 6 has shown from model tests that serious compressibility losses are incurred when the advancing tip Mach Number exceeds 0.85 to 0.90. This conclusion was reached based on a 161-knot forward speed with varying rotor speed (and thus advance ratio). In the present study, advance ratio was held constant at 0.40 while rotor speed and forward velocity were adjusted to increase tip Mach number.

The results are presented in Figure 36 for eight combinations of disc loading and rotor drag coefficient. Constant drag coefficient means constant equivalent parasite area, f, since the advance ratio is also held constant. Advancing tip Mach number cubed is used as the independent variable, since one can calculate incompressible torque requirements to rise linearly with the cube of the rotor speed (and therefore approximately with the cube of the tip Mach number). This calculation (incompressible, $M = 0.1$) is shown for the lowest disc loading case; as may be noted, correlation improves considerably when the normal theory of this study is used (Reference 4), which utilizes compressible two-dimensional airfoil data (dashed line of Figure 36).

As tip Mach number decreases below a certain value, power loading begins to rise because of the onset of blade stall. This is particularly well illustrated at the 4-pound-per-square-foot disc loading of Figure 36. Since it is desirable from a performance point of view to operate the rotor at minimum power loading, it becomes necessary to determine the optimum Mach number, the low point on the power loading curve. Note that as disc loading and propulsive force are varied, the best Mach number at which to operate also varies, and optimum Mach number (or operating tip speed) is not necessarily concurrent with the onset of compressibility. However, the accuracy with which this point can be found depends on both reliable stall prediction and reliable compressibility power rise prediction. As will be discussed in a later section, stall

13

prediction is pessimistic. This, too, is well illustrated at the 4-pound-per-square-foot disc loading of Figure 36, where, as Mach number is decreased, the theory predicts a substantially greater power loading than test due to blade stall.

As for the compressible (high Mach number) regions in Figure 36, correlation is generally good at all disc loadings, especially in the drag mode. For zero force and for propulsive force modes, however, theory is optimistic (low) at medium Mach numbers and predicts a greater-than-measured rise in power required as Mach number increases. This behavior leads to a crossover point at Mach numbers of about 0.85 to 0.90 for these cases. (An exception to this trend is seen at the highest disc loading of 5 pounds per square foot, where the zero force calculation predicts the rotor to be stalled at all Mach numbers, producing a conservative power estimate throughout the range.)

Full-scale flight tests such as those reported in Reference 8 indicated that measured compressibility losses above $M_{(1.0, 90)} = 0.80$ were substantially less than predicted by the same theory as used herein. That result was arrived at by constraining theory and experiment to agree at lower Mach numbers. This constraint would effectively translate upwards the theoretical curves, increasing the apparent torque discrepancy at high Mach number. In normal use of the theory as a prediction tool, this type of adjustment would not be made and the present results indicate that over a wide range of lift and drag, power correlations with this theory at high Mach numbers do not display any unusually large errors. However, it is desirable to improve the slope in the correlation shown in Figure 36 at high Mach numbers so that if good low Mach number agreement were to be obtained, this agreement could then be expected to extend to very high Mach numbers as well.

One possible cause of the slope discrepancy is the flexibility of the blade, which is unaccounted for in the theory used. Even small angle-of-attack variations due to dynamic twisting, flapwise bending, or wake geometry can cause significant changes in section lift and drag at higher Mach numbers. Reference 6, however, reports good correlation of measured and predicted Mach number effects in the propulsive mode for dynamically scaled model blades (CH-37), using synthesized airfoil data obtained in hover, which may contribute to the agreement. At small scale, the good correlation with rigid blade theory may also be caused, in part, by less blade flexure due to the slightly higher stiffness characteristics of the CH-37 blades from which the model blades were scaled.

To examine the problem more closely, the variation of zero-lift profile torque with advancing tip Mach number was computed and is compared

14

with the test results in Figure 37. Since the blades have no physical
twist, little or no blade flexure would be expected at zero lift. Also, no
significant wake-induced effects would be generated. It is seen, for this
set of circumstances that agreement between theory and experiment is
good over the whole range of Mach numbers, lending support to the con-
jecture that blade flexure and wake-induced effects need to be better
accounted for at normal lifts in the high Mach number region. A con-
sideration of finite span effects on airfoil characteristics in compressible
flow would also perhaps shed further light on the matter, but it is beyond
the scope of the present study.

EFFECT OF ADVANCE RATIO ON PERFORMANCE

A direct measure of the aerodynamic efficiency of a rotor is the equiv-
alent L/D, defined in Reference 9 as rotor lift divided by an equivalent
rotor drag, where

$$\text{Equivalent Drag} = \text{Rotor Drag} + \frac{\text{Rotor Shaft Power}}{\text{Forward Speed}}$$

The above relation assumes a direct thrust transmitting efficiency of
100 percent. An equivalent drag is required, as the actual rotor drag
may be positive, zero, or negative, the latter corresponding to a rotor
propulsive force.

Optimum rotor operation from a performance standpoint occurs at max-
imum L/D, arrived at through correct balancing of rotor lift, drag (or
propulsive force), and power. Until the advent of the compound heli-
copter, these parameters could not be chosen at will, but were fixed by
the helicopter design speed, fuselage drag, and gross weight. Since lift
and thrust augmentation permit infinite combinations of rotor operating
parameters, it is necessary to determine the optimum lift and shaft
power for a rotor being used over a wide range of advance ratios.

The experimental and theoretical effect of advance ratio on rotor L/D is
shown in Figure 38 for two low values of disc loading and for several
values of power loading (zero power loading corresponds to autorotation).
The figure shows clearly the manner in which reductions in both power
loading and disc loading move the rotor maximum L/D point to higher
advance ratios. At normal disc loading for the H-34 rotor (4 to 5 pounds
per square foot), the optimum L/D would occur at its design advance
ratio (approximately 0.30). Lift-drag ratios over 6 are seen to be
achieved at 0.8 advance ratio, and over 5 at an advance ratio of 1.0.
The theory, however, predicts even higher values of L/D than expe-

15

rienced in the wind tunnel. Although the discrepancy seems large, because of the low lift considered, the actual contributing drag error is relatively small. For instance, at HP/L = 0 and μ = 0.88 (point of maximum discrepancy at the lower disc loading), the difference amounts to only 165 pounds of drag, or a parasite area of about 1.5 square feet. This is less than 10 percent of the parasite area of a clean fuselage which would be designed for this high-speed operation, and thus the prediction of overall aircraft L/D would not be appreciably affected. The discrepancy is still somewhat disturbing, however, and this overestimation of high advance ratio efficiency will be shown later to be the result of too low a rotor drag prediction.

In general, Figure 38 shows the theory to calculate well which disc loading and power loading will give the best L/D at the desired advance ratio, so that rotor performance may be successfully optimized. As mentioned in a previous section, when this information is known the required shaft angle of attack and collective pitch may then be found from the basic performance data or from calculated results such as those presented in Reference 4. However, using rigid blade theory to find the proper collective pitch setting may lead to error because of blade dynamic twist effects as discussed in Reference 6. Current flexible blade theory, such as the one described in Reference 3, would be more suitable for this purpose.

The above efficiency relationships may be also examined in terms of total power, where

Total Power = (Rotor Drag) x (Forward Speed) + Rotor Power

The results are shown in Figure 39, with optimum rotor operation now appearing as minimum power points instead of maximum L/D points. Relative rotor parasite area changes can easily be seen in this type of presentation, since they are directly proportional to total power at constant rotor power, forward speed, and free-stream dynamic pressure. This is due to the fact that a rotor drag change (and thus effective parasite area change, Δf, at constant q) is the only parameter that may cause a variation in total power when rotor shaft power and forward speed are constant, as may be seen from the expression above for total power. For the data of Figure 39 (V = 195 knots and q = 110 pounds per square foot), it may be calculated that a change in total horsepower of 100 (at constant rotor power) is the result of a rotor Δf of 1.5 square feet, as indicated on the figure. Note, for example, that at an advance ratio of 0.88, a disc loading of 0.85 pounds per square foot, and zero rotor power loading, the difference between theory and experiment is seen to be about 1.5 square feet, the value stated in connection with Figure 38.

16

Achievement of high-advance-ratio flight also involves consideration of rotor control, aeroelastic stability, and blade stress characteristics. A thorough analysis of rotor blade aeroelastic stability will be found in Reference 10, while blade stress behavior experienced in the present tests will be discussed in a later section. Although no calculated blade stresses are presented here, Reference 3 has shown very good correlation of calculated and measured blade flapwise stresses at moderate lifts and advance ratios. The present test results should provide suitable reference data for analysis of high-advance-ratio stress prediction techniques.

The optimum method of controlling rotor lift as advance ratio is increased can be found by comparison of the performance maps at a high and at a low advance ratio. For example, comparison of Figure 16 (μ = 0.30) and Figure 27 (μ = 1.05) indicates that by operating the rotor at constant collective pitch and varying α_c through some means (either by changing α_s or B_{1s} , since $\alpha_c = \alpha_s - B_{1s}$), significant lift control is achievable at both the high and low advance ratio condition. On the other hand, operation at zero flapping (all data points shown have nominally zero flapping with respect to the shaft) and at constant shaft angle of attack is seen to give significant lift control through collective pitch change only at lower advance ratios (Figure 16 versus Figure 27). In particular, at an advance ratio of 1.05 (Figure 27), operation at zero flapping and constant shaft angle of attack yields essentially zero mean lift variation with collective pitch. Thus, from a lift control point of view, high-advance-ratio operation at constant collective pitch appears desirable, provided the collective pitch is chosen so as to provide optimum performance as previously discussed in connection with rotor equivalent lift-drag ratios. For an articulated rotor operating at constant collective pitch and at high advance ratio, it is also possible to control rotor lift while keeping a constant body (or shaft angle) attitude as well, since rotor angle of attack (α_c), and thus lift, may be controlled by changes in longitudinal cyclic pitch, B_{1s} , without incurring large one-per-revolution flapwise bending stress.

GENERAL CORRELATION OF THEORY AND EXPERIMENT

In previous sections, the experimental results have been compared with theory, but further discussion of correlation has been deferred until now so that more general conclusions could be drawn to explain trends which appear at all rotor operating conditions.

Figures 40 through 51 present the cross-plotted results of 12 of the 15 conditions tested in the wind tunnel along with theoretical comparisons. The data plotted in this manner eliminate collective pitch as a parameter, since correlation of this quantity was shown by Reference 6 to be sensitive to dynamic twist, which is not included in the theory used here. The three highest advance ratio conditions (0.71, 0.82, 1.05) are not shown in this form because, for constant C_L/σ, torque becomes double-valued with drag at high advance ratio, as is shown in Figure 52. These high-advance-ratio data are thus more useful when rotor angle of attack is included as a variable, as will be examined later.

Figures 40 through 51 provide a useful reference as to what accuracy of torque and drag estimation is possible with simple rigid blade theory over a wide range of rotor operating conditions. Figures 40 through 42 (-8 degrees twist) and Figures 43 through 46 (zero twist) represent conditions of increasing advance ratio. Figures 47 through 51 represent conditions of increasing advancing tip Mach number at constant advance ratio.

Examination of correlation at the low and medium lift coefficients of Figures 40 through 46 indicates that theory and experiment start out in good agreement but that theory becomes increasingly optimistic as advance ratio increases. As Mach number is increased (Figures 47 through 51), the theory starts out optimistic but correlation improves at higher Mach numbers because the theory predicts a greater-than-measured rise in power required with increasing Mach number. This behavior was illustrated and discussed in the previous section dealing with Mach number effects.

At the highest lift coefficient(s) shown for each of the conditions represented by Figures 40 through 51, the theory is conservative, regardless of advance ratio or tip Mach number. It has been calculated that the combinations of lift and propulsive force coefficients at which the theory becomes conservative are generally near the theoretical lower stall limit, defined as the point which the profile drag torque parameter of Reference 9, bC_{Q_D}/σ, exceeds a value of 0.004. This is also the point where theory became notably conservative for scale-model tests as reported in Reference 6, which postulated that centrifugal pumping of the boundary layer, if present, may contribute to delayed stall in model-scale testing significantly more than in full-scale testing. However, the present results indicate that the theory predicts stall prematurely for full-scale rotors as well.

The general areas of disagreement between theory and experiment having been noted, it is desirable to determine what causes the pertinent dif-

18

ferences in the correlation. Since drag and torque are dependent variables at constant lift, the difference between a theoretical and an experimental curve could be caused by a lack of correlation of either drag or torque. The rotor control axis angle of attack, α_c , was chosen as an independent parameter to examine torque and drag separately, since it is a function only of shaft angle of attack and longitudinal cyclic pitch. For example, in Figure 40 (where drag and torque are plotted dependently), note that at a lift coefficient-solidity ratio of 0.04 good correlation is obtained. At higher lifts (C_L/σ = 0.09 and 0.10) the theory is optimistic, but becomes increasingly conservative as the theoretical stall region is entered. (The calculation for the stalled C_L/σ = 0.11 is off-scale.)

Drag and Torque Correlation

If for this same condition, drag and torque are plotted separately versus angle of attack, as in Figure 53, it is seen that drag (Figure 53a) is predicted as being too low except for the very highly stalled lift (C_L/σ = 0.11). Figure 53b shows the torque calculation to be conservative at all lifts and especially so at the theoretically stalled lift (C_L/σ = 0.11). These trends in drag and torque correlation are typical of all conditions tested.

It has been suggested in Reference 6 that radial flow corrections such as those outlined in Reference 11 may be useful in improving rotor performance correlation. However, this type of correction increases the local section drag forces, which results in an increase in not only the predicted overall rotor drag but also rotor torque. This type of correction would help the correlation of drag shown by Figure 53a at the two lower lifts, but would adversely affect the torque correlation of Figure 53b. The results thus indicate a need for inclusion in the theory of an additional rotor drag force (of unknown origin at present) which, if influenced by advance ratio, would help to explain the increasing optimism of the theory with increasing advance ratio, as pointed out in connection with Figures 40 through 46. It could be shown that skin friction drag alone due to the radial component velocity is not significant compared to the differences in theory and experiment, although further study of radial flow phenomena appears desirable in light of the present results. Other possible causes for low drag prediction include rotor-fuselage interference and an unknown blade attachment fitting drag, which is not accounted for in the tares or in the spar section data employed in the calculations. To aid in evaluating the latter possibility, the effect of doubling the inboard spar's section drag characteristics was investigated.

19

Although arbitrarily doubling the spar's drag cannot necessarily be justified, the effect on performance correlation will be illustrated subsequently for a high advance ratio condition.

The conservative calculation of torque in the low and moderate lift range, seen in Figure 53b, was noted also in small-scale testing. This discrepancy in torque correlation was found in the present study to increase with Mach number. For example, at an advancing tip Mach number of 0.89 (Figure 50), note the seemingly good overall performance prediction at C_L/σ = 0.06. For this same (unstalled) lift coefficient, the drag and torque were examined independently as functions of rotor angle of attack. The result is shown in Figure 54. The good overall correlation is seen here to be a product of an excessively high torque prediction, and, as in Figure 53, too low a drag prediction. The fact that the conservative torque prediction increases at higher Mach number (Figure 53b versus Figure 54), despite a still too low drag prediction, indicates that the previously suggested inflow and three-dimensional compressibility refinements to the theory, in order to be effective, should produce a decrease in the calculated torque coefficient, independent of any effect on the calculated drag coefficient.

Stall Prediction

Conservative stall prediction, characteristic of small-scale tests as well, is not fully understood. The discrepancy is caused primarily by an excessively high torque (rather than high drag) calculation at the higher lift coefficients, such as in Figure 53 at C_L/σ = 0.11. The use of steady-state airfoil data in an unsteady flow environment undoubtedly contributes to the discrepancy, since Reference 3 has shown that at the advancing blade tip, where rapid loading fluctuations are present, a lifting surface theory may be necessary to accurately predict chordwise pressure distributions and, therefore, pressure drag. Thus at very high lifts, rotor torque calculations could be significantly affected. The assumption of the correct wake can also be important in the prediction of retreating blade stall. Examination of the blade loading time histories of Reference 3 indicates that nonuniform inflow combined with torsionally flexible blades tends to reduce predicted loading on the outboard retreating side of the rotor disc, where stall onset is likely to occur. The unaccounted-for stabilizing effect on the chordwise boundary layer induced by the spanwise boundary layer has also been offered in explanation for conservative stall prediction. Reference 12 gives an excellent discussion of this point.

High Advance Ratio Drag and Torque Correlation

The correlation of theoretical and experimental performance at the three highest advance ratios tested (0.71, 0.82 and 1.05) is shown in Figures 55 through 57, which clearly demonstrate low drag prediction at all lift coefficients (Figures 55a through 57a). Intermediate lift coefficient calculations are not shown here for the sake of clarity. As previously shown in the section dealing with advance ratio effects, the discrepancy in terms of parasite area is relatively small. In an effort to account for this discrepancy as being caused by the previously discussed blade attachment fitting, a twice normal spar drag coefficient was used in the calculation. That result is compared to the normal theory and to the test data at an advance ratio of 1.05 (Figure 57). As expected, the torque (Figure 57b) is not significantly affected because of the small moment arm involved. The predicted drag is increased by about 25 percent (Figure 57a), which is significant since the portion of the rotor blade affected by the drag change is small (approximately 6 percent). Although this correction is shown here to be not large enough to produce the required drag increase for correlation, the exercise does point out the effect of small section drag changes on rotor performance at high dynamic pressure and low lift.

With regard to torque correlation, it is noteworthy in Figures 55b through 57b that compressibility considerations are not of importance due to the relatively low advancing tip Mach numbers (0.68, 0.62, 0.54). The torque calculations bracket experimental results quite well, especially since at an advance ratio of 1.05 (Figure 57b), for example, a spread in torque coefficient from -0.002 to +0.002 represents less than 70 horsepower. However, at more realistic values of advancing tip Mach number (such as 0.9), the absolute differences in shaft horsepower would be considerably greater than the values shown here, because of other factors previously discussed.

Summary of Overall Trends

A summary of the discussion of this section is illustrated by Figure 58, showing the effect of advance ratio and Mach number on correlation. In order to eliminate compressibility as a variable, Figure 58a shows three conditions at the same nominal advancing tip Mach number ($M_{(1.0, 90)} = 0.82$). The three plots thus represent increasing advance ratio at the same drag coefficient-solidity ratio of 0.004. This value of C_D/σ was chosen since sufficient test data were available at that drag to form the required cross plots at all three advance ratios. The results are, however, typical of a wide range of drag coefficients. Note that once again all the

21

variables are dependent, so that what is being observed is the combined effect on correlation of any error in either the calculation or the measurement of rotor drag or torque. The most striking aspect of the correlation is the absence in the test data of the sharp break and excessive power rise at theoretical stall that typifies the calculated results. The more rapid increase of the experimental data with lift coefficient in the medium lift range suggests that wake-induced affects (which would be expected to increase with lift) need to be better accounted for. Reference 3, for example, has shown that wake geometry is significant in determining predicted blade loading distribution to speeds of at least 175 knots. The tendency of the optimistic performance prediction (below stall) to increase with advance ratio may reflect the influence of optimistic drag calculations, previously discussed.

Figure 58b summarizes the effect of increasing advancing tip Mach number on correlation over a broad range of lift. Advance ratio is approximately constant at 0.40 to eliminate it as a variable, and a C_D/σ of zero was chosen simply for convenience of cross plotting. Note that the last curve, at an advancing tip Mach number of 0.93, is not strictly comparable to the other curves, since it represents a C_D/σ of 0.004 instead of zero, due to the lack of sufficient data at zero drag and 0.93 Mach number. However, the correlation trends are again typical of a wide range of drag coefficient. The curves reflect the previously discussed tendency of the theory to predict a greater-than measured increase in power with Mach number. Thus, at high Mach number, the result is the elimination of the otherwise optimistic calculation of performance in the moderate lift range. The behavior of theory and experiment above theoretical stall is seen to be substantially unaffected by Mach number.

22

Because of the extremely large amount of blade stress data that was obtained, it is impractical to present all of the individual data points. Typical plots of the basic vibratory stress amplitude (one half peak-to-peak value) versus rotor angle of attack at constant values of collective pitch are presented in Figures 59 and 60 for the production -8-degree twist and zero-twist blades respectively. Flapwise, chordwise, and torsional stress are presented, and it can be seen that the basic data are of good quality, with little scatter. Data in the form of Figures 59 and 60 were cross plotted to yield the more meaningful form of stress versus drag coefficient-solidity ratio at constant lift coefficient-solidity ratio and are presented in the Appendix for the complete range of operating conditions. An exception to this format is the presentation of the vibratory stress data at the highest advance ratios (μ = 0.71, 0.82, 1.05), which are presented as functions of rotor angle of attack at constant lift coefficient-solidity ratio due to the frequent double-valued nature of stress versus drag. This double-valued behavior is demonstrated in Figure 61.

EFFECT OF ROTOR DRAG
AND SHAFT ANGLE OF ATTACK ON BLADE STRESS

The effects of rotor drag or propulsive force on blade vibratory stress are shown in Figures 62 through 65 for the untwisted and -8-degree twist blades for advance ratios of 0.30 and 0.46. At higher advance ratios, only the untwisted blades were tested, and representative data are presented in Figure 66 for an advance ratio of 0.62.

At the lowest advance ratio of 0.30, Figures 62 and 63, both blade sets are relatively insensitive to variations in rotor drag coefficient-solidity ratio for both flapwise and chordwise bending. Comparison of Figures 62a and 63a indicates somewhat of a trend for a reduction in flapwise stress amplitude with increasing propulsive force for the -8-degree twist blade compared to the untwisted blade set.

This trend is sharply accentuated at a higher advance ratio of 0.46, Figures 64 and 65, where variation in rotor drag has a distinctly opposite effect on the untwisted and -8-degree twist blade sets. In Figure 64, an increase in rotor propulsive force, or a reduction in drag, results in a marked increase in both flapwise and chordwise vibratory stress amplitude for the untwisted blade at essentially all values of rotor lift. In contrast,

23

for the -8-degree-twist blade set, shown in Figure 65, increased rotor propulsive force results in a sharp reduction in the flapwise vibratory stress and a less, but still significant, reduction in chordwise stress. The reduction in flapwise stress with propulsive force is in agreement with the model test results of Reference 6.

The variation of blade vibratory stress with rotor drag coefficient-solidity ratio is even more pronounced at the higher advance ratios, as typified in Figure 66 for an advance ratio of 0.62, for the untwisted blade set. As the rotor is not capable of producing a useful propulsive force at this advance ratio, all data are in the positive rotor drag regime. An increase in rotor drag from the minimum value produces a sharp drop in both flapwise and chordwise blade stress to a minimum, followed by a rise as the rotor approaches autorotation. Autorotation generally corresponds approximately to the maximum rotor drag condition, and Figure 66 shows that the minimum stress point occurs when the rotor is near autorotation.

Blade torsion stress is not presented in this section (although complete data are presented in the Appendix) because the torsion stress is essentially constant with drag for either blade set, and in any case it is small compared to the flapwise and chordwise stress.

Instead of rotor drag, the preceding discussion could have been presented in terms of rotor shaft angle. For example, in Figures 62 and 63, lines of constant shaft angle are shown in addition to lines of constant lift coefficient-solidity ratio, and it can be seen that going from a rotor propulsive force to a drag force corresponds to going from a negative to a positive shaft angle (or tip path plane angle as the first harmonic flapping is trimmed to zero). It is felt, however, that the rotor drag coefficient-solidity ratio defines the stress in a more useful manner, and therefore the blade vibratory stress are presented in the Appendix as a function of C_L/σ and C_D/σ.

EFFECT OF BLADE TWIST ON BLADE STRESS

The effect of blade twist on vibratory stress amplitude is shown in Figures 67 through 75 as flapwise, chordwise, and torsional stress amplitude versus lift coefficient-solidity ratio for both the production -8-degree linear twist blade and the untwisted blade set. The comparison is made at three advance ratios (0.30, 0.40 and 0.46) and for three values of rotor drag (C_D/σ = 0.004, 0, and -0.004) at each advance ratio. Figures 67 through 69 show a substantial reduction in vibratory stress amplitude with reduction in twist, typically on the order

24

of 1,000 to 2,000 psi at the normally critical mid-span area, 45 to 65 percent radius. To gain some insight into the cause of the reduction in flapwise stress associated with a reduction in blade twist, a brief theoretical analysis was conducted at an advance ratio of 0.30. The theory used, described in detail in Reference 1, is an extension of the rigid blade theory used in the performance section, which represents the elastic blade by a series of rigid segments connected by pin joints and springs to provide bending stiffness equivalent to the flexible blade. Flapwise bending only is considered in this analysis, and uniform inflow is assumed, although more sophisticated programs are available, as in Reference 3. The simpler theory was used herein, as only qualitative results were desired and, at the advance ratios considered, torsion would not be expected to be an important factor. Blade airload and flapwise stress distributions were computed for both the untwisted and the -8-degree twist blades. The results showed that the radial and azimuthal lift distributions for the twisted and untwisted blades were essentially the same except in the vicinity of the 90-degree azimuth position. In this region, the centroid of the radial lift distribution of the twisted blade was considerably inboard of that of the untwisted blade. Also, the outer 10 percent of the twisted blade experienced a negative loading while the untwisted blade did not. The implication is that the increase in flapwise vibratory stress due to twist is caused by a negative lift at the advancing blade tip and a corresponding inboard shift of the radial airload distribution on the advancing side.

The analysis of the effect of twist on the chordwise vibratory stress uncovered an unanticipated behavior. At the lowest advance ratio, $\mu = 0.30$, Figure 70, negative twist generally increased chordwise vibratory stress for all values of rotor drag considered. As the advance ratio increases, however, the effect of twist reverses as the rotor goes from a drag to a propulsive condition (propulsive defined as negative C_D/σ). This is best shown in Figure 71, where at $C_D/\sigma = 0.004$ (Figure 71a), negative twist increases the chordwise vibratory stress, while at C_D/σ -0.004 (Figure 71c), negative twist has the opposite effect. A similar trend is indicated in Figure 72. This effect was also briefly indicated in Reference 7, wherein the behavior was attributed to faulty lag damper settings which restricted the lag motion of one set of blades. In the present case, however, an examination of the hunting behavior of the untwisted and twisted blades revealed no restrictions or significant differences in the steady or vibratory lag motion.

An explanation of this behavior of the chordwise vibratory stress is not currently known, although the emergence of the behavior with increasing advance ratio implies that it may be connected with the growth of the reverse flow region.

25

The effect of blade twist on vibratory torsional stress is presented in Figures 73 through 75. There is a trend for the -8-degree twist blade to exhibit higher values of torsional stress than the untwisted blade, but the differences are small and in either case the absolute torsional stress levels are low compared to the flapwise and chordwise stress amplitudes. These results are generally in line with the model test data of Reference 7. An exception to this trend is exhibited in Figure 75 at the highest forward speed under consideration, 177 knots, at high lift coefficient-solidity ratios, where the -8-degree twist blades maintain a significantly lower torsional vibratory stress level than the untwisted blades. Since this combination of high lift and advance ratio (μ = 0.46) would be expected to precipitate blade stall, it is believed that the -8-degree twist blades reduce the retreating blade angle of attack sufficiently to produce a noticeable decrease in stall-associated aerodynamic pitching moment (and thus torsional stress) over that experienced by the untwisted blades.

EFFECT OF ADVANCING TIP MACH NUMBER ON BLADE STRESS

The effect of advancing tip Mach number on blade vibratory stress amplitude is shown in Figure 76 for the untwisted blade at three disc loadings. In this portion of the study, the effects of advance ratio are eliminated by holding it constant for each Mach number tested, thereby permitting the examination of Mach number effects only. Also, the constant advance ratio allows the examination of the stresses at constant C_D/σ, which corresponds to constant equivalent parasite area. Using this procedure, advancing tip Mach numbers of 0.67, 0.83, 0.87, 0.89, and 0.93 were attained.

Upon examination of the variation of blade stress with Mach number in Figure 76, it is seen that, generally, flapwise and chordwise vibratory stress exhibit a "U-shaped" behavior with increasing Mach number for all disc loadings considered. For torsional vibratory stress, however, this "U-shaped" behavior is seen only at the high disc loadings, while at a disc loading of 2 pounds per square foot, the torsional vibratory stress increases slightly but steadily with increasing Mach number. This "U-shaped" behavior of vibratory stress with increasing Mach number is probably a function of the interaction between stall effects at low Mach number and compressibility effects at high Mach number. At a low Mach number, the dynamic pressure on the retreating side is low, and therefore the retreating blade must operate near stall conditions to provide the required lift to balance the rotor rolling moment for trim. As the dynamic pressure is increased, this condition is eased and, as would be expected, the vibratory stress amplitude is decreased.

26

Associated with the increase in dynamic pressure on the retreating side, however, is an increase in advancing tip Mach number. As this occurs, compressibility effects predominate, tending to increase vibratory stress amplitude. Therefore, there is a neutral point (in this test, approximately $M_{(1.0,90)} = 0.85$) where the beneficial effects of increased dynamic pressure on the retreating side are balanced by the detrimental effects of compressibility on the advancing side.

At disc loadings of 4 and 5 pounds per square foot, however, another effect, aside from the general effects described above, becomes apparent in the flapwise and torsional stress. In Figure 76, the variation of flapwise and torsional stress with Mach number exhibits two distinct inflection points between the Mach numbers of 0.83 and 0.93. Although the chordwise vibratory stress curves of Figure 76 are shown to be smoothly continuous, data at 0.375R were not obtained at advancing tip Mach numbers of 0.87 and 0.89. Therefore, the possibility of inflections in the chordwise stress at these Mach numbers at 0.375R is not precluded, although such effects are absent from the chordwise stress measured at 0.65R.

Based on the calculated blade resonance diagram of Figure 4, it might be expected that the fifth and eighth harmonics of airloads could contribute to the vibratory blade stress. At a tip speed of 720 feet per second (corresponding to the test Mach number of 0.87), the fifth and eighth harmonics of rotor speed equal the third and fourth flapwise bending frequencies, respectively. However, an examination of the flapwise stress signature for Mach numbers of 0.87, 0.89, and 0.93 (tip speeds of 720, 750, and 775 feet per second, respectively) reveals no significant difference in their fifth and eighth harmonic content. This indicates that the unexpected behavior of the vibratory stress versus Mach number curve is not due to resonance at any one particular Mach number.

An analytical investigation of this phenomenon is beyond the scope of the present study and would be predicated on the availability of adequate two- and three-dimensional airfoil characteristics at Mach numbers approaching one. Assumed nonlinear aerodynamic pitching moments in combination with blade flexibility were shown in Reference 13 to explain a split tip path plane phenomenon encountered on the Sikorsky NH-3A flight research compound helicopter at advancing tip Mach numbers on the order of 0.94. These phenomena point out areas in which further effort could be profitably placed.

EFFECT OF ADVANCE RATIO ON BLADE STRESS

The effects of advance ratio on blade vibratory stress amplitude were investigated for a range of advance ratios between 0.50 and 1.05. The data were taken by maintaining a tunnel speed of approximately 195 knots and decreasing the tip speed from 651 feet per second to 315 feet per second. As previously discussed, blade stress data for the complete test range are presented in the Appendix, and representative test results are summarized in Figures 77 and 78. The dotted line at an advance ratio of 1.05 in Figure 77, which presents vibratory stress amplitude versus radius for constant advance ratios, again reflects the previously mentioned double-valued nature of stress versus drag (or torque) at the highest advance ratios. Results are presented for two disc loadings of 0.85 and 1.5 pounds per square foot for the rotor in autorotation. Autorotation was chosen because at high advance ratios this corresponds approximately to the point of maximum equivalent rotor lift-drag ratio, as was shown in the performance section. Similar comparisons may be made at other operating conditions by use of the complete vibratory stress data in the Appendix and the basic performance data found in Figures 13 through 27.

The increase in the vibratory stress amplitude of all three vibratory modes (flapwise, chordwise, and torsional) due to increasing advance ratio is shown in Figure 77 as stress amplitude versus radius. The predominant response, however, is seen to be in the flapwise stress, with moderate increases in chordwise stress and little change in torsional stress amplitude. The static energy balance theory of Reference 10 was used to compute the torsional divergence advance ratio for the CH-34 rotor blade, and an advance ratio of 1.6 was derived, well above the maximum test value of 1.05. Therefore, no marked increase in torsion stress with advance ratio would be expected due to divergence, as is borne out by the experimental data.

The effect of advance ratio and rotor loading on the flapwise vibratory stress is more clearly illustrated in Figure 78, which presents flapwise vibratory stress amplitude versus advance ratio for two values of disc loading for the 60 percent radial station as obtained by cross plotting Figure 77. The disc loadings of 0.85 and 1.5 are low for this basic rotor design at low speed, but correspond to a substantial blade loading at these high advance ratios (13.7 and 24.2 pounds per square foot respectively). Figure 78 shows that increasing either advance ratio or, particularly, blade loading results in a marked increase in flapwise vibratory stress. For example, at a disc loading of 0.85 pound per square foot (blade loading of 13.7 pounds per square foot) the vibratory stress at an advance ratio of 1.05 is approximately 1.7 times that at an advance ratio of 0.7. While high, this increase is in line with the

analytical study of Reference 14, which predicted an increase in stress by a factor of 2 between an advance ratio of 0.7 and 1.0 for a rotor system with a lower blade loading of 9.5 pounds per square foot. The greater increase in stress for the rotor system of Reference 14 can be attributed to the slight negative blade twist of -2 degrees and operation at higher dynamic pressure for the same advance ratio (300 knots for μ = 1.0 compound compared to 195 knots for the present test data).

EFFECT OF BLADE TWIST, MACH NUMBER, AND ADVANCE RATIO ON CONTROL LOADS

The effects of blade twist, advancing tip Mach number, and advance ratio on vibratory control loads are shown in Figures 79 through 81. The four control loads measured were a blade pitch control rod (push rod load) and three stationary star control inputs: right lateral servo (at 45 degrees azimuth), left lateral servo (225 degrees azimuth), and longitudinal servo (315 degrees azimuth).

Figure 79 shows the effect of twist on vibratory control loads. In this figure, the untwisted and -8-degree linearly twisted blade are compared and a reduction in both rotating and stationary vibratory control load amplitudes due to a negative twist is shown for high lifts. At low lifts, however, the vibratory control loads of the untwisted blade are slightly lower than those of the twisted blade. As negative blade twist is particularly beneficial at high values of rotor lift, the implication is that the results shown are due to a reduction in retreating blade stall, shown as a power saving in Figure 35 in the performance section. These results are similar to the flight test results of Reference 15.

As shown in Figure 80, vibratory control loads vary with advancing tip Mach number in a smooth "U-shaped" manner for the high disc loadings (4 and 5 pounds per square foot), similar to the variation of vibratory blade stress with Mach number, shown in Figure 76. At a disc loading of 2 pounds per square foot, however, the vibratory control loads remain constant (typically 200 pounds) up to a Mach number of approximately 0.87; they then rise sharply as at the high disc loadings.

At high disc loadings and low Mach numbers ($M_{(1.0,90)} \leq 0.8$), the vibratory control loads are large due to the effect of retreating blade stall. At low Mach numbers, the dynamic pressure on the retreating side is low, and therefore the retreating blade must operate near stall conditions to provide the required lift to balance the rotor rolling moment for trim. As the Mach number increases (keeping advance ratio constant), the dynamic pressure on the retreating side increases, resulting in a

reduction in retreating blade angle of attack and therefore in vibratory control loads. As the Mach number approaches high subsonic values, however, the control loads increase rapidly due to compressibility effects. This rapid rise in control loads at high subsonic Mach numbers is also shown in Reference 16, where the severity of the rise in control loads was decreased significantly by tapering the thickness of the outer 20 percent of the rotor blades. This procedure reduced the sensitivity of the outer portion of the blade to compressibility effects and shows the connection between the rise in control loads at high Mach numbers and compressibility.

The abrupt rise in control loads shown in Reference 16 occurs at an advancing tip Mach number of 0.87. A similar rise at this Mach number occurs for a disc loading of 2 pounds per square foot in Figure 80. In this figure, however, the behavior is investigated further, and it is seen that at higher disc loadings, the abrupt rise occurs at lower Mach numbers. This behavior is to be expected, as the rotor would become more sensitive to compressibility effects at higher lifts.

The effect of advance ratio on vibratory control loads is shown in Figure 81. The dotted lines in this figure denote areas in which the control load is double-valued in the same manner as the vibratory stress. The rise in control loads with an increase in advance ratio due to the growth of the reverse flow region is shown as well as the rise in control loads due to an increase in lift. The sensitivity to lift is due to the increasing difficulty of the retreating blade in maintaining the required lift as the advance ratio increases.

CONCLUSIONS

1. At low advance ratios, rotor power and drag vary linearly with tip path plane angle of attack, provided lift is held constant. For advance ratios up to at least 0.62, drag sensitivity to tip path plane angle change decreases with advance ratio while power sensitivity increases in magnitude.

2. A linear blade twist of -8 degrees improves rotor performance over that of untwisted blades in all pure helicopter operating regimes, especially at higher lifts. However, a reduction in twist which is sometimes desirable for reduction of blade stress (see Conclusion 9), would incur little performance penalty, and sometimes a benefit in higher speed helicopter configurations such as the compound, where the rotor is partially or fully unloaded and producing little or negative propulsive force. Rigid blade theory successfully predicts these trends.

3. The advancing tip Mach number at which power loading becomes a minimum depends upon disc loading and propulsive force, as well as forward speed, and the tip Mach number required for optimum operation is not necessarily concurrent with the onset of compressibility effects. The measured and predicted values of power required at high Mach number were in good agreement, but the predicted power rate of increase with Mach number was somewhat greater than measured in the rotor propulsive mode.

4. A reduction in either rotor power loading or disc loading moves the rotor maximum L/D operating point to higher advance ratio. In particular, rotor lift-drag ratios above 5 are obtainable at an advance ratio of 1.0. Although the calculation of rotor equivalent parasite area is too low, rigid blade theory predicts well which values of disc loading and power loading yield optimum rotor performance throughout the advance ratio range of 0.5 to 1.0.

5. As advance ratio approaches 1.0, collective pitch effectiveness in controlling lift diminishes to zero at a constant tip path plane angle.

6. Low rotor drag prediction is apparent over a wide range of conditions, and there is evidence of a need for including in the theory a term that affects rotor drag without increasing predicted rotor torque.

7. As with small-scale tests, the onset of rotor stall is more gradual than predicted by the theory used, indicating that delayed stall is not primarily a scale effect.

8. The inclusion of wake-induced velocity, boundary layer, and unsteady effects in the theory appears desirable for improved prediction of high-speed helicopter performance.

9. A fundamental parameter influencing blade vibratory stress is twist. Substantial reductions in flapwise and chordwise vibratory stress amplitude were found for the untwisted blade compared to the -8-degree linearly twisted blade. The reduction in chordwise stress, however, was found to be a function of rotor drag: the magnitude of the reduction decreased as rotor drag decreased. The effect of twist on torsional stress was small except at the highest forward speed, where the twisted blade had lower stress levels at high lifts than the untwisted blade.

10. The effects of twist on vibratory control loads are twofold. At low lifts, the vibratory control loads of the untwisted blade were slightly lower than those of the -8-degree twisted blade. At high lifts, however, significant increases in control loads were found for the untwisted blade compared to the twisted blade.

11. Sharp rises in vibratory stress and control loads are seen at low Mach numbers due to stall, while high levels of stress and control loads are also found at high subsonic Mach numbers due to compressibility.

12. An increase in advance ratio caused an increase in the vibratory stress amplitude in all three vibratory modes. The predominant response was in the flapwise stress, with moderate increases in chordwise stress and little change in torsional stress amplitude. Vibratory control loads are also increased by increases in advance ratio, and these increases are sharply accentuated by increases in lift.

13. Propulsive force has a significant effect on vibratory stress amplitude at all advance ratios. At low advance ratios, an increase in propulsive force decreases the flapwise and chordwise stresses of the twisted and untwisted blades. At high advance ratios, however, only the flapwise and chordwise stresses of the twisted blade are reduced by increases in propulsive force, while the flapwise and chordwise stresses of the untwisted blade are increased by increasing propulsive force. The torsional vibratory stress of either the twisted or the untwisted blade varies

32

little with propulsive force and at any advance ratio remains small relative to the chordwise and flapwise stresses.

14. The fully articulated rotor tested, although designed for a moderate-speed pure helicopter, was able to operate without difficulty over a substantial range of conditions at the maximum tunnel speed of slightly under 200 knots, including high advance ratio operation corresponding to 300 knots design speed.

RECOMMENDATIONS

1. Current research dealing with wake geometry, unsteady flow, and boundary layer effects should be intensified for better comprehension of the mechanism of rotary-wing stall.

2. Studies of the effect of compressibility on rotor torque calculations should be expanded to include the potential influence of blade flexibility, non-uniform inflow, and finite span effects.

3. More experimental and analytical work is required to determine the contribution of radial flow to rotor drag.

4. With present experimental data as a basis, correlation of measured time histories and harmonic content of blade stress and control loads with results of flexible blade theory should be undertaken in order to provide improved understanding of blade stress and control load behavior, particularly at high advancing tip Mach number and high advance ratio.

REFERENCES CITED

1. Fradenburgh, E. A., HIGH PERFORMANCE SINGLE ROTOR
   HELICOPTER STUDY, SER-50174, Sikorsky Aircraft Division
   of United Aircraft Corporation, Stratford, Connecticut;
   USAAVLABS Technical Report 61-44, U. S. Army Aviation
   Materiel Laboratories, Fort Eustis, Virginia, April 1961.

2. Sheiman, J. A., TABULATION OF HELICOPTER ROTOR-BLADE
   DIFFERENTIAL PRESSURES, STRESSES, AND MOTIONS AS
   MEASURED IN FLIGHT, NASA TM X-952, Langley Research
   Center, Langley Station, Hampton, Virginia, March 1964.

3. Rabbott, J. P., Jr., Lizak, A. A., Paglino, V. M., A
   PRESENTATION OF MEASURED AND CALCULATED FULL-SCALE
   ROTOR BLADE AERODYNAMIC AND STRUCTURAL LOADS, SER-
   58398, Sikorsky Aircraft Division of United Aircraft Corporation,
   Stratford, Connecticut; USAAVLABS Technical Report 66-31,
   U. S. Army Aviation Materiel Laboratories, Fort Eustis,
   Virginia, July 1966.

4. Tanner, W. H., CHARTS FOR ESTIMATING ROTARY WING
   PERFORMANCE IN HOVER AND AT HIGH FORWARD SPEEDS,
   SER-50379, Sikorsky Aircraft Division of United Aircraft
   Corporation, Stratford, Connecticut; NASA CR-114, National
   Aeronautics and Space Administration, Washington, D. C.,
   November 1964.

5. Heyson, H. H., JET-BOUNDARY CORRECTIONS FOR LIFTING
   ROTORS CENTERED IN RECTANGULAR WIND TUNNELS, NASA
   TR R-71, National Aeronautics and Space Administration,
   Washington, D. C., 1960.

6. Rabbott, J. P., Jr., COMPARISON OF THEORETICAL AND
   EXPERIMENTAL MODEL HELICOPTER ROTOR PERFORMANCE
   IN FORWARD FLIGHT, SER-50129, Sikorsky Aircraft Division
   of United Aircraft Corporation, Stratford, Connecticut; USAAVLABS
   Technical Report 61-103, U. S. Army Aviation Materiel
   Laboratories, Fort Eustis, Virginia, July 1961.

7. Rabbott, J. P., Jr., A STUDY OF THE OPTIMUM ROTOR GEOMETRY FOR A HIGH SPEED HELICOPTER, SER-50254, Sikorsky Aircraft Division of United Aircraft Corporation, Stratford, Connecticut; USAAVLABS Technical Report 62-53, U. S. Army Aviation Materiel Laboratories, Fort Eustis, Virginia, May 1962.

8. Norman, D. C., Somsel, J. R., DETERMINATION OF HELICOPTER ROTOR BLADE COMPRESSIBILITY EFFECTS - PREDICTION VS. FLIGHT TEST, Paper presented before the American Helicopter Society Twenty-Third Annual National Forum, Washington, D. C., May 10-12, 1967.

9. Fradenburgh, E. A., AERODYNAMIC EFFICIENCY POTENTIALS OF ROTARY WING AIRCRAFT, Paper presented before the American Helicopter Society Sixteenth Annual National Forum, Washington, D. C., May 11-14, 1960.

10. Niebanck, C. F., et al, PREDICTION OF ROTOR INSTABILITY AT HIGH FORWARD SPEEDS, SER-50469, Sikorsky Aircraft Division of United Aircraft Corporation, Stratford, Connecticut; USAAVLABS Technical Report (in preparation), U. S. Army Aviation Materiel Laboratories, Fort Eustis, Virginia.

11. Sikorsky, I. A., CORRELATION OF HELICOPTER PERFORMANCE EQUATIONS, Institute of the Aeronautical Sciences, Preprint No. 694, Paper presented at the Twenty-Fifth Annual Meeting, January 28-31, 1957.

12. Velkoff, H. R., A PRELIMINARY STUDY OF THE EFFECT OF A RADIAL PRESSURE GRADIENT ON THE BOUNDARY LAYER ON A ROTOR BLADE, Ohio State University, Paper presented before the Cornell Aeronautical Laboratory, Inc. - U. S. Army Aviation Materiel Laboratories Symposium on Aerodynamic Problems Associated With V/STOL Aircraft, Buffalo, New York, June 22-24, 1966.

13. Fradenburgh, E. A., REQUIRED AERODYNAMIC RESEARCH FOR V/STOL AIRCRAFT, Paper presented before the Cornell Aeronautical Laboratory, Inc. - U. S. Army Aviation Materiel Laboratories Symposium on Aerodynamic Problems Associated With V/STOL Aircraft, Buffalo, New York, June 22-24, 1966.

14. Bergquist, R. R., Tanner, W. H., SOME PROBLEMS OF DESIGN AND OPERATION OF A 250 KNOT COMPOUND HELICOPTER ROTOR, Paper Presented before the American Institute of Aeronautics and

Astronautics General Aircraft Design and Operations Meeting, Wichita, Kansas, May 25-27, 1964.

15. Anonymous, FINAL REPORT OF NH-3A FLIGHT TEST PROGRAM, in preparation, SER-611344, Sikorsky Aircraft Division of United Aircraft Corporation, Stratford, Connecticut, NOw 64-0528-f.

16. Van Wyckhouse, J. F., HIGH PERFORMANCE HELICOPTER PROGRAM, SUMMARY REPORT, PHASE II, Bell Helicopter Company; USAAVLABS Technical Report 64-61, U. S. Army Aviation Materiel Laboratories, Fort Eustis, Virginia, October 1964.
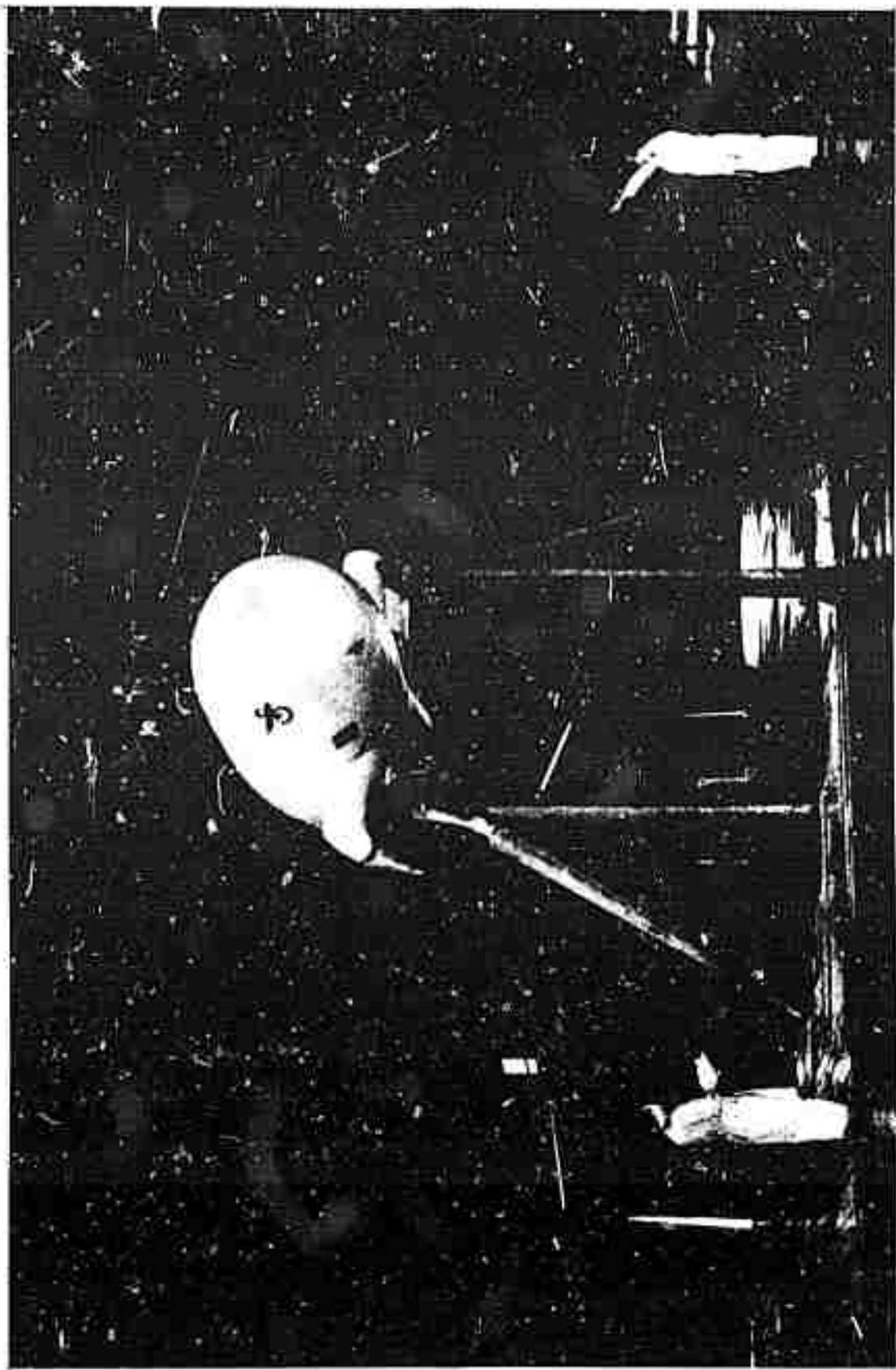
Figure 1. Sikorsky CH-34 Rotor Installed in the NASA/Ames Full-Scale Wind Tunnel.
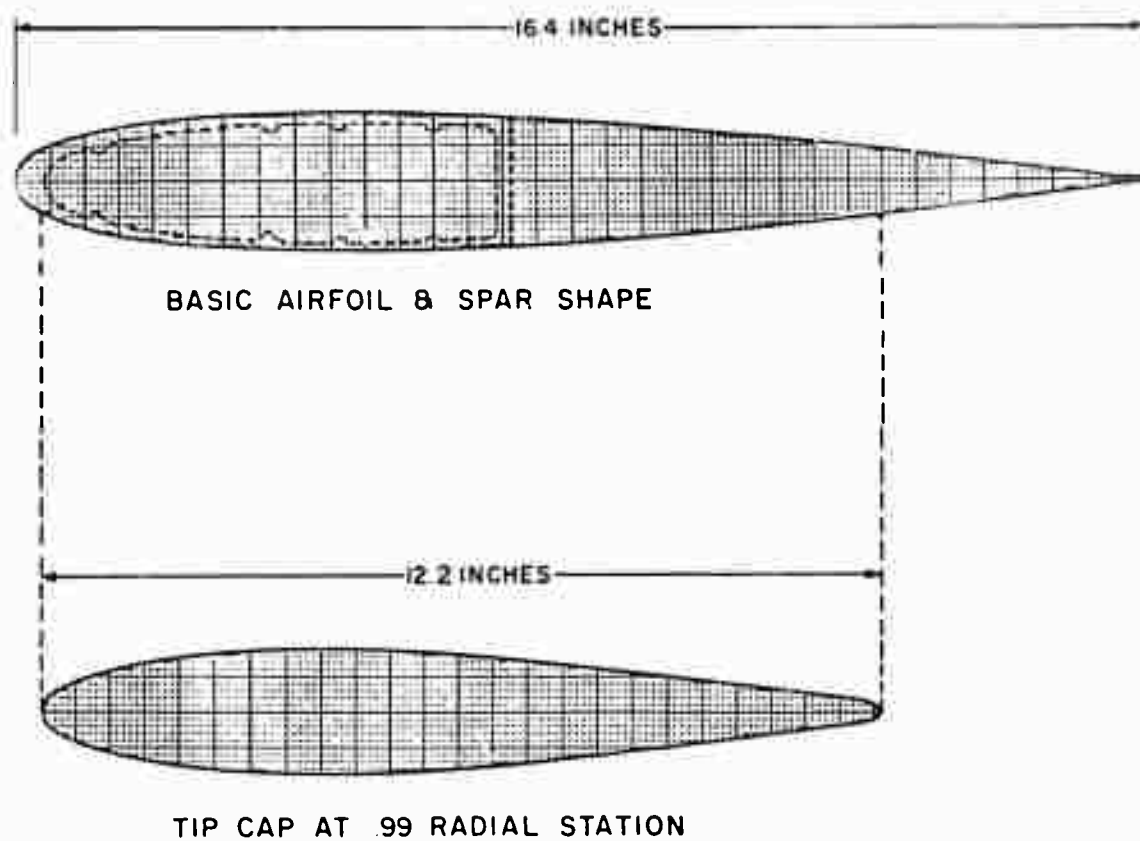
Figure 2.   A Comparison of Basic Airfoil, Spar and Tip
            Cap Cross Sections.
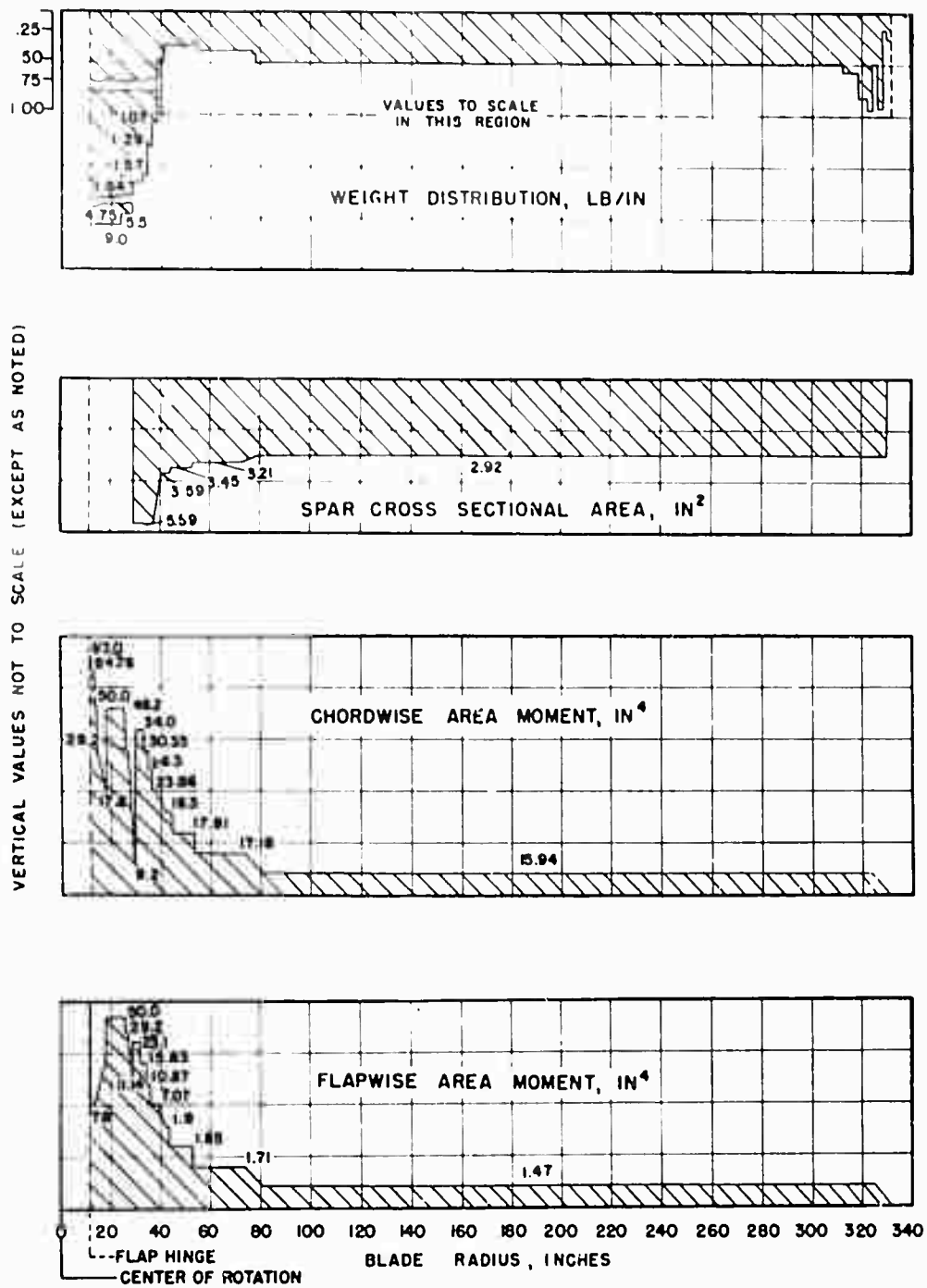
Figure 3.   Rotor Blade Structural Characteristics.

40
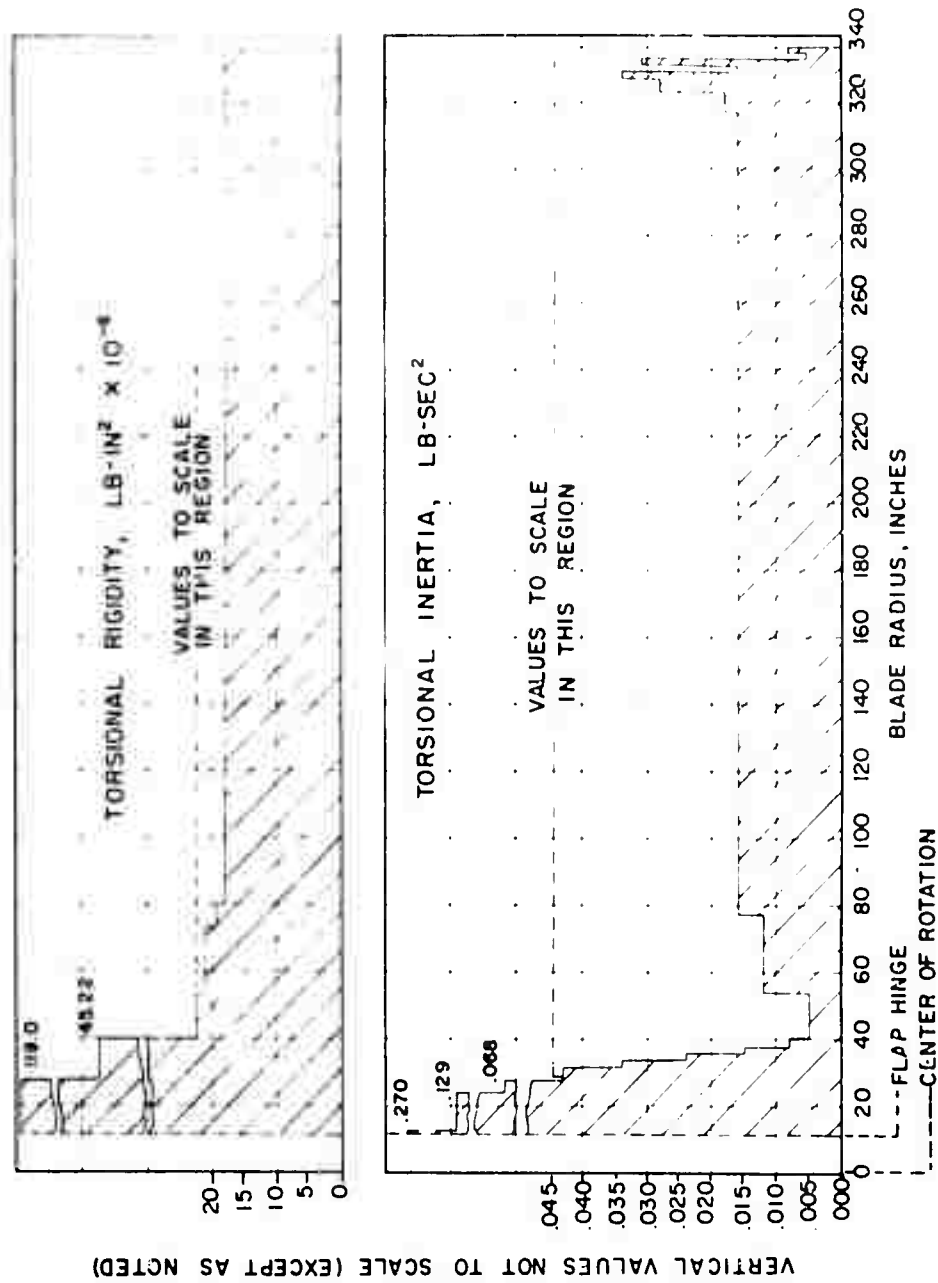
Figure 3. Concluded.

41
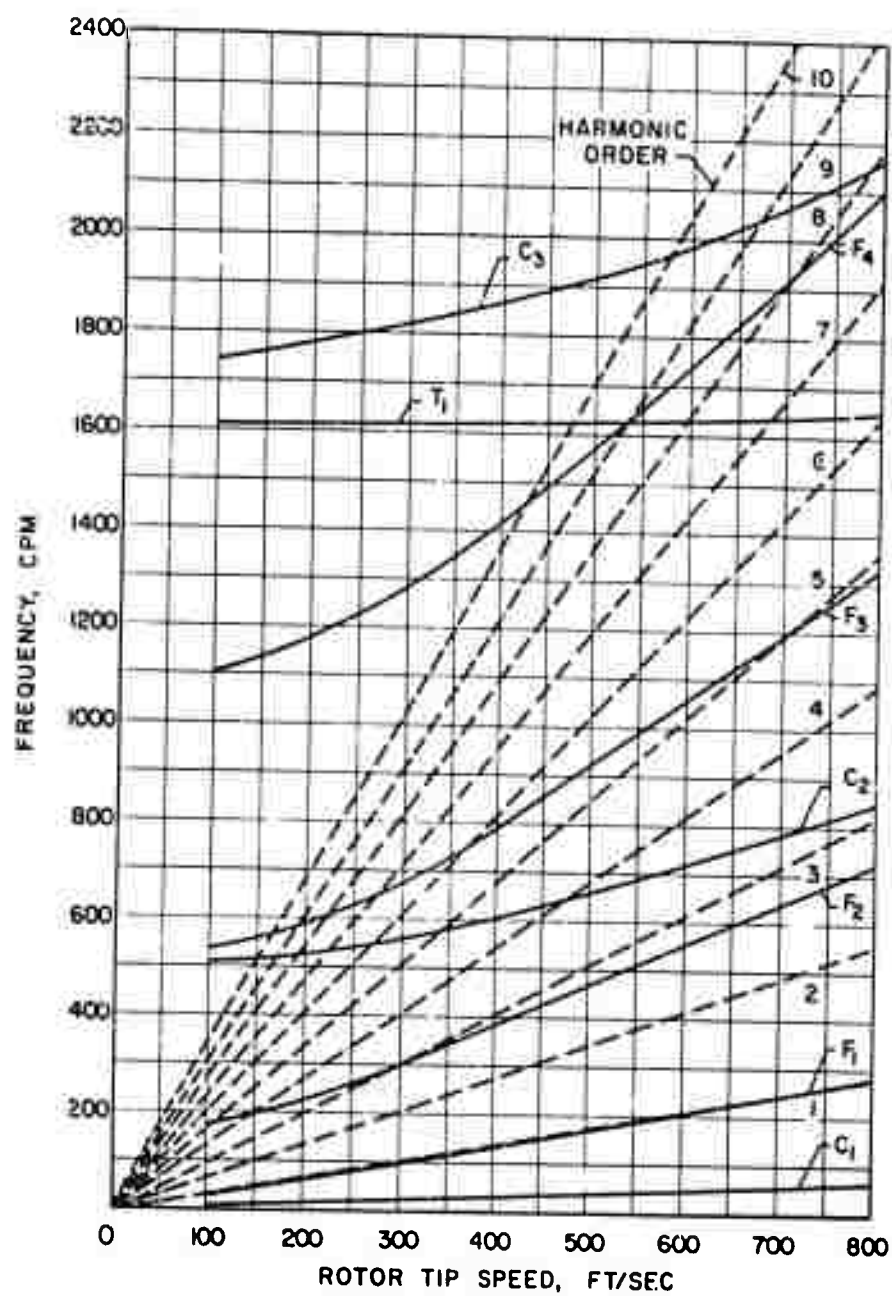
Figure 4. Rotor Blade Natural Frequency Diagram.

42
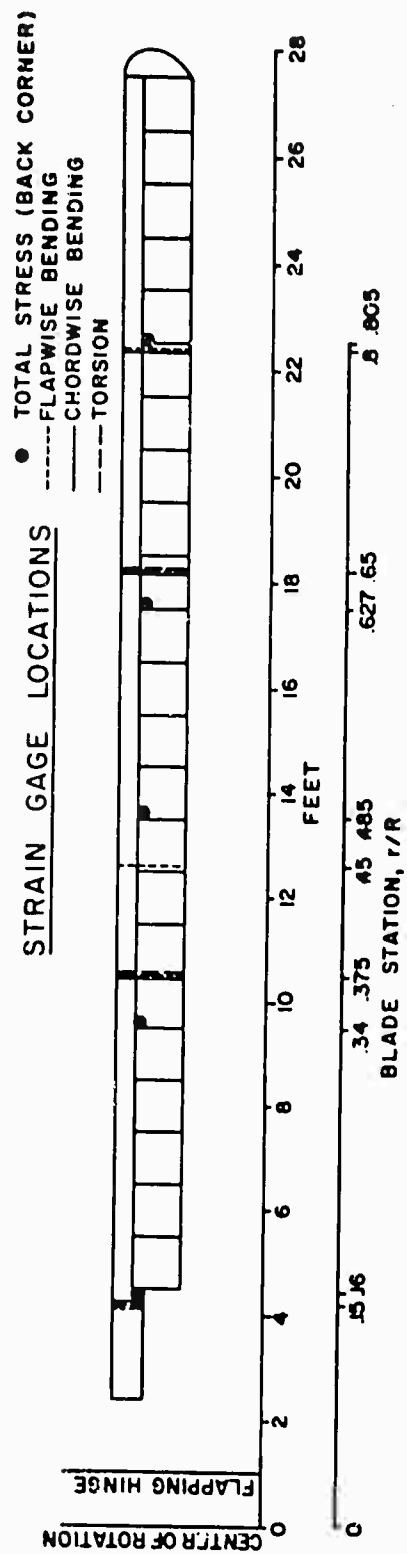
Figure 5.   Location of Blade Strain Gages.

43
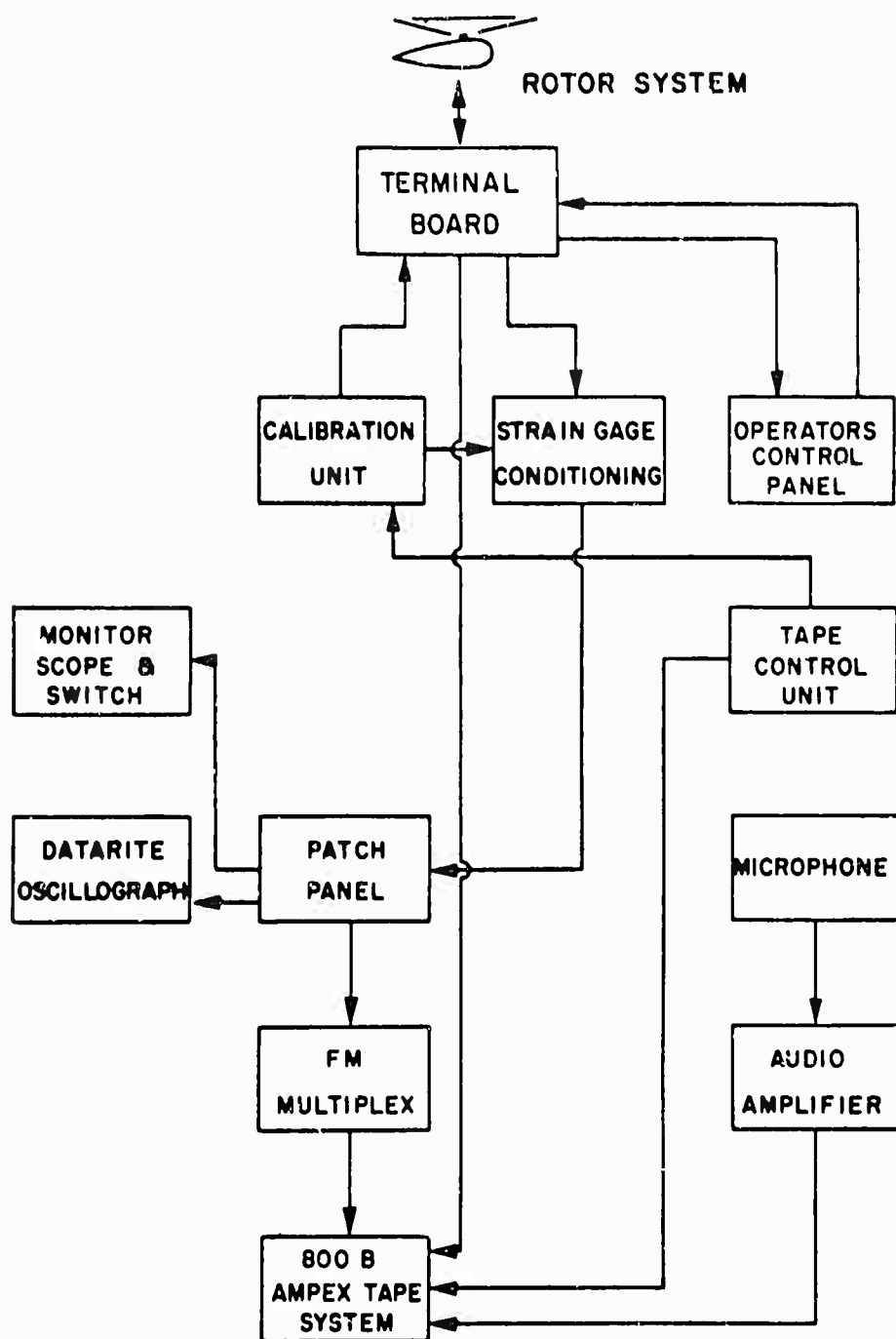
Figure 6.   Flow Chart of Data Acquisition System.
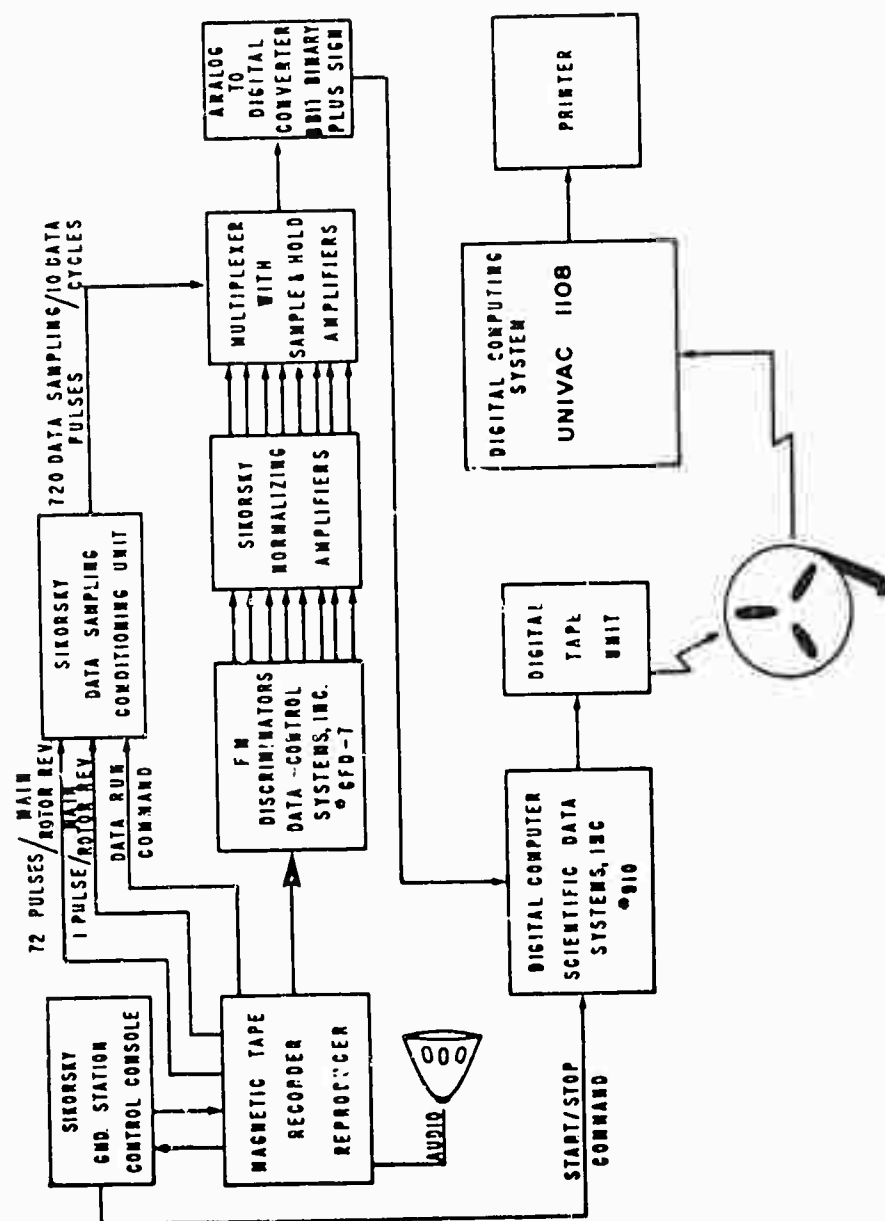
Figure 7. Flow Chart of Data Processing System.

45
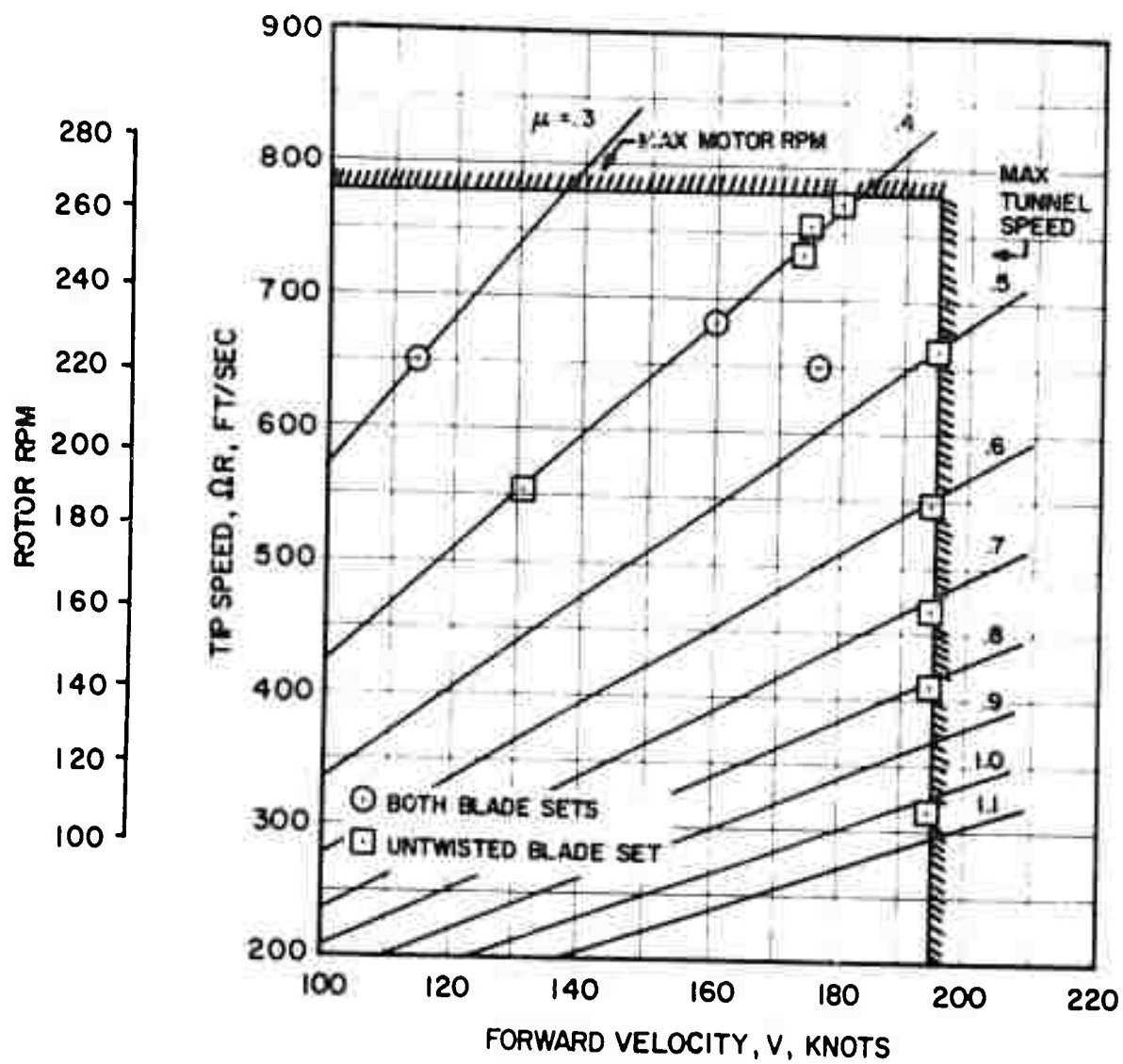
Figure 8. Diagram of the Combinations of Tip Speed and
Forward Velocity Investigated.

46
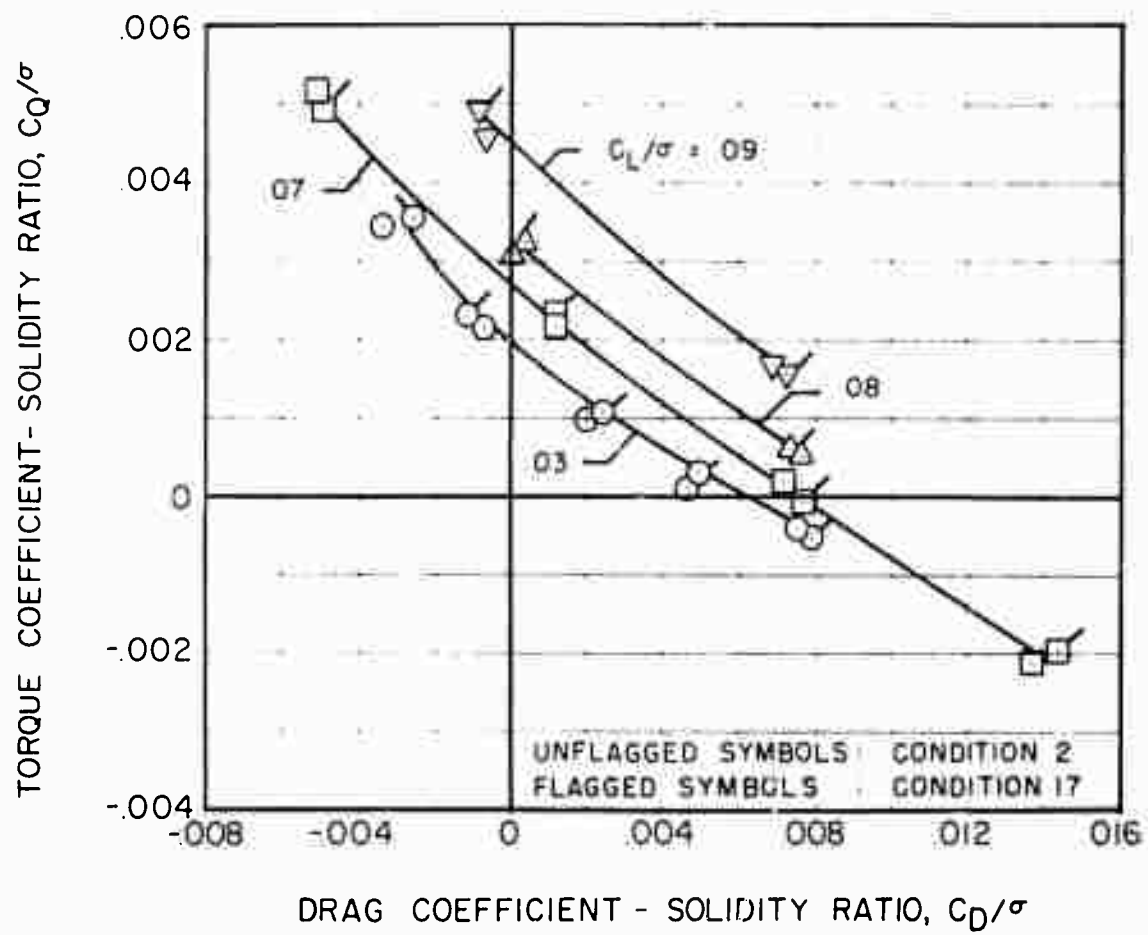
Figure 9. Sample Repeatability of Torque Versus Drag at Several Values of Lift for Two Separate Test Runs, $V \approx 162$ Knots, $\mu = 0.40$, $\theta_1 = -8°$, $M_{(1.0, 90)} = 0.82$.

47
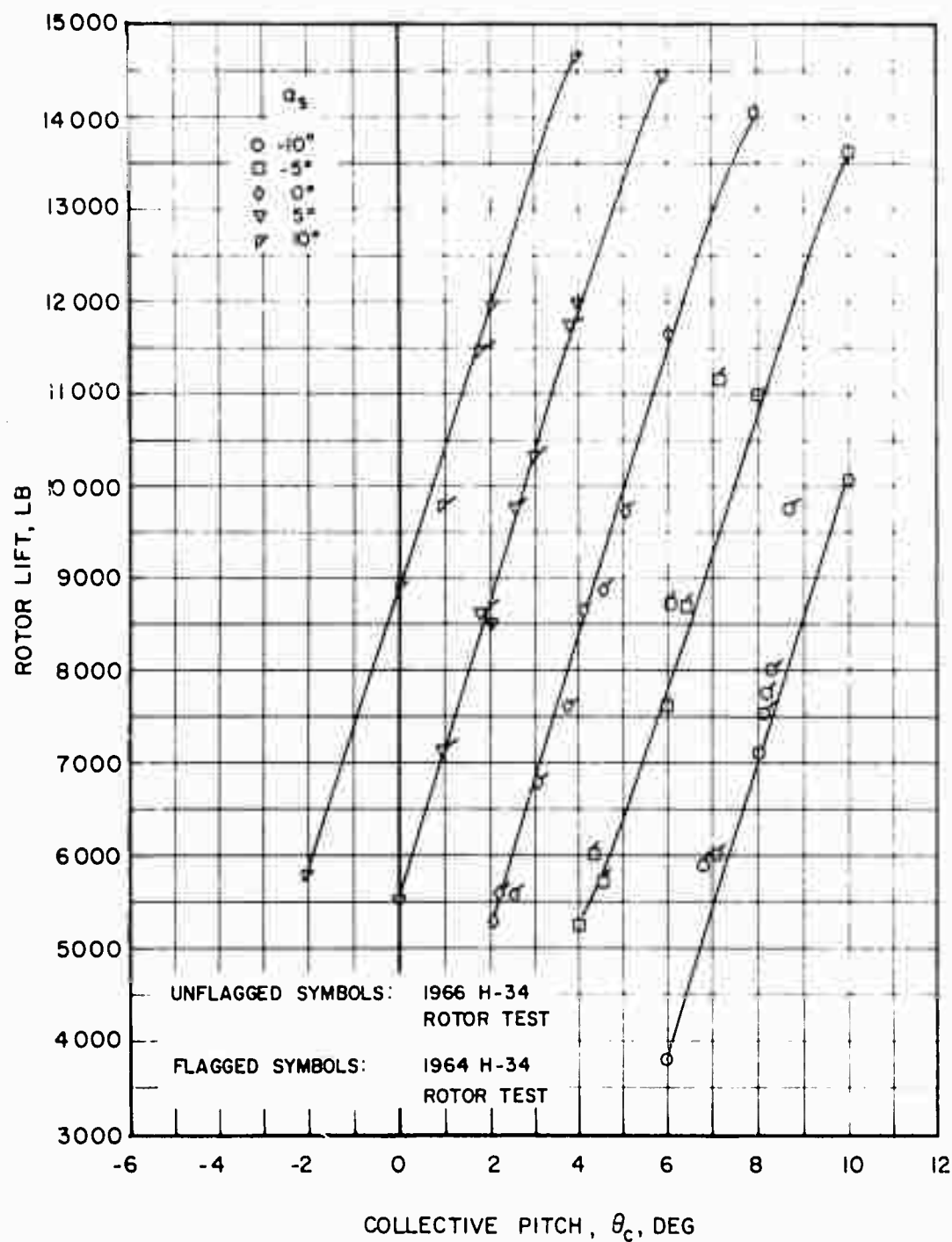
Figure 10. A Comparison of Rotor Lift, Drag, and Horsepower
Versus Collective Pitch at Various Shaft Angles for
Two Separate Wind Tunnel Entries, θ_1 = -8°;
1966 Test: V = 117 Knots, μ = 0.30;
1964 Test: V = 110 Knots, μ = 0.28.

48
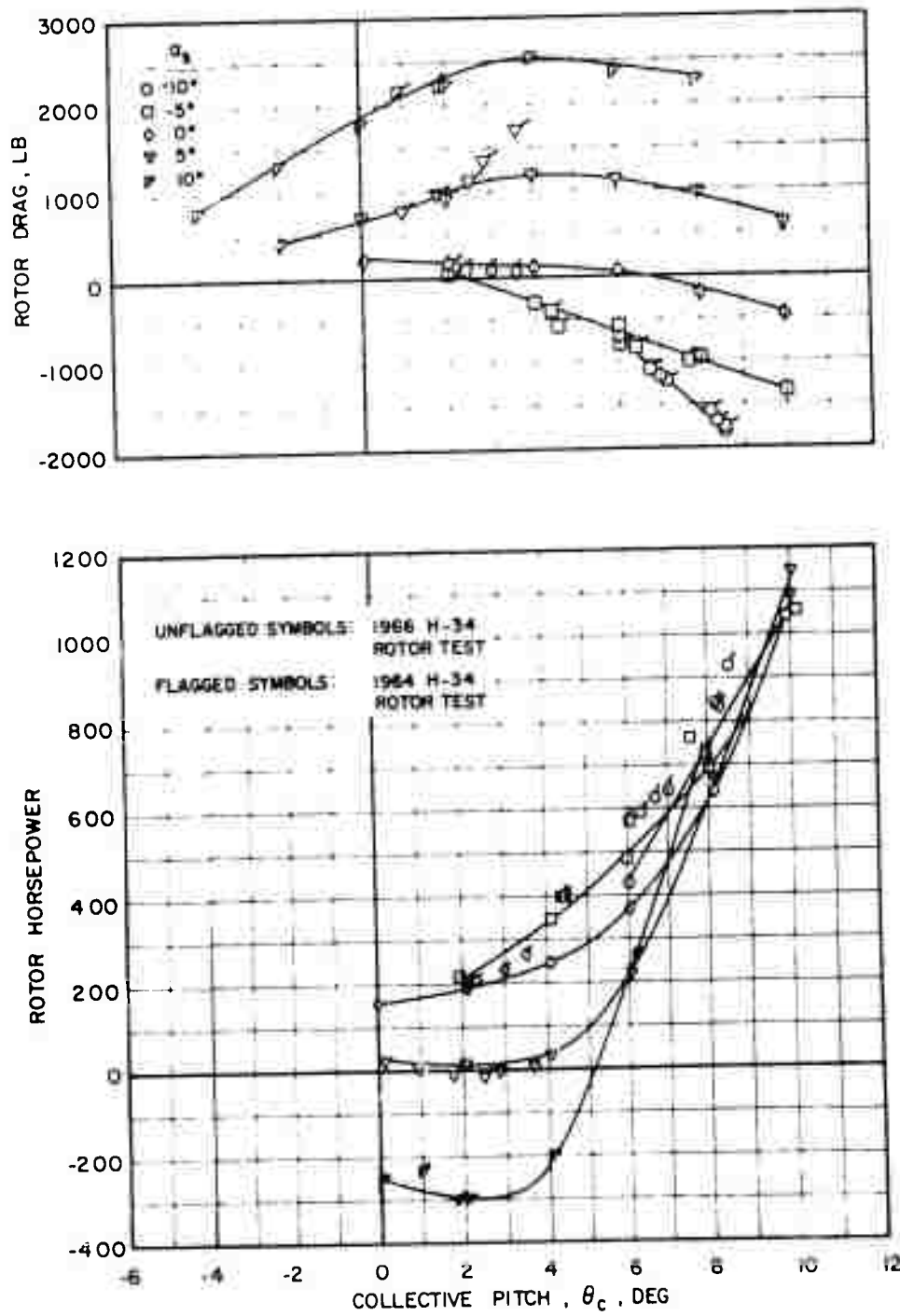
Figure 10. Concluded.

49
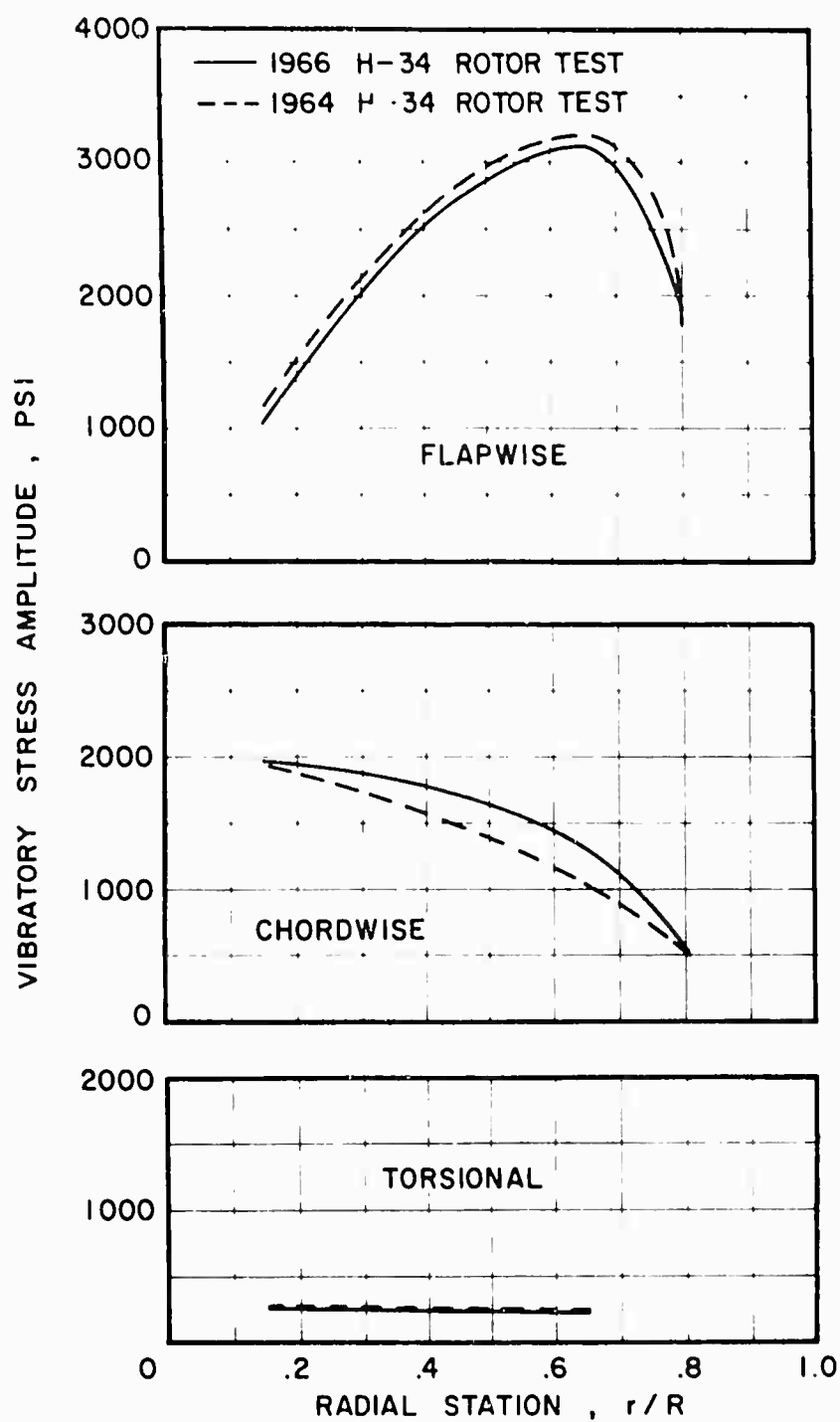
Figure 11. A Comparison of Rotor Flapwise, Chordwise, and Torsional Vibratory Stress Amplitude Versus Radial Station for Two Separate Wind Tunnel Entries, $\theta_1 = -8°$, $\alpha_s = 0°$; 1966 Test: V = 117 Knots, μ = 0.30, C_L/σ = 0.071, 1964 Test: V = 110 Knots, μ = 0.23, C_L/σ = 0.069.

50

VIBRATORY STRESS AMPLITUDE , PSI

◊ EXPERIMENTAL DATA FROM NASA
TM X – 952 FLIGHT # 22

⁄⁄⁄⁄⁄⁄ WIND TUNNEL DATA

FLAPWISE

CHORDWISE

TORSIONAL
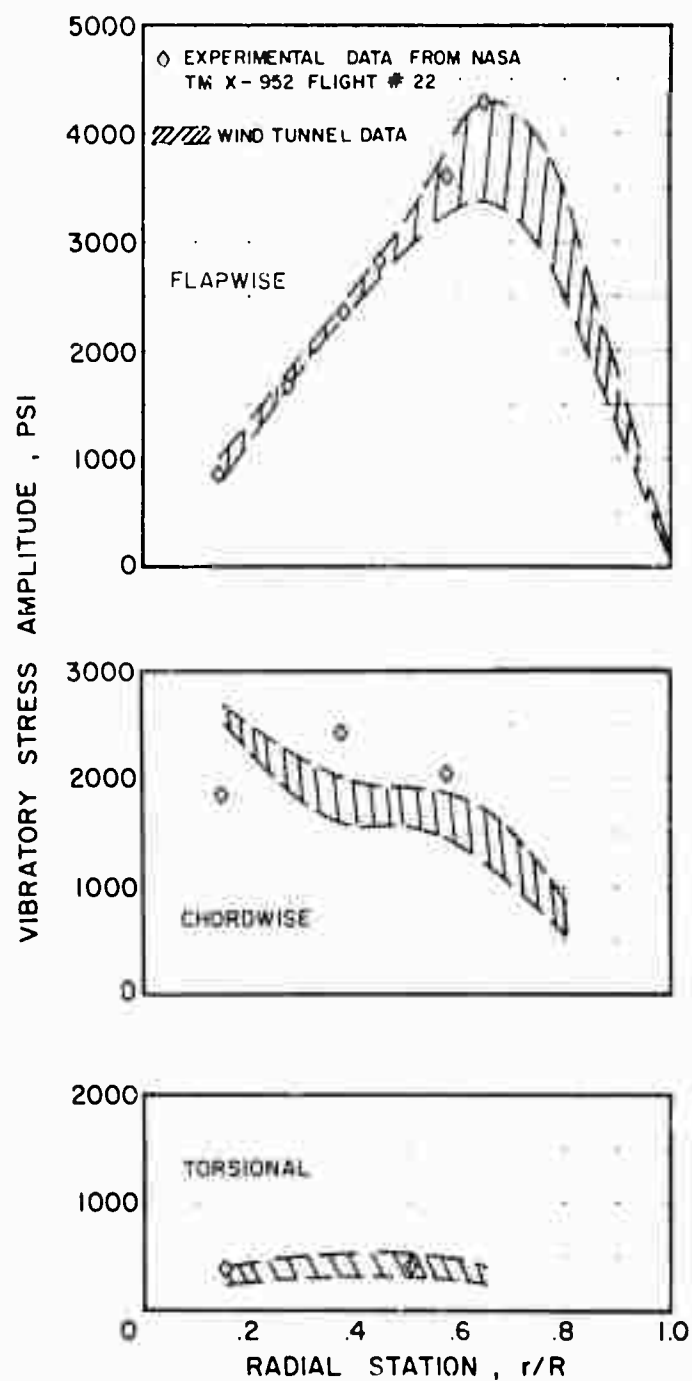
RADIAL STATION , r/R

Figure 12.   A Comparison of Flapwise, Chordwise, and
Torsional Vibratory Stress Amplitude Versus
Radial Station for Both Wind Tunnel and Flight
Test Results, V = 117 Knots, μ = 0.30,
α_s = -5°, θ_1 = -8°.

51
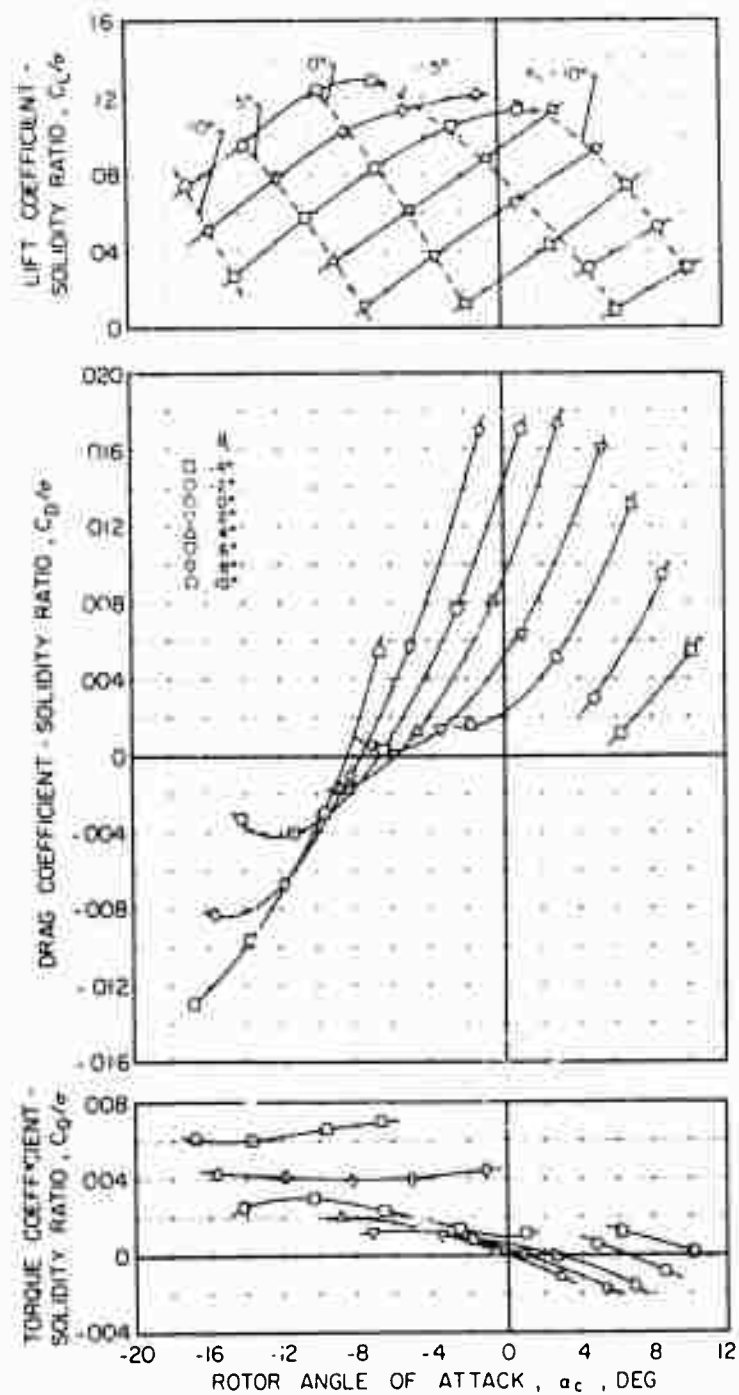
Figure 13. Variation of Lift, Drag, and Torque With Rotor Angle of Attack for Various Shaft Angle and Collective Pitch Settings, $V = 117$ Knots, $\mu = 0.30$, $\theta_1 = -8°$, $M_{(1.0, 90)} = 0.74$.

52
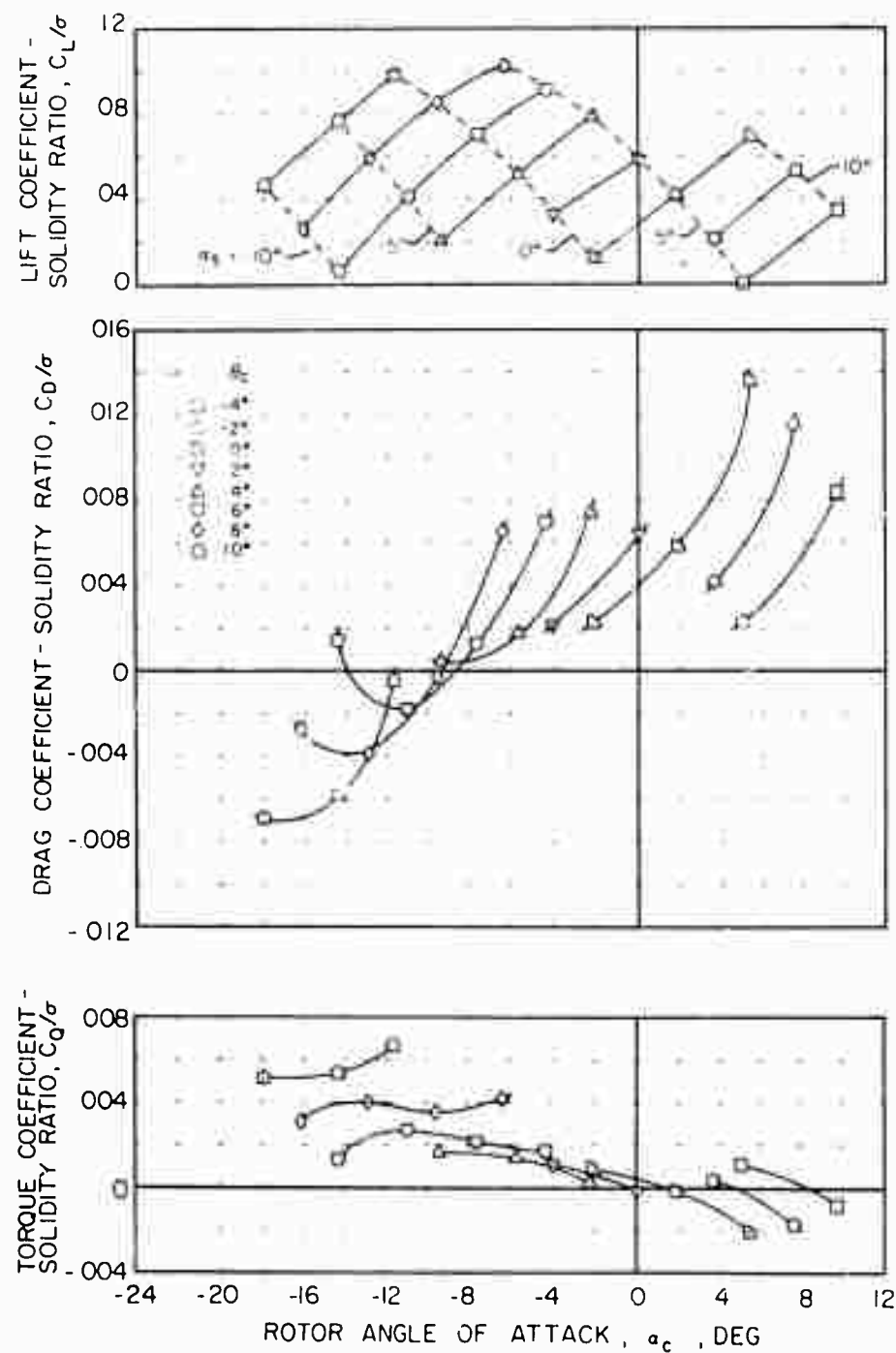
Figure 14.   Variation of Lift, Drag, and Torque With Rotor
Angle of Attack for Various Shaft Angle and
Collective Pitch Settings, V = 161 Knots,
μ = 0.40, θ_1 = -8°, $M_{(1.0, 90)}$ = 0.82.

53
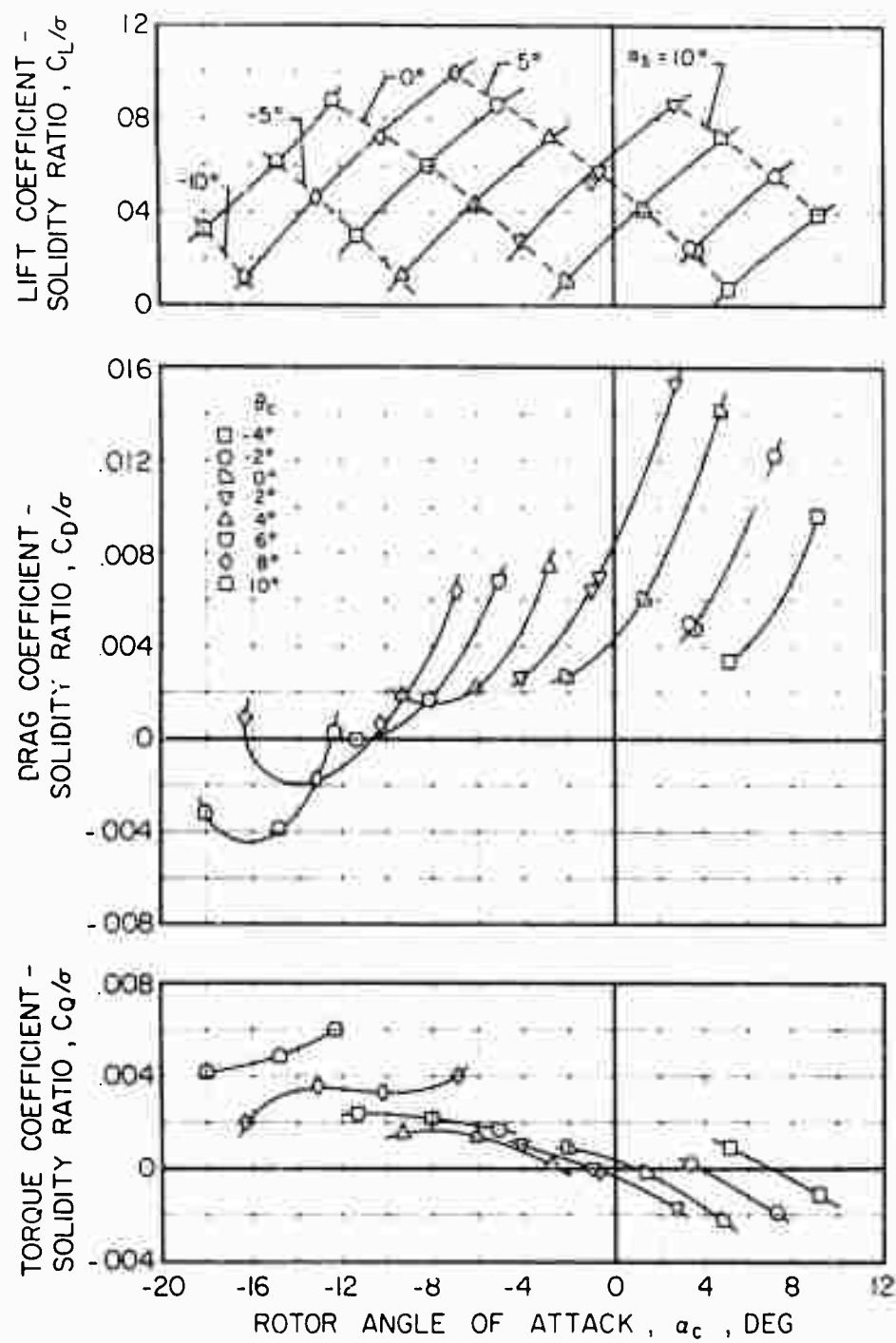
Figure 15.   Variation of Lift, Drag, and Torque With Rotor
Angle of Attack for Various Shaft Angle and
Collective Pitch Settings, V = 177 Knots,
$\mu = 0.46$, $\theta_1 = -8°$, $M_{(1.0, 90)} = 0.82$.

54
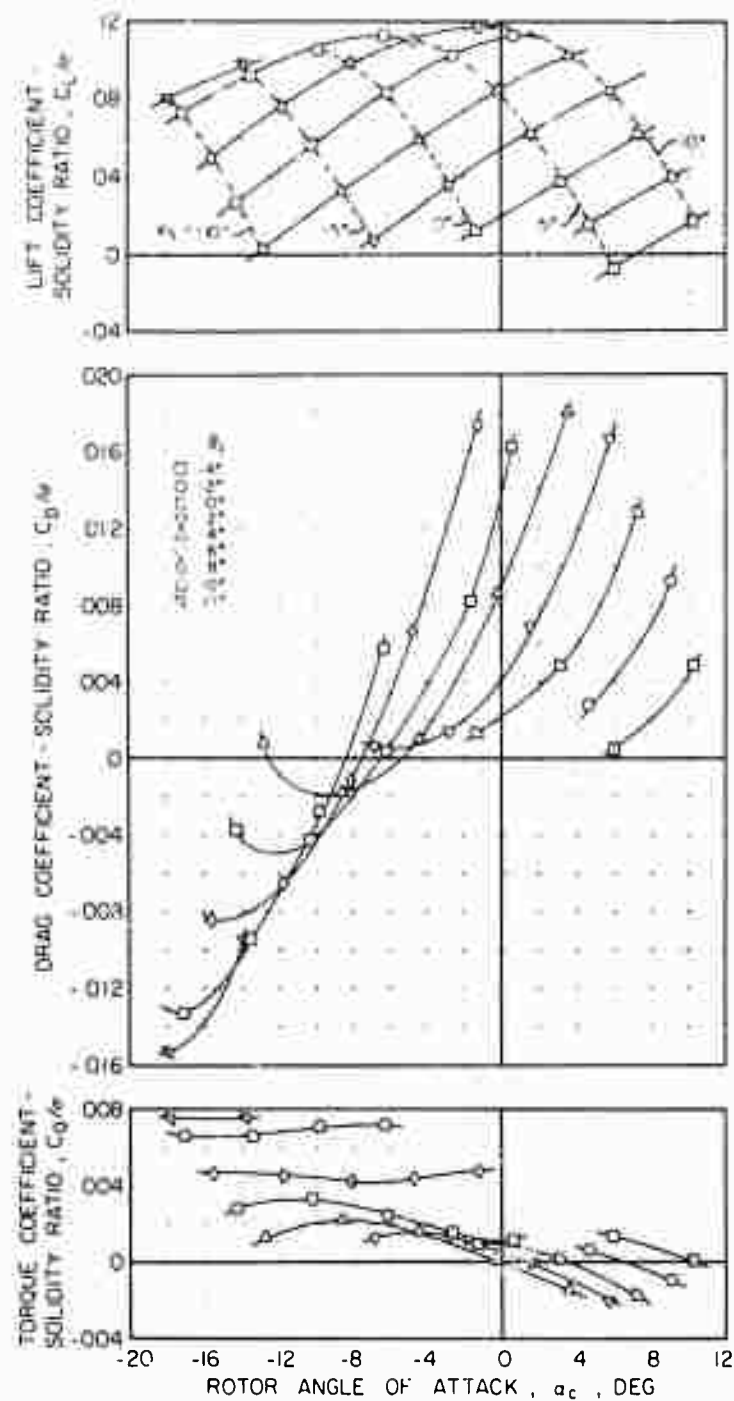
Figure 16. Variation of Lift, Drag, and Torque With Rotor
Angle of Attack for Various Shaft Angle and
Collective Pitch Settings, V = 116 Knots,
$\mu = 0.30$, $\theta_1 = 0°$, $M_{(1.0, 90)} = 0.74$.

55
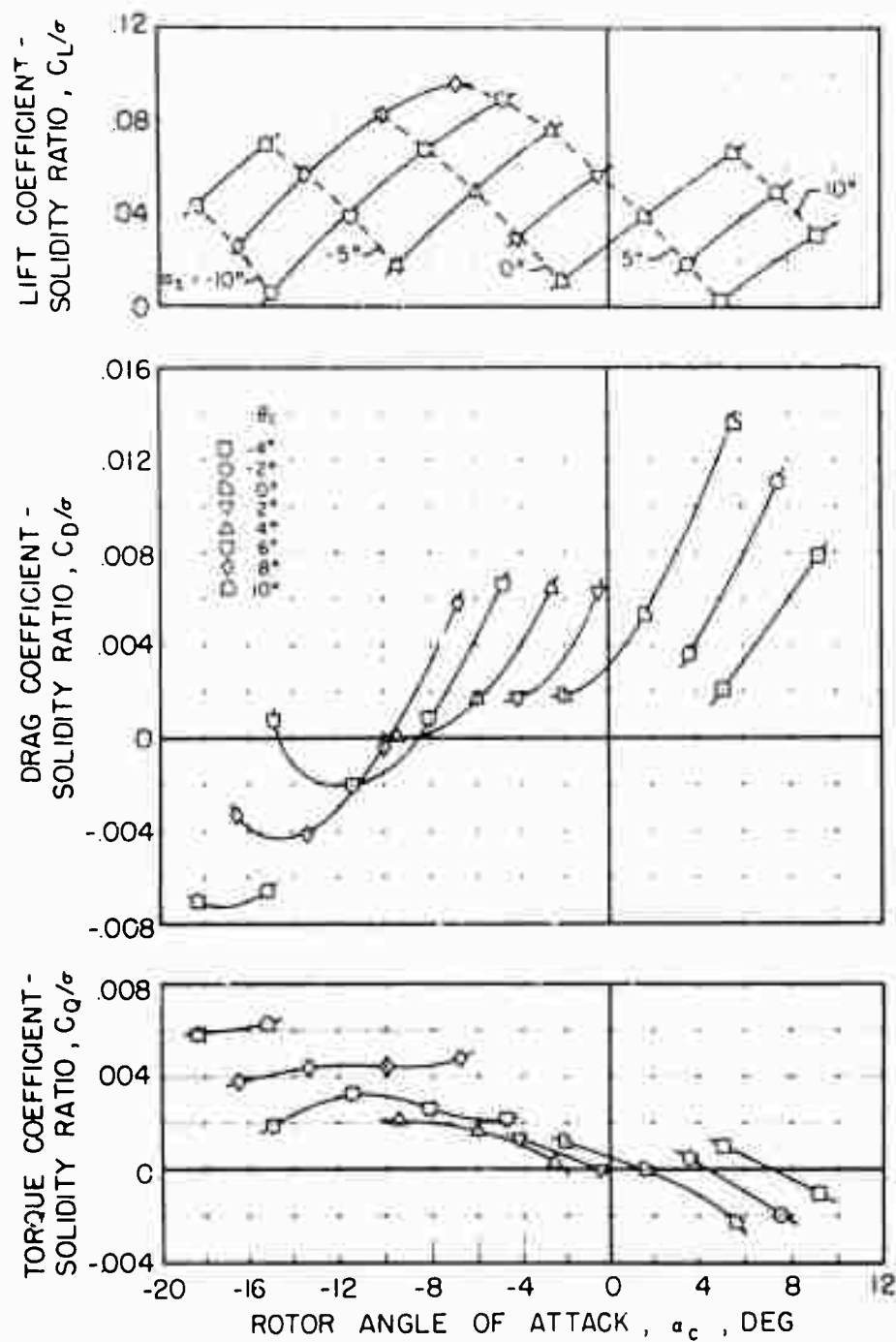
Figure 17. Variation of Lift, Drag, and Torque With Rotor Angle of Attack for Various Shaft Angle and Collective Pitch Settings, V = 162 Knots, μ = 0.40, θ_1 = 0°, $M_{(1.0, 90)}$ = 0.83.

56
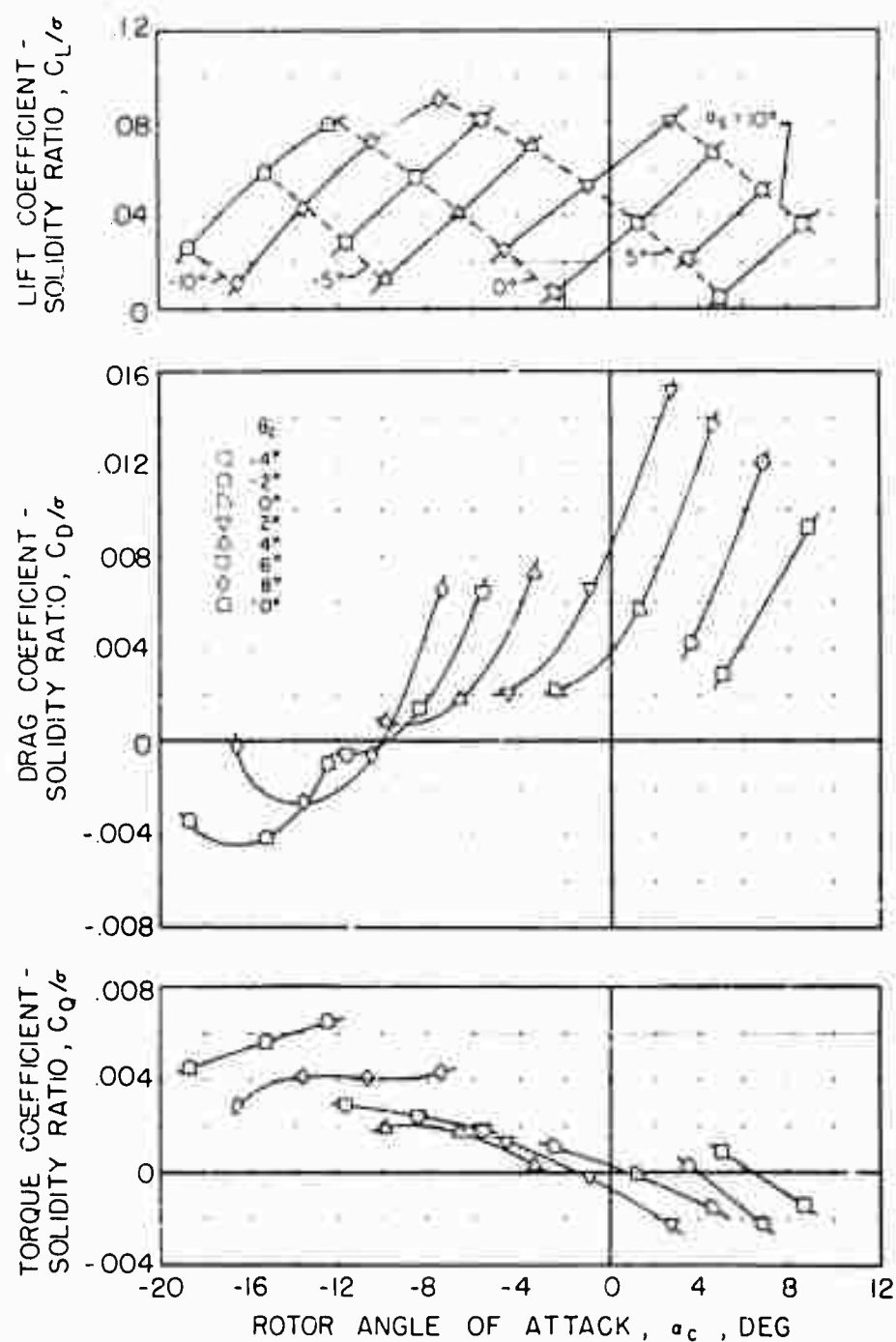
Figure 18. Variation of Lift, Drag, and Torque With Rotor Angle of Attack for Various Shaft Angle and Collective Pitch Setting, V = 178 Knots, μ = 0.46, θ_1 = 0°, $M_{(1.0, 90)}$ = 0.82.

57
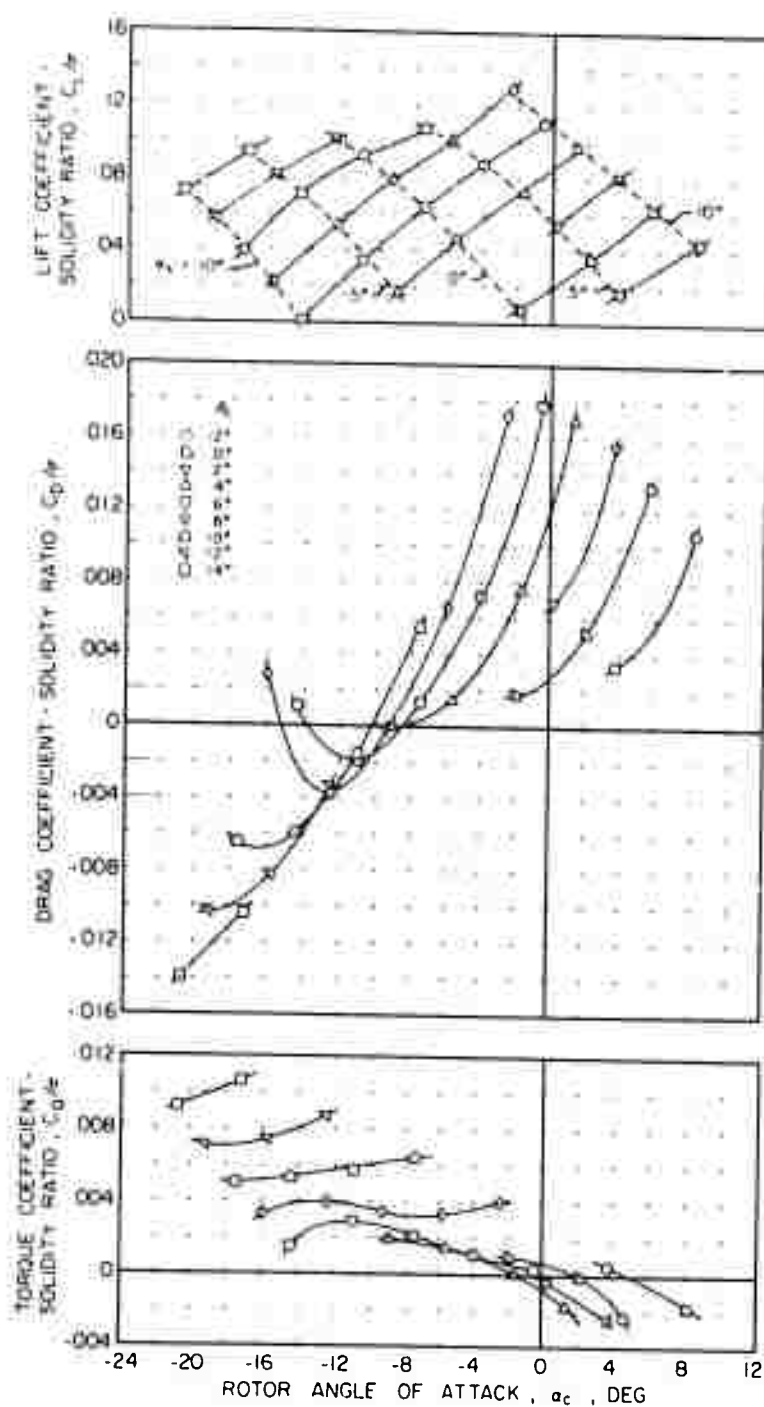
Figure 19. Variation of Lift, Drag, and Torque With Rotor Angle of Attack for Various Shaft Angle and Collective Pitch Settings, V = 132 Knots, μ = 0.40, θ_1 = 0°, $M_{(1.0, 90)}$ = 0.67.

58
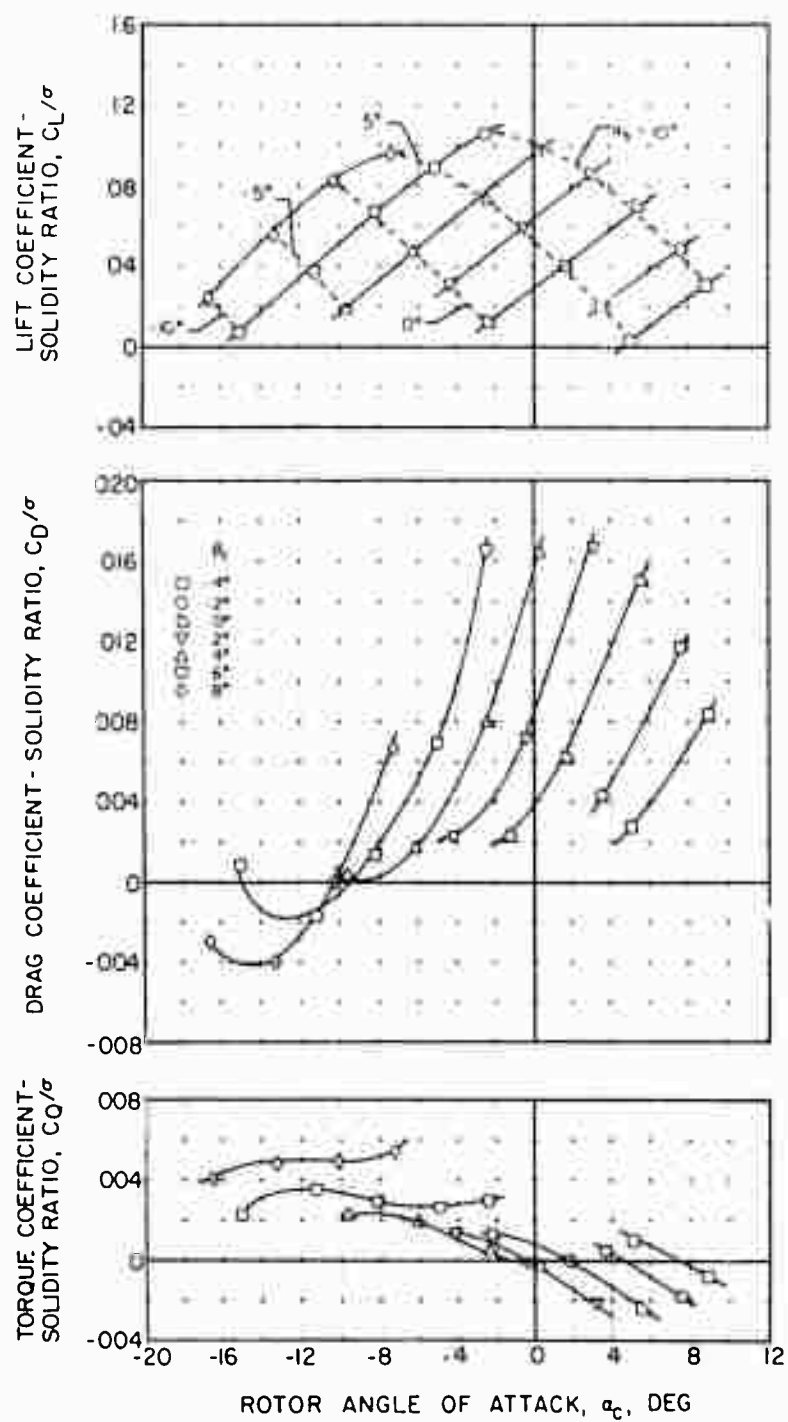
Figure 20. Variation of Lift, Drag, and Torque With Rotor
Angle of Attack for Various Shaft Angle and
Collective Pitch Settings, V = 174 Knots,
$\mu = 0.41$, $\theta_1 = 0°$, $M_{(1.0, 90)} = 0.87$.

59
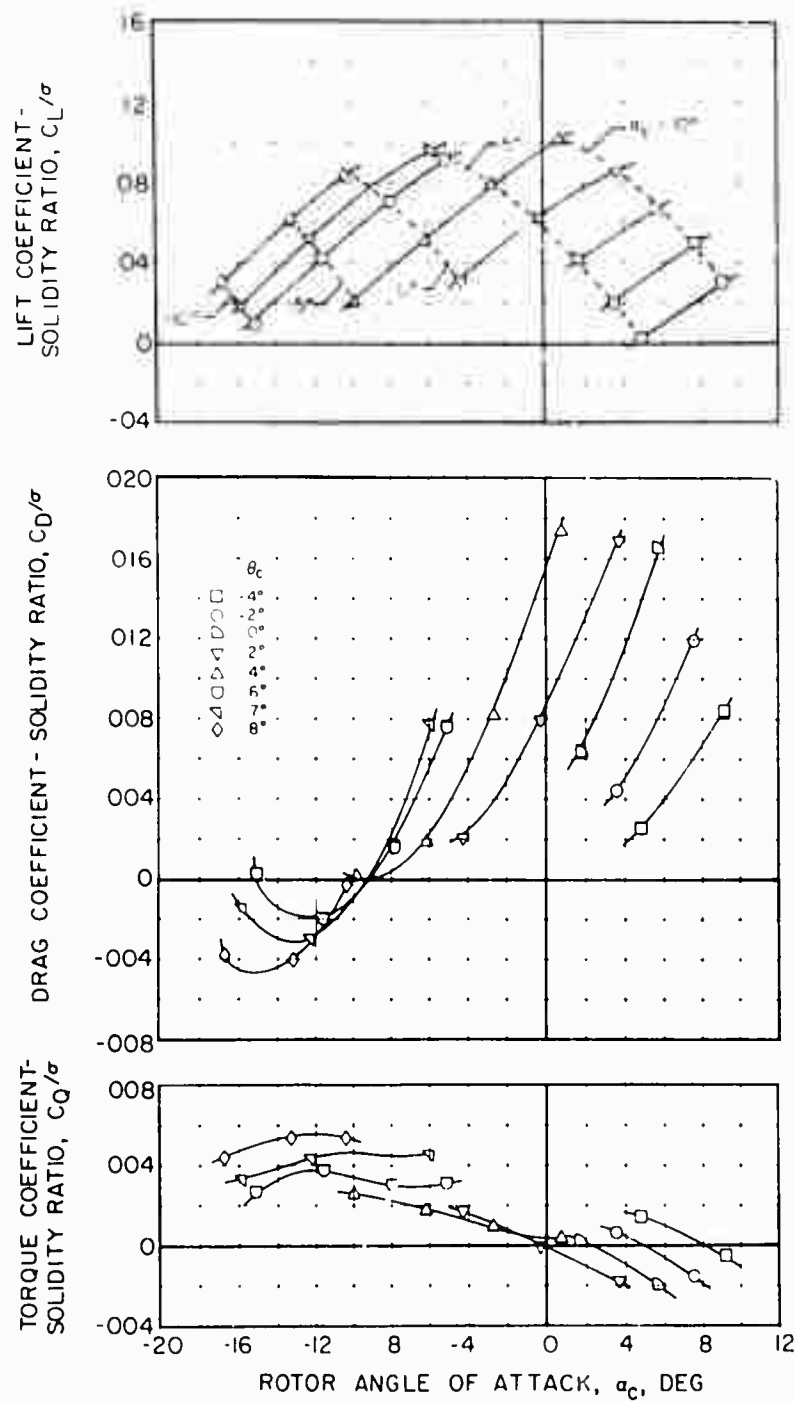
Figure 21. Variation of Lift, Drag, and Torque With Rotor
Angle of Attack for Various Shaft Angle and
Collective Pitch Settings, V = 175 Knots,
$\mu = 0.39$, $\theta_1 = 0°$, $M_{(1.0, 90)} = 0.89$.

60
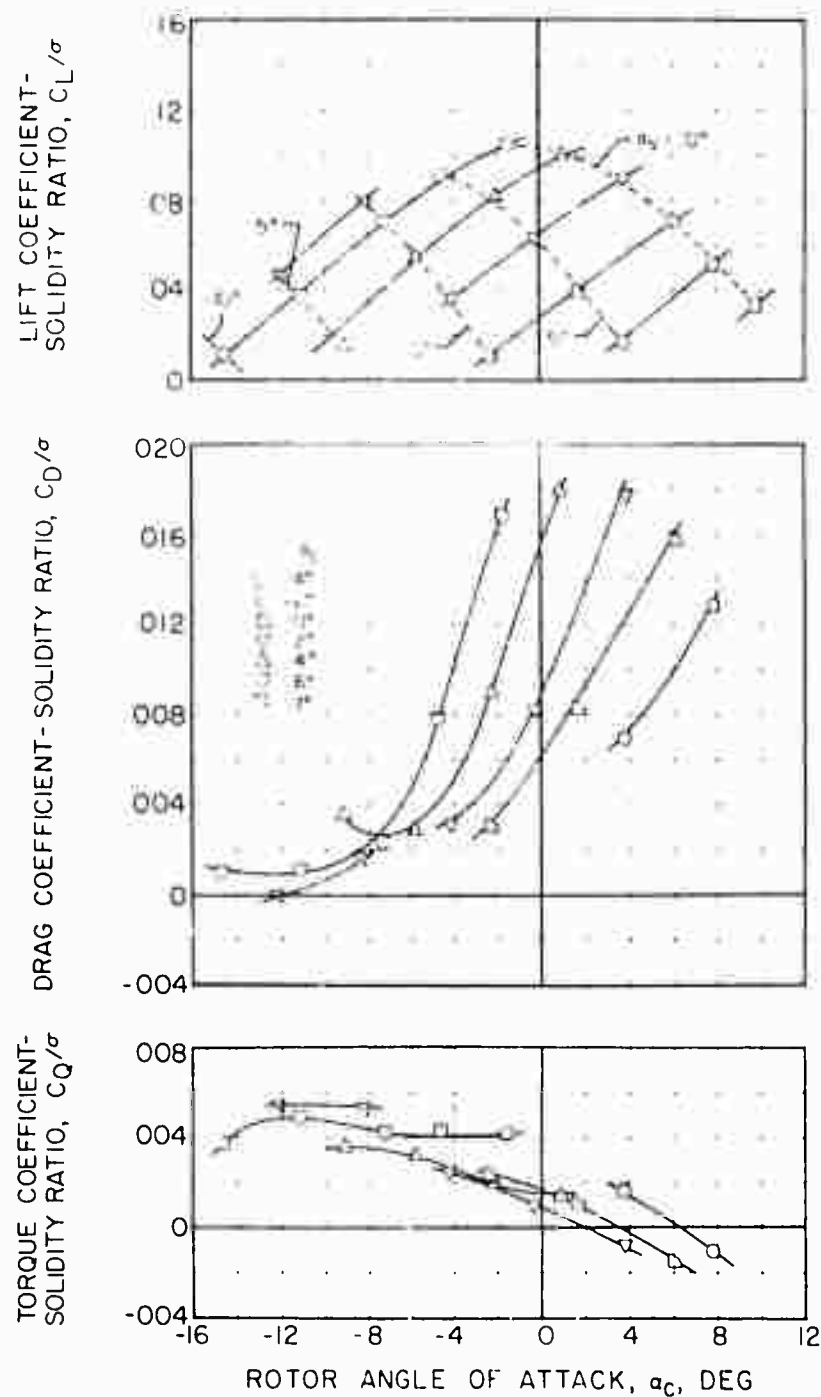
Figure 22.   Variation of Lift, Drag, and Torque With Rotor
             Angle of Attack for Various Shaft Angle and
             Collective Pitch Settings. $V = 180$ Knots,
             $\mu = 0.39$, $\theta_1 = 0°$, $M_{(1.0, 90)} = 0.93$.
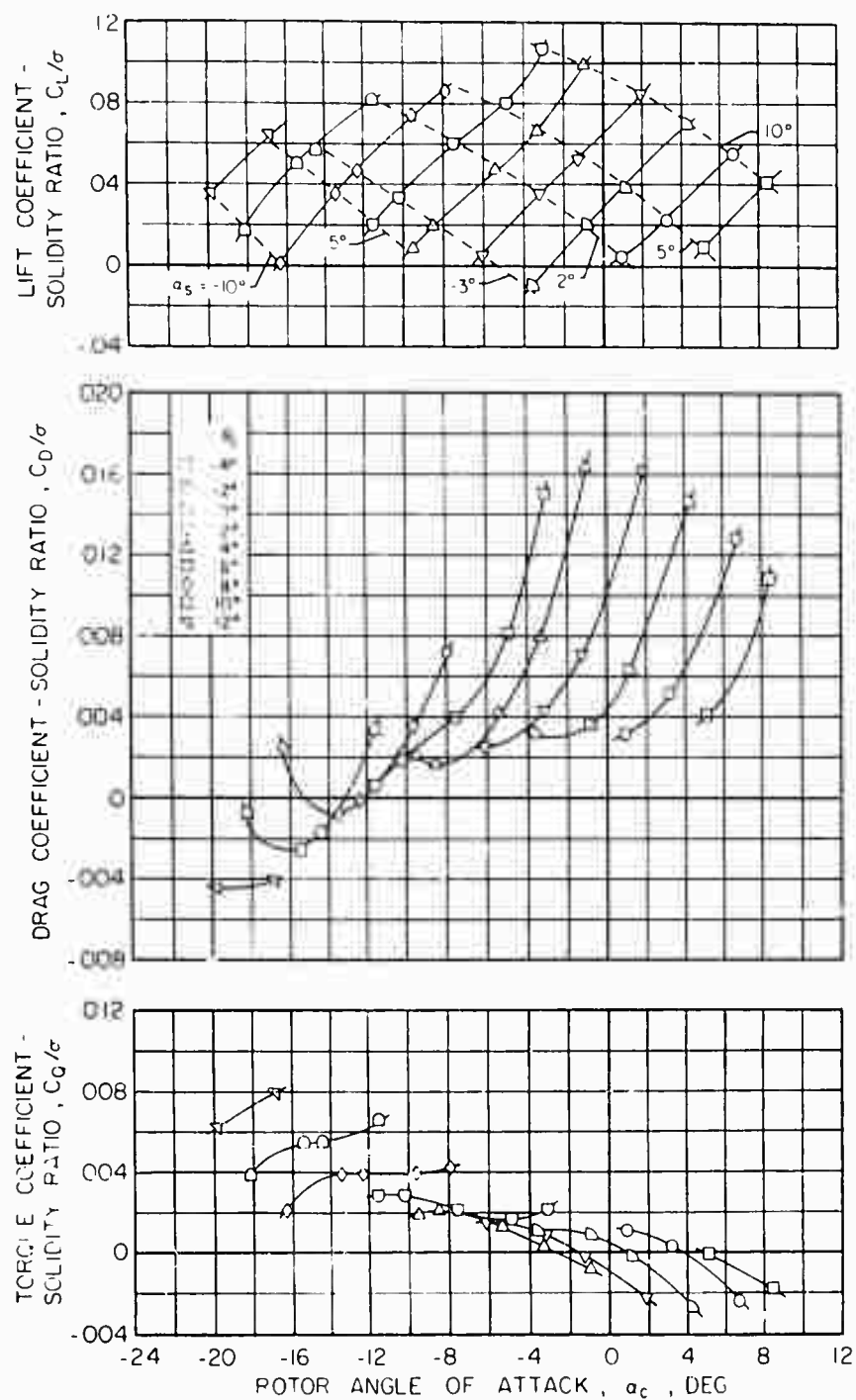
Figure 23.   Variation of Lift, Drag, and Torque With Rotor
Angle of Attack for Various Shaft Angle and
Collective Pitch Settings, V = 194 Knots,
μ = 0.50, θ_1 = 0°, $M_{(1.0, 90)}$ = 0.83.

62
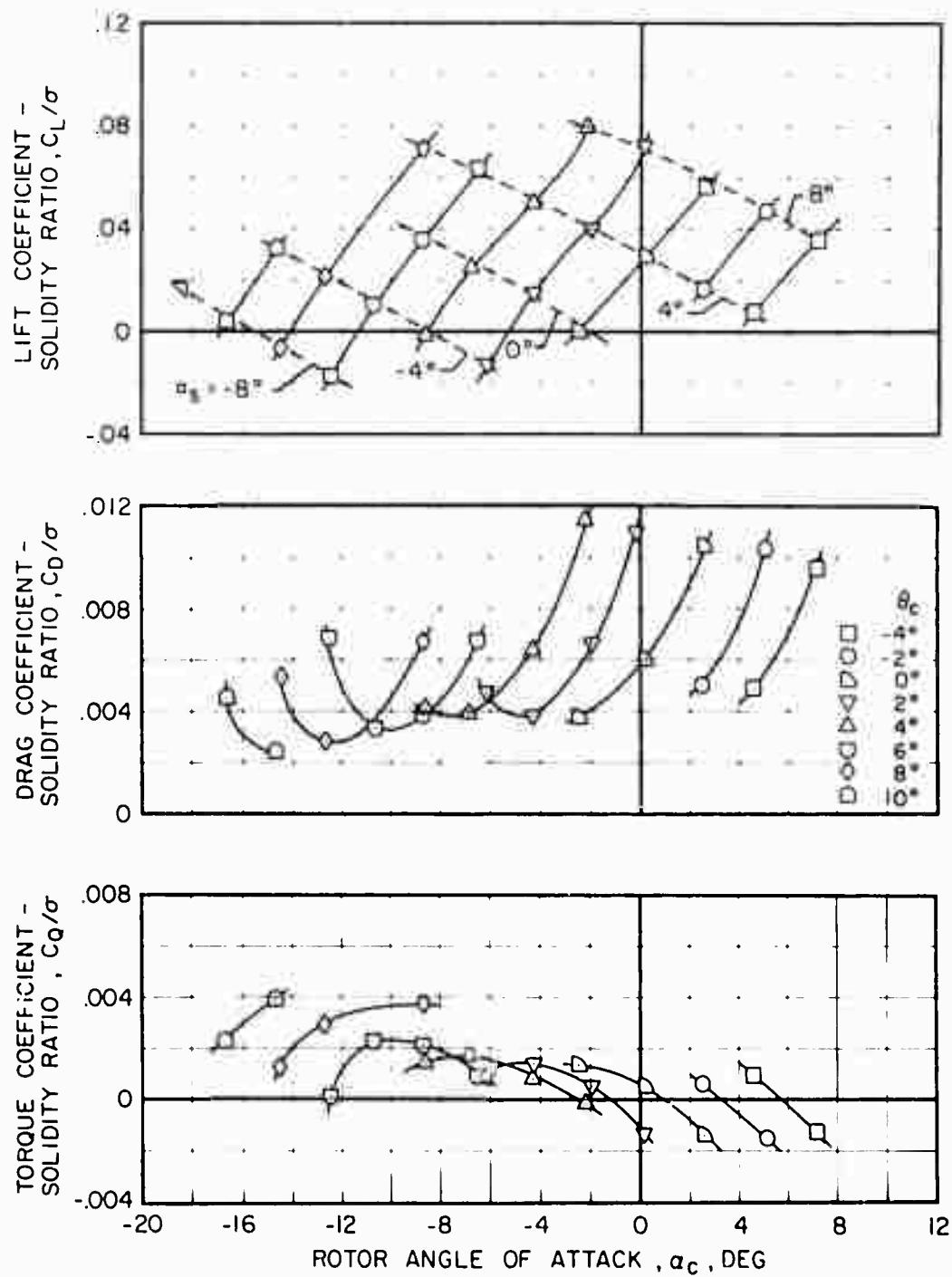
Figure 24. Variation of Lift, Drag, and Torque With Rotor Angle of Attack for Various Shaft Angle and Collective Pitch Settings, V = 194 Knots, $\mu = 0.62$, $\theta_1 = 0°$. $M_{(1.0, 90)} = 0.73$.

63
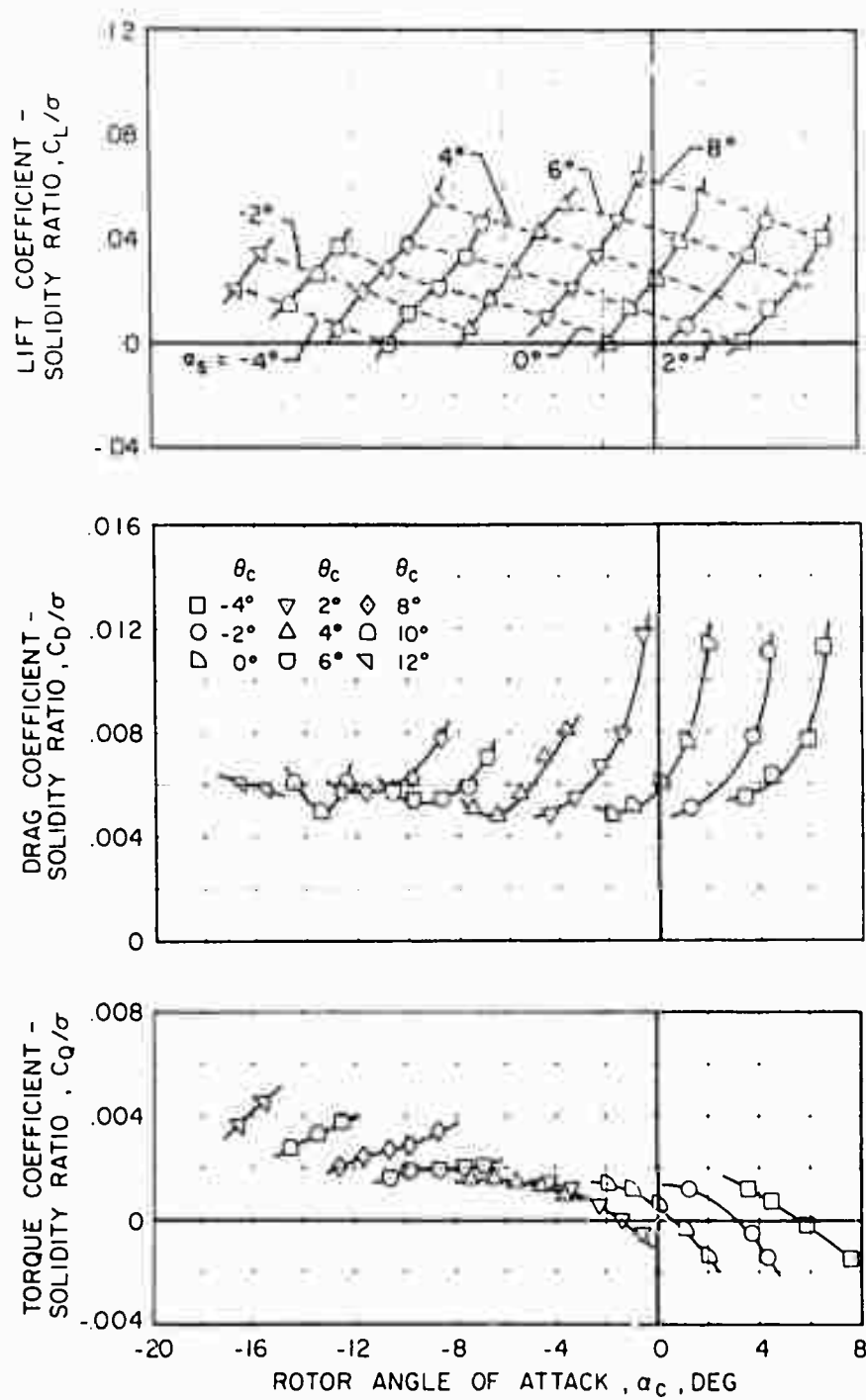
Figure 25. Variation of Lift, Drag, and Torque With Rotor
Angle of Attack for Various Shaft Angle and
Collective Pitch Settings, V = 193 Knots,
$\mu = 0.71$, $\theta_1 = 0°$, $M_{(1.0, 90)} = 0.68$.

64
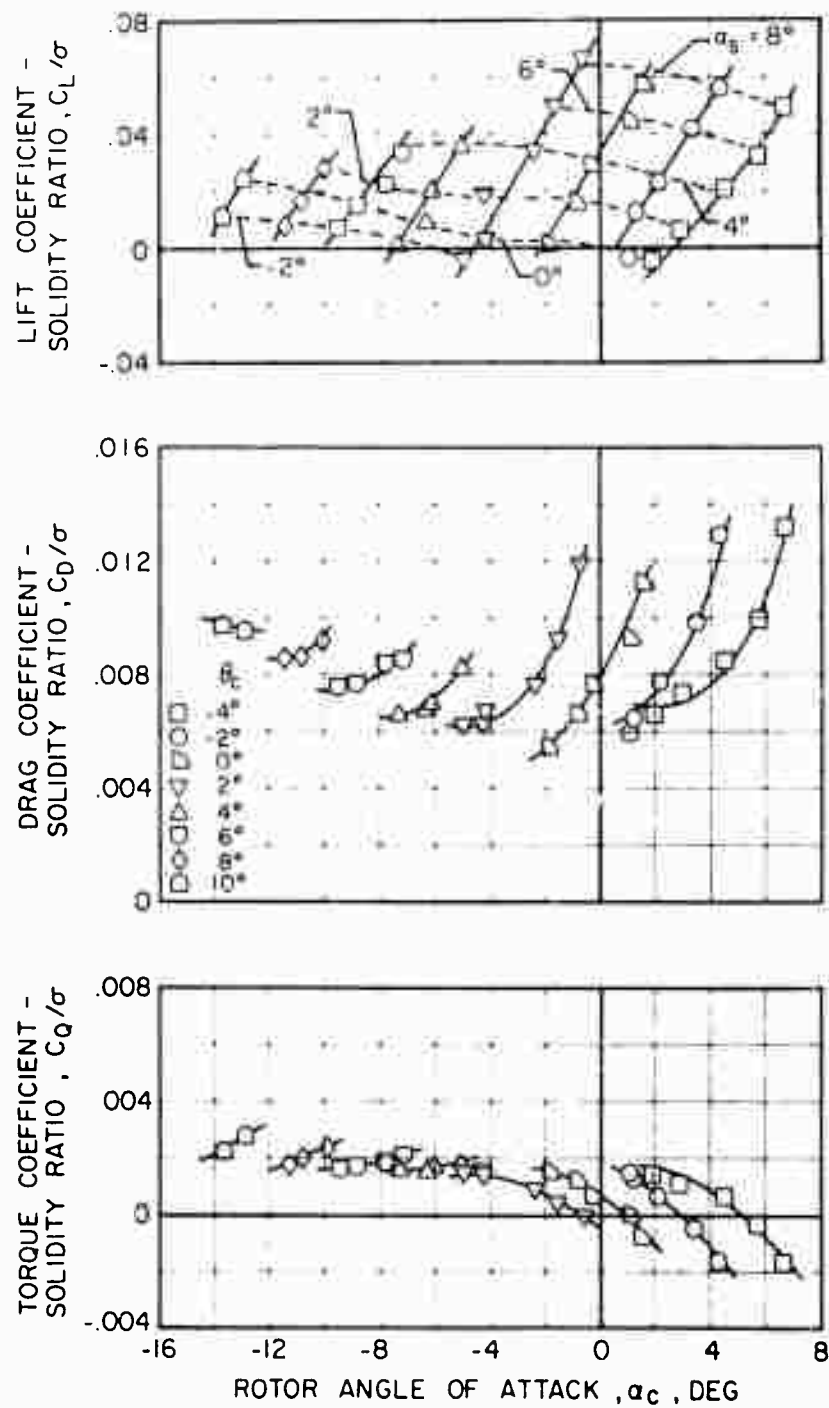
Figure 26. Variation of Lift, Drag, and Torque With Rotor
Angle of Attack for Various Shaft Angle and
Collective Pitch Settings, V = 195 Knots,
$\mu = 0.82$, $\theta_1 = 0°$, $M_{(1.0, 90)} = 0.62$.
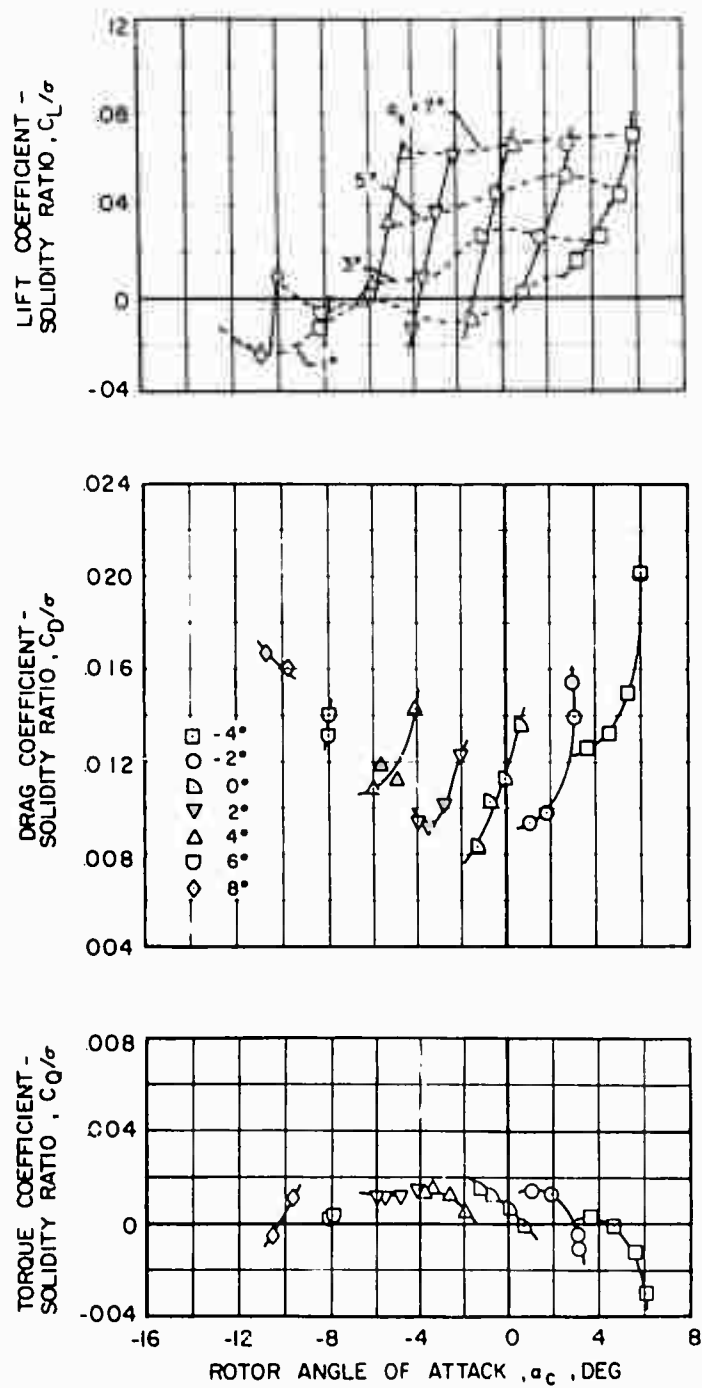
Figure 27. Variation of Lift, Drag, and Torque With Rotor
Angle of Attack for Various Shaft Angle and
Collective Pitch Settings, V = 197 Knots,
$\mu = 1.05$, $\theta_1 = 0°$, $M_{(1.0, 90)} = 0.54$.

66
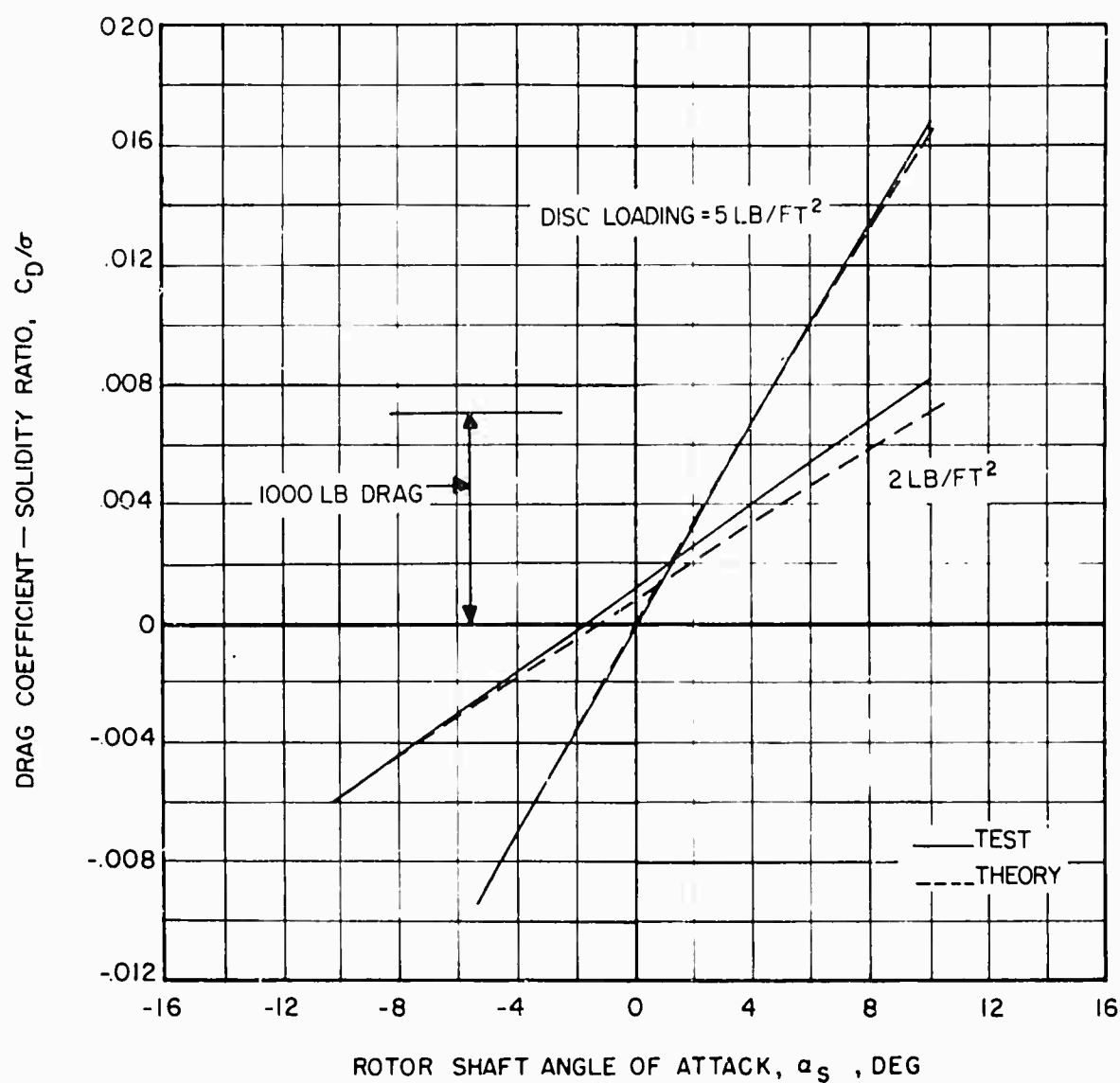
(a) Rotor Drag

Figure 28. The Measured and Calculated Effect of Shaft Angle on Drag and Torque for Two Values of Disc Loading. $V = 117$ Knots, $\Omega R = 650$ Ft/Sec, $\mu = 0.30$, $\theta_1 = 0°$, $M_{(1.0, 90)} = 0.74$.
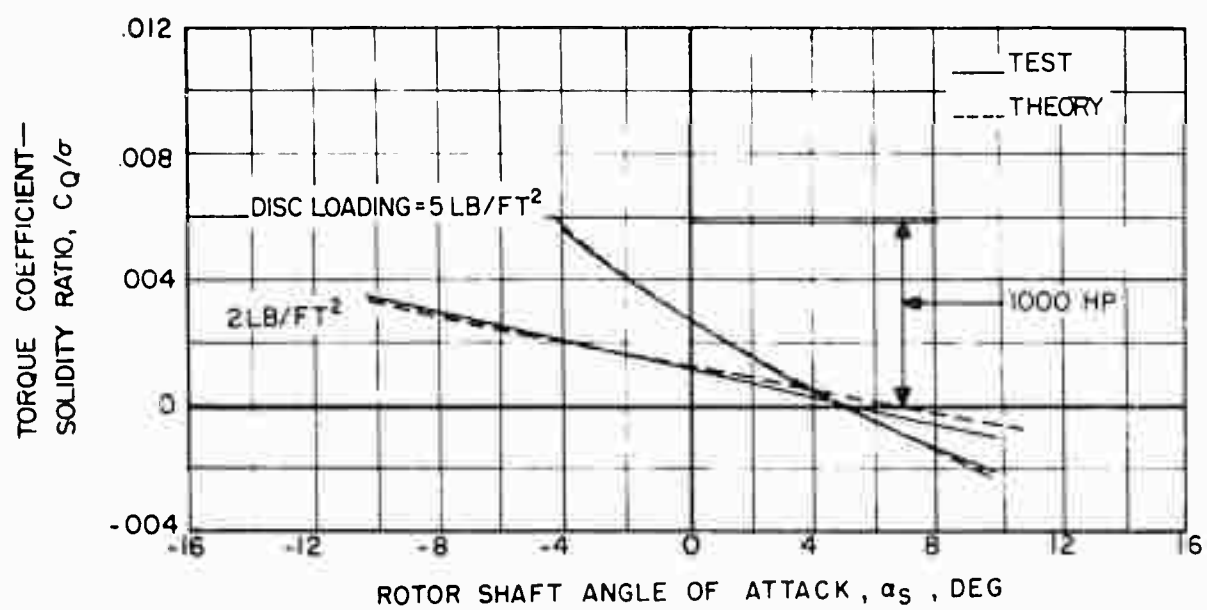
(b) Rotor Torque

Figure 28. Concluded.

68
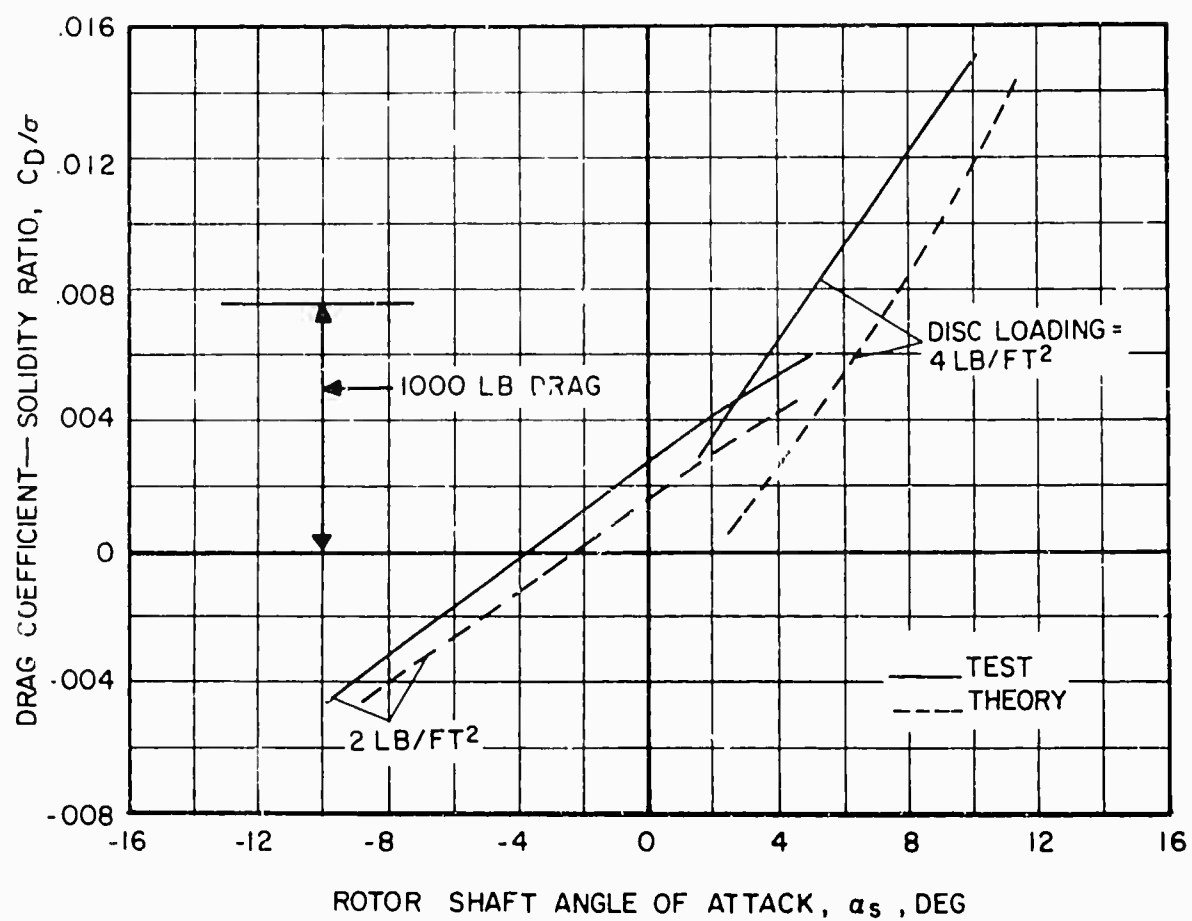
(a) Rotor Drag

Figure 29.   The Measured and Calculated Effect of Shaft Angle
on Drag and Torque for Two Values of Disc
Loading, V = 194 Knots, $\Omega R = 650$ Ft/Sec,
$\theta_1 = 0°$, $\mu = 0.50$, $M_{(1.0, 90)} = 0.83$.
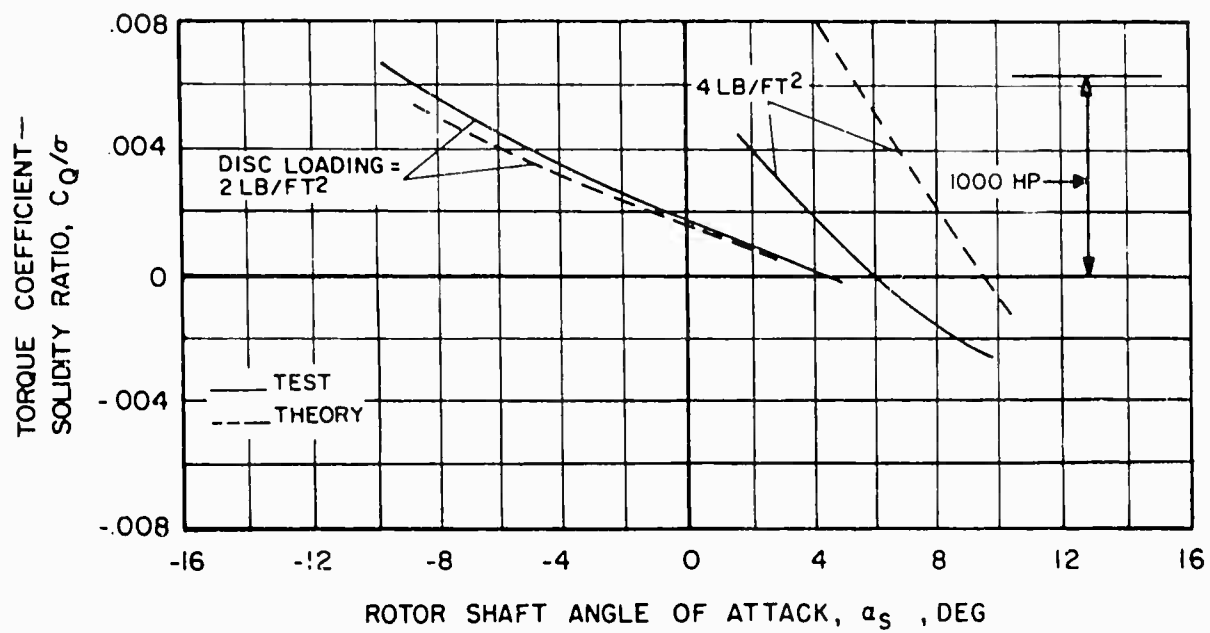
(b) Rotor Torque

Figure 29. Concluded.

70
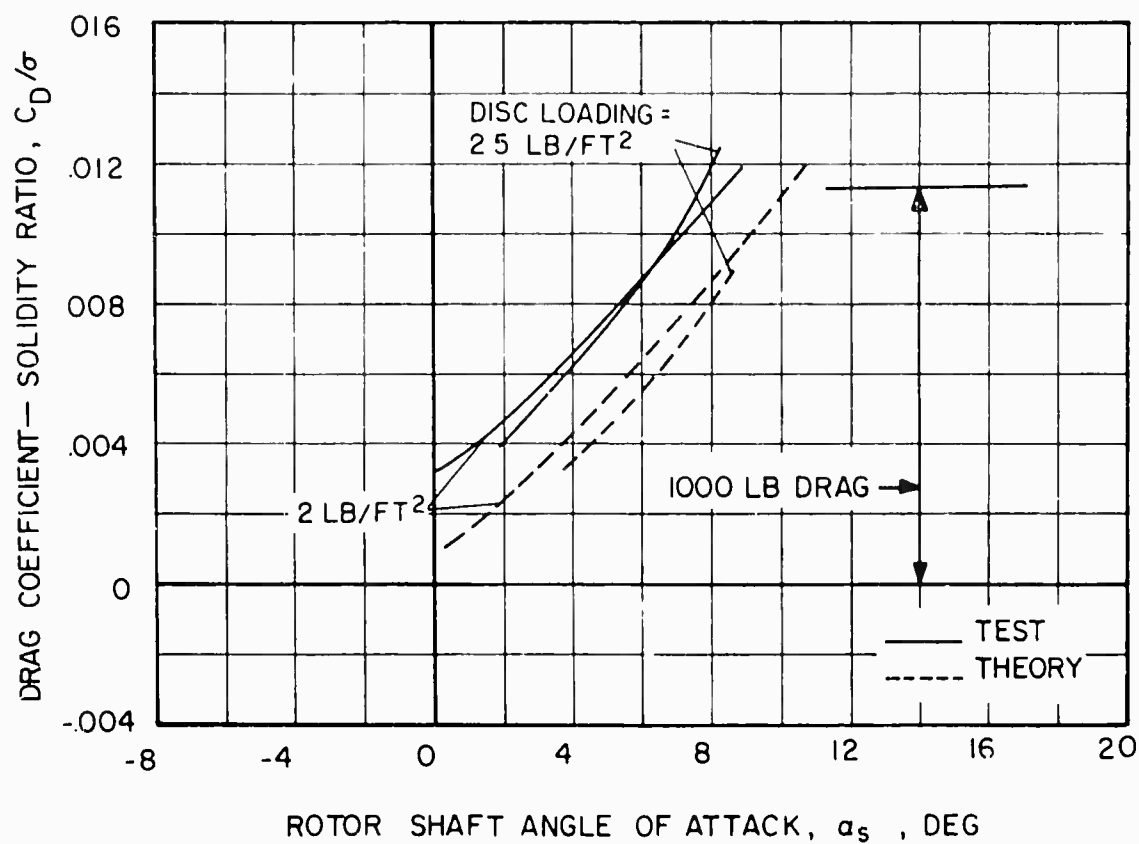
(a) Rotor Drag

Figure 30. The Measured and Calculated Effect of Shaft
Angle on Drag and Torque for Two Values of Disc
Loading. $V = 194$ Knots, $\Omega R = 530$ Ft/Sec,
$\theta_1 = 0°$, $\mu = 0.62$, $M_{(1.0, 90)} = 0.73$.

71
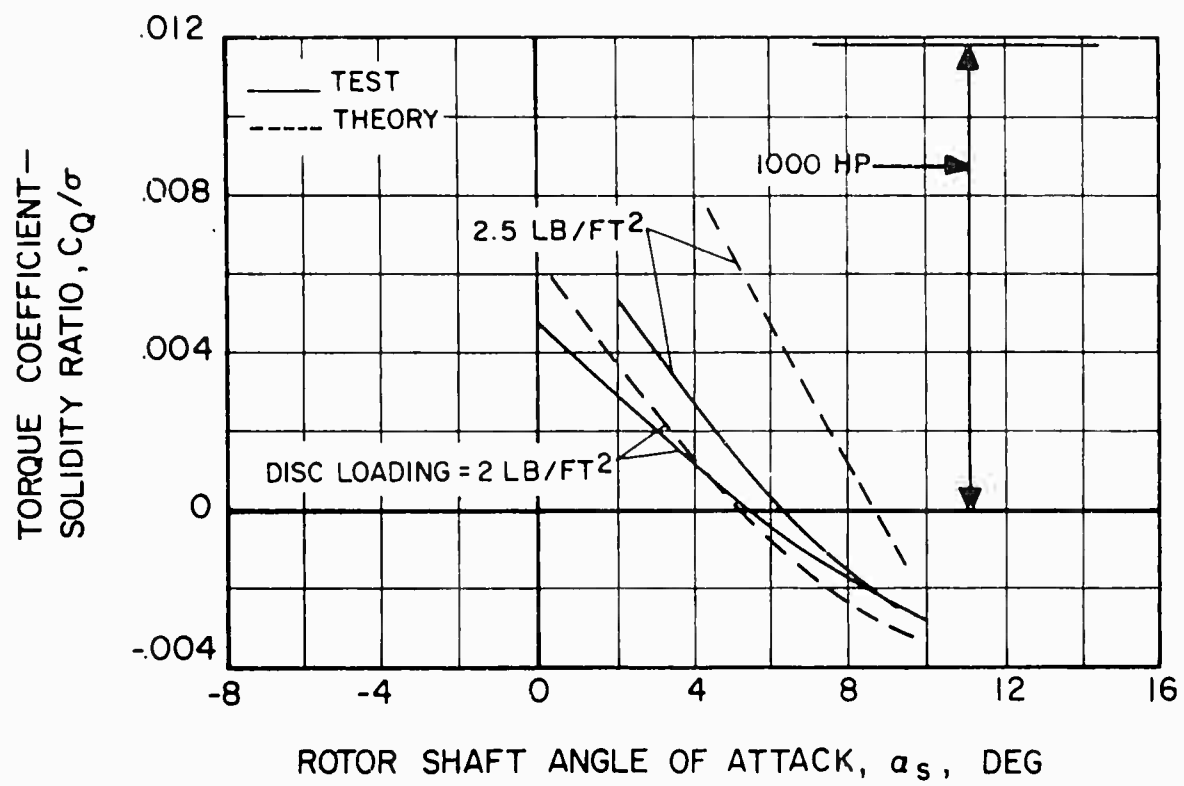
(b) Rotor Torque

Figure 30. Concluded.
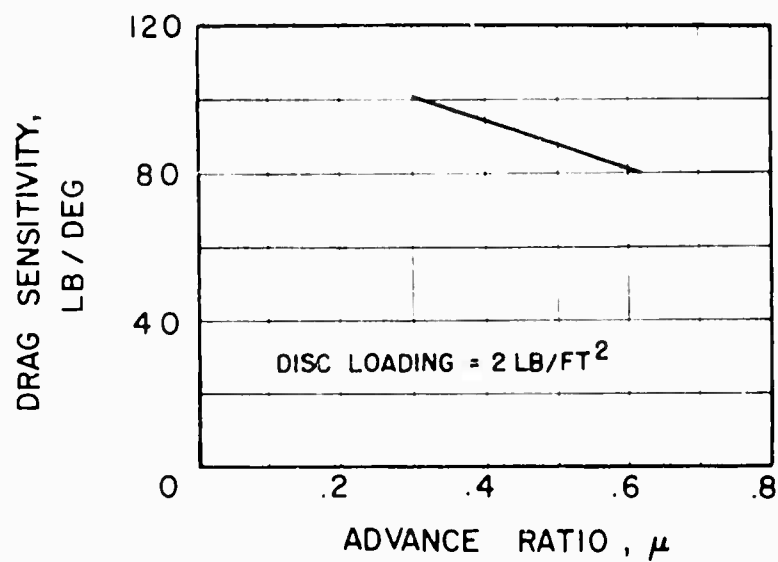
(a) Rotor Drag
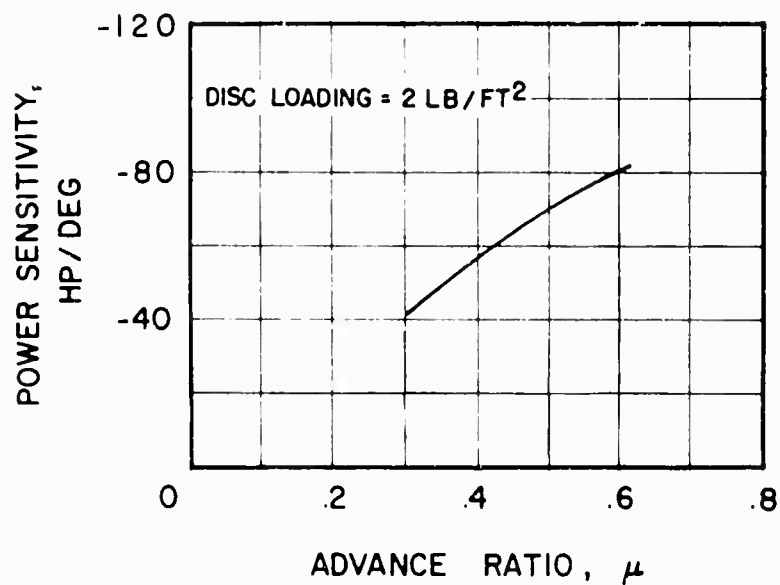
(b) Rotor Power

Figure 31. The Effect of Advance Ratio on Drag and Power
Sensitivity to Shaft Angle Change at Constant
Disc Loading, $\theta_1 = 0°$, Disc Loading = 2 Lb/Ft.^{2}

73
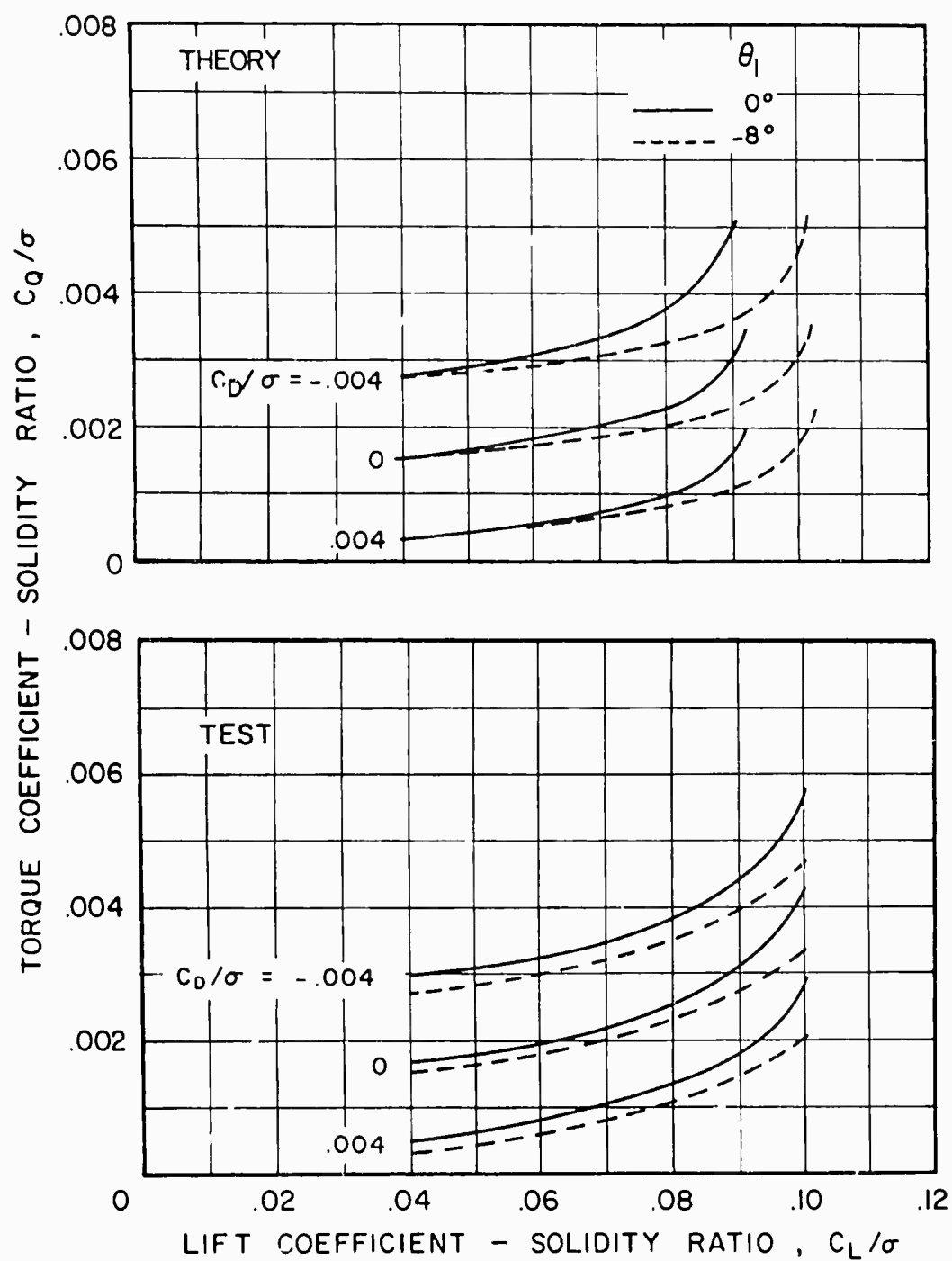
Figure 32. The Measured and Calculated Variation of Torque
With Lift for 0° and -8° Twisted Blades at Three
Values of Drag, V = 117 Knots, μ = 0.30,
$M_{(1.0, 90)}$ = 0.74.

74
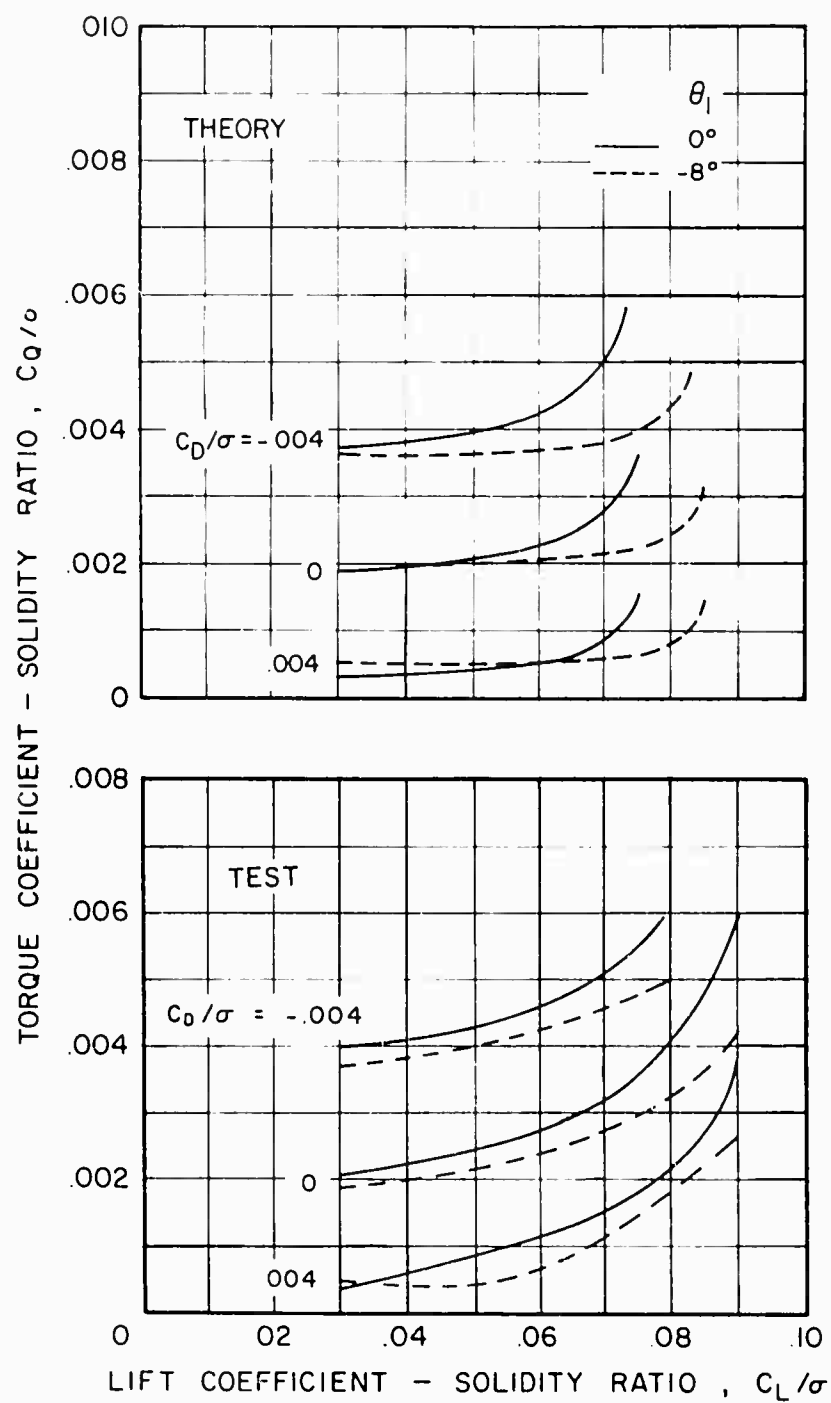
Figure 33. The Measured and Calculated Variation of Torque With Lift for 0° and -8° Twisted Blades at Three Values of Drag. V = 161 Knots, μ = 0.40, M(1.0, 90) = 0.82.

75
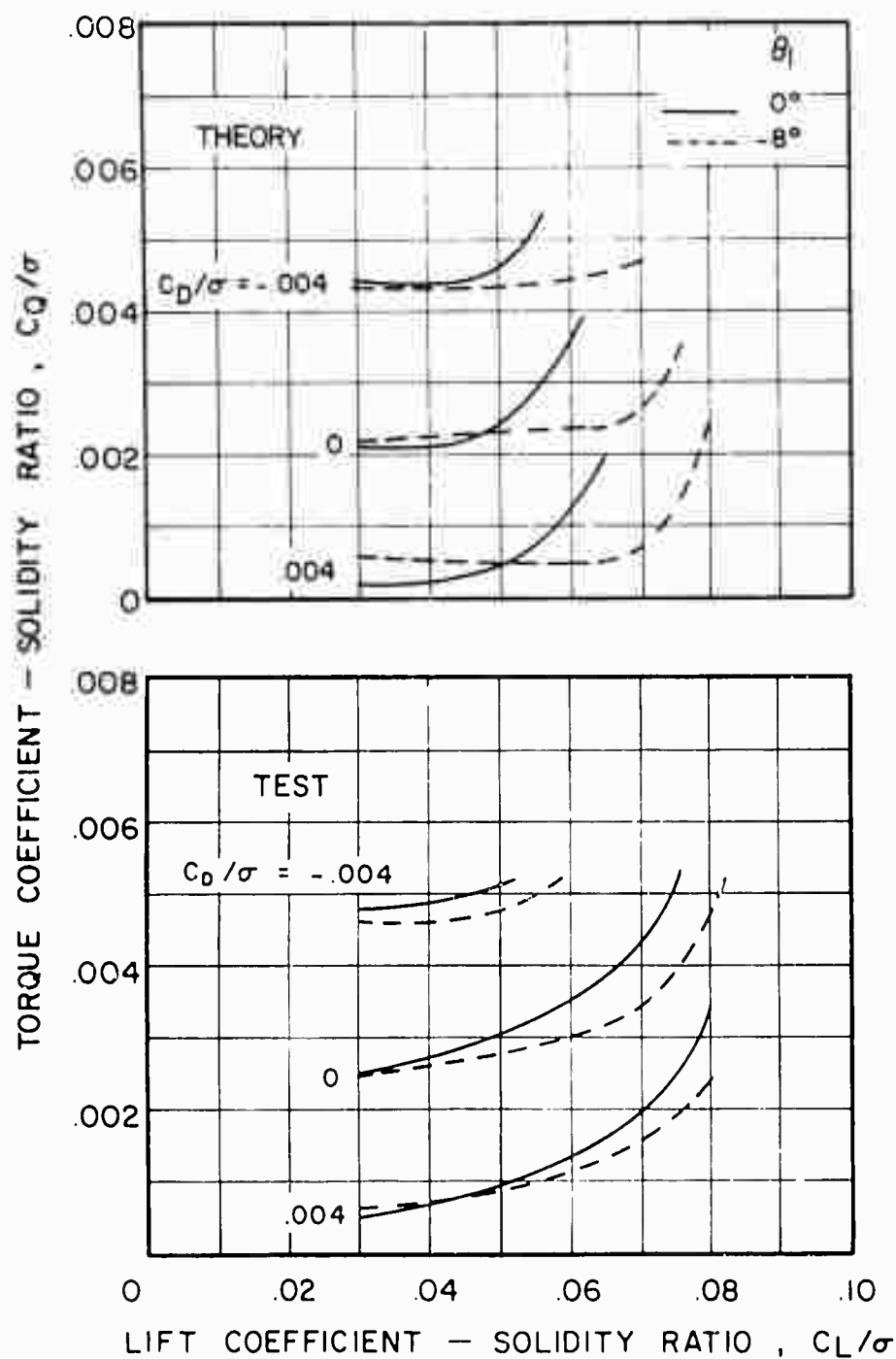
Figure 34. The Measured and Calculated Variation of Torque With Lift for 0° and -8° Twisted Blades at Three Values of Drag, $V = 177$ Knots, $\mu = 0.46$, $M(1.0, 90) = 0.82$.
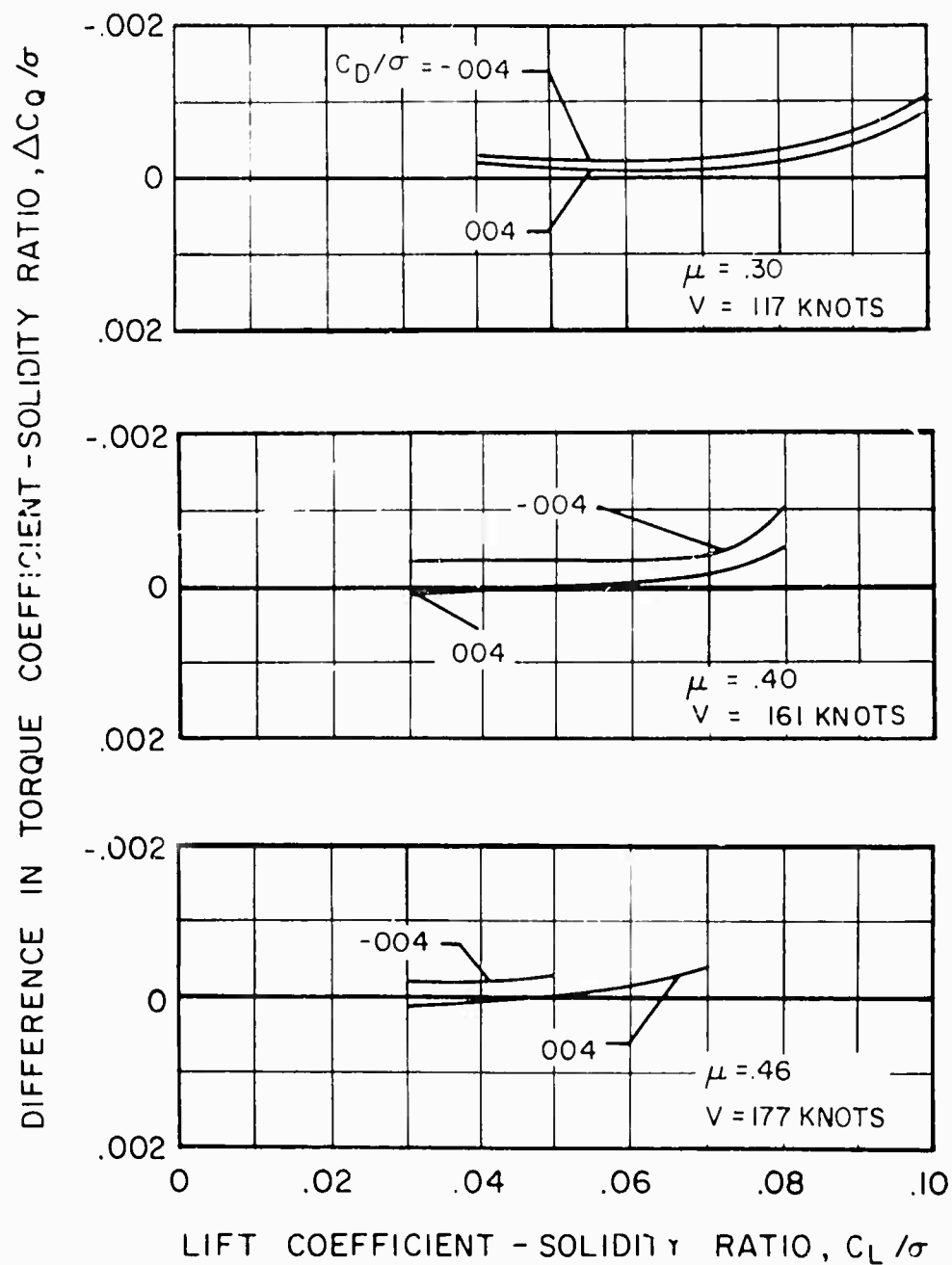
Figure 35. The Effect of Lift on the Reduction in Torque Caused by Changing Blade Twist From 0° to -8° at Various Combinations of Drag Coefficient-Solidity Ratio and Advance Ratio.

77
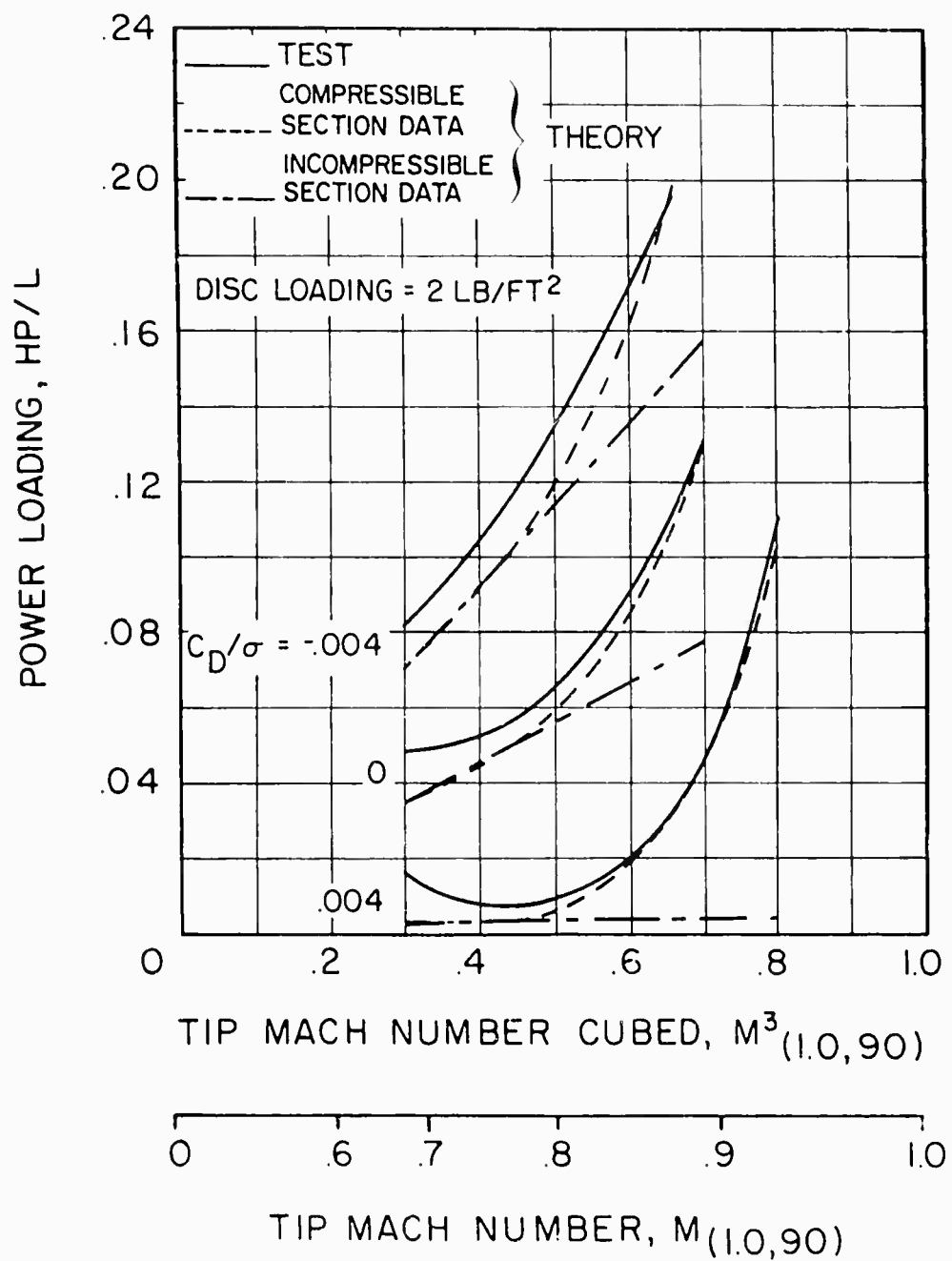
Figure 36. The Measured and Calculated Effect of Advancing Tip Mach Number on Power Loading at Various Combinations of Disc Loading and Drag Coefficient-Solidity Ratio, $\mu \approx 0.40$, $\theta_1 = 0°$.

78
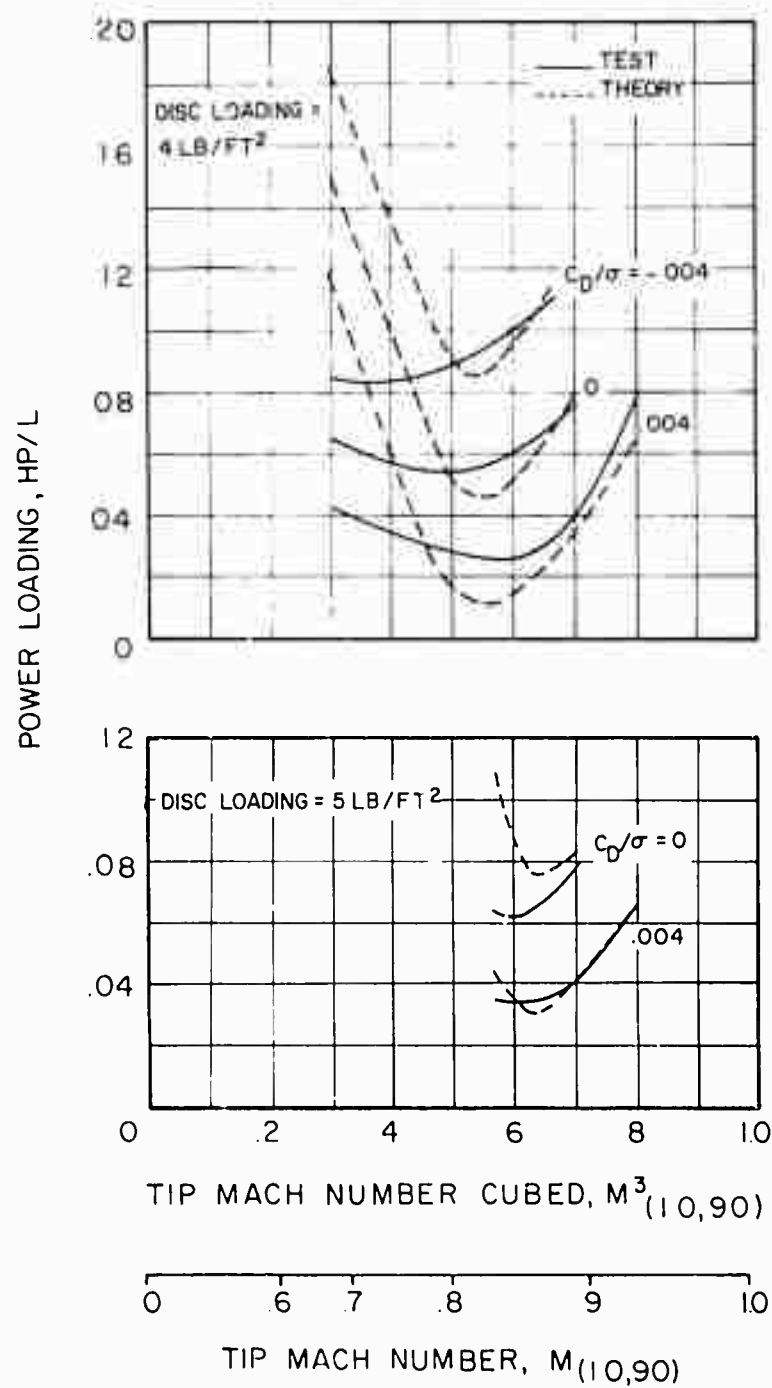
Figure 36. Concluded.
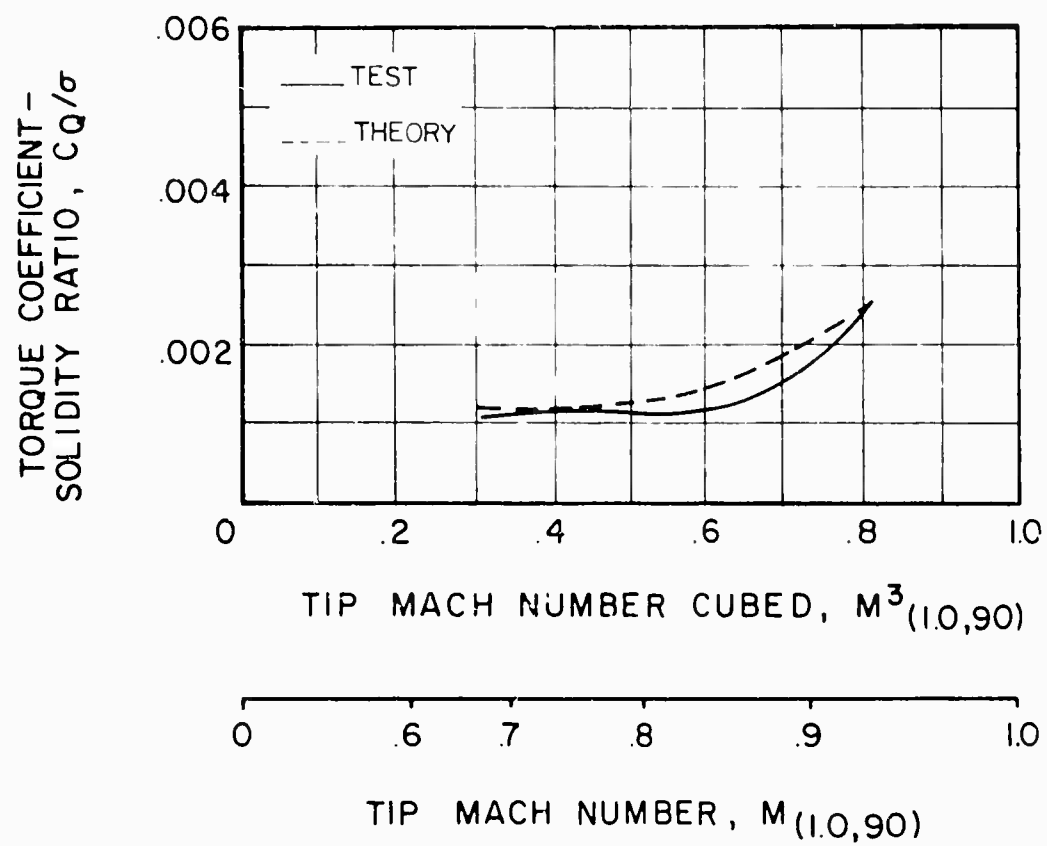
Figure 37.   The Measured and Calculated Effect of Advancing
              Tip Mach Number on Torque Coefficient-Solidity
              Ratio at Zero Lift. $\alpha_s = 0°$, $\mu \approx 0.40$.
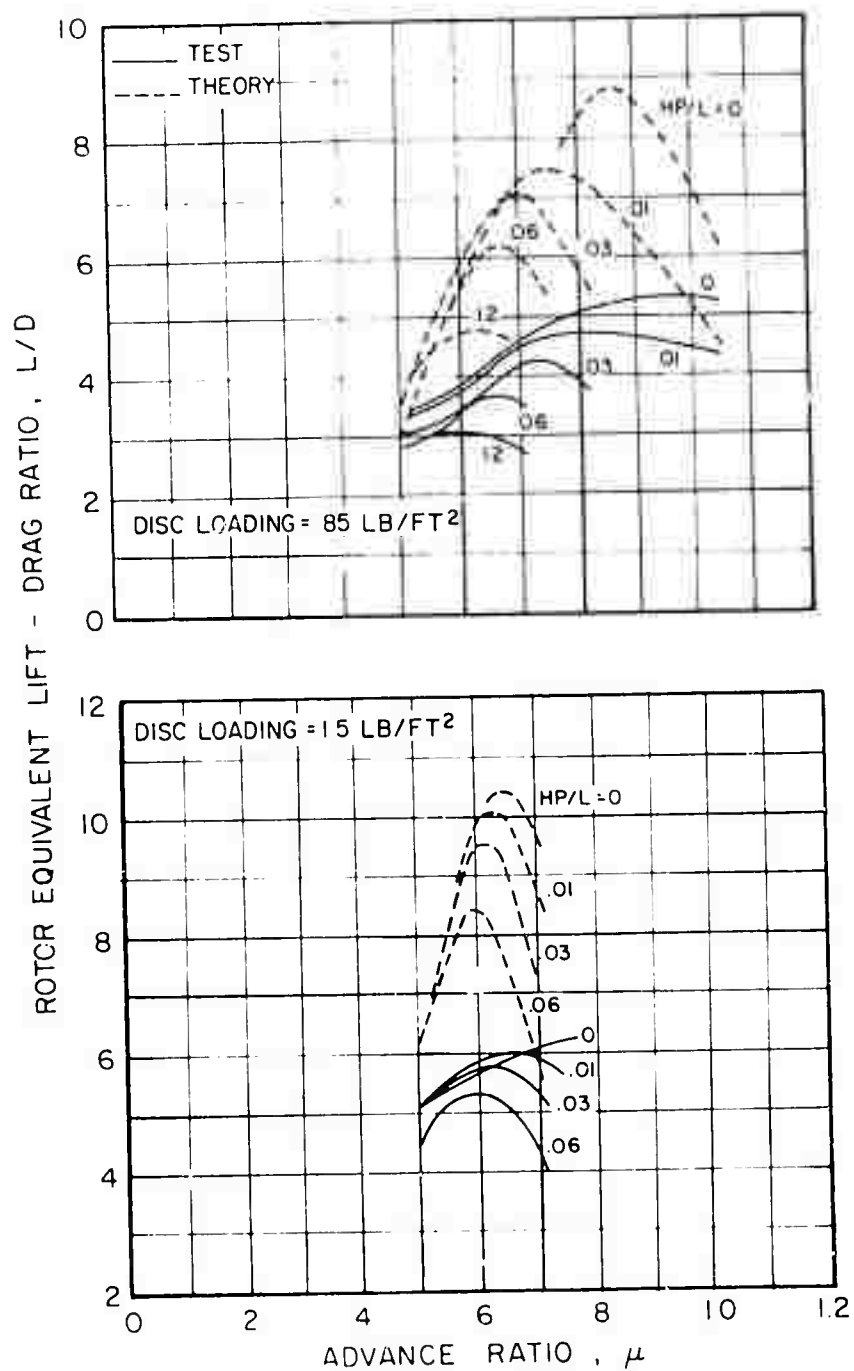
Figure 38.   The Measured and Calculated Effect of Advance
Ratio on Equivalent L/D at Various
Combinations of Disc Loading and Power Loading,
$V \approx 195$ Knots, $\theta_1 = 0°$.

81
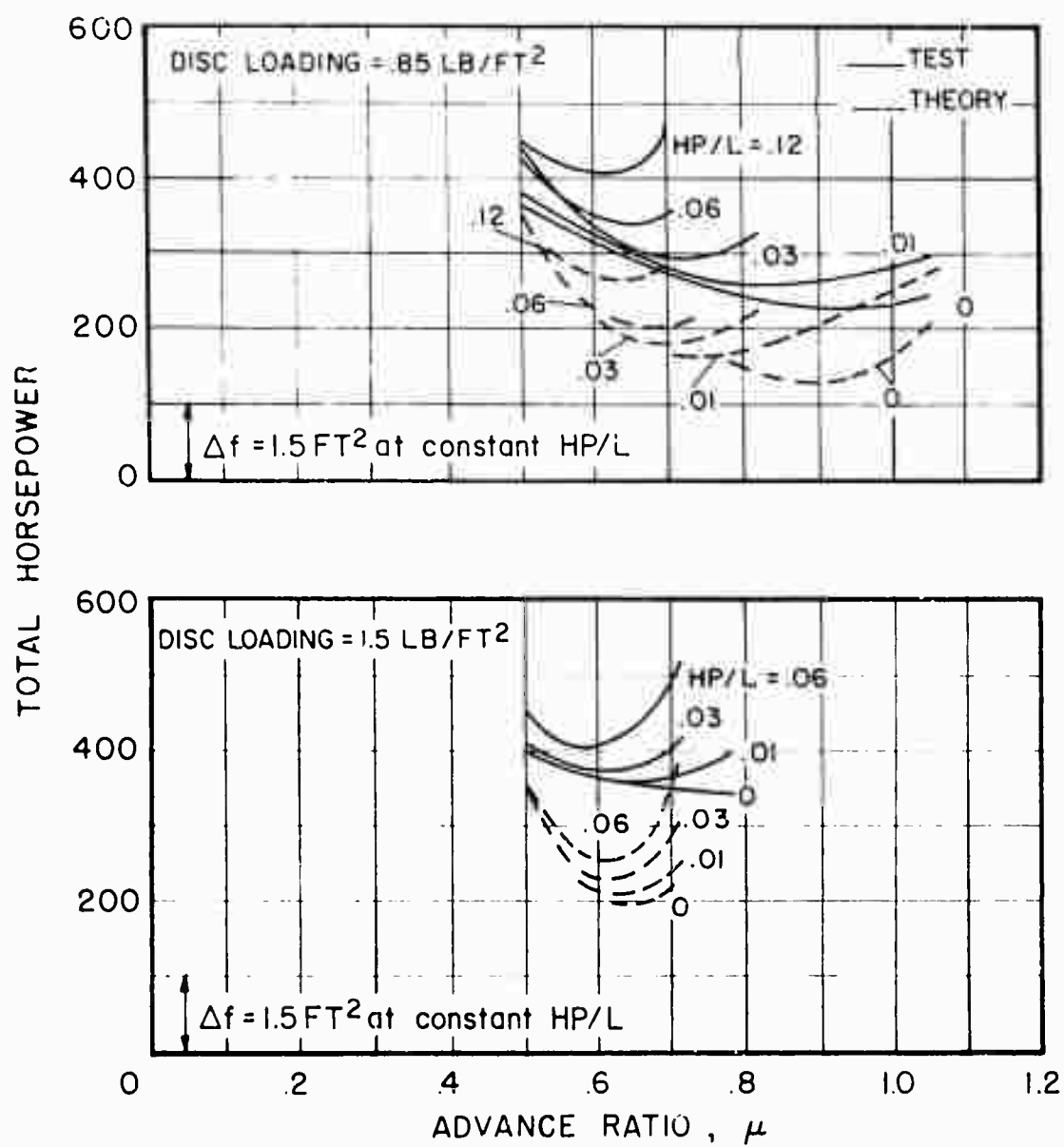
Figure 39. The Measured and Calculated Effect of Advance Ratio on Total Horsepower at Various Combinations of Disc Loading and Power Loading, $V \approx 195$ Knots, $\theta_1 = 0°$.

82
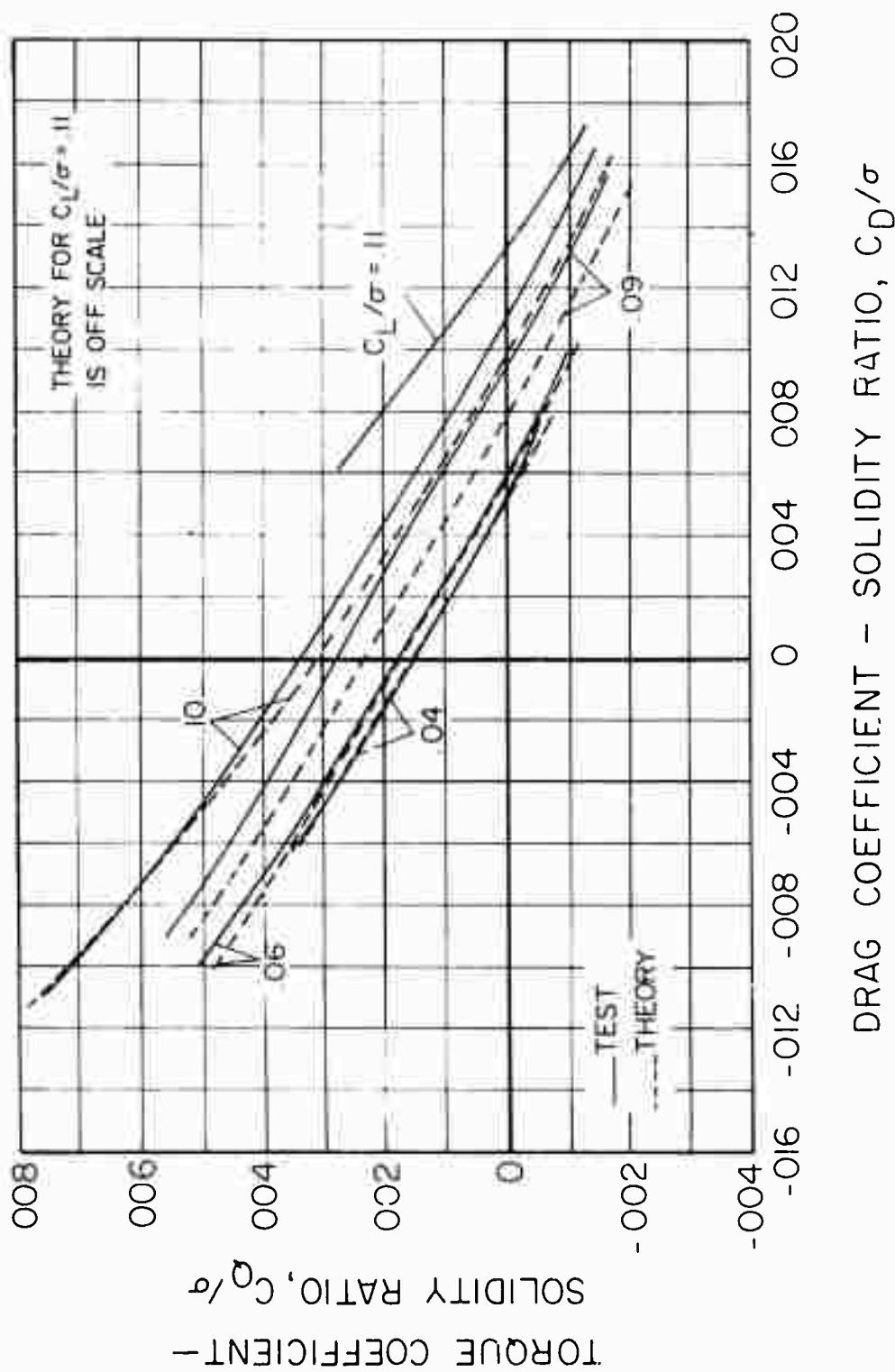
Figure 40. The Measured and Calculated Variation of Torque With Drag at Various Values of Lift, V = 117 Knots, μ = 0.30, θ_1 = -8°, $M_{(1.0, 90)}$ = 0.74.

Figure 41. The Measured and Calculated Variation of Torque With Drag at Various Values of Lift, $V = 161$ Knots, $\mu = 0.40$, $\theta_1 = -8°$, $M_{(1.0, 90)} = 0.82$.

84
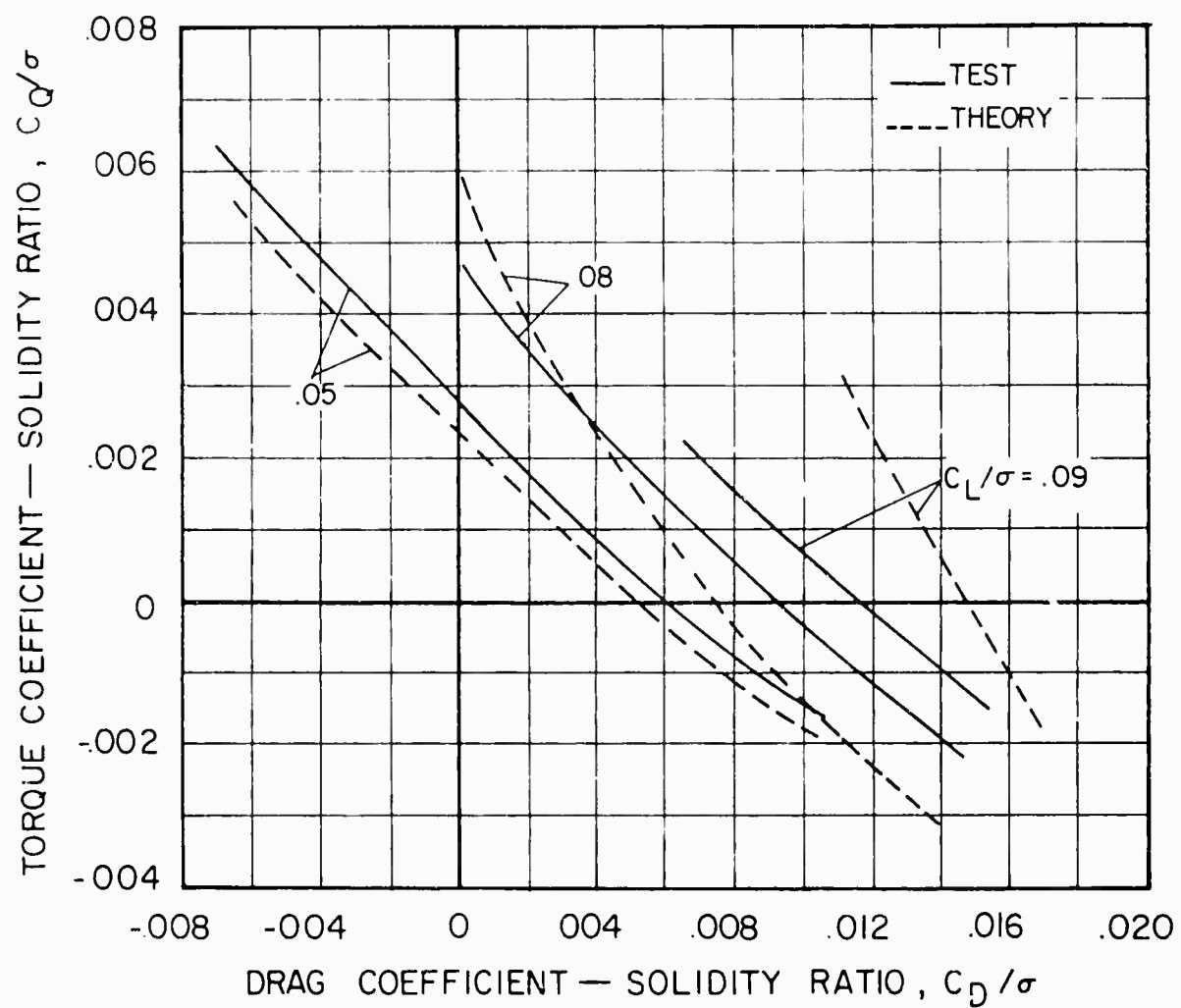
Figure 42. The Measured and Calculated Variation of Torque With Drag at Various Values of Lift. V = 177 Knots, μ = 0.46, θ_1 = -8°, $M_{(1.0, 90)}$ = 0.82.

85
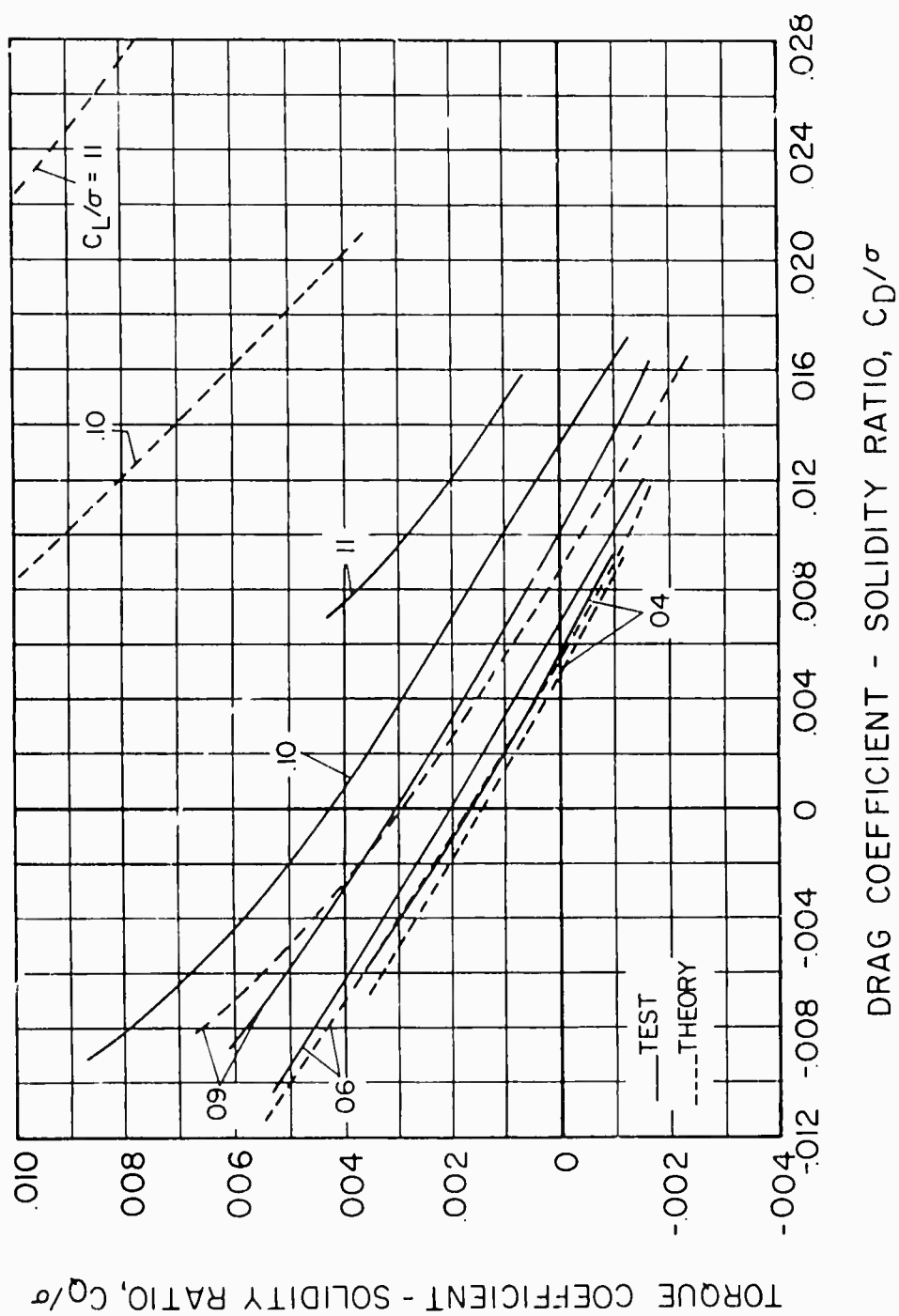
Figure 4.3. The Measured and Calculated Variation of Torque With Drag at Various Values of Lift, $V = 116$ Knots, $\mu = 0.30$, $\theta_1 = 0°$, $M(1.0.90) = 0.74$.

86
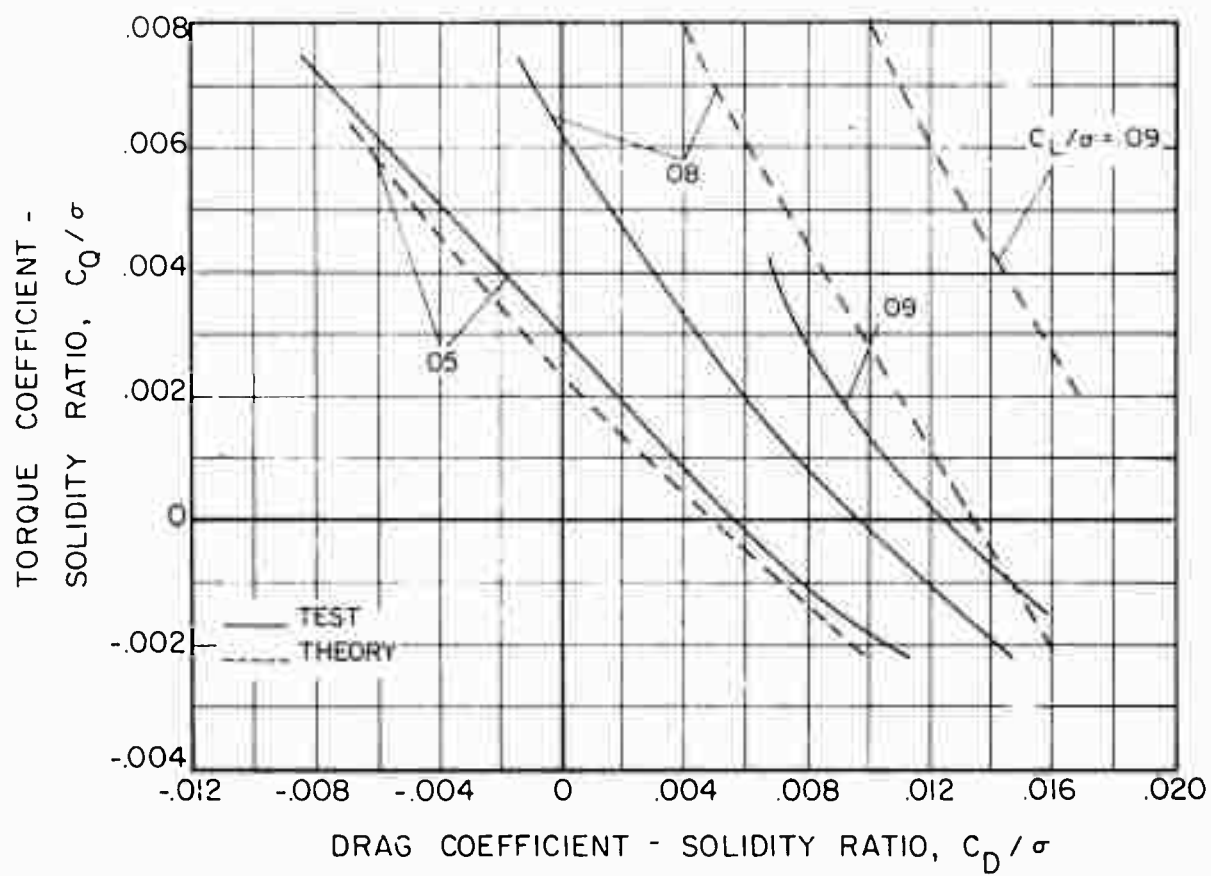
Figure 44.   The Measured and Calculated Variation of Torque
                With Drag at Various Values of Lift, V = 178
                Knots, μ = 0.46, θ_1 = 0°. $M_{(1.0, 90)}$ = 0.82.
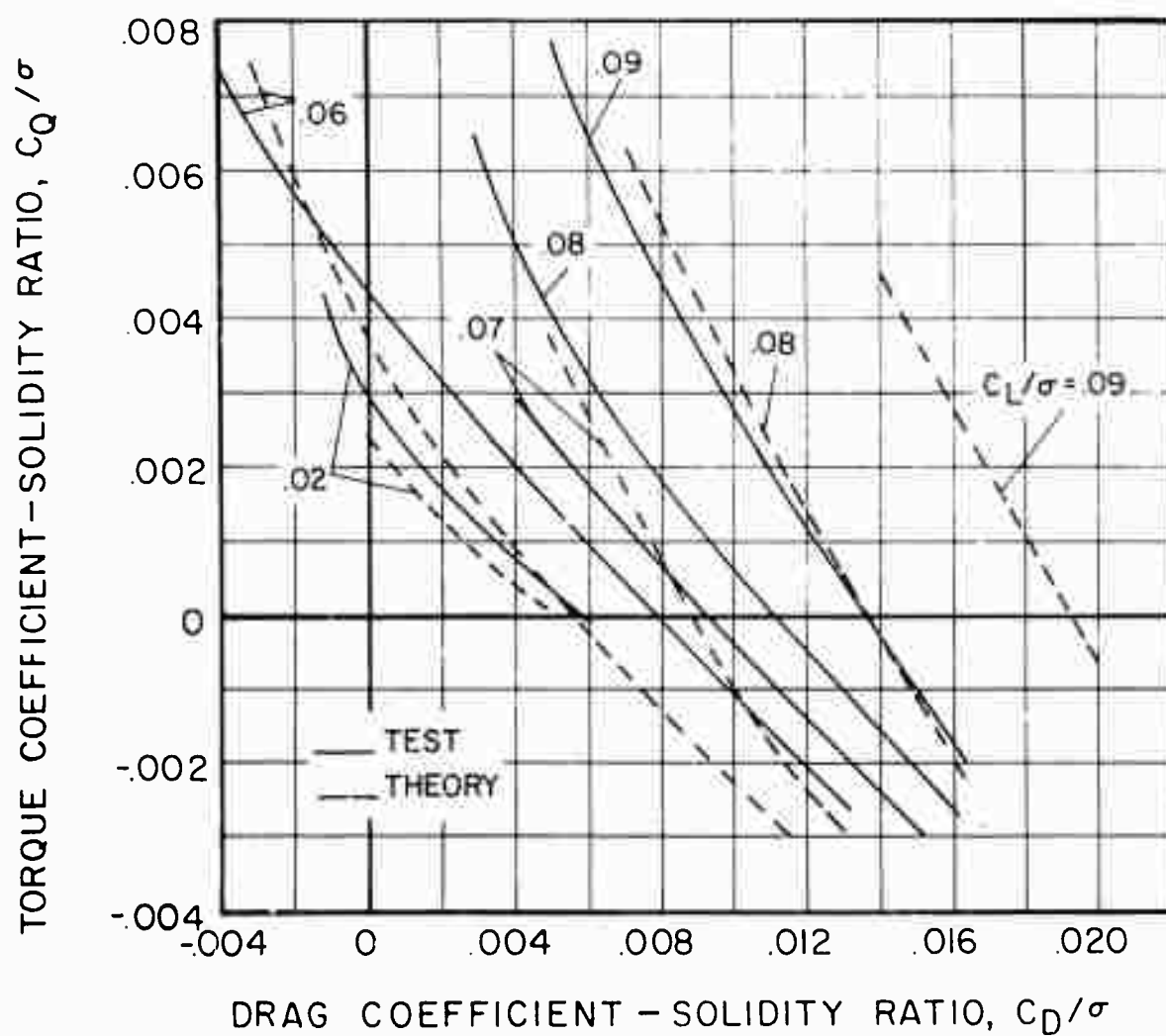
Figure 45. The Measured and Calculated Variation of Torque
With Drag at Various Values of Lift, V = 194 Knots,
$\mu = 0.50$, $\theta_1 = 0°$, $M(1.0, 90) = 0.83$.
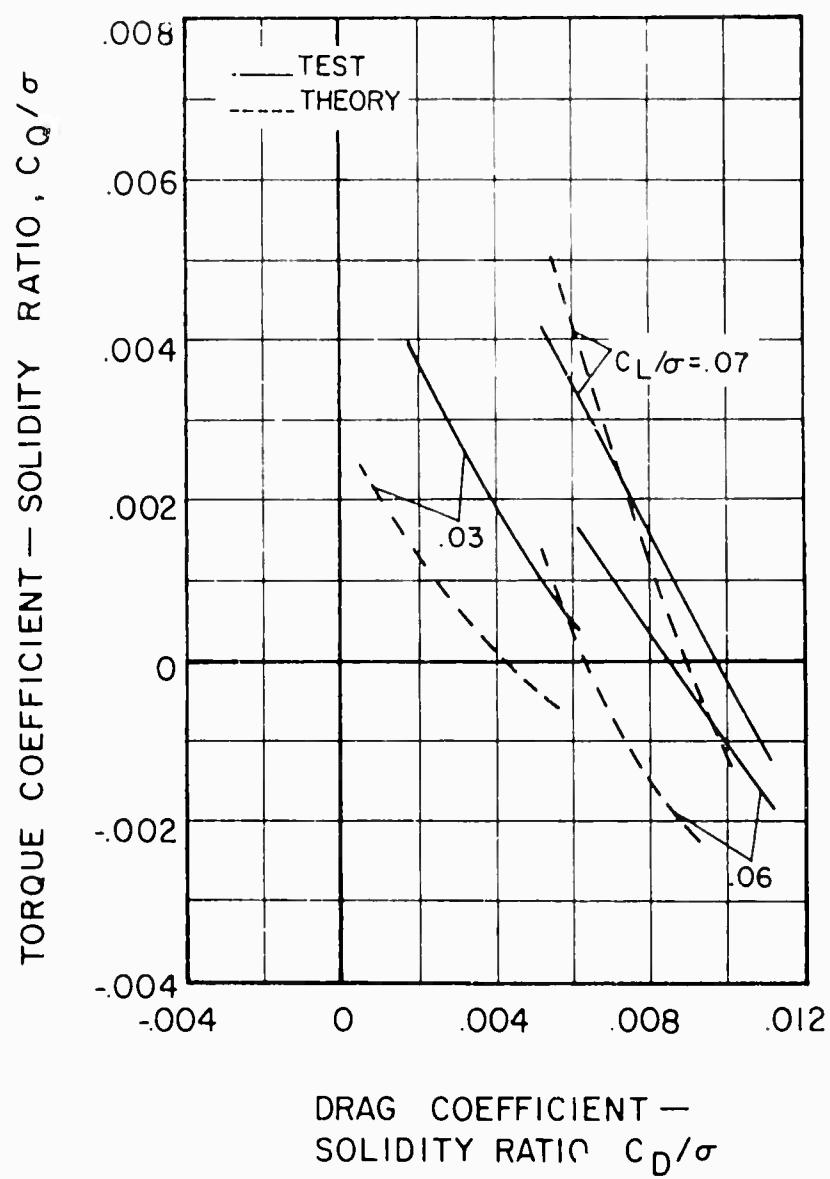
Figure 46. The Measured and Calculated Variation of Torque With Drag at Various Values of Lift, $V = 194$ Knots, $\mu = 0.62$, $\theta_1 = 0°$, $M_{(1.0, 90)} = 0.73$.

89
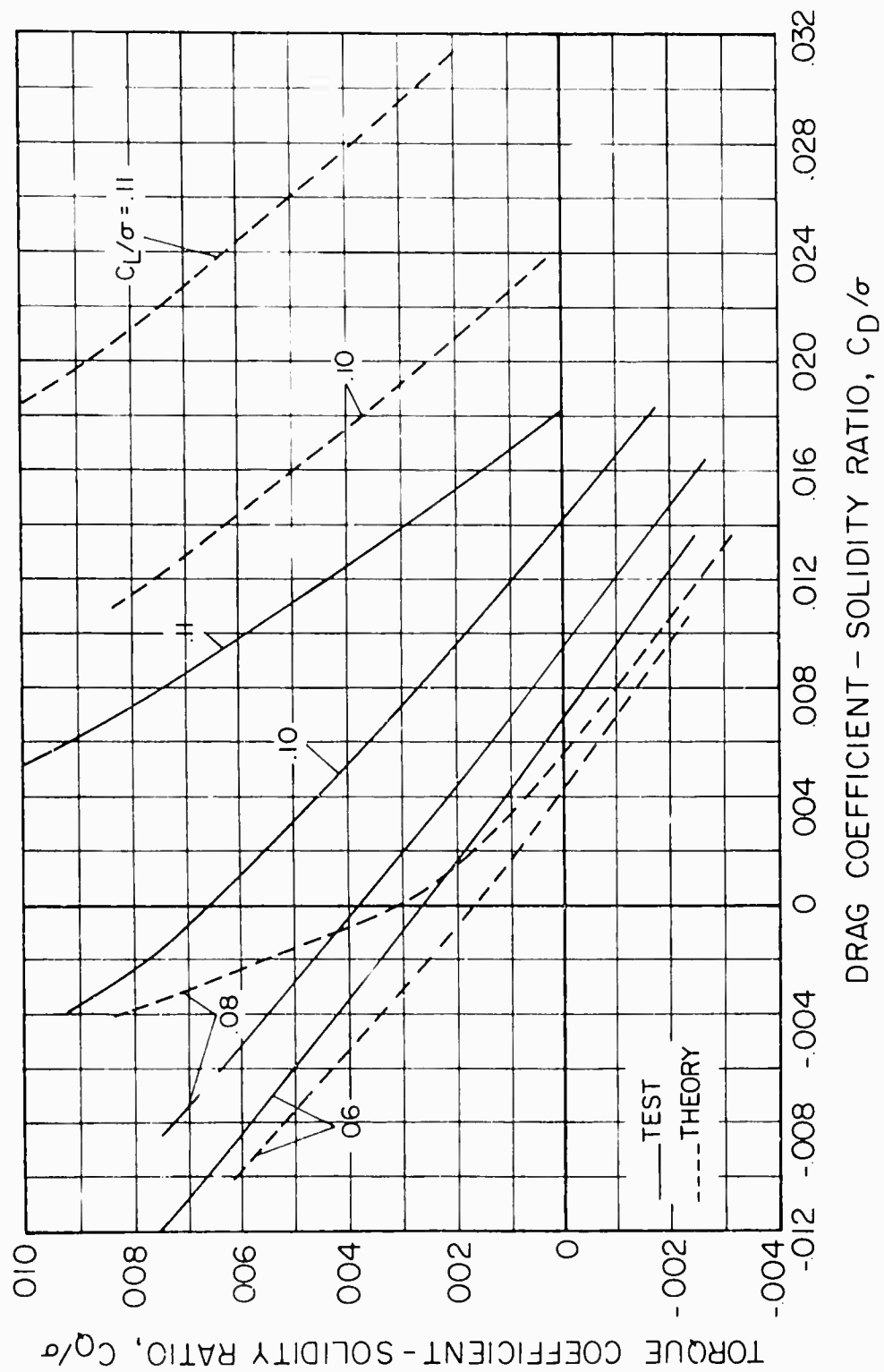
Figure 47. The Measured and Calculated Variation of Torque With Drag at Various Values of Lift, $V = 132$ Knots, $\mu = 0.40$, $\theta_1 = 0°$, $M(1.0, 90) = 0.67$.
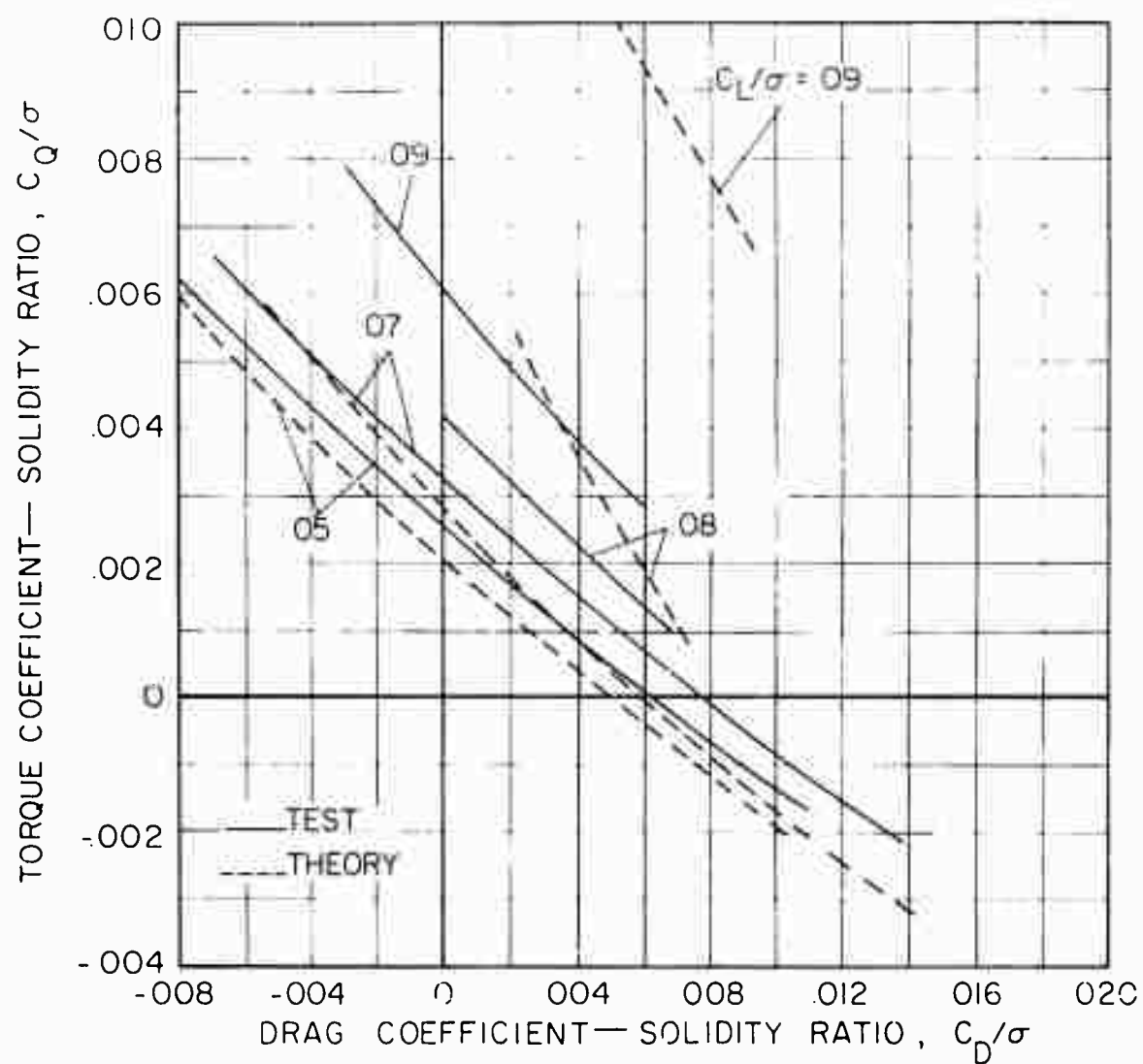
Figure 48. The Measured and Calculated Variation of Torque
With Drag at Various Values of Lift, $V = 162$
Knots, $\mu = 0.40$, $\theta_1 = 0°$, $M_{(1.0.90)} = 0.83$.

91
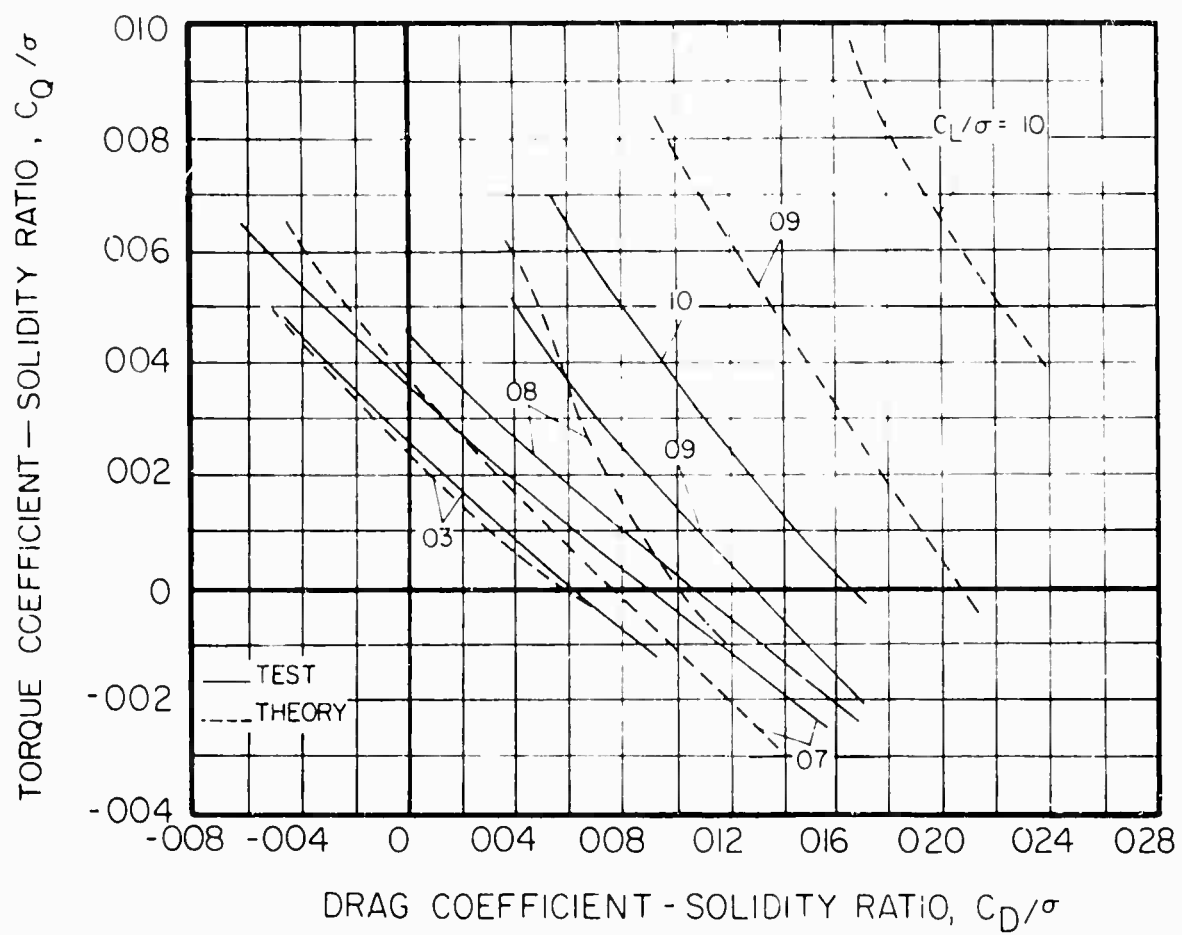
Figure 49. The Measured and Calculated Variation of Torque
With Drag at Various Values of Lift. $V = 174$
Knots, $\mu = 0.41$, $\theta_1 = 0°$, $M_{(1.0, 90)} = 0.87$.

92
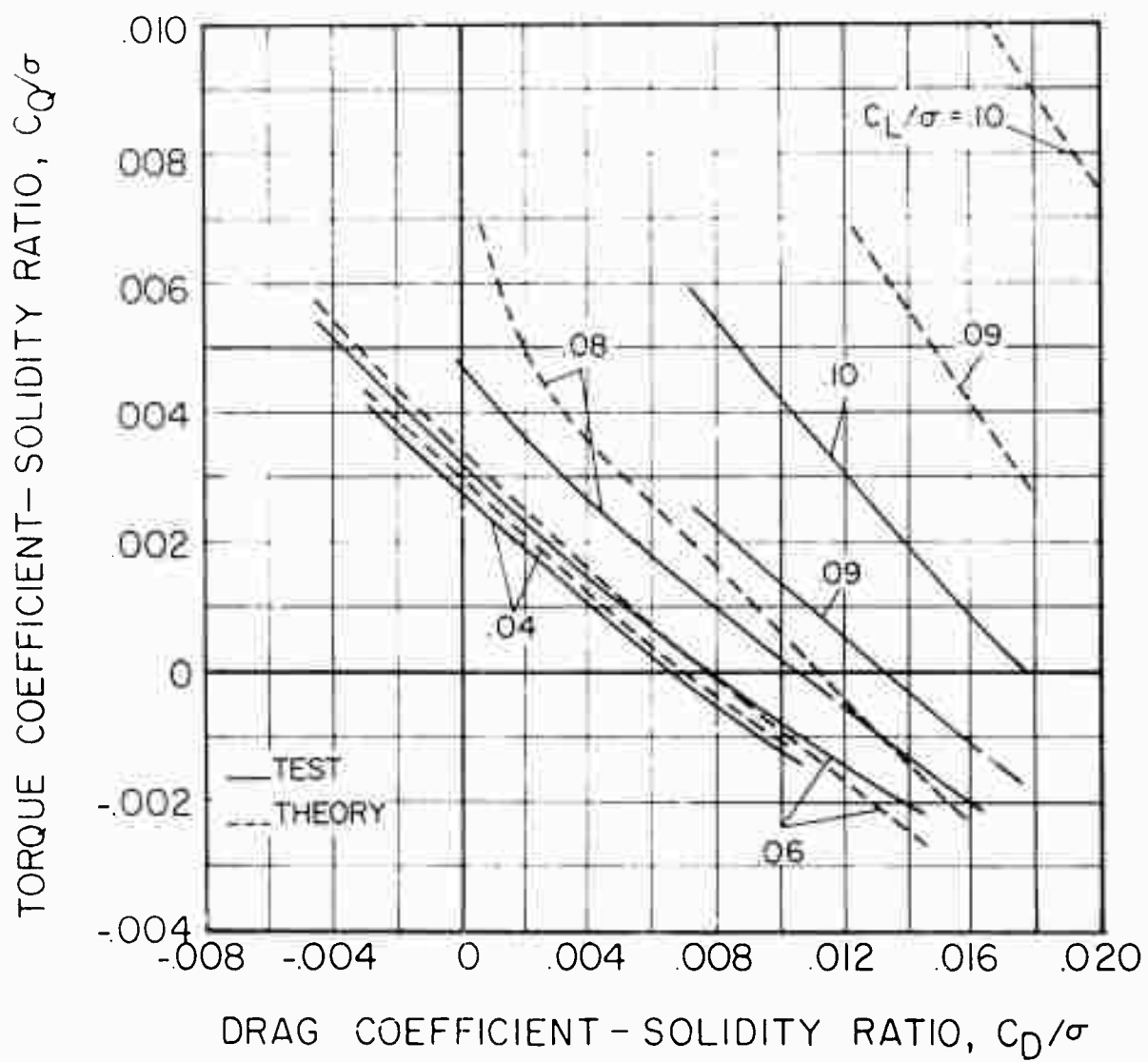
Figure 50. The Measured and Calculated Variation of Torque With Drag at Various Values of Lift, V = 175 Knots. $\mu = 0.39$, $\theta_1 = 0°$, $M_{(1.0, 90)} = 0.89$.

93
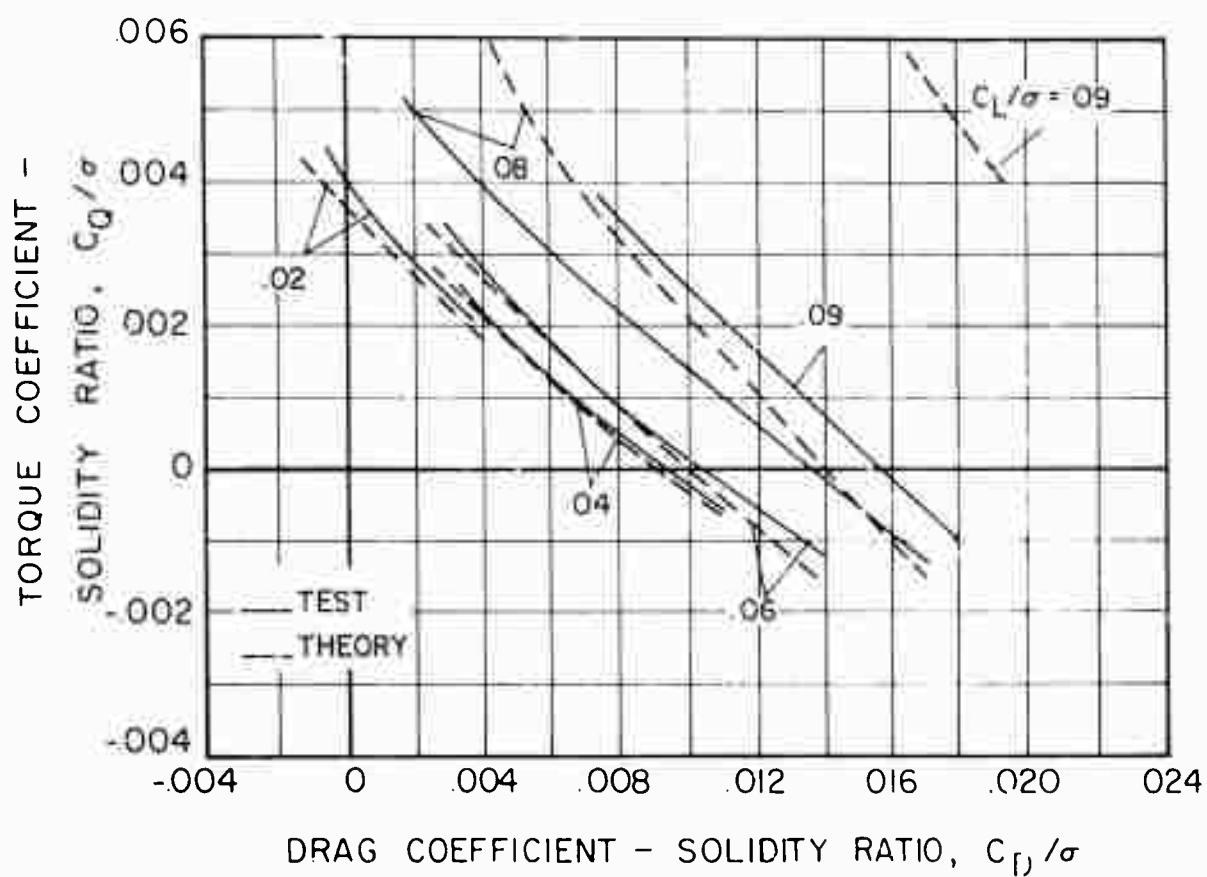
Figure 51. The Measured and Calculated Variation of Torque With Drag at Various Values of Lift, $V = 180$ Knots, $\mu = 0.39$, $\theta_1 = 0°$, $M_{(1.0, 90)} = 0.93$.
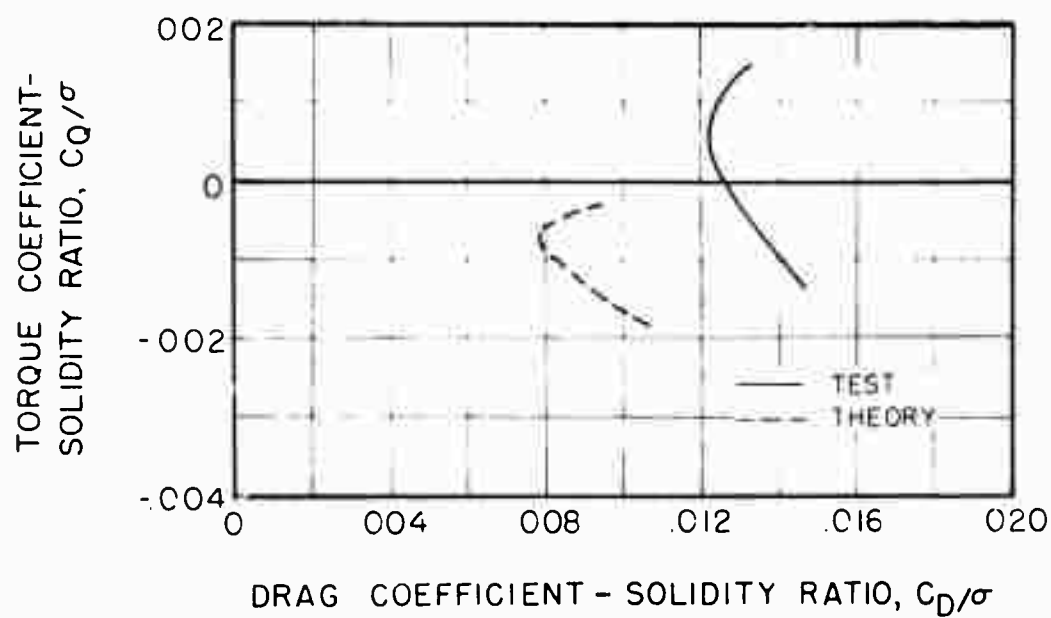
Figure 52.   A Sample of the Measured and Calculated
             Variation of Torque With Drag at High Advance
             Ratio, $V = 197$ Knots, $\mu = 1.05$, $\theta_1 = 0°$,
             $M_{(1.0, 90)} = 0.54$, $C_L/\sigma = 0.06$.

95
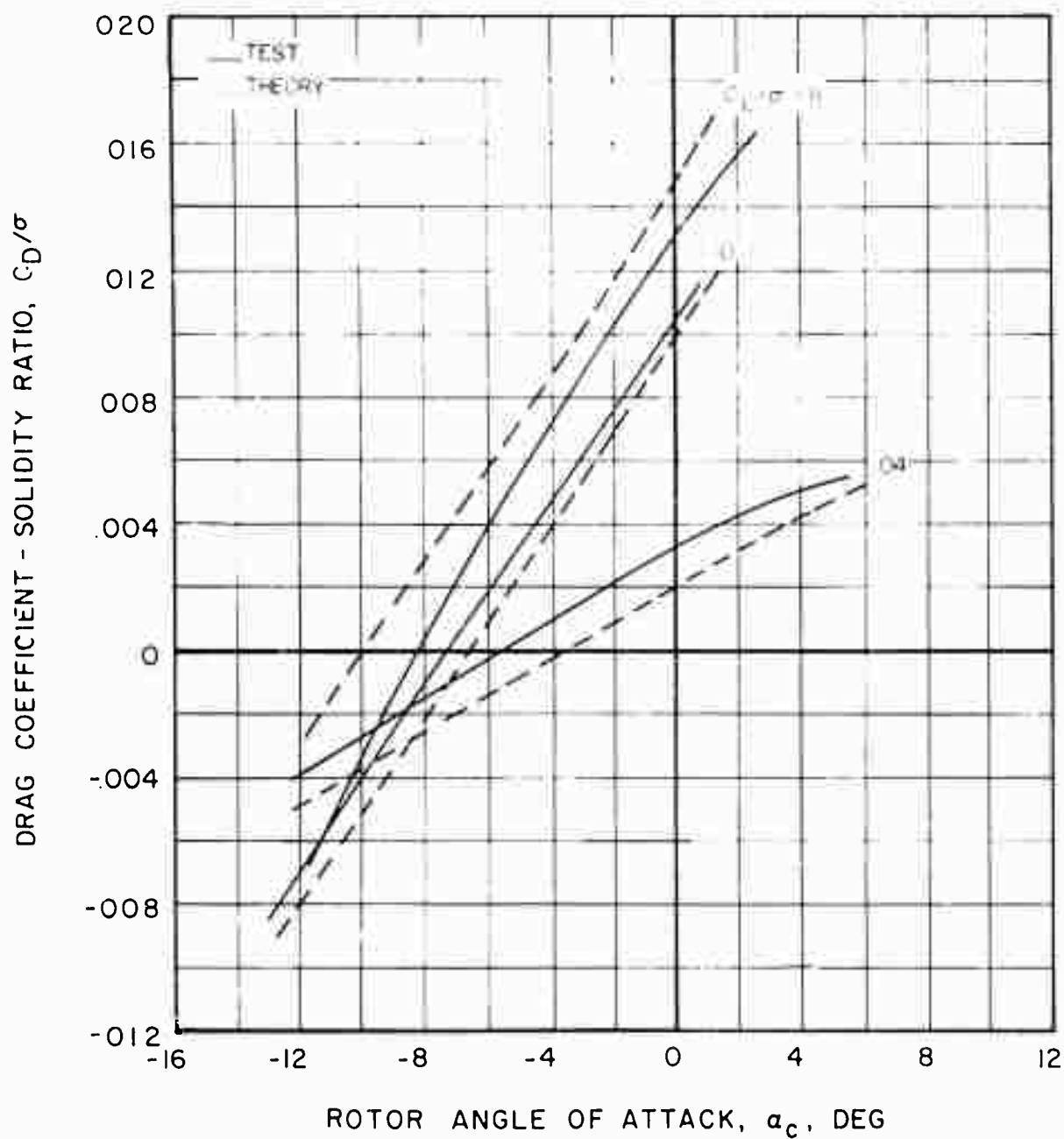
(a) Rotor Drag

Figure 53. The Measured and Calculated Variation of Drag and Torque With Rotor Angle of Attack at Various Values of Lift, $V = 117$ Knots, $\mu = 0.30$, $\theta_1 = -8°$, $M_{(1.0, 90)} = 0.74$.
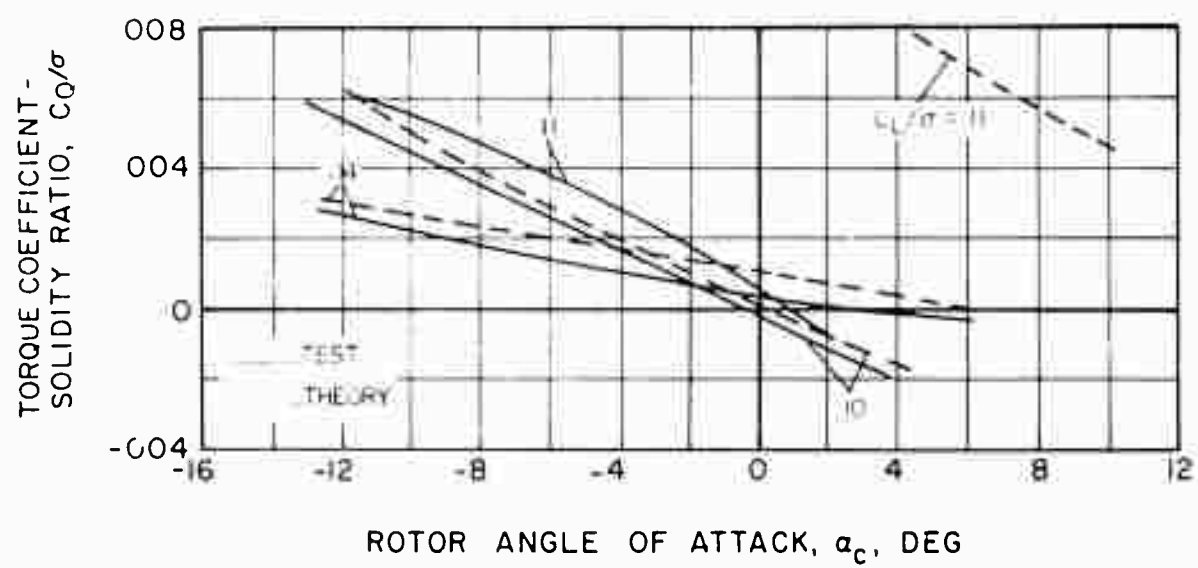
(b) Rotor Torque

Figure 53. Concluded.

97
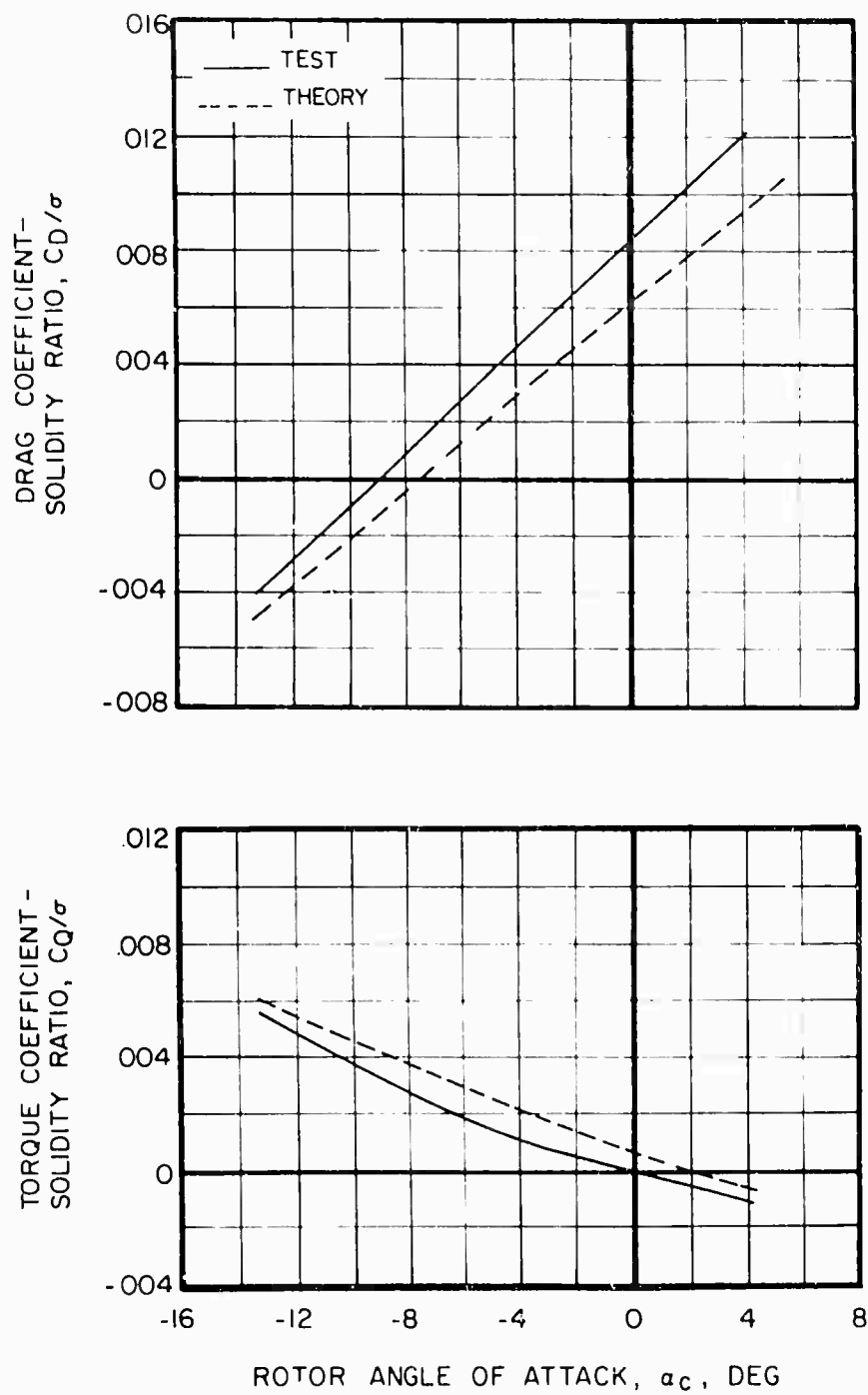
Figure 54. A Sample of the Measured and Calculated Variation of Drag and Torque With Rotor Angle of Attack at High Advancing Tip Mach Number, V = 175 Knots, μ = 0.39, θ_1 = 0°, $M_{(1.0, 90)}$ = 0.89, c_L/σ = 0.06.

98
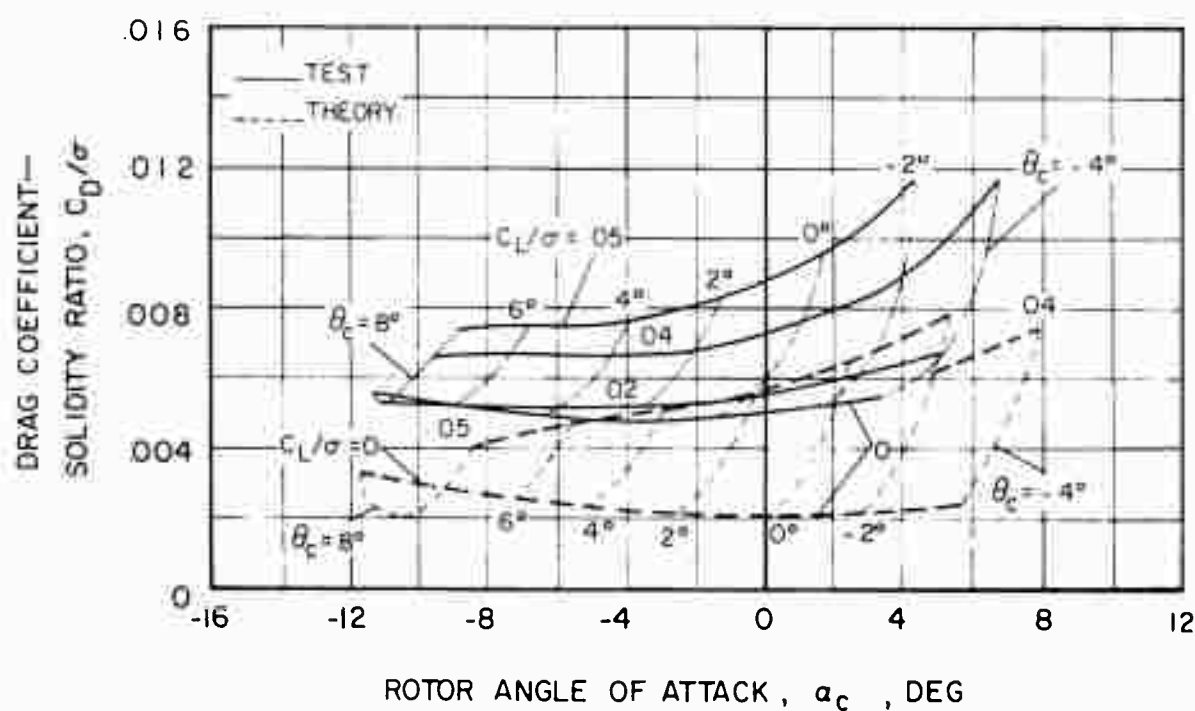
(a) Rotor Drag

Figure 55. The Measured and Calculated Variation of Drag and Torque With Rotor Angle of Attack at Various Values of Lift, V = 193 Knots, μ = 0.71, θ_1 = 0°, M(1.0, 90) = 0.68.

99
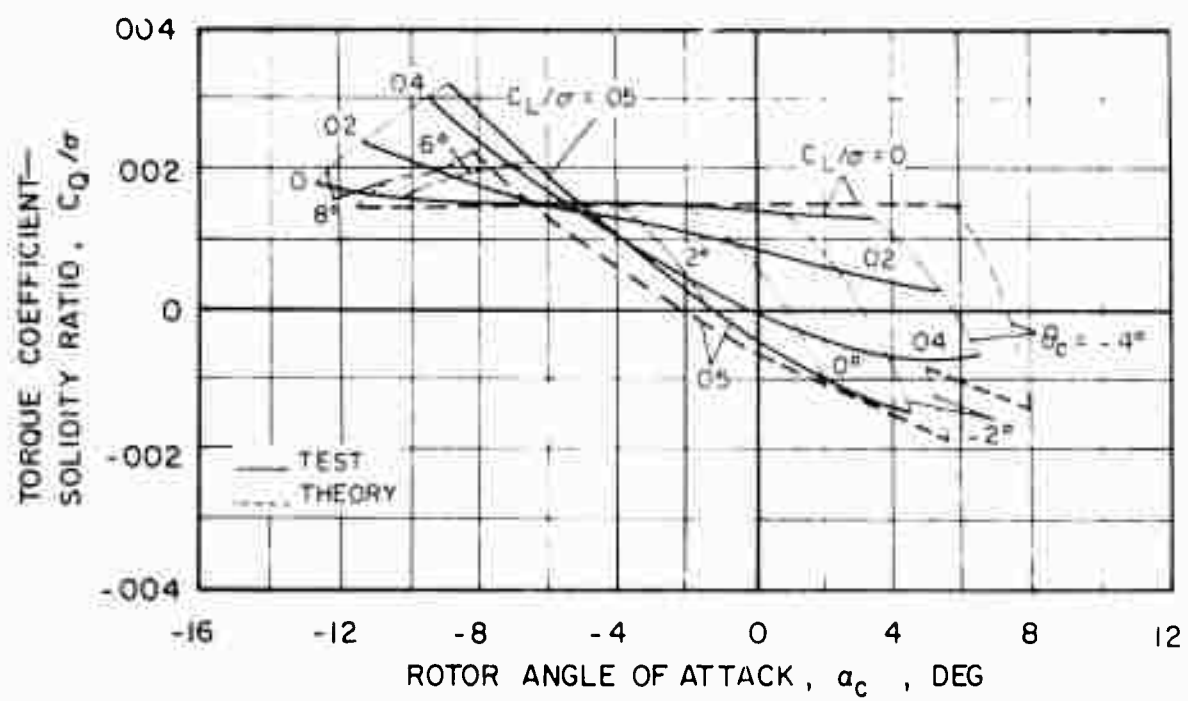
(b) Rotor Torque

Figure 55. Concluded.

100
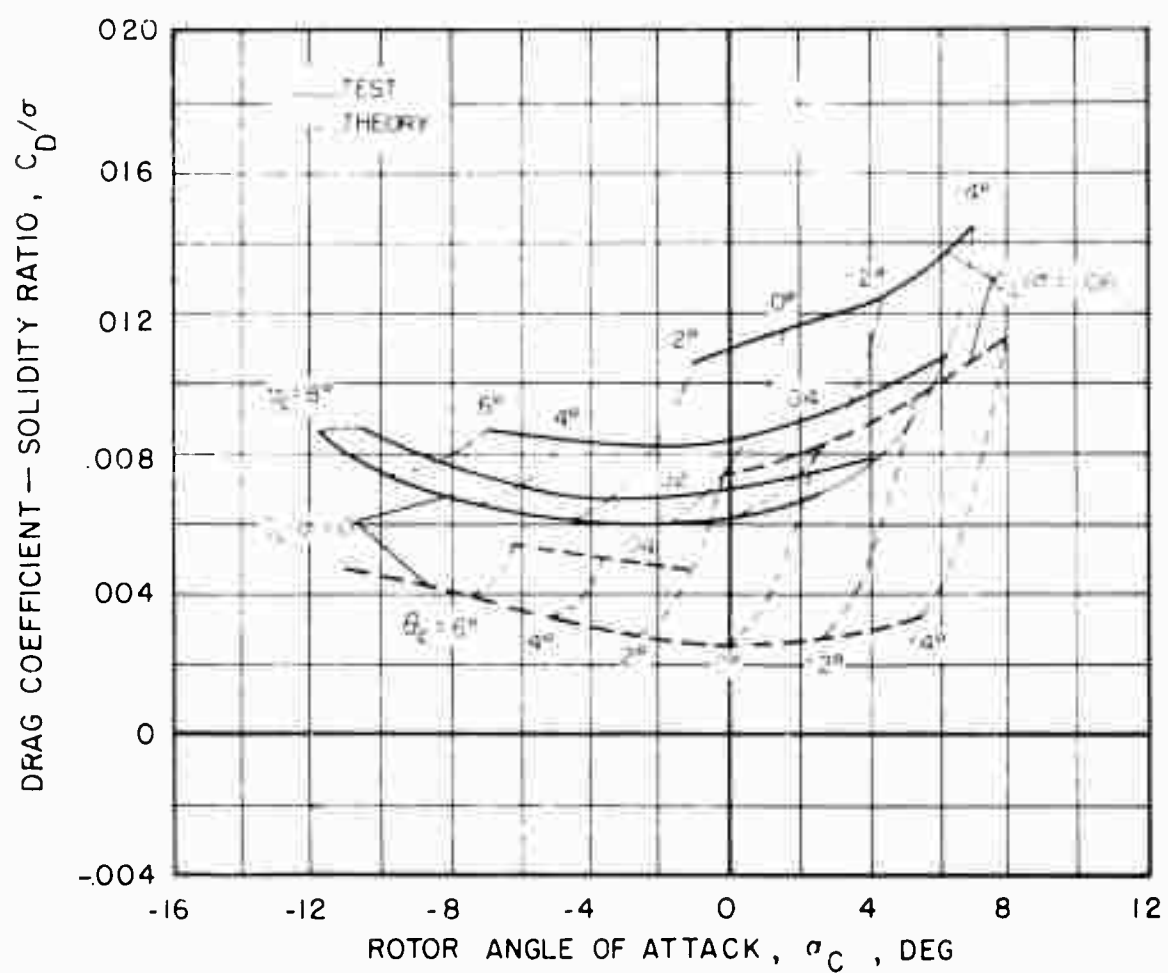
(a) Rotor Drag

Figure 56. The Measured and Calculated Variation of Drag and Torque With Rotor Angle of Attack at Various Values of Lift, $V = 195$ Knots, $\mu = 0.82$, $\theta_1 = 0°$, $M_{(1.0, 90)} = 0.62$.
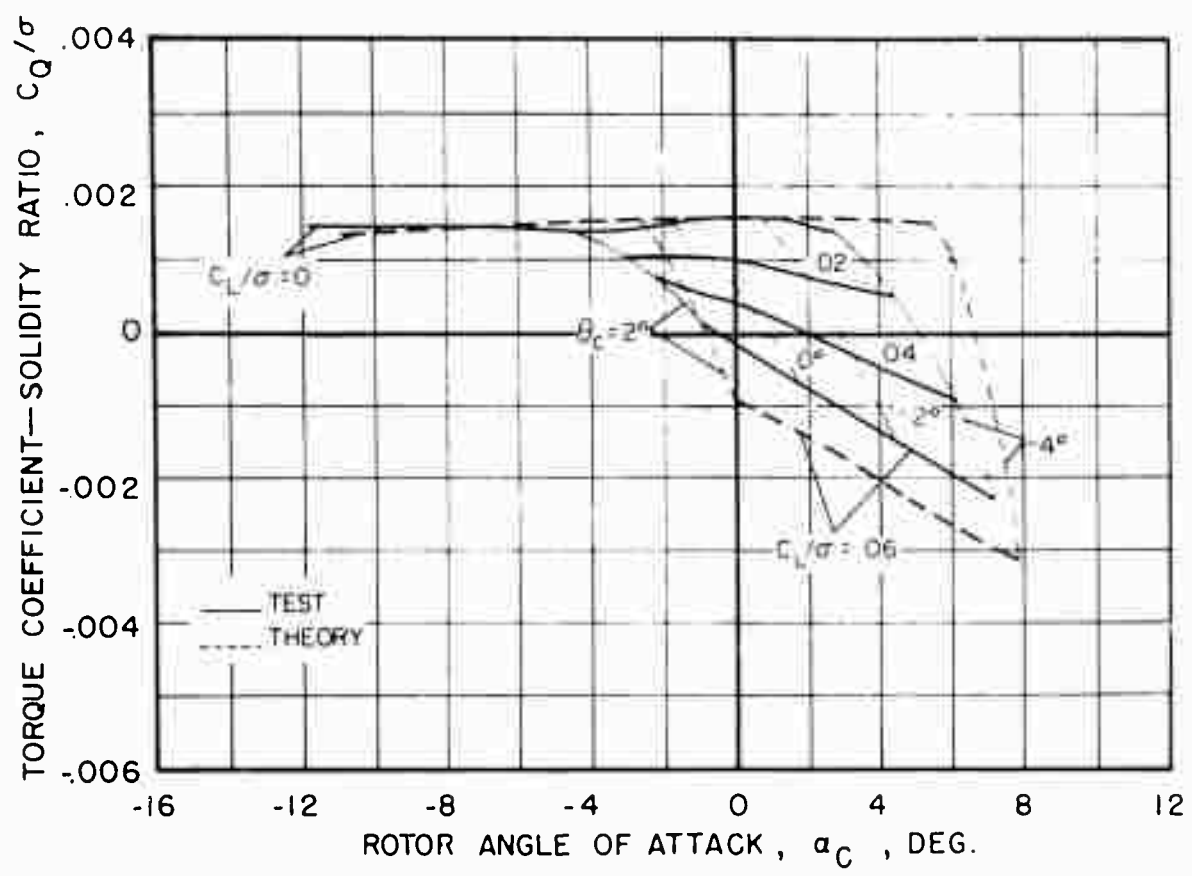
(b) Rotor Torque

Figure 56. Concluded.
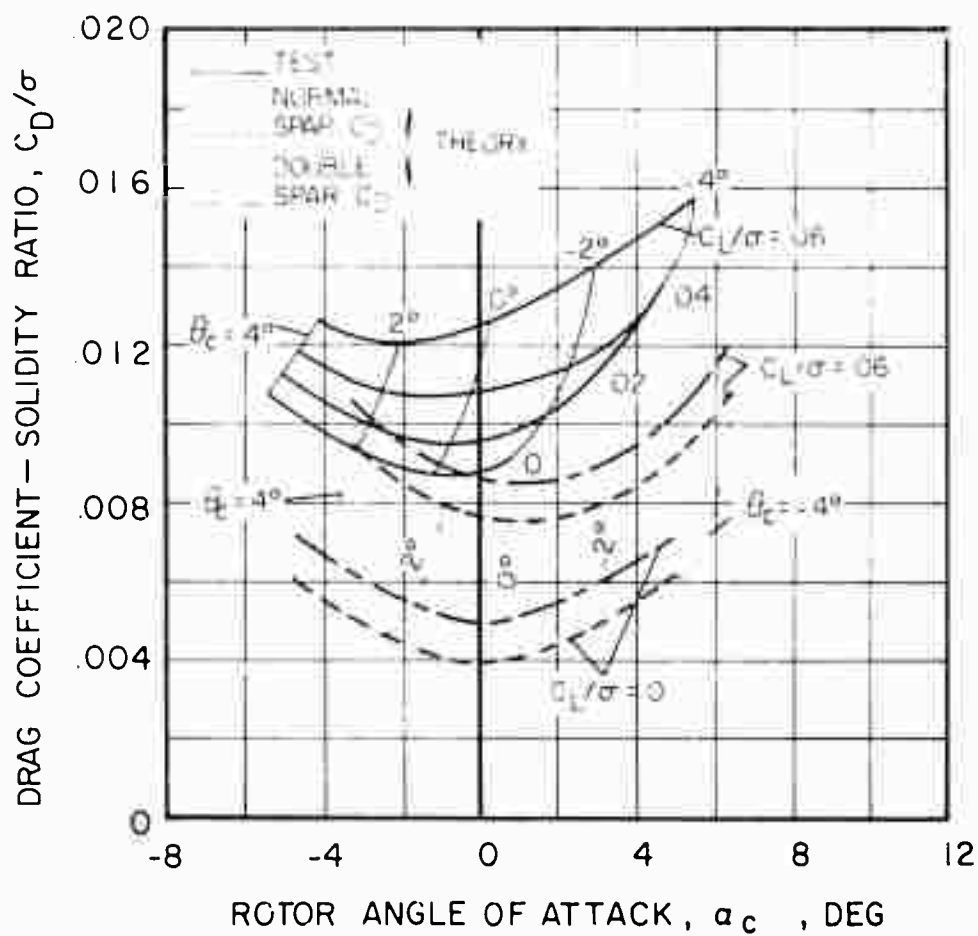
(a) Rotor Drag

Figure 57. The Measured and Calculated Variation of Drag
and Torque With Rotor Angle of Attack at Various
Values of Lift, $V = 197$ Knots, $\mu = 1.05$,
$\theta_1 = 0°$, $M(1.0, 90) = 0.54$.

103

(b) Rotor Torque

Figure 57. Concluded.
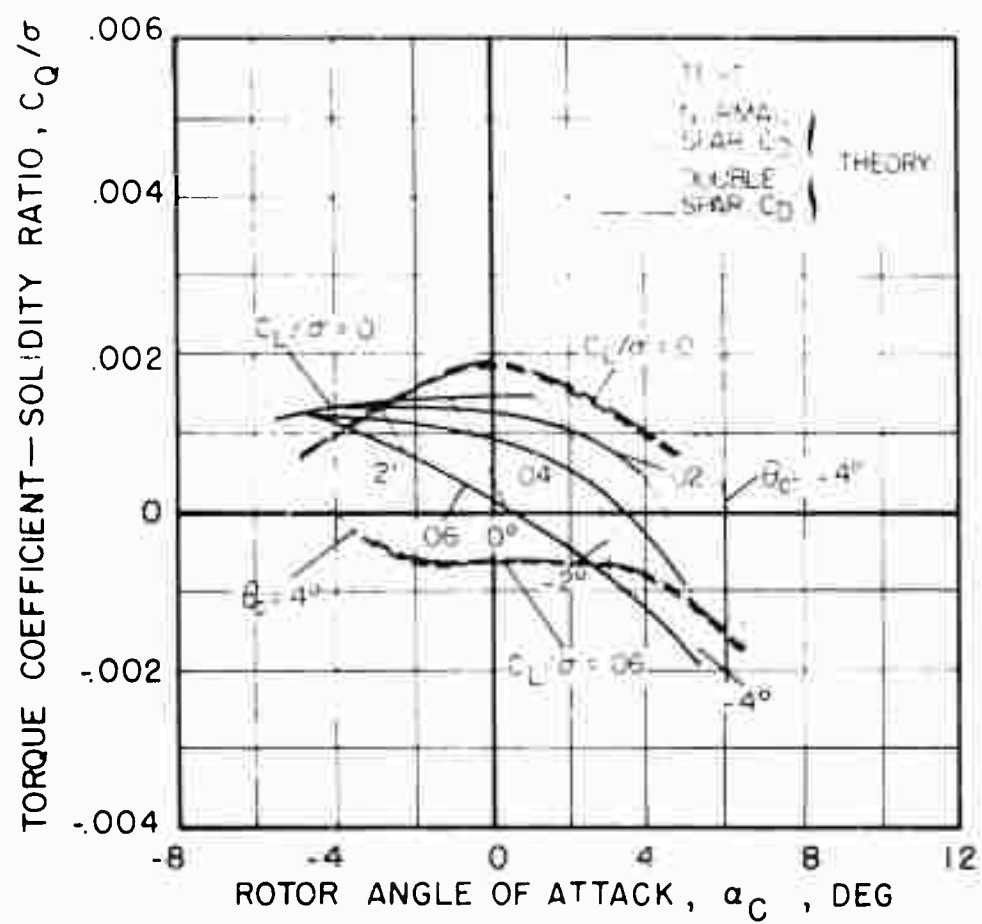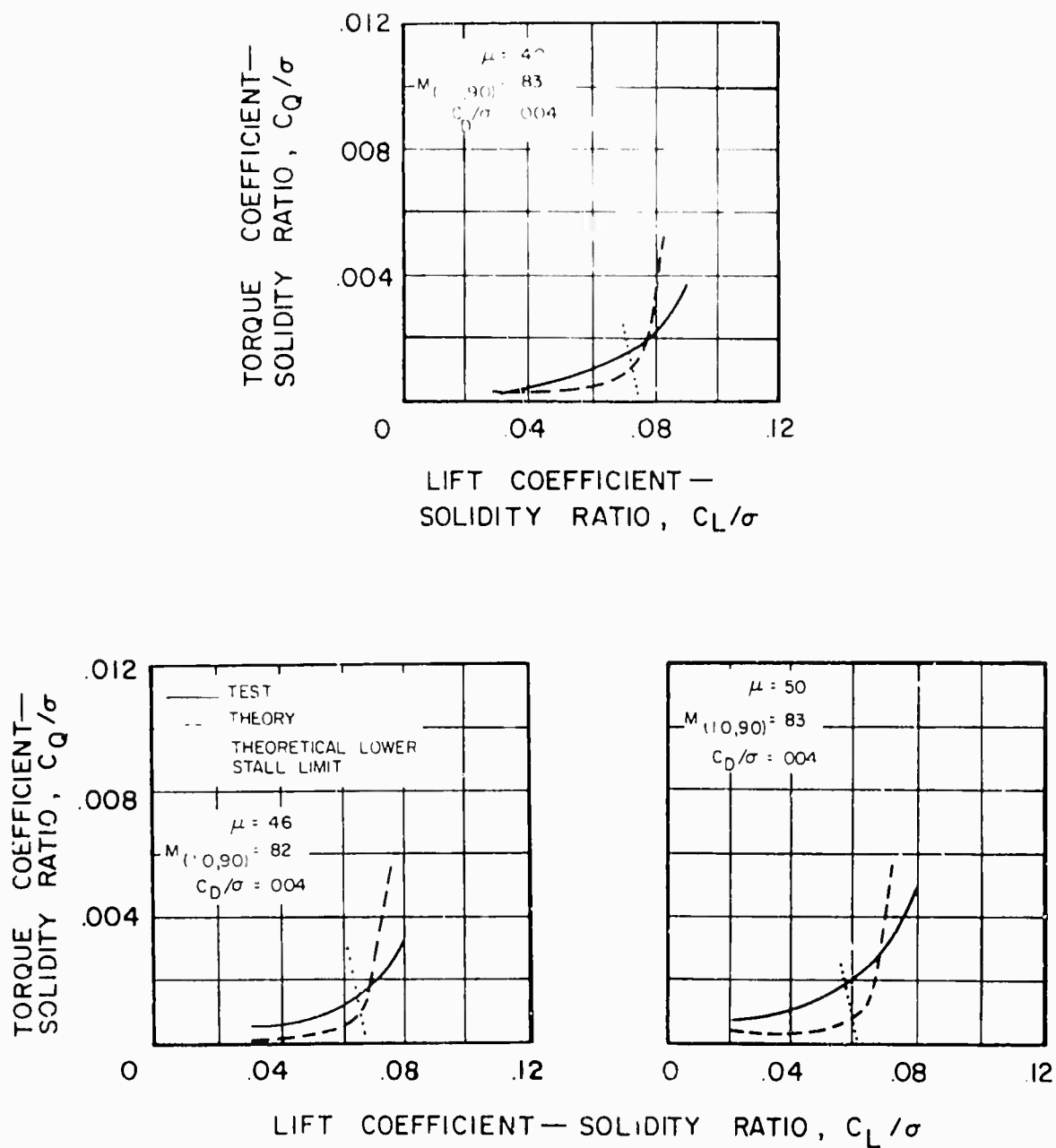
(a) Constant Advancing Tip Mach Number.

Figure 58. A General Comparison of Measured and
Calculated Torque Versus Lift at a Representa-
tive Value of Drag Coefficient-Solidity Ratio,
$\theta_1 = 0°$.

105
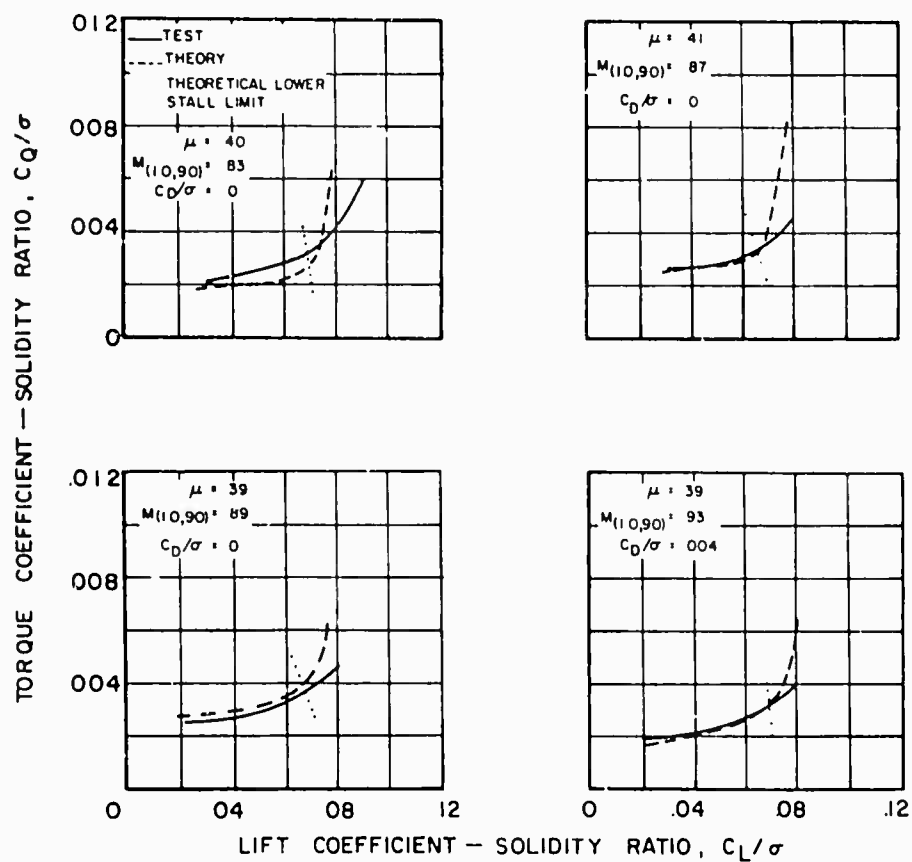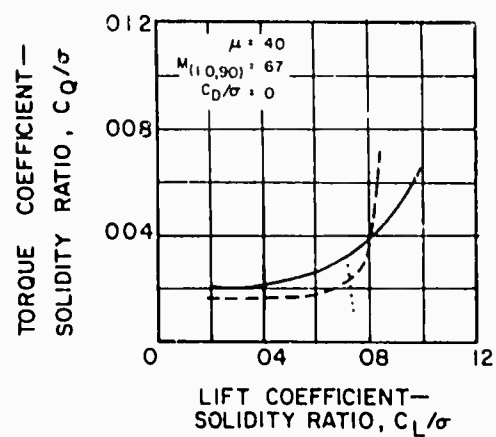
(b) Constant Advance Ratio

Figure 58. Concluded.

106
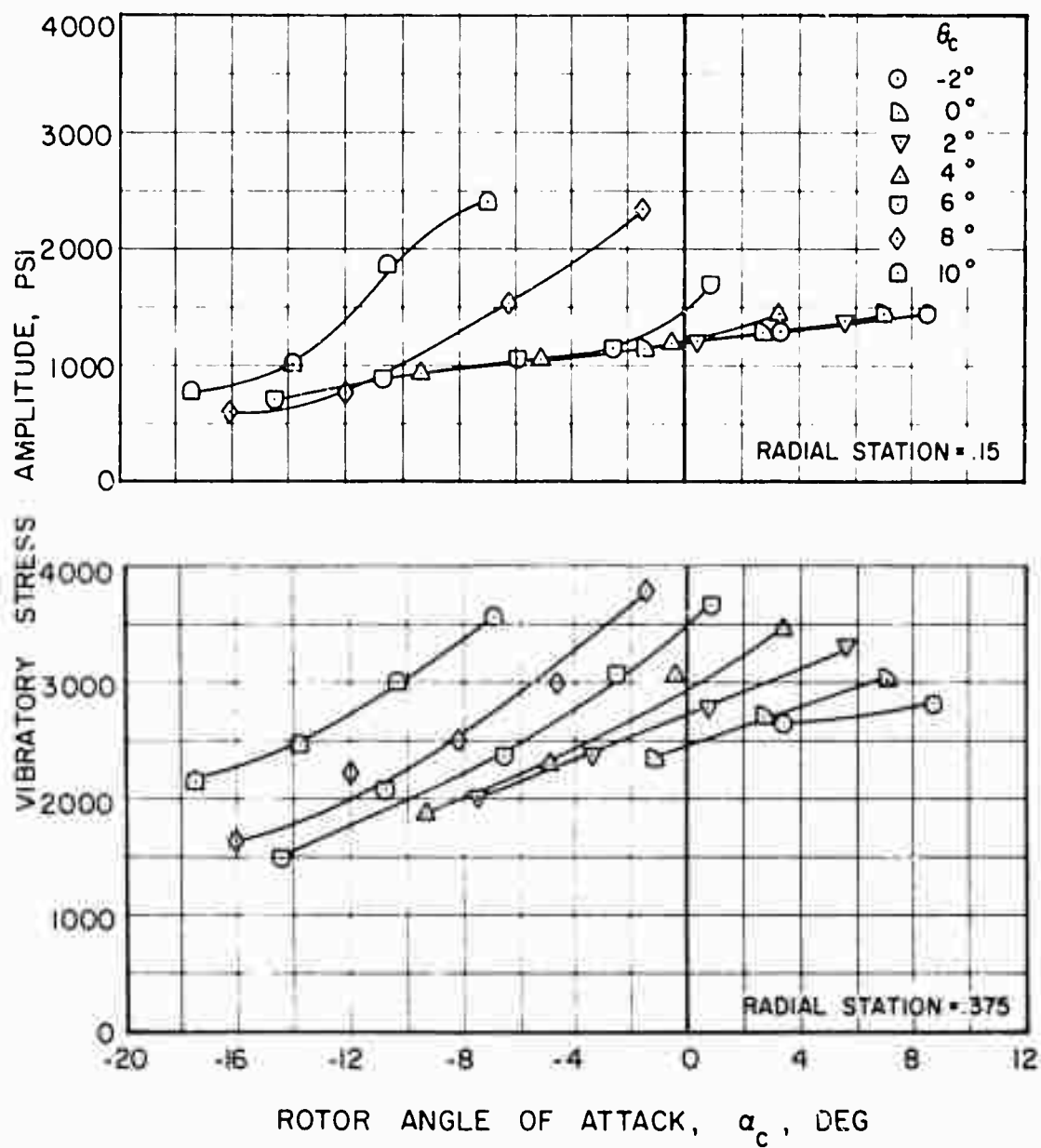
(a) Flapwise

Figure 59.   A Sample of Basic Flapwise, Chordwise and
Torsional Vibratory Stress Data at Several
Radial Stations, V = 117 Knots, μ = 0.30,
θ_1 = -8°, M(1.0, 90) = 0.74.

107

(a) Flapwise Concluded

Figure 59. Continued.

108
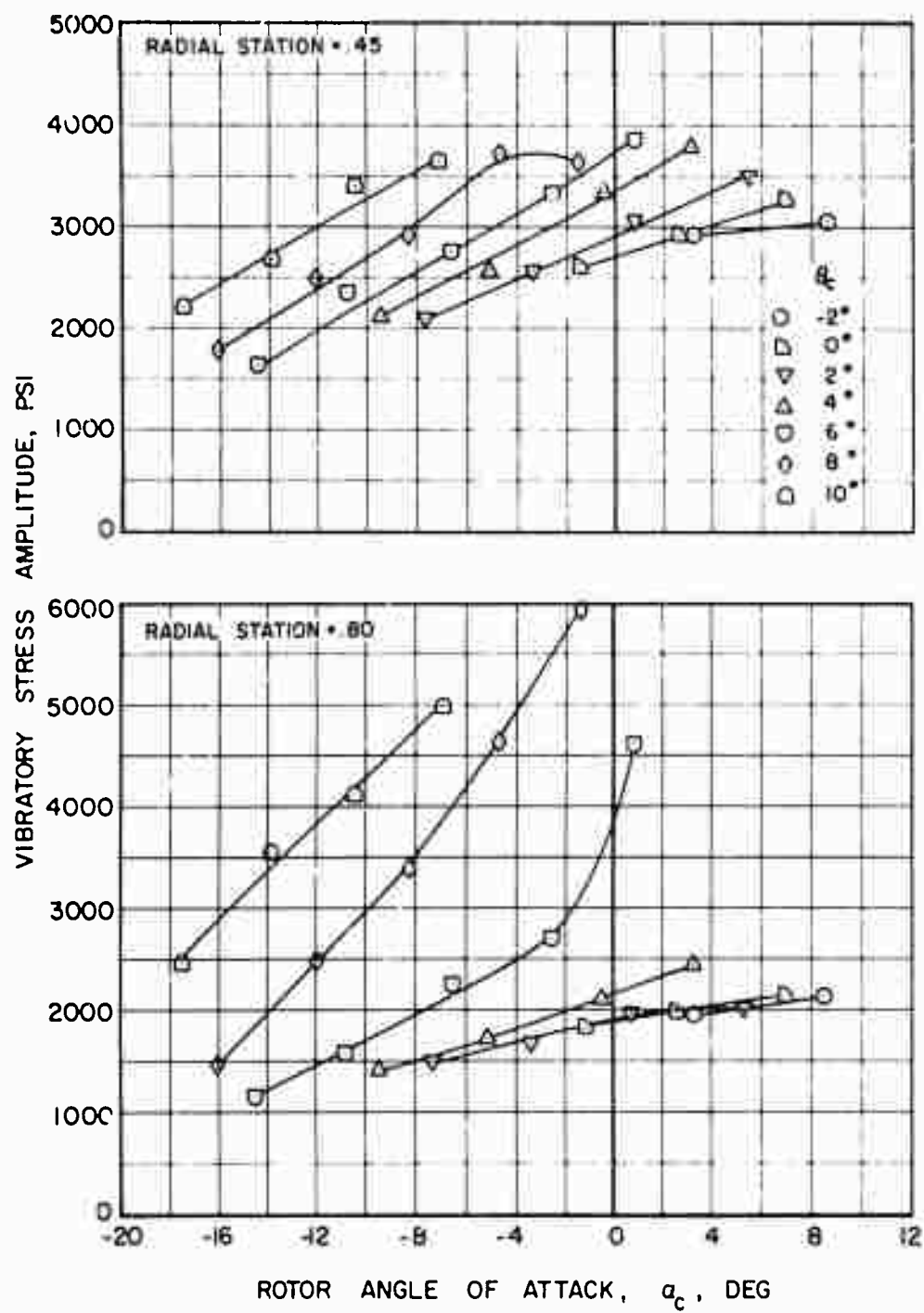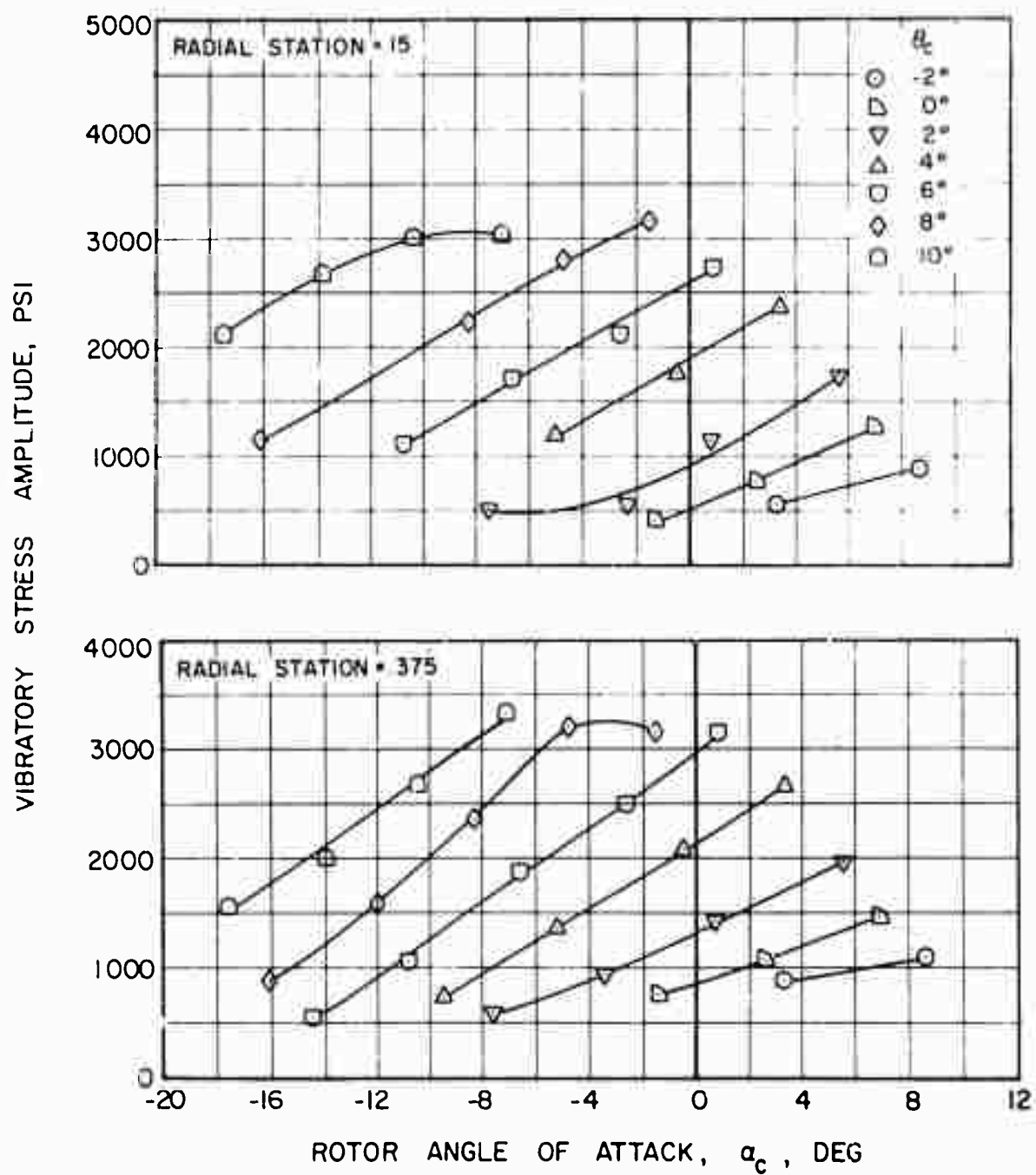
(b) Chordwise

Figure 59. Continued.

109

(b) Chordwise Concluded

Figure 59. Continued.

110
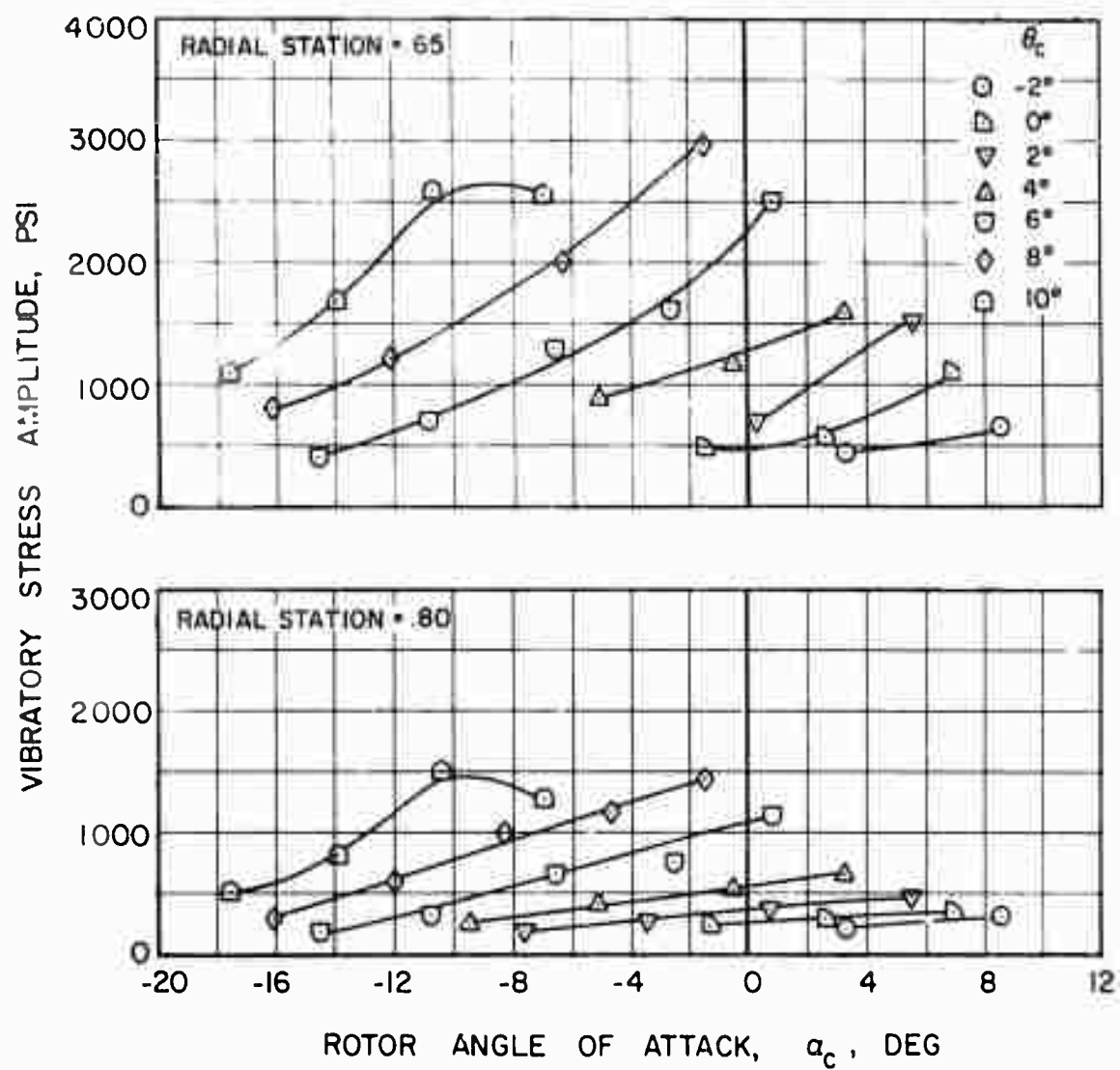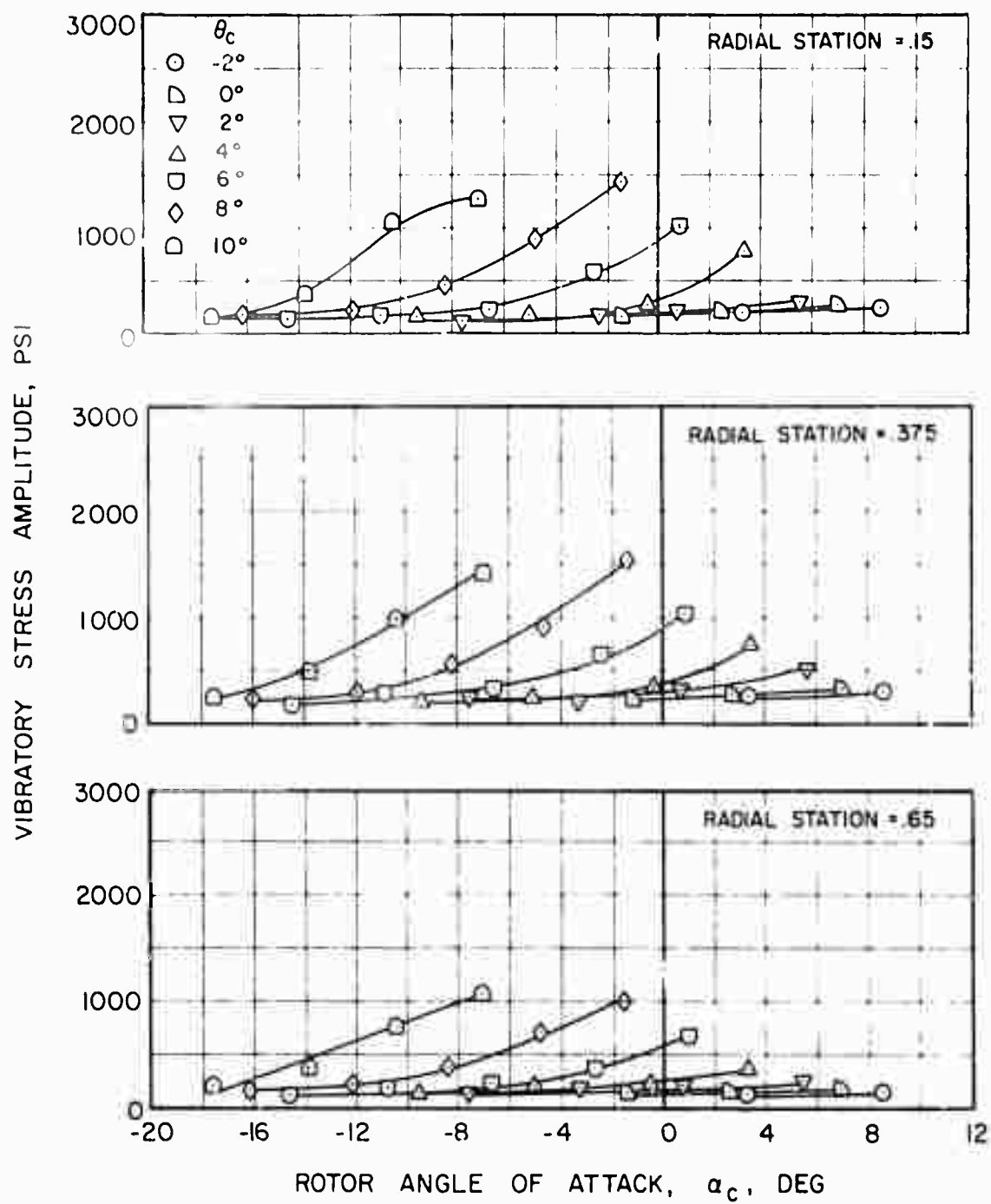
(c) Torsional

Figure 59. Concluded.

111
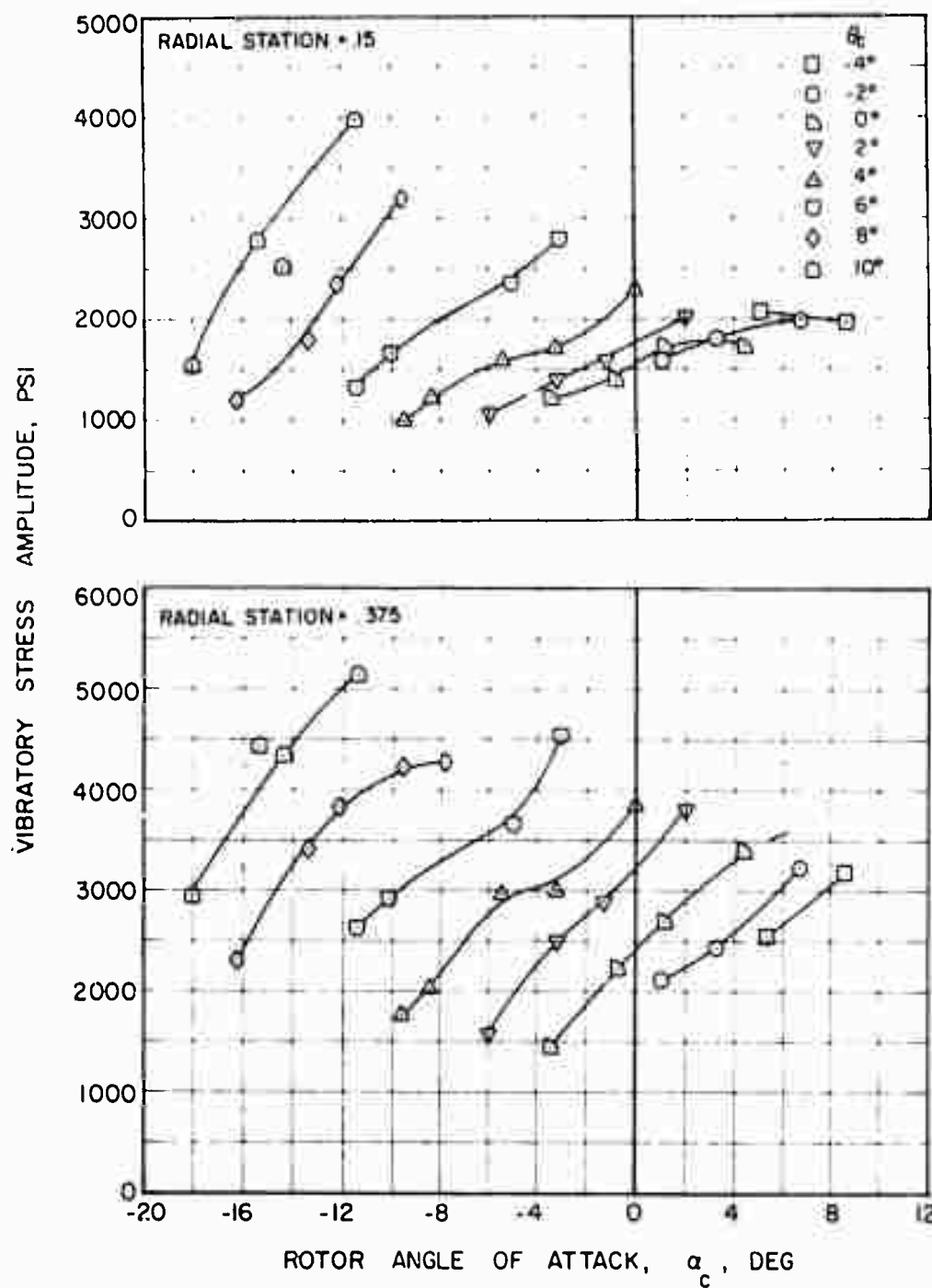
(a) Flapwise

Figure 60. A Sample of Basic Flapwise, Chordwise and Torsional Vibratory Stress Data at Several Radial Stations, V = 194 Knots, μ = 0.50, θ_1 = 0°, $M_{(1.0, 90)}$ = 0.83.

112

(a) Flapwise Concluded

Figure 60. Continued.

113
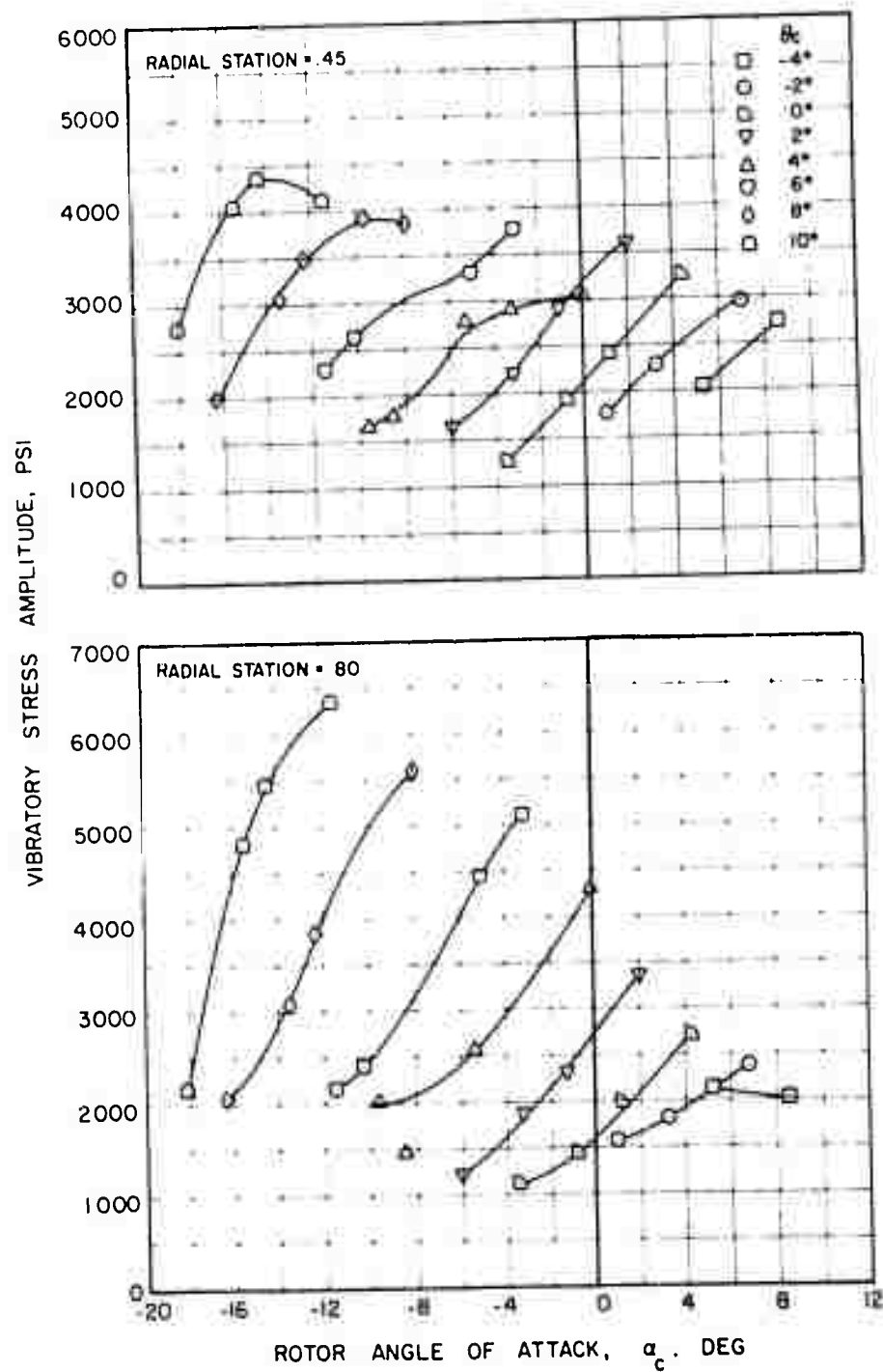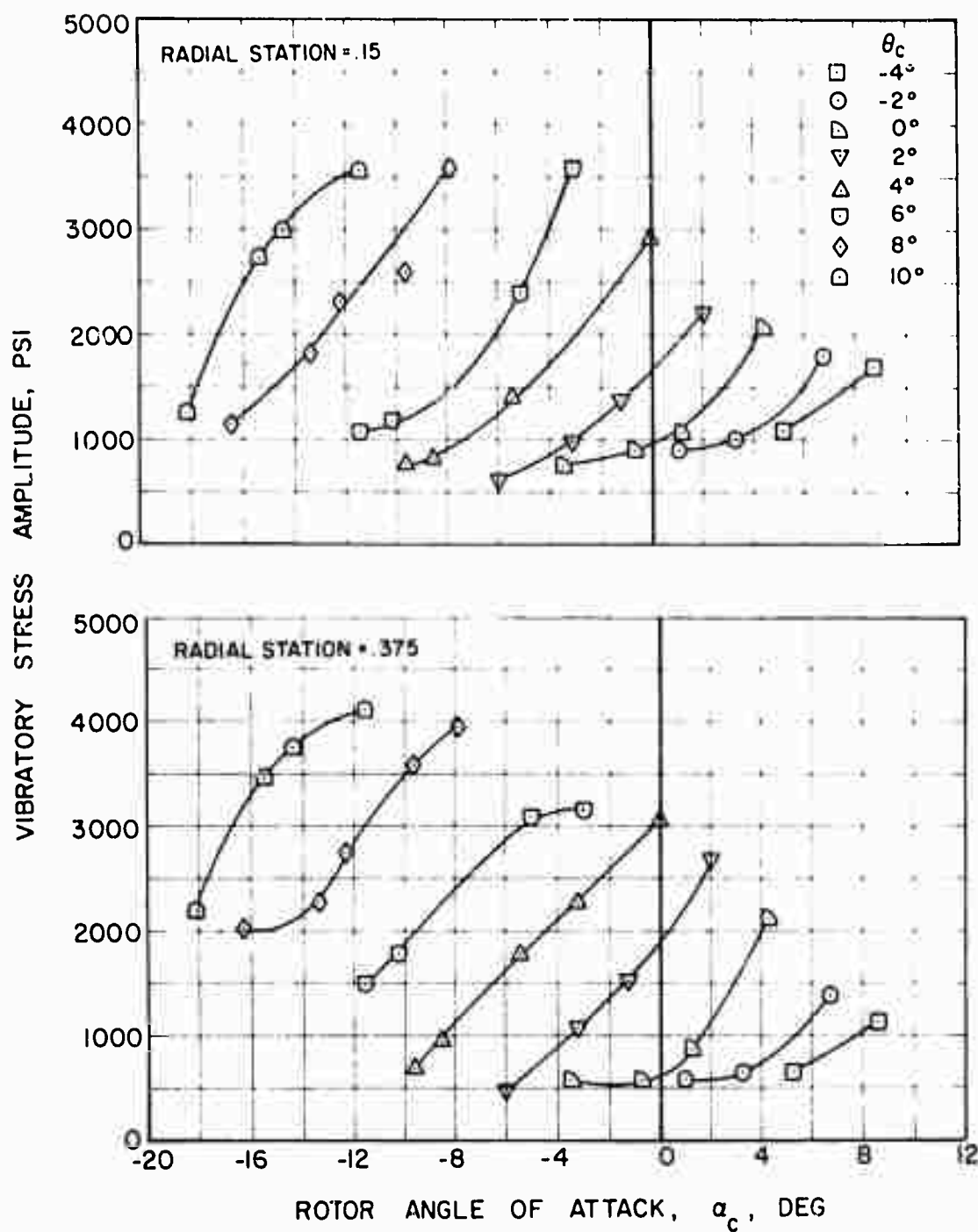
(b) Chordwise

Figure 60. Continued.

114

(b) Chordwise Concluded

Figure 60. Continued.

115
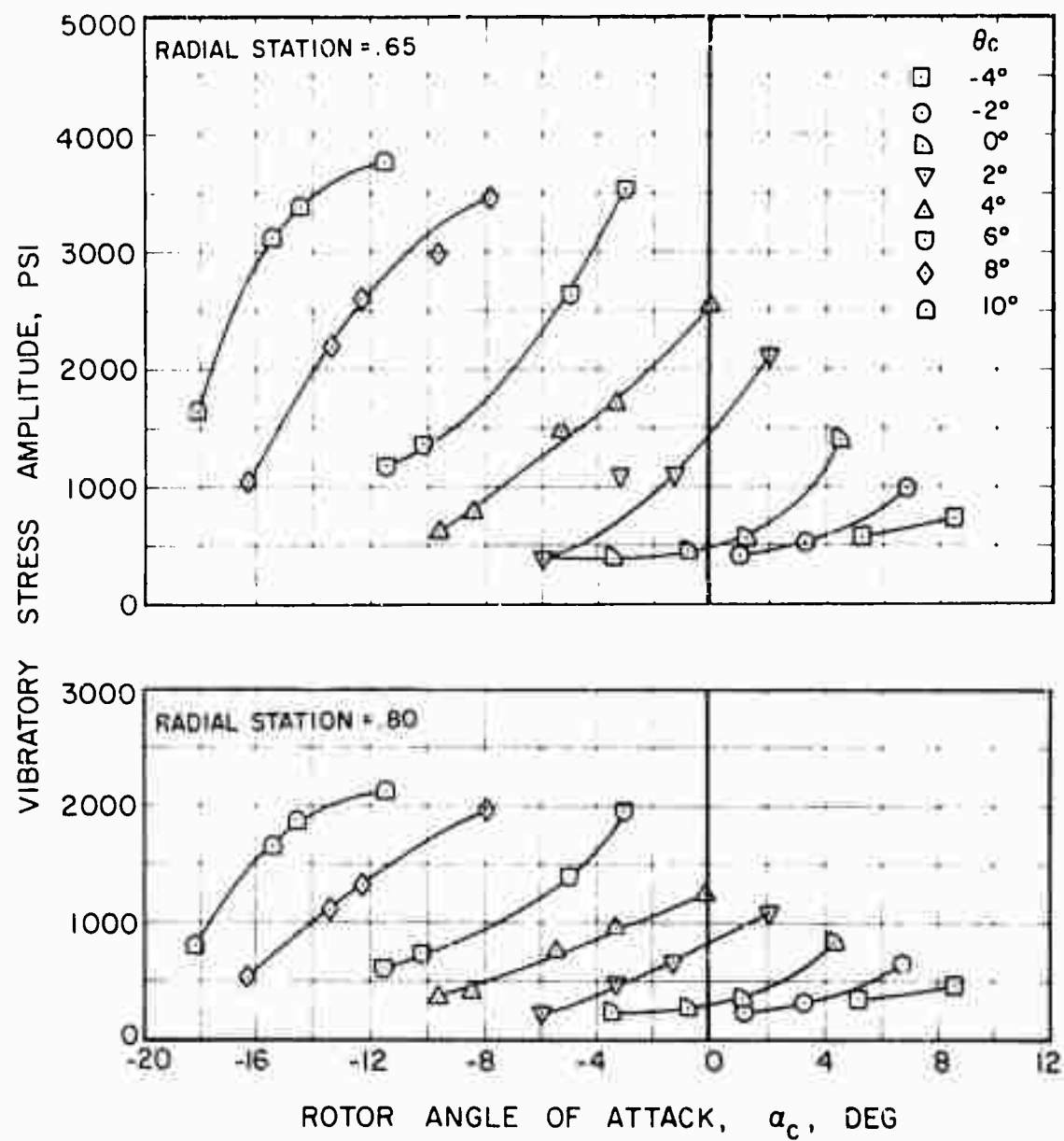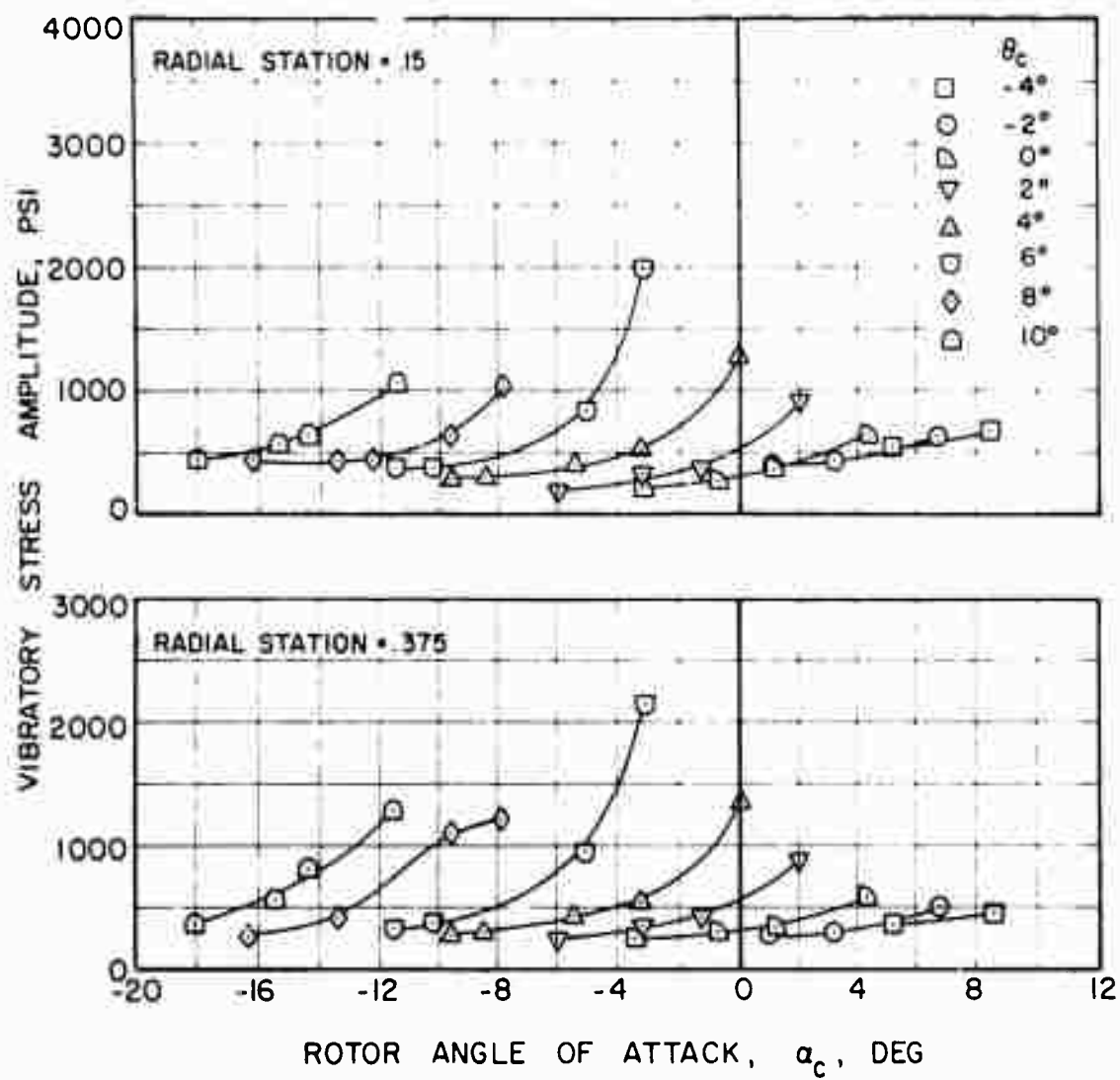
(c) Torsional

Figure 60. Concluded.

116
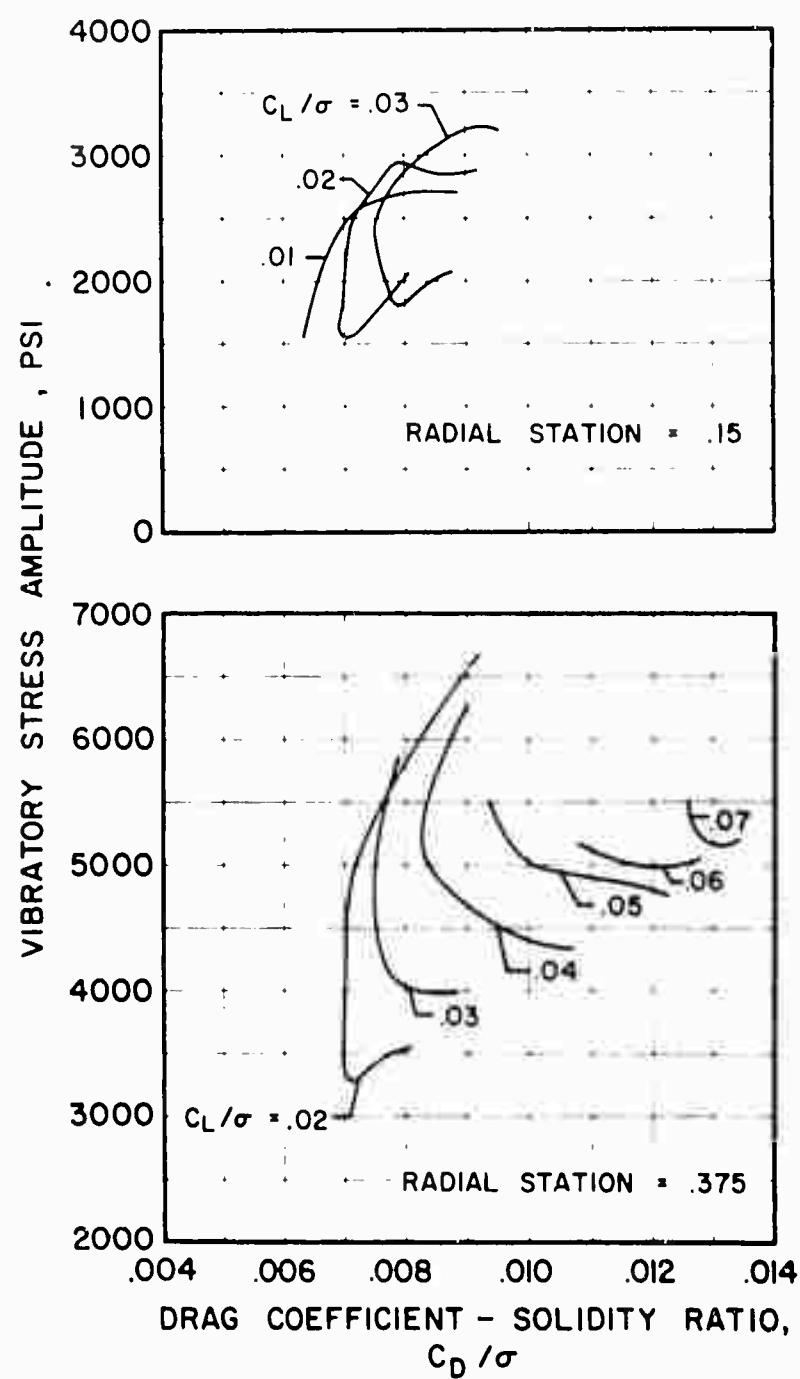
(a) Flapwise

Figure 61. The Effect of Drag on Flapwise, Chordwise, and
Torsional Vibratory Stress Amplitude at Constant
Lift at Various Radial Stations, V = 195 Knots,
μ = 0.82, θ_1 = 0°, M(1.0, 90) = 0.62.

117
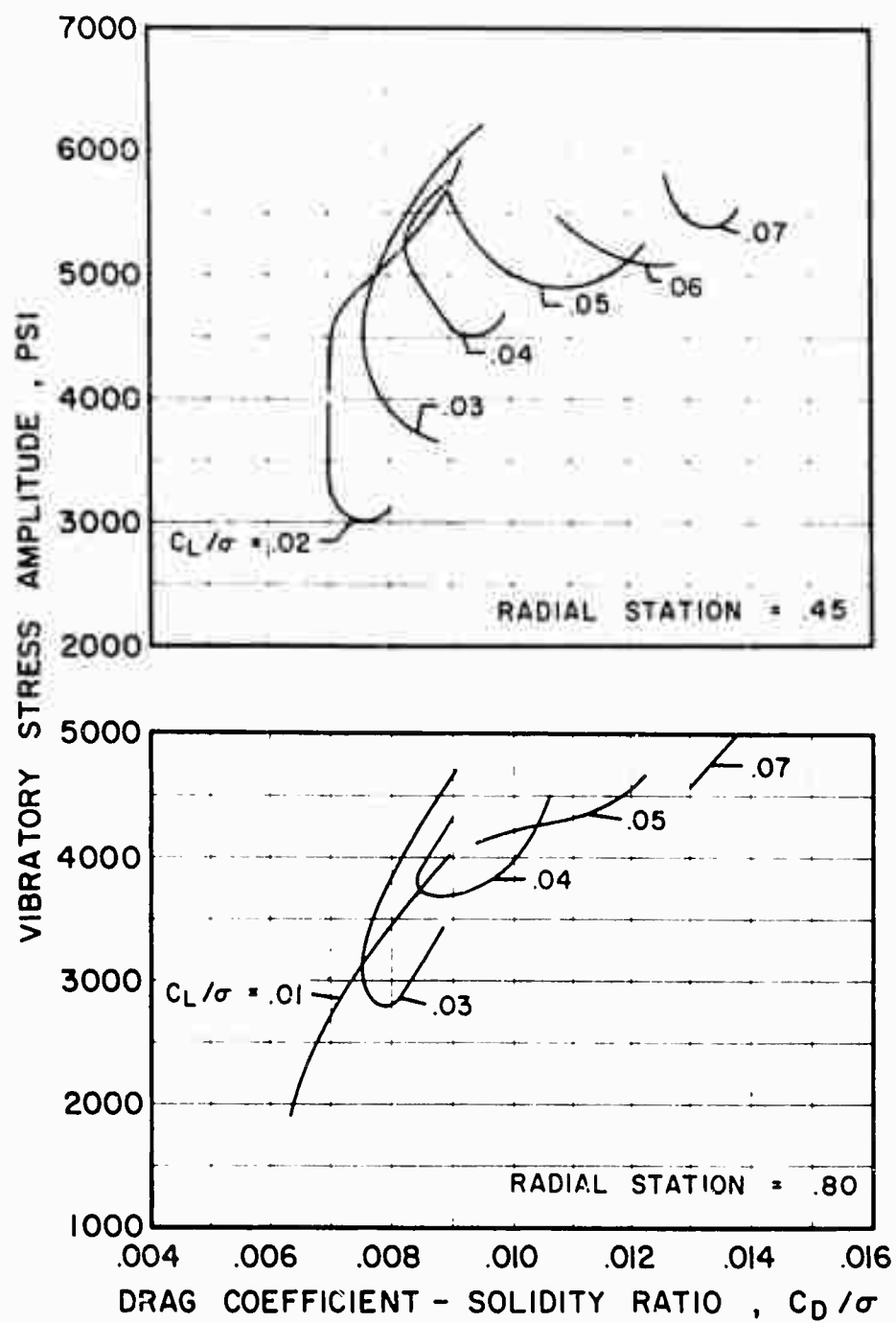
(a) Flapwise Concluded

Figure 61. Continued.

118
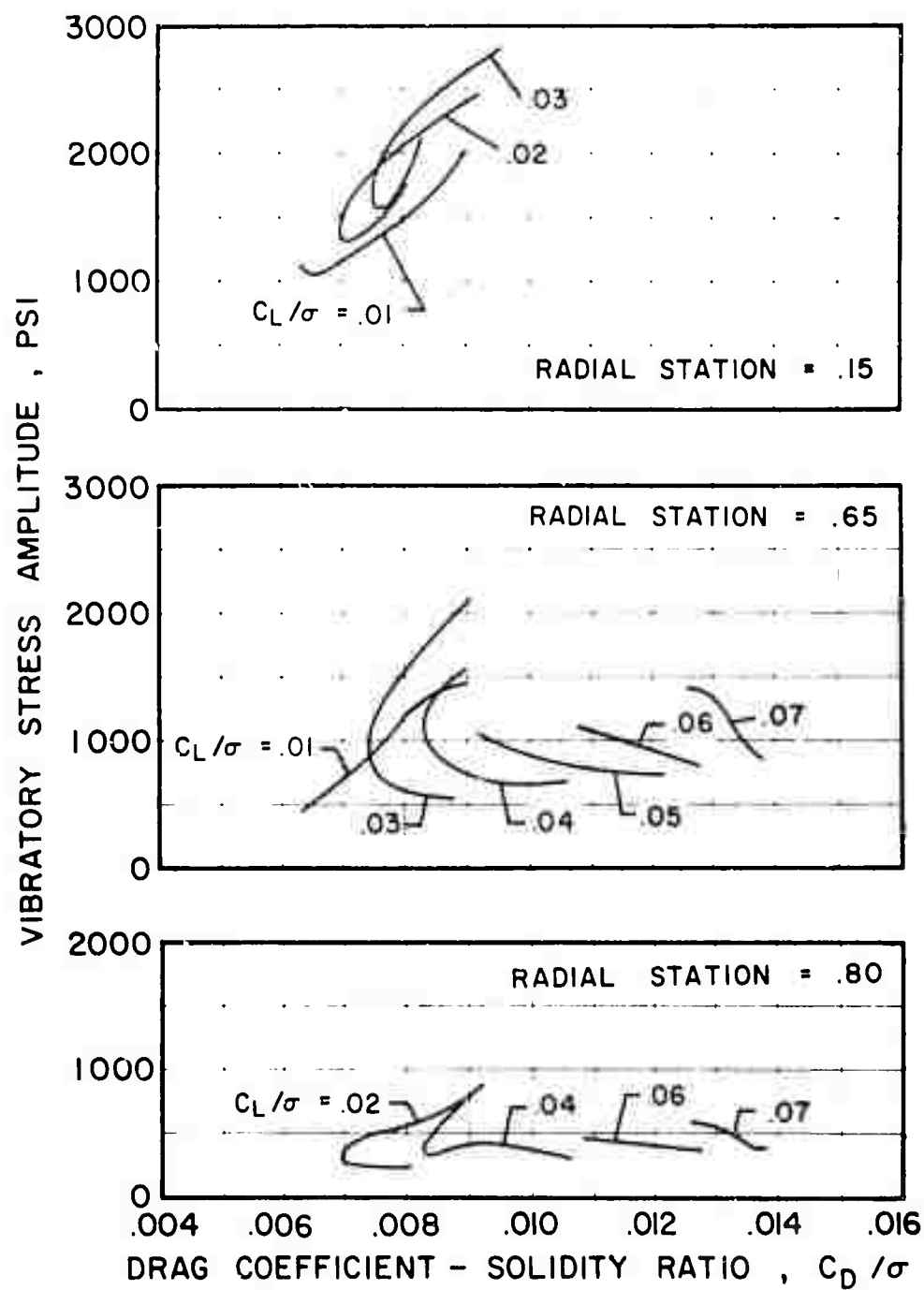
(b) Chordwise

Figure 61. Continued.

119
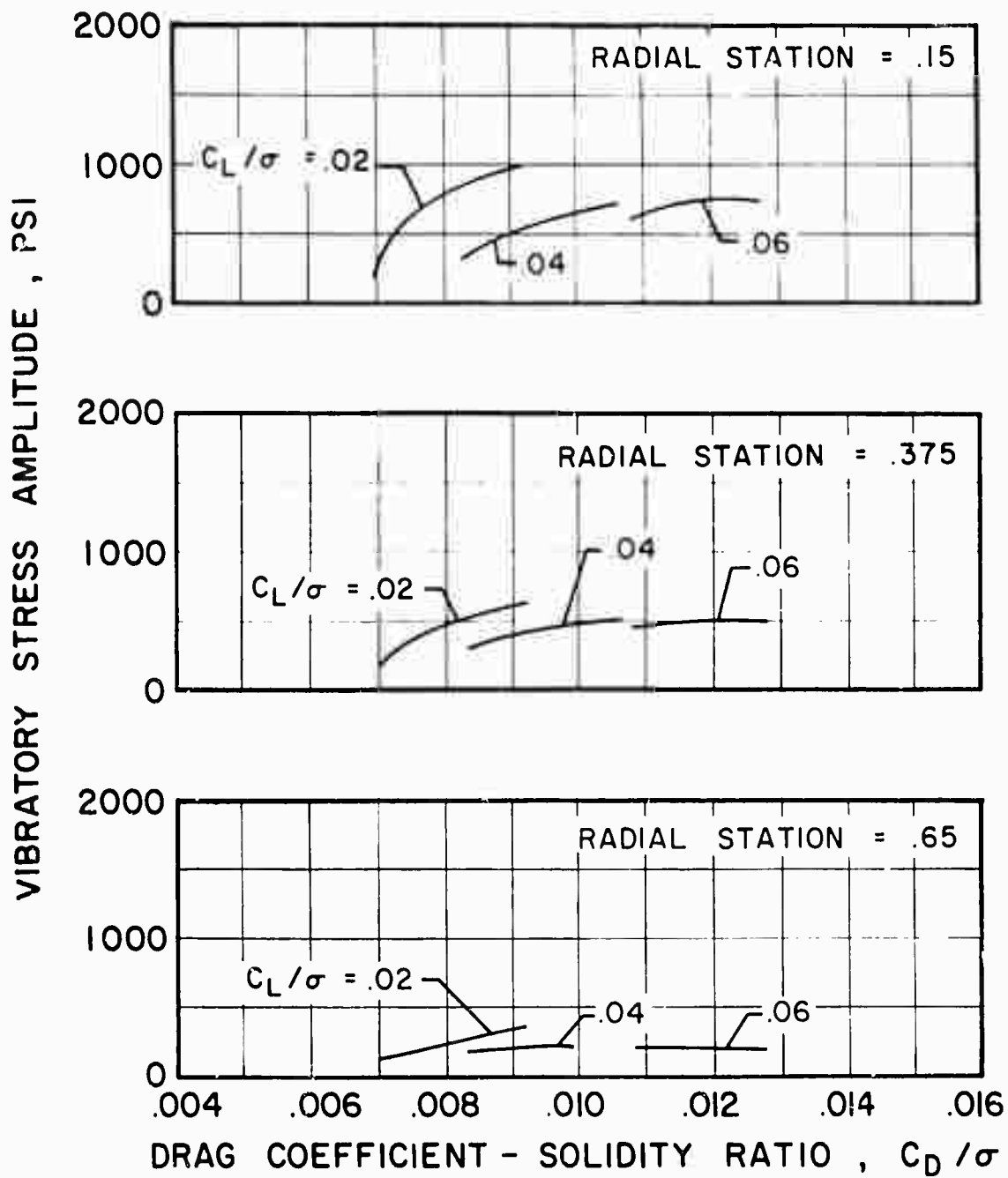
(c) Torsional

Figure 61   Concluded.

120
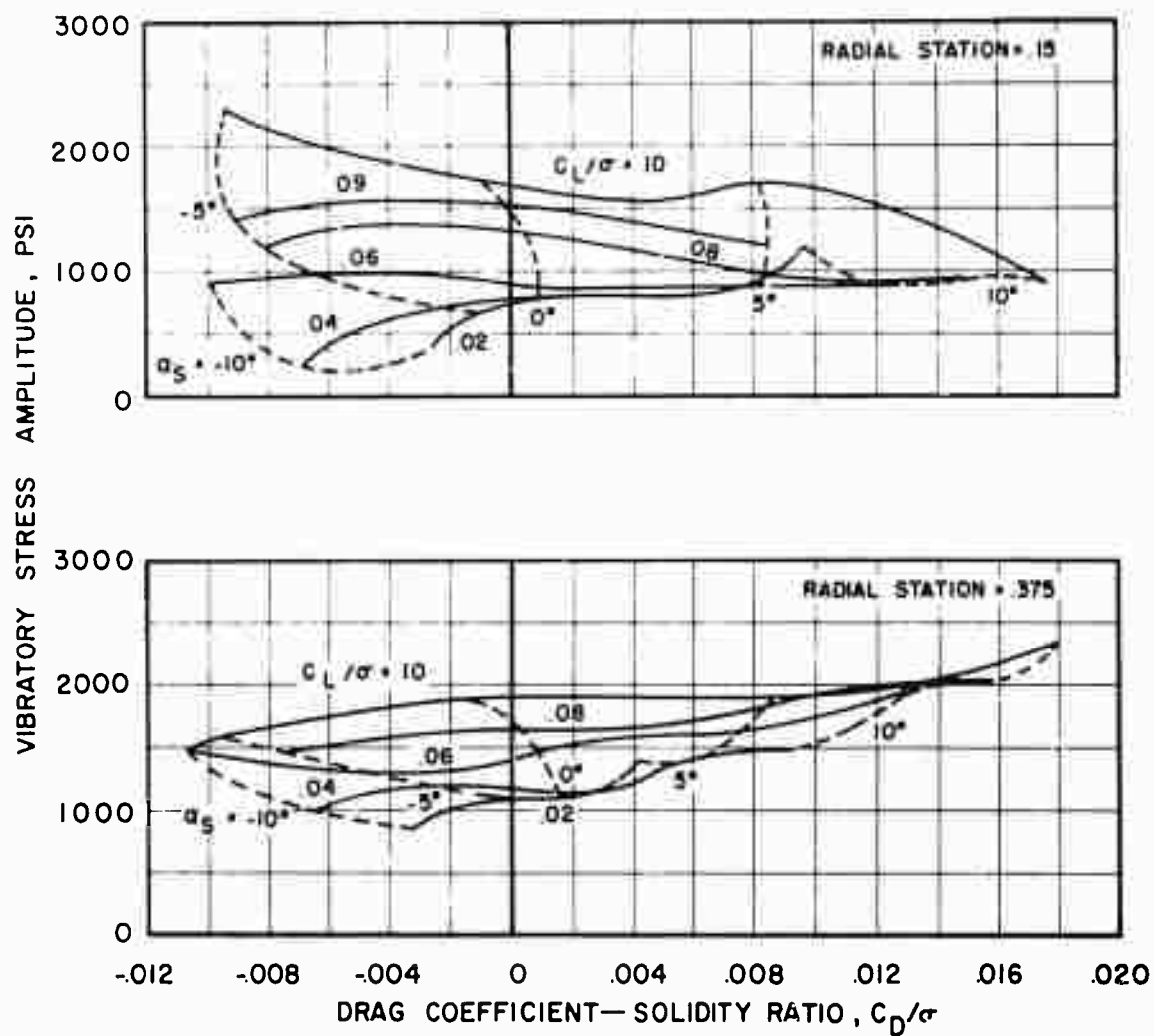
(a) Flapwise

Figure 62. The Effect of Drag and Shaft Angle on Flapwise and Chordwise Vibratory Stress Amplitude at Constant Lift at 15% and 37.5% Radius, V = 116 Knots, μ = 0.30, θ_1 = 0°, $M_{(1.0, 90)}$ = 0.74.

121
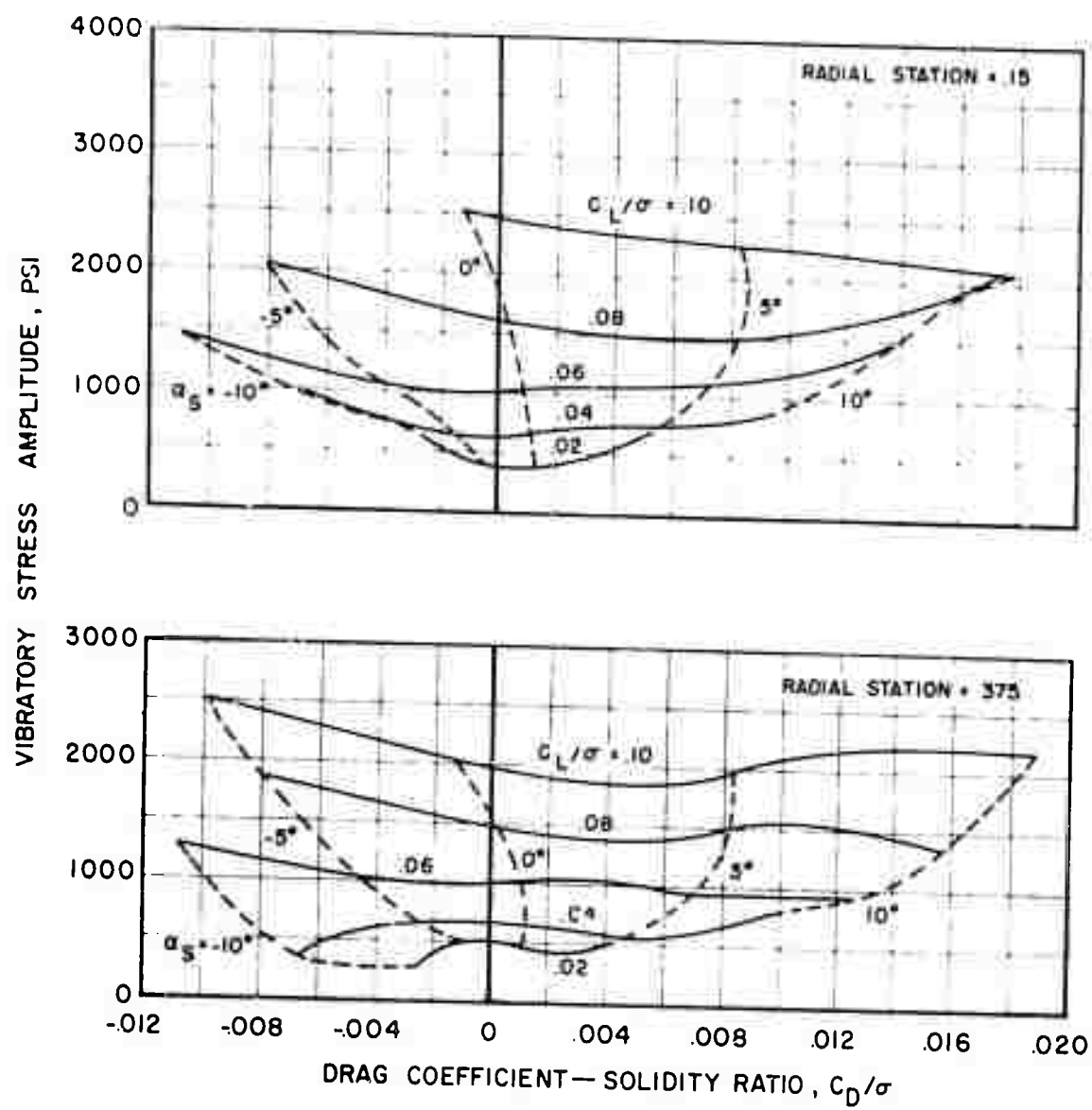
(b) Chordwise

Figure 62. Concluded.

122
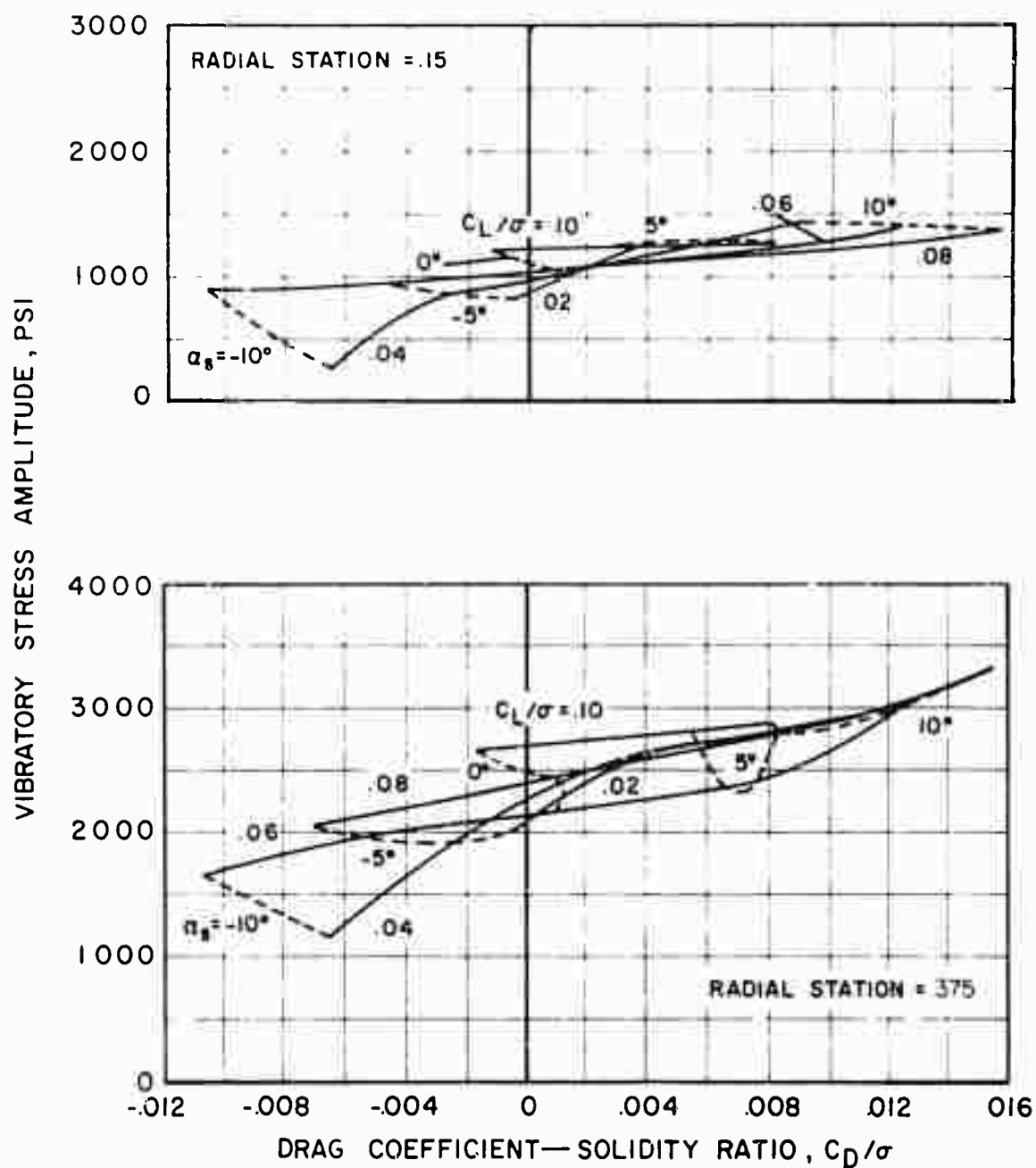
(a) Flapwise

Figure 63. The Effect of Drag and Shaft Angle on Flapwise and Chordwise Vibratory Stress Amplitude at Constant Lift at 15% and 37.5% Radius, V = 117 Knots, μ = 0.30, θ_1 = -8°, $M_{(1.0, 90)}$ = 0.74.

123
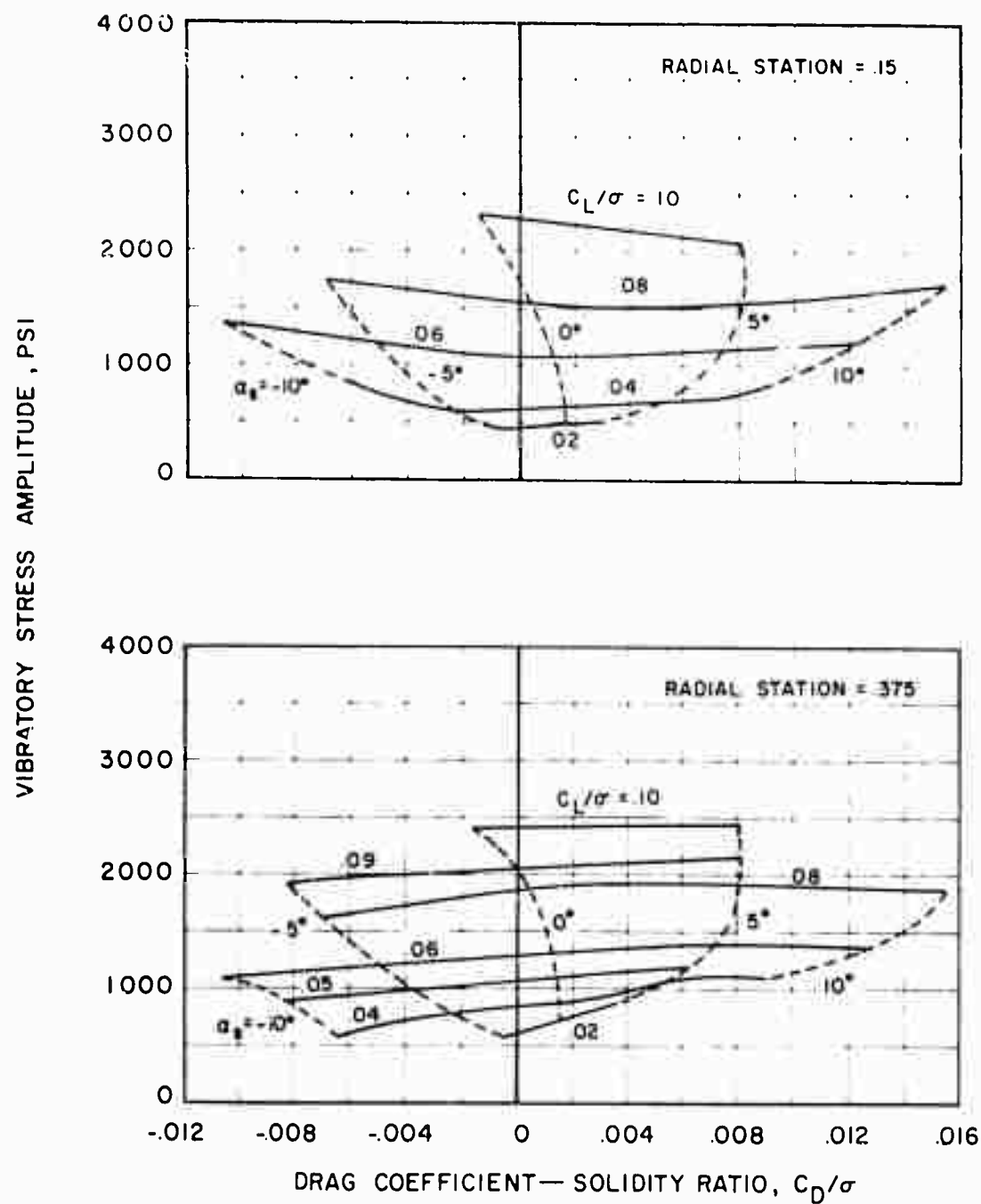
(b) Chordwise

Figure 63. Concluded.

124
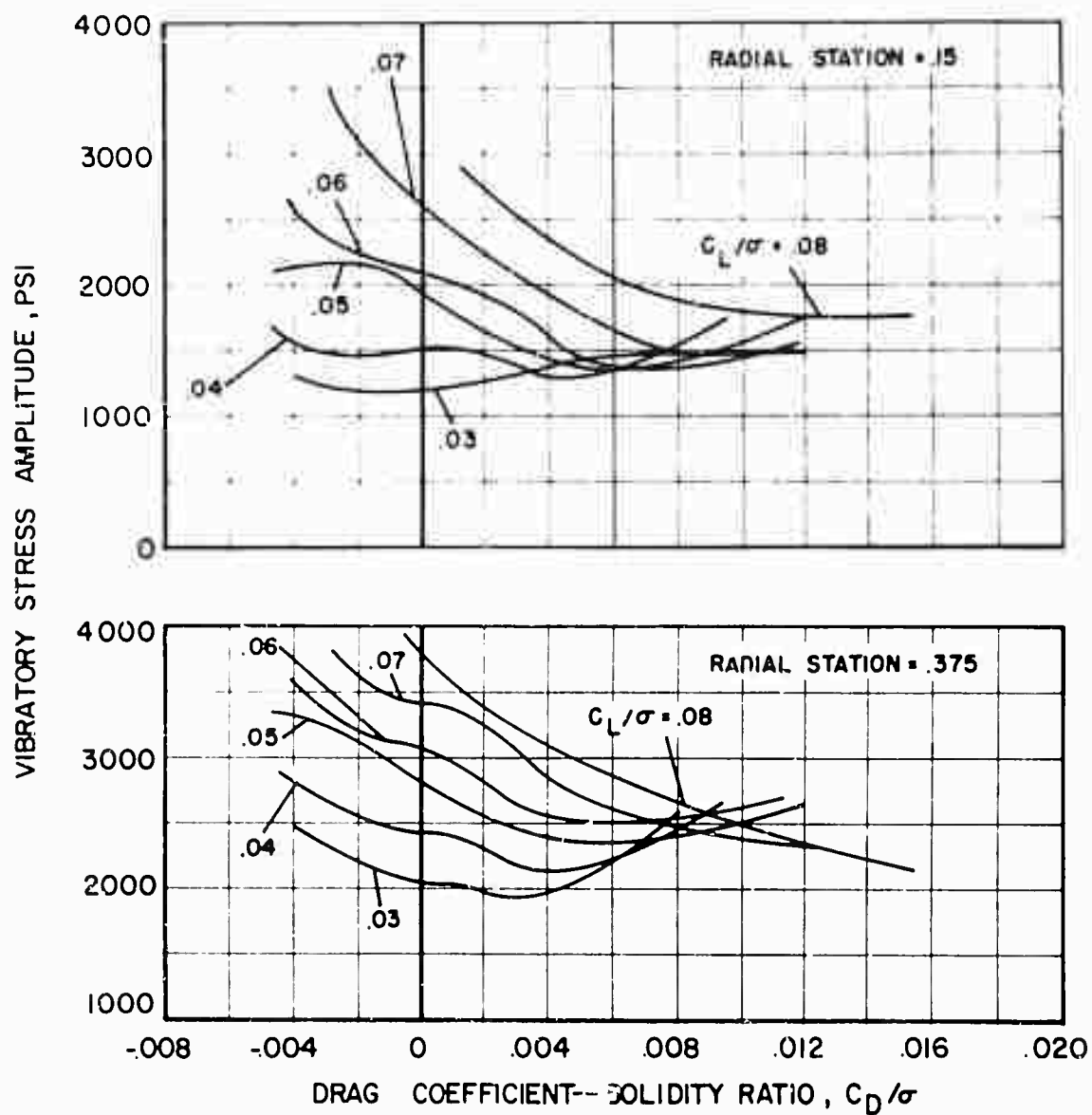
(a) Flapwise

Figure 64. The Effect of Drag on Flapwise and Chordwise Vibratory Stress Amplitude at Constant Lift at 15% and 37.5% Radius, V = 178 Knots, μ = 0.46, θ_1 = 0°, $M_{(1.0, 90)}$ = 0.82.

125
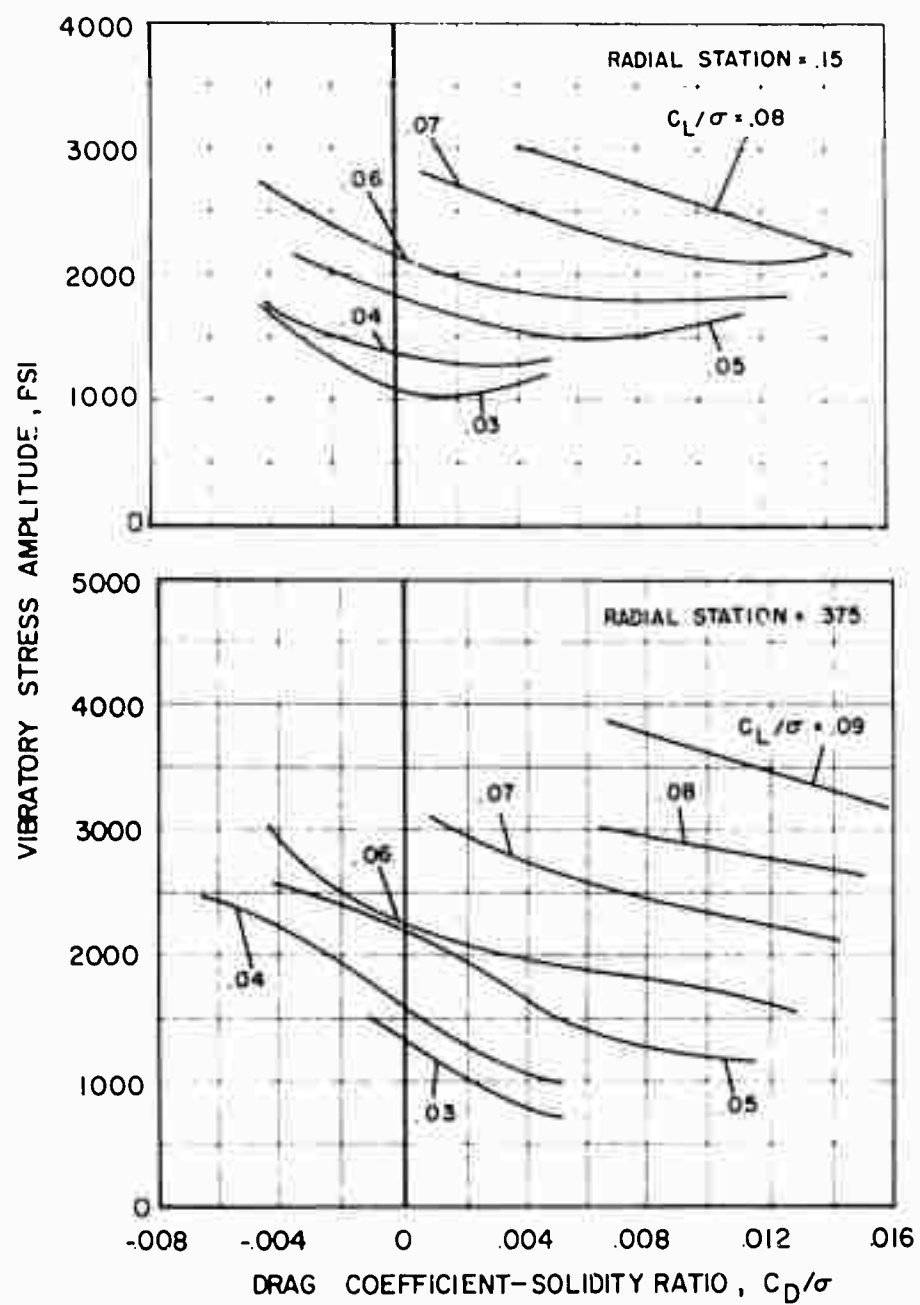
(b) Chordwise

Figure 64. Concluded.

126
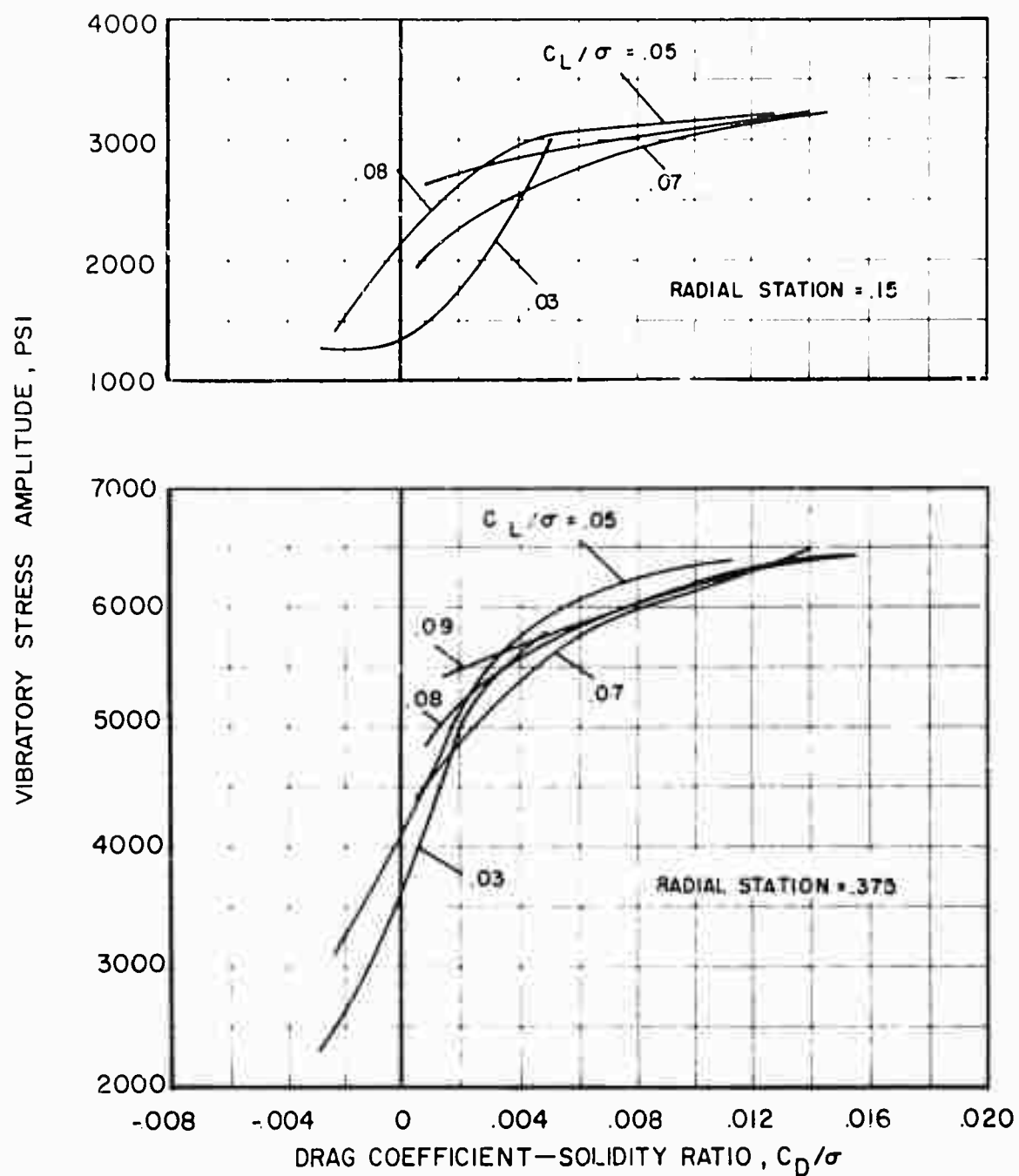
(a) Flapwise

Figure 65. The Effect of Drag on Flapwise and Chordwise Vibratory Stress Amplitude at Constant Lift at 15% and 37.5% Radius, $V = 177$ Knots, $\mu = 0.46$, $\theta_1 = -8°$, $M_{(1, 0, 90)} = 0.82$.

127
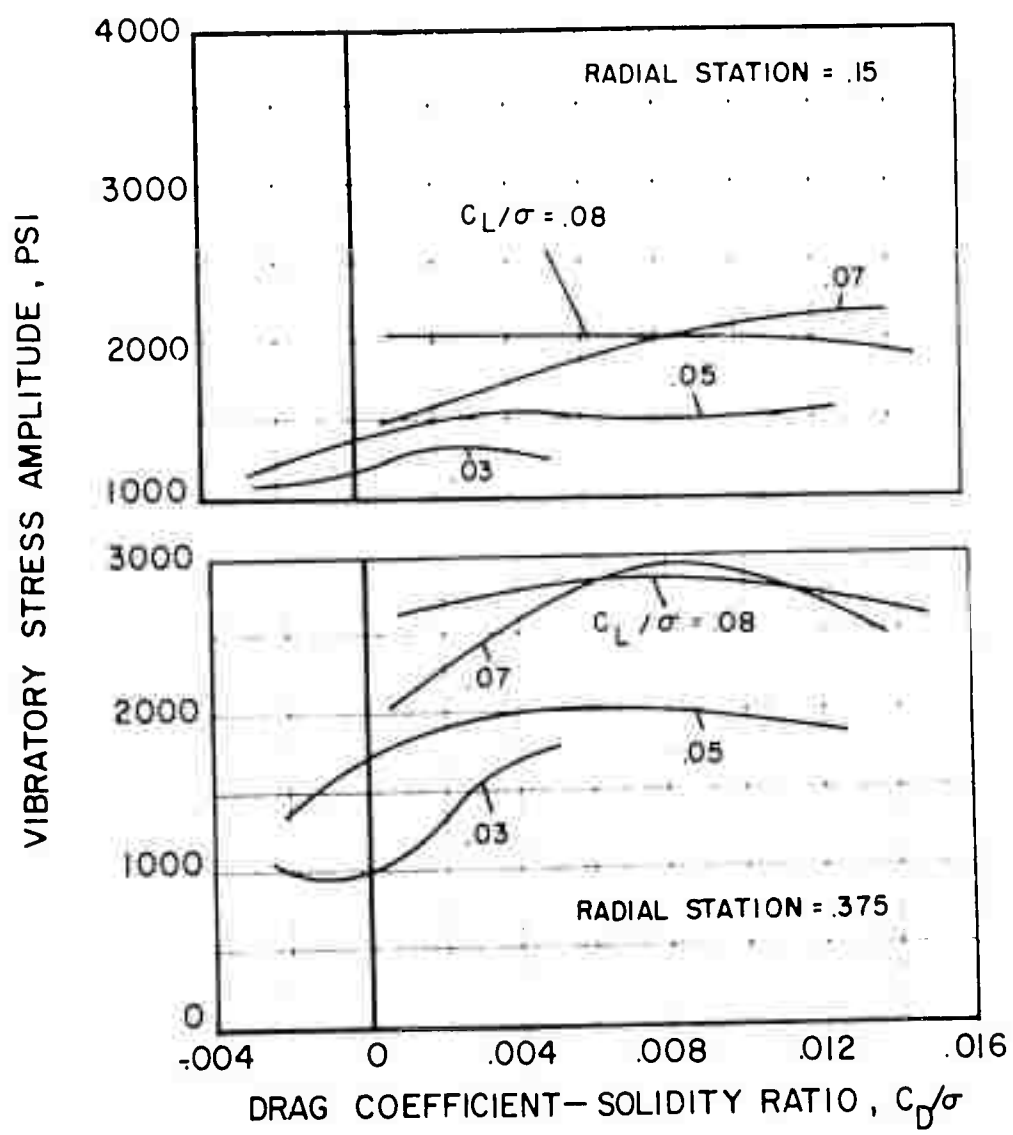
(b) Chordwise

Figure 65. Concluded.

128
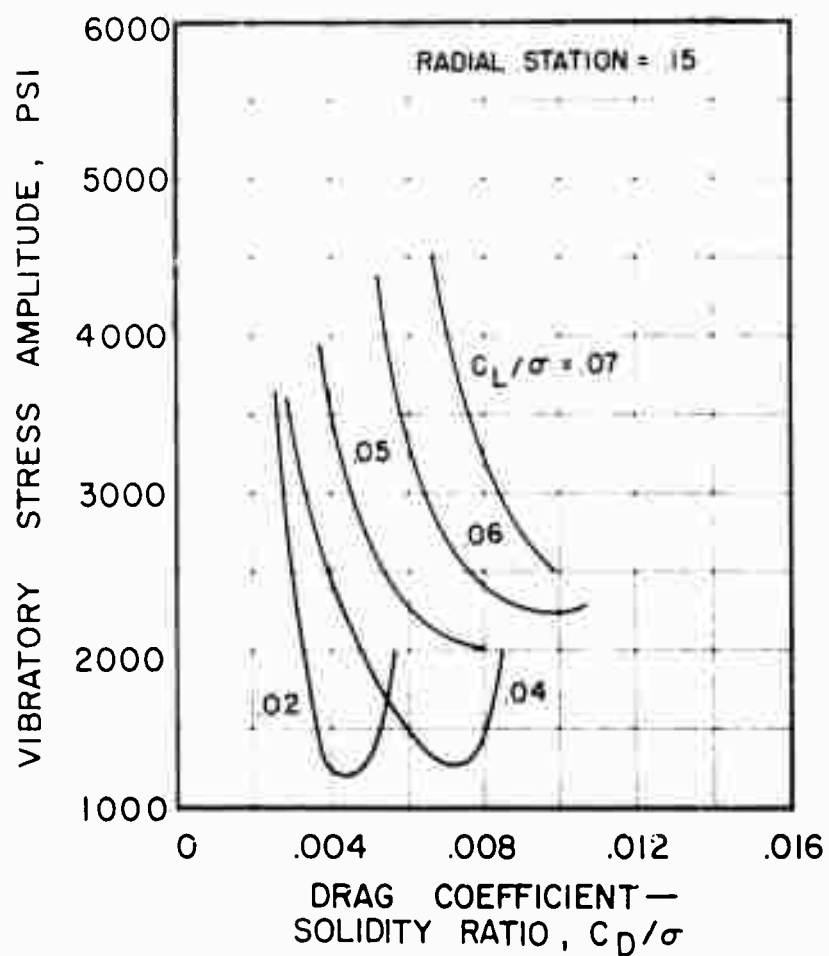
(a) Flapwise

Figure 66. The Effect of Drag on Flapwise and Chordwise Vibratory Stress Amplitude at 15% Radius, V = 194 Knots, μ = 0.62, θ_1 = 0°, $M_{(1,0,90)}$ = 0.73.

129
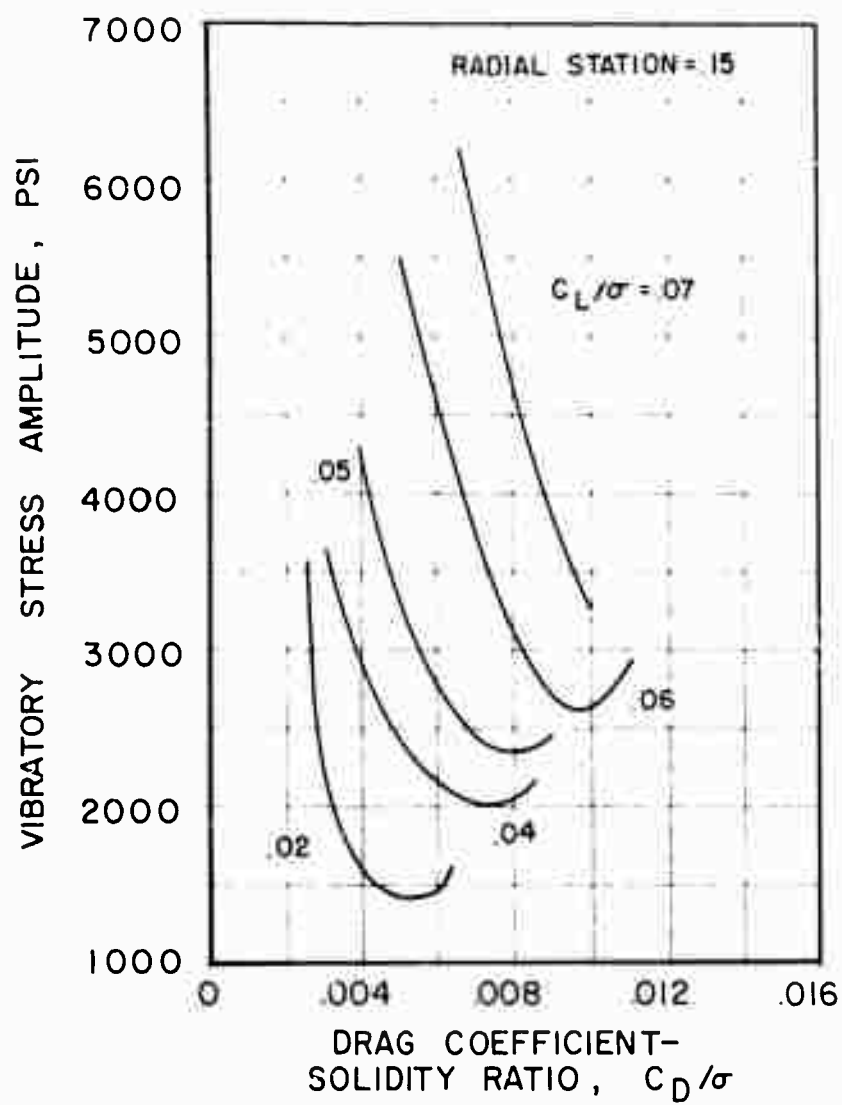
(b) Chordwise

Figure 66. Concluded.

130
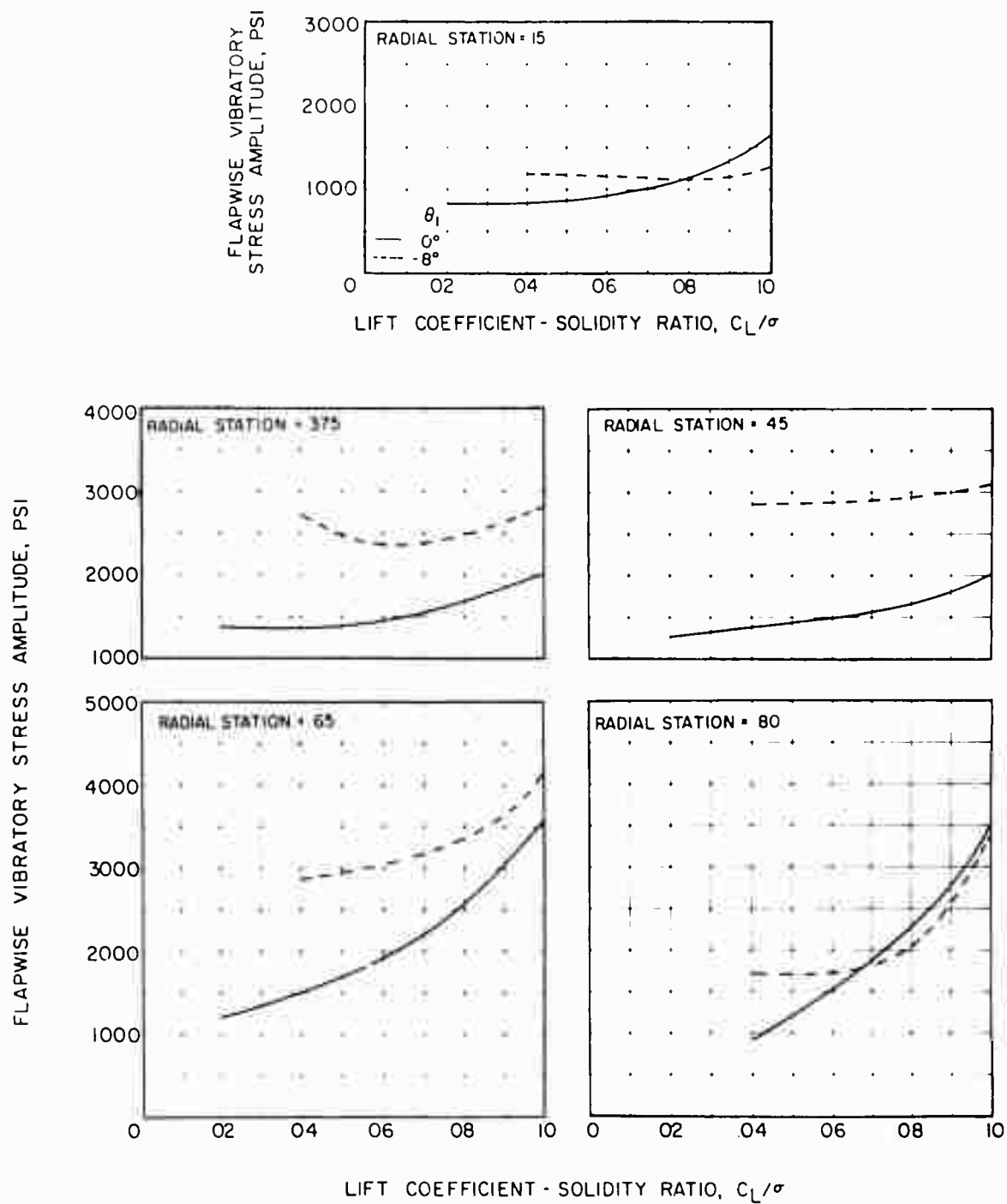
(a) $C_d \, \sigma = 0.004$

Figure 67. The Effect of Twist on Flapwise Vibratory Stress Amplitude as a Function of Lift at Three Values of Drag for Five Radial Stations. $V = 117$ Knots, $\mu = 0.30$, $M_{(1.0, 90)} = 0.74$.

131
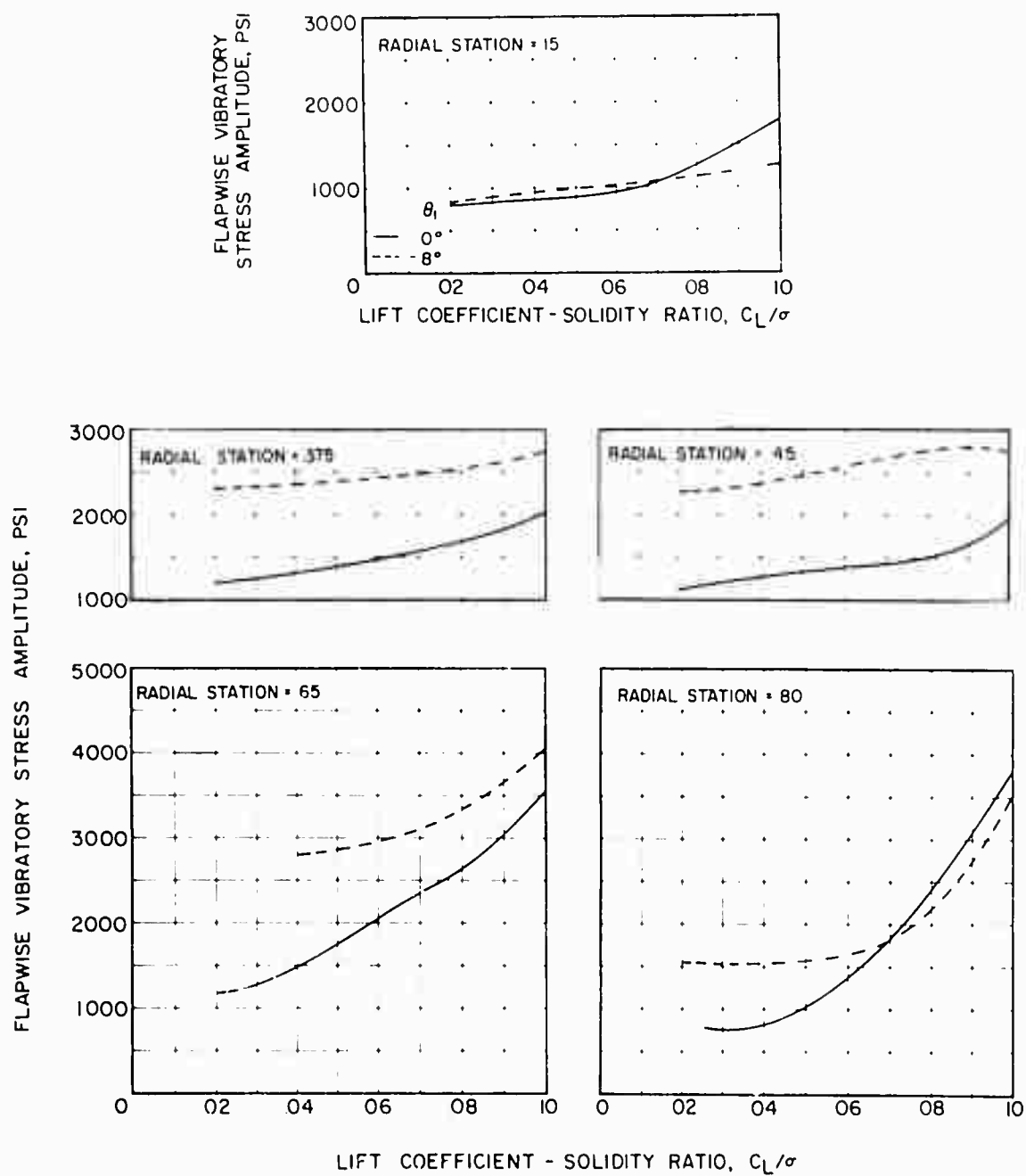
(b) $C_D/\sigma = 0$

Figure 67. Continued.

132
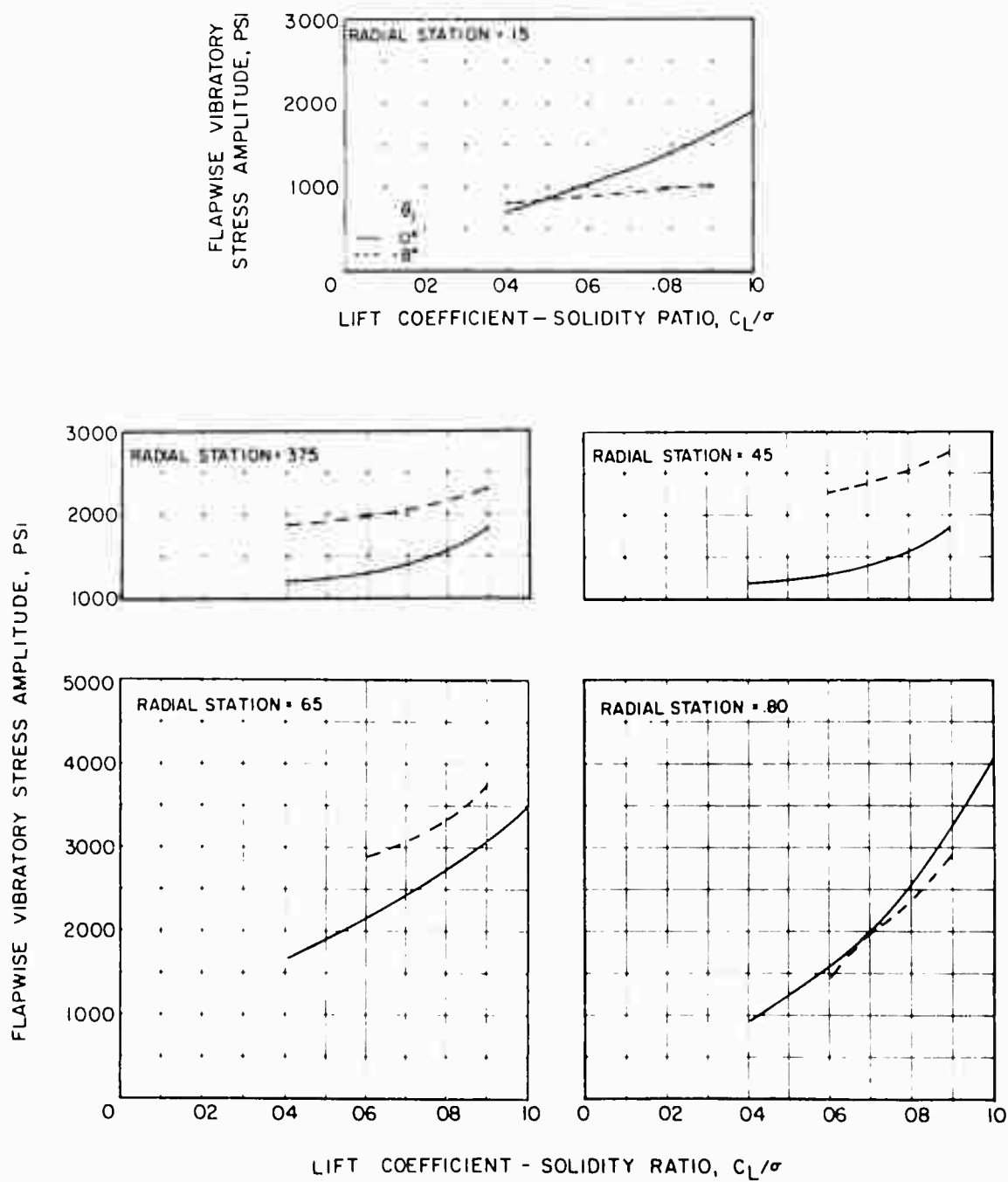
(c) $C_D/\sigma = -0.004$

Figure 67. Concluded.

133
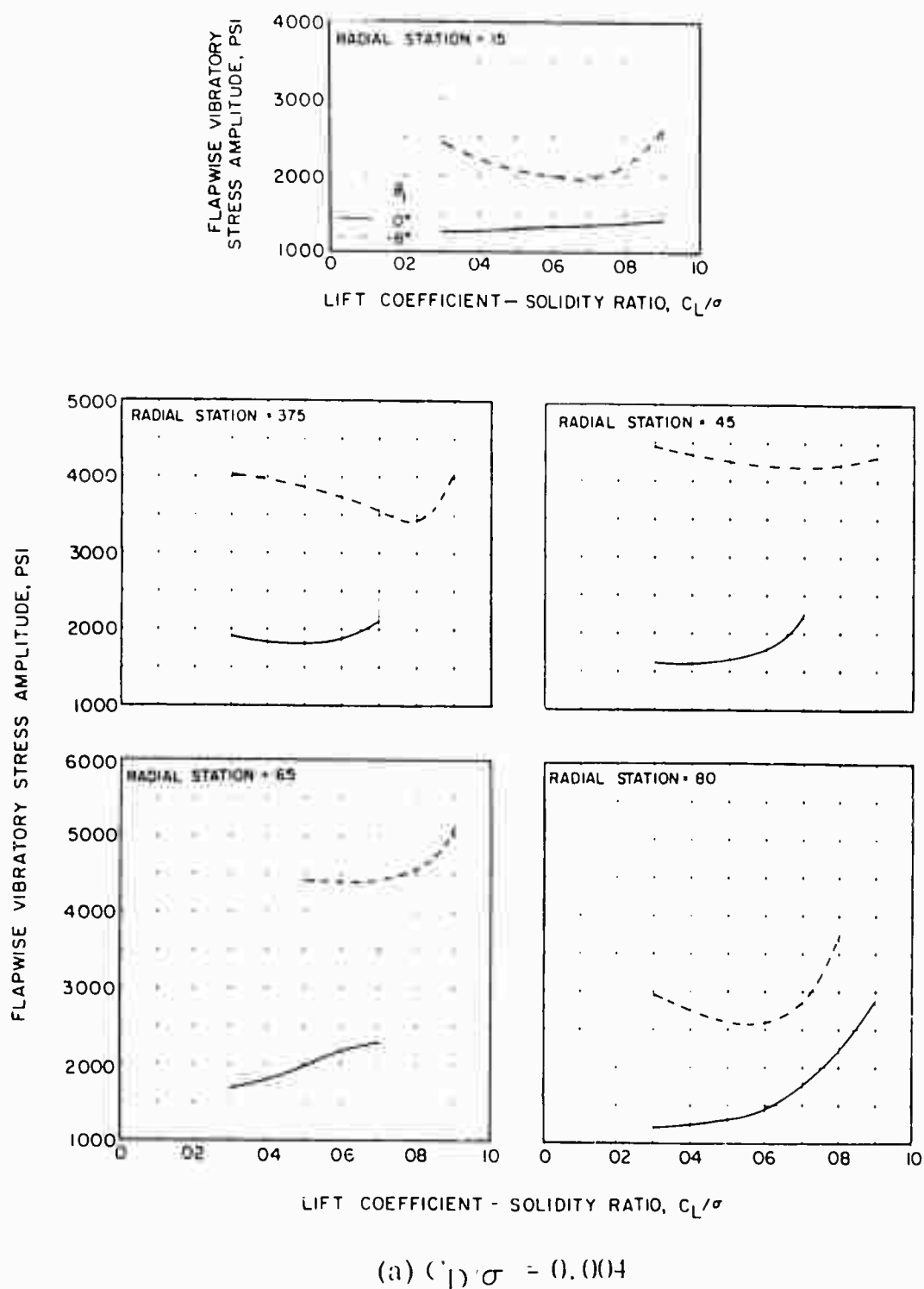
(a) $C_D/\sigma = 0.004$

Figure 68. The Effect of Twist on Flapwise Vibratory Stress Amplitude as a Function of Lift at Three Values of Drag for Five Radial Stations. $V = 163$ Knots. $\mu = 0.40$, $N_i(1.0, 90) = 0.82$.

134
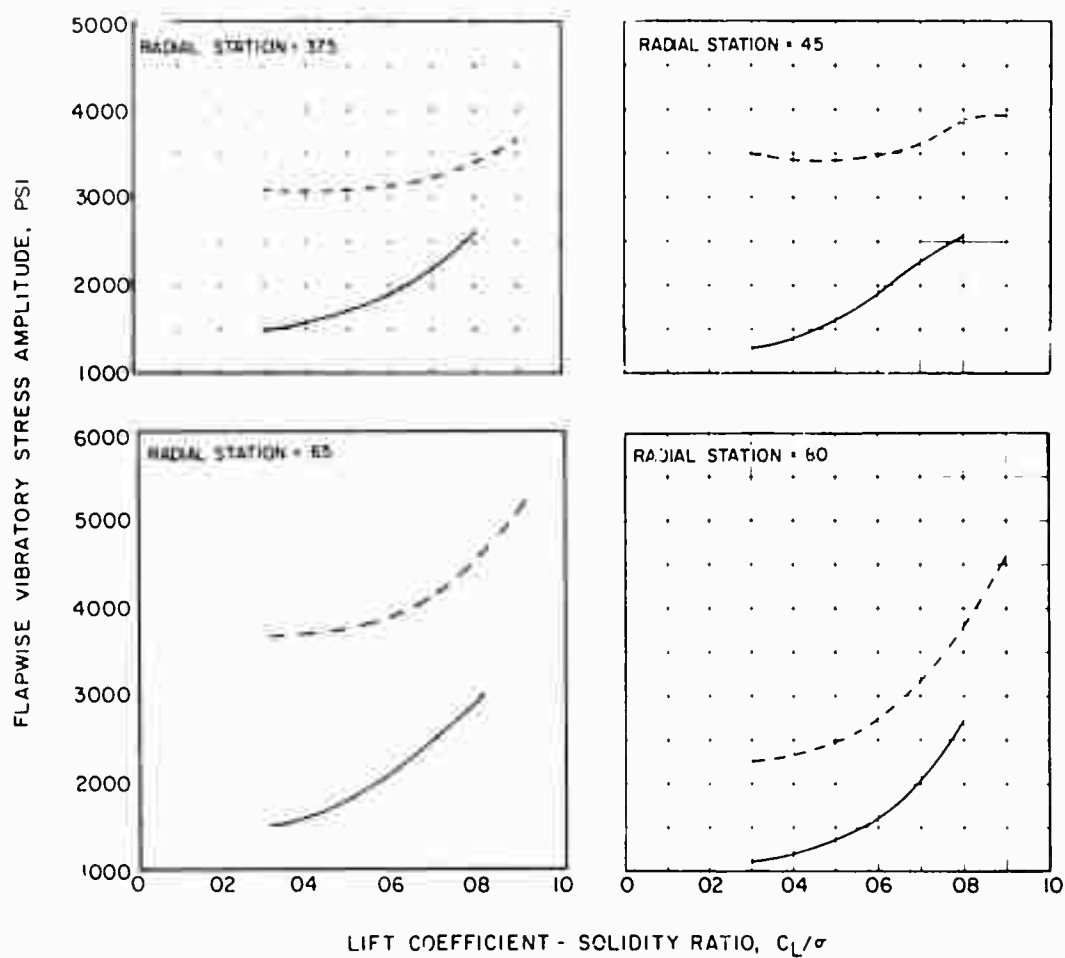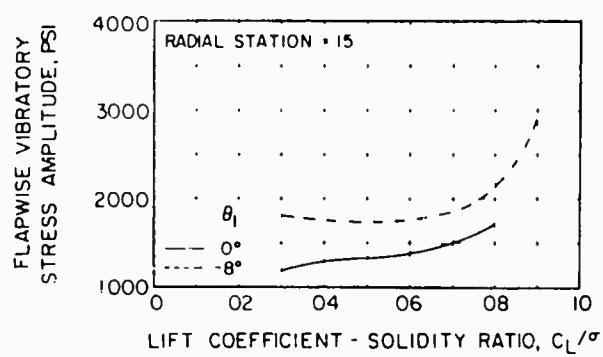
(b) $C_D\sigma = 0$

Figure 68. Continued.

135
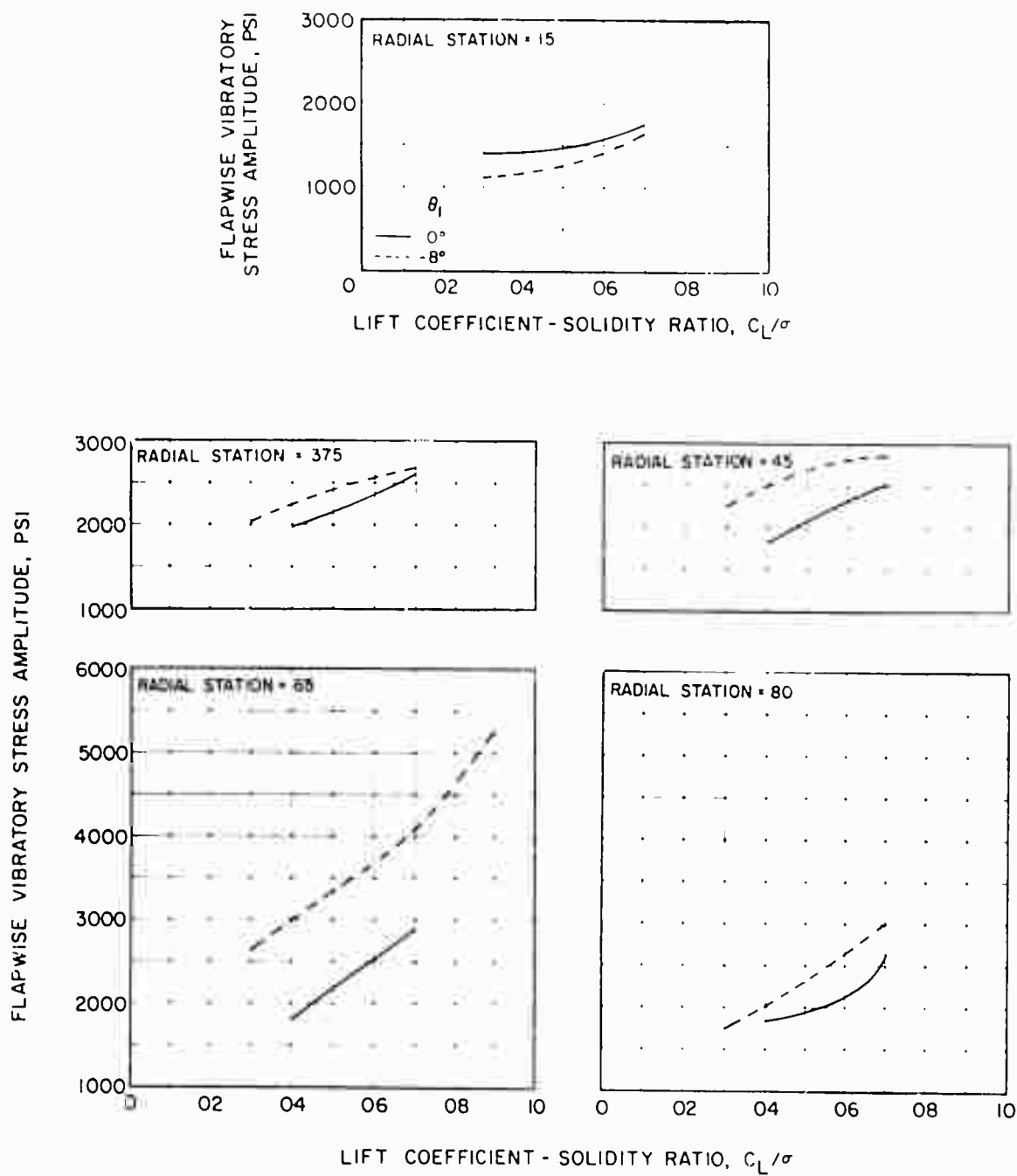
(c) $C_D/\sigma = -0.004$

Figure 68. Concluded.

136
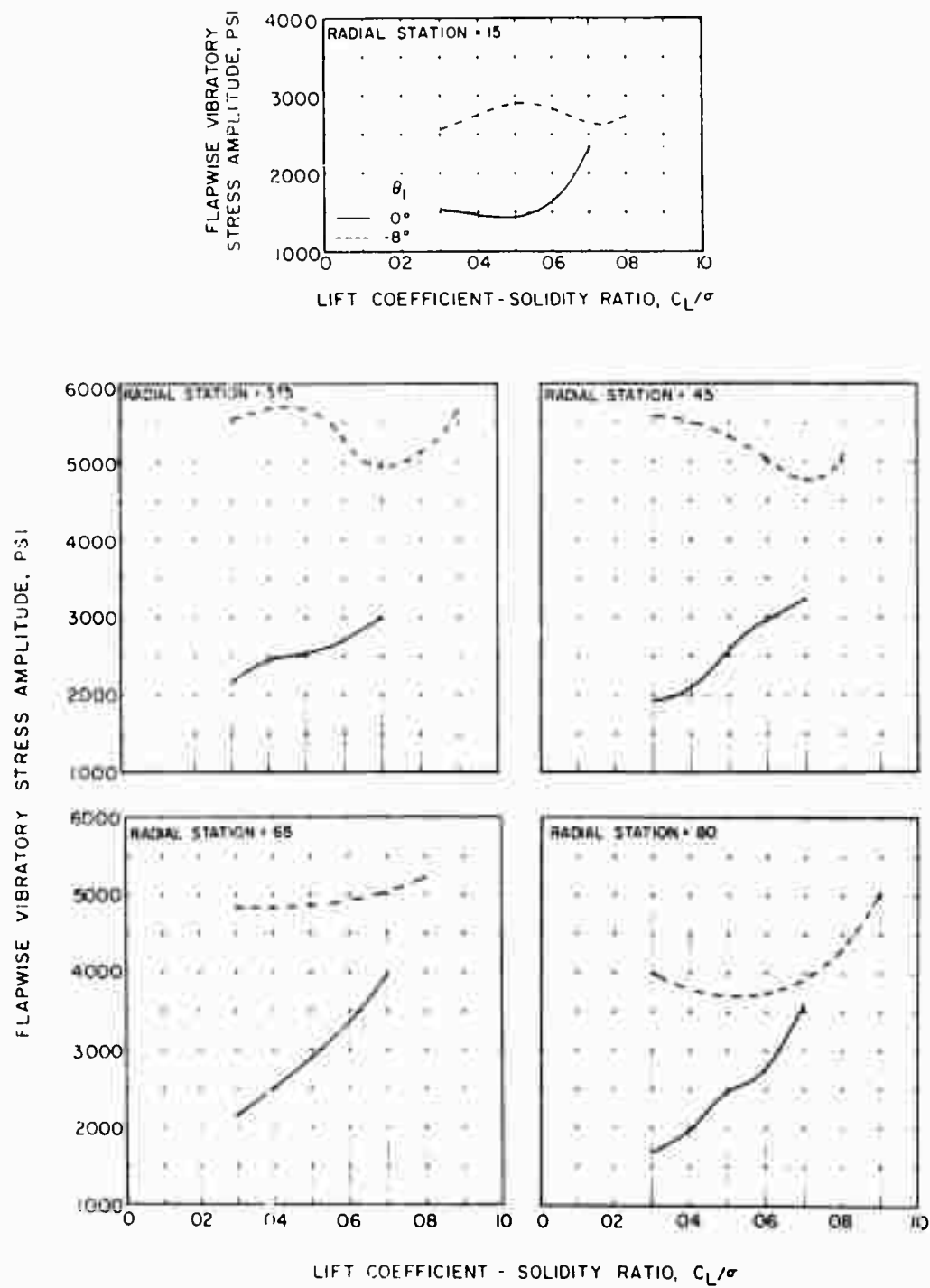
(a) $C_D/\sigma = 0.004$

Figure 69. The Effect of Twist on Flapwise Vibratory Stress
Amplitude as a Function of Lift at Two Values of
Drag for Five Radial Stations, $V = 177$ Knots,
$\mu = 0.46$, $M_{(1.0, 90)} = 0.82$.

137
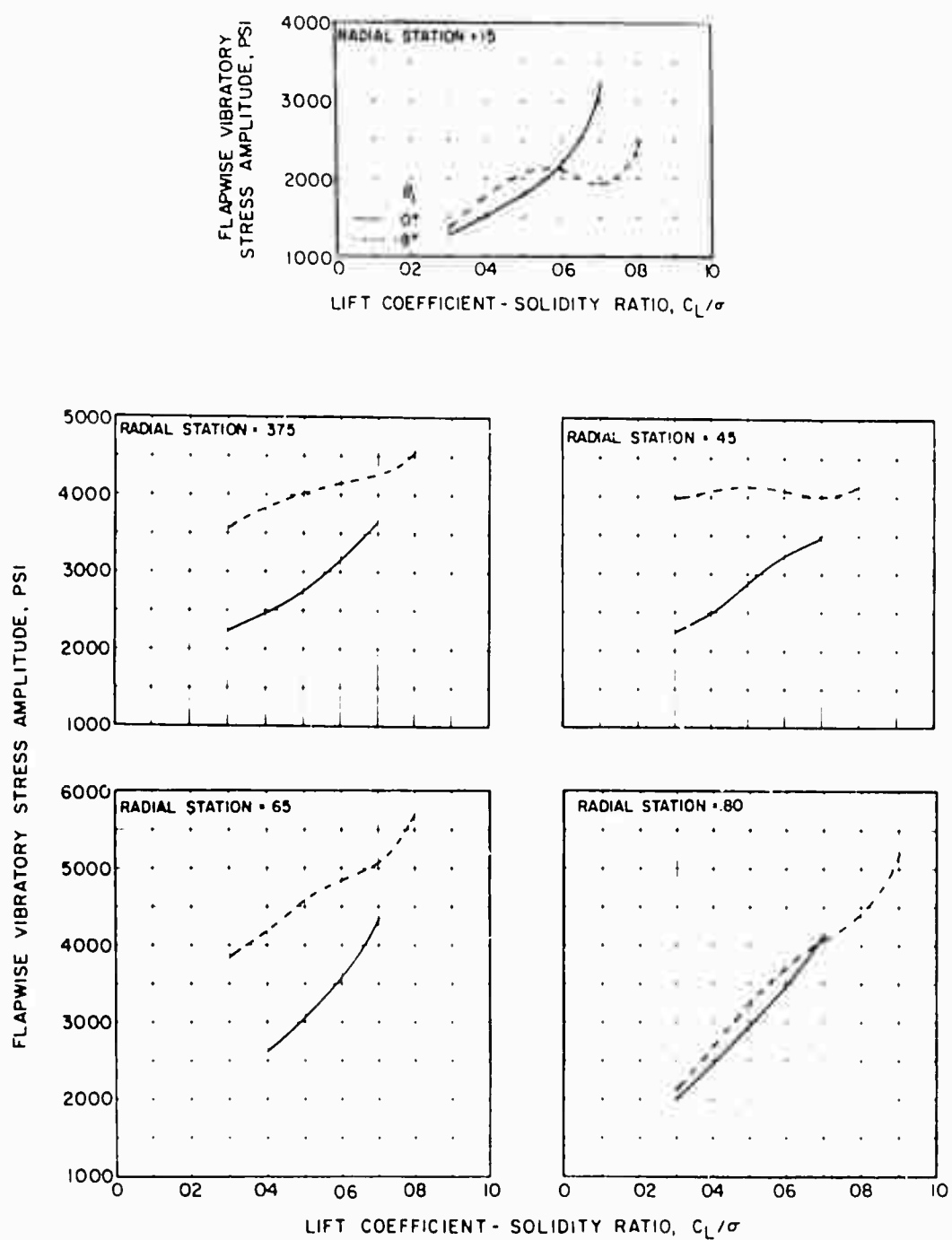
(b) $C_D/\sigma = 0$

Figure 69. Concluded.

138

LIFT COEFFICIENT - SOLIDITY RATIO, C_L/σ
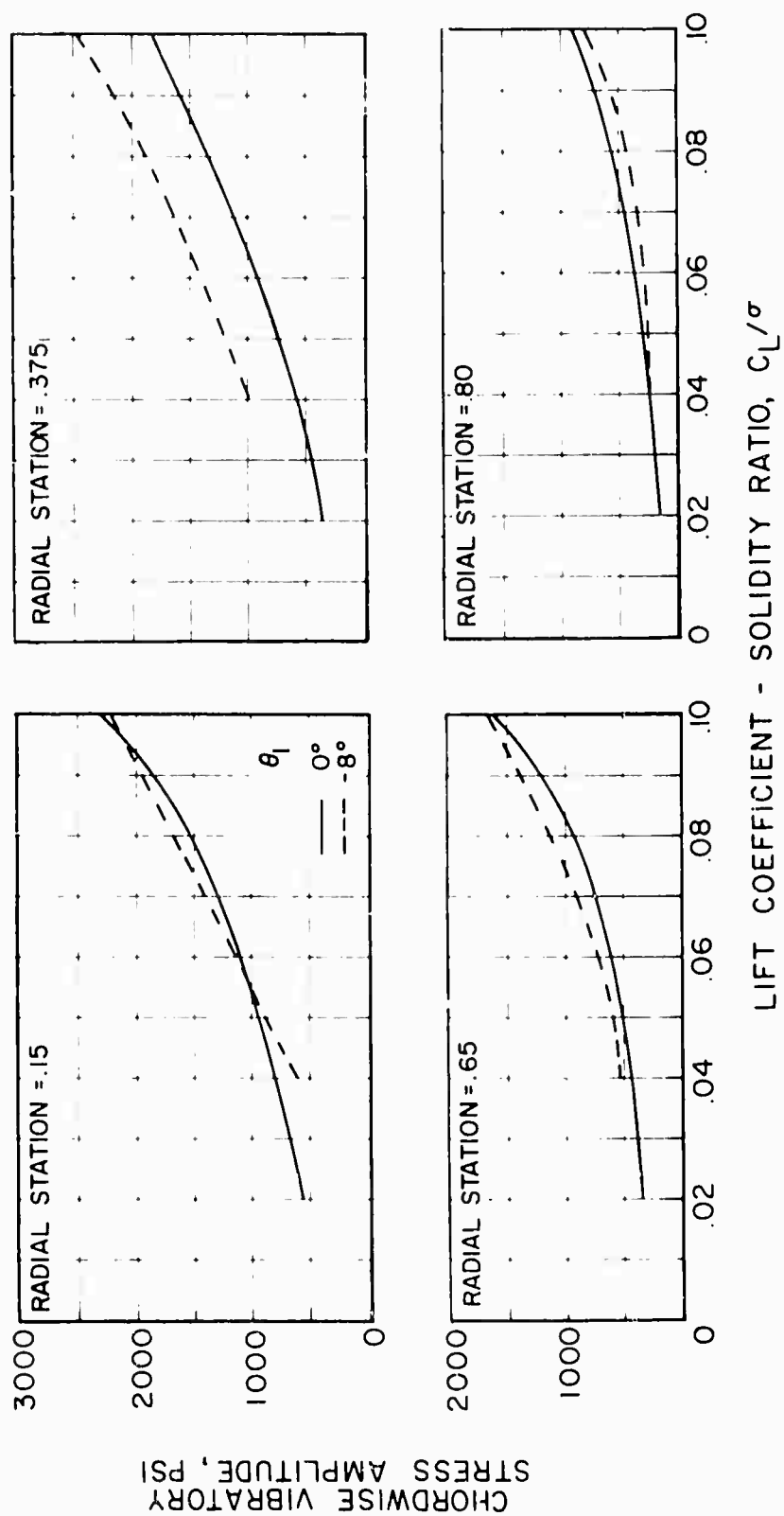
(a) $C_D/\sigma = 0.004$

Figure 70. The Effect of Twist on Chordwise Vibratory Stress Amplitude as a Function of Lift at Three Values of Drag for Four Radial Stations, $V = 117$ Knots. $\mu = 0.30$, $M(1.0, 90) = 0.74$.

139
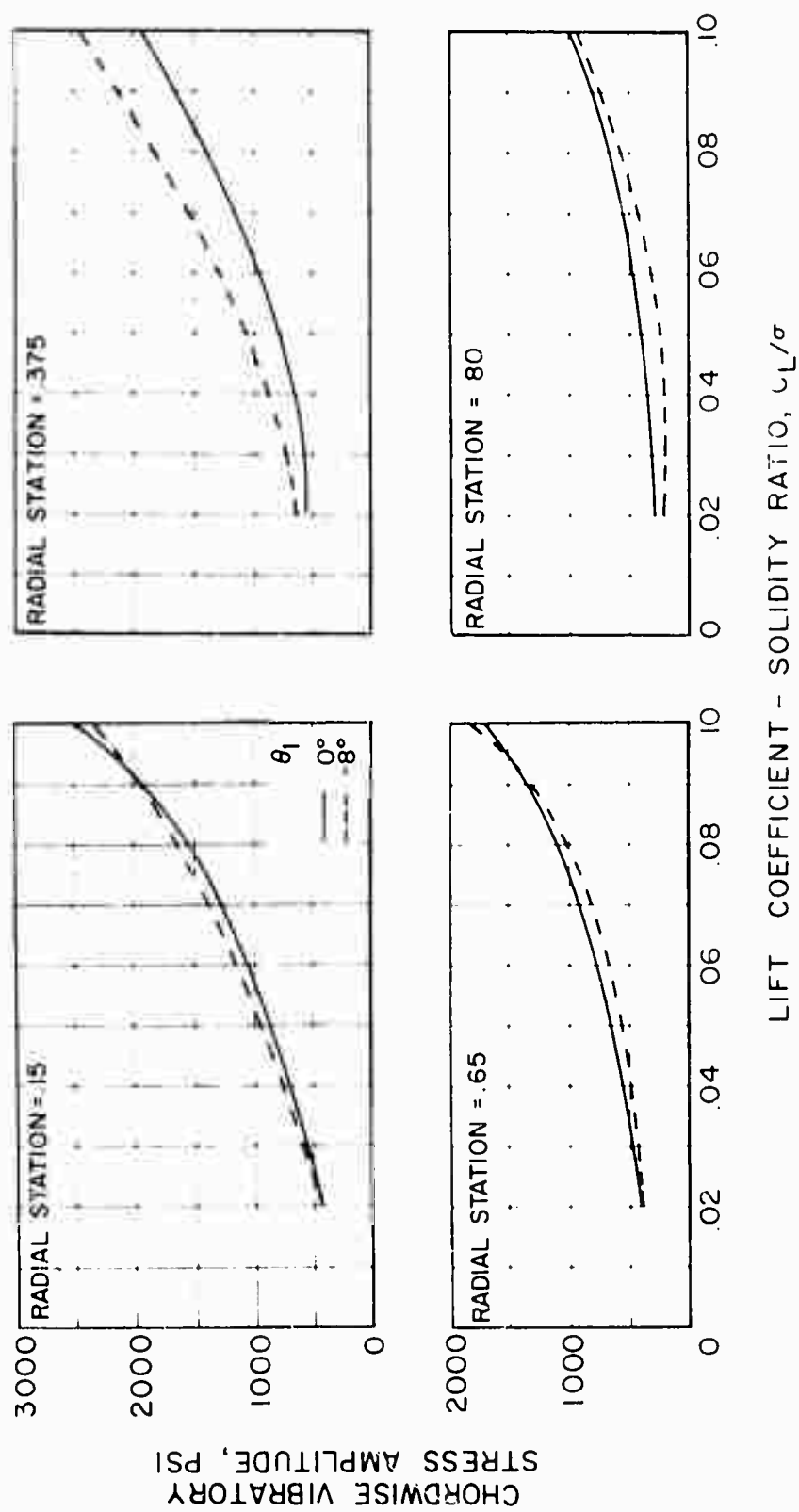
(b) $c_D/\sigma = 0$

Figure 70. (Continued)

140
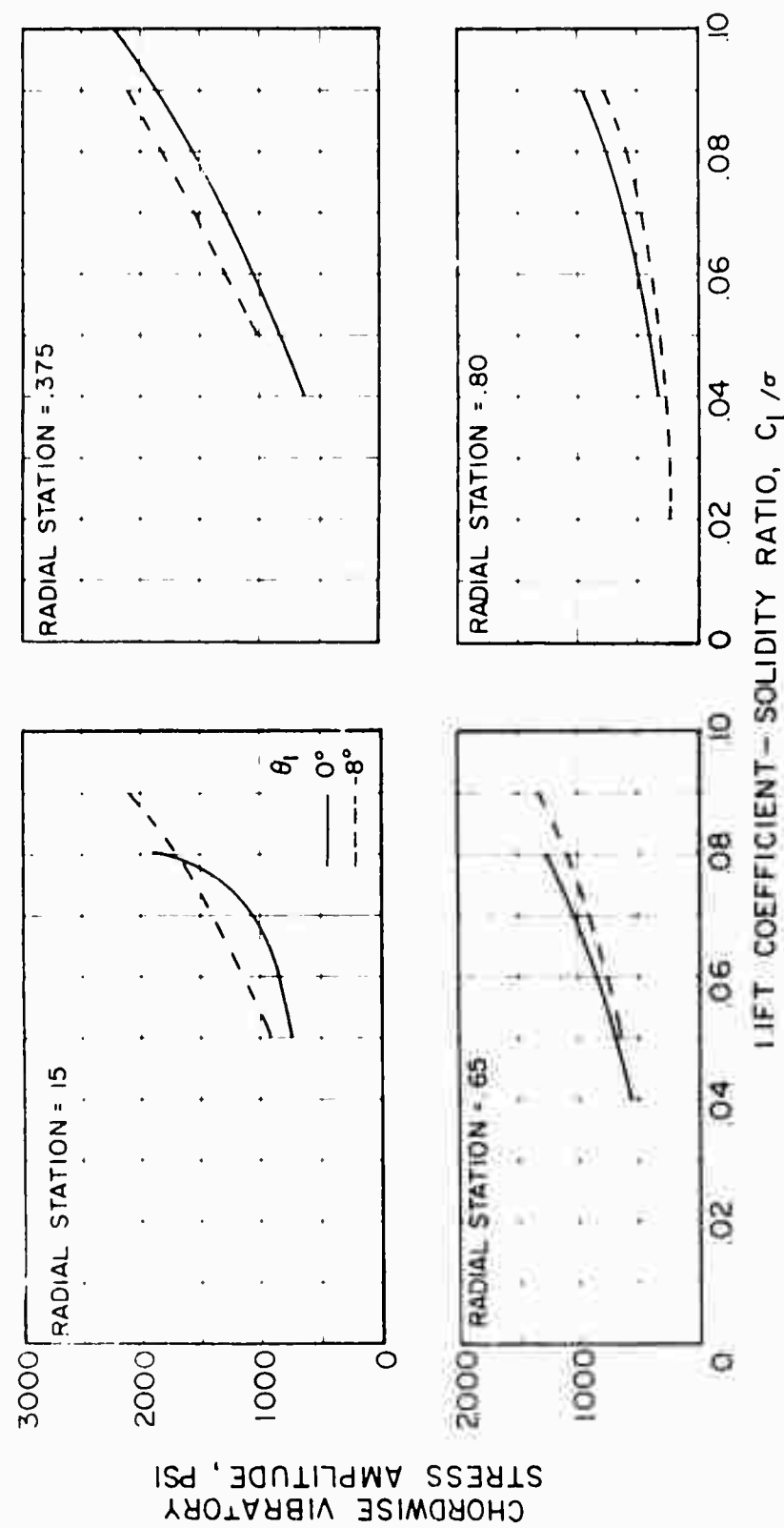
(c) $C_D/\sigma = -0.004$

Figure 70. Concluded.

141

(a) $CD_i/\sigma = 0.004$
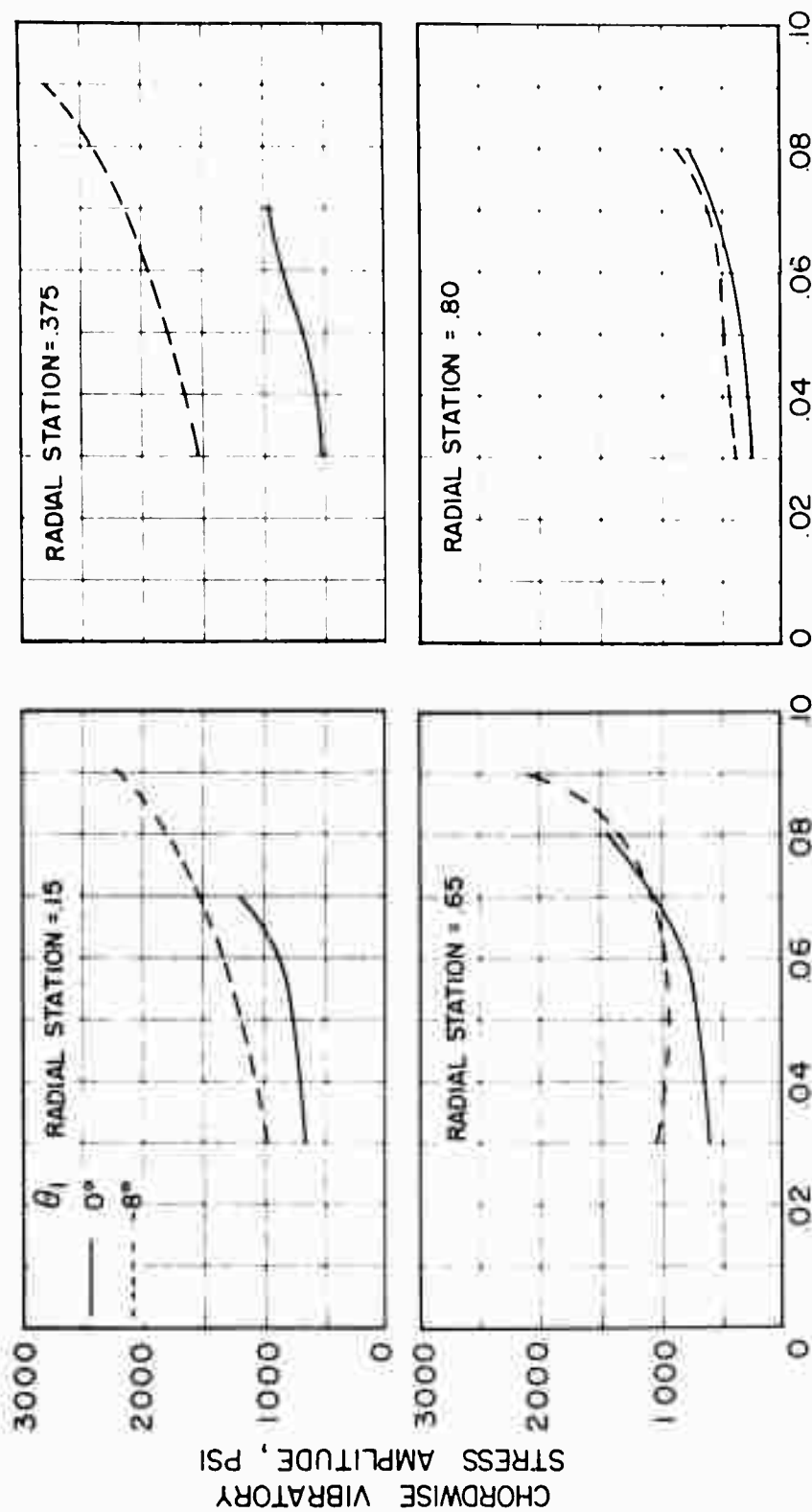
Figure 71. The Effect of Twist on Chordwise Vibratory Stress Amplitude as a Function of Lift at Three Values of Drag for Four Radial Stations. V = 163 Knots. $\mu = 0.40$. $M_{(1.0.90)} = 0.82$.
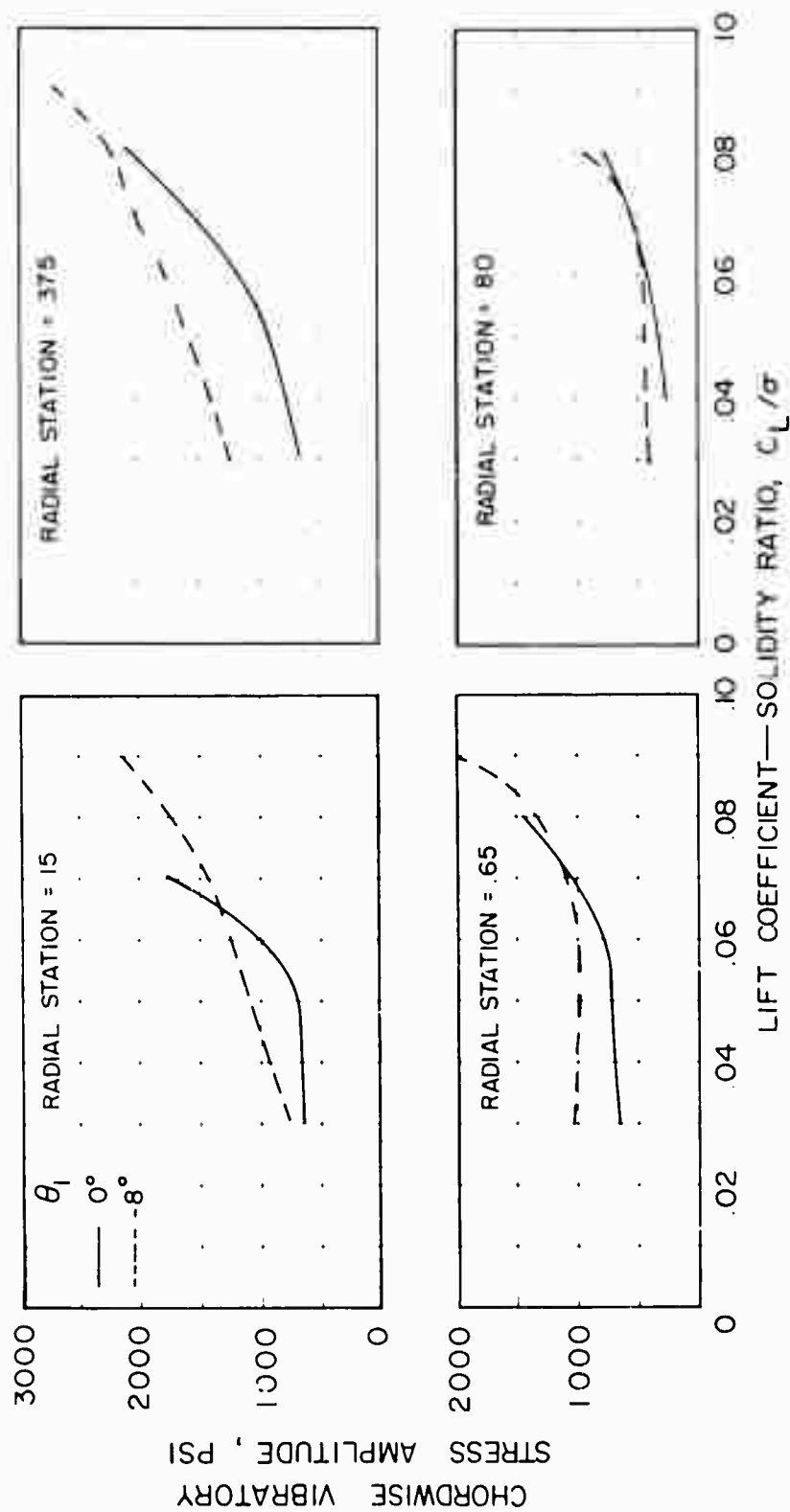
(b) $C_D/\sigma = 0$

Figure 71. Continued.

143
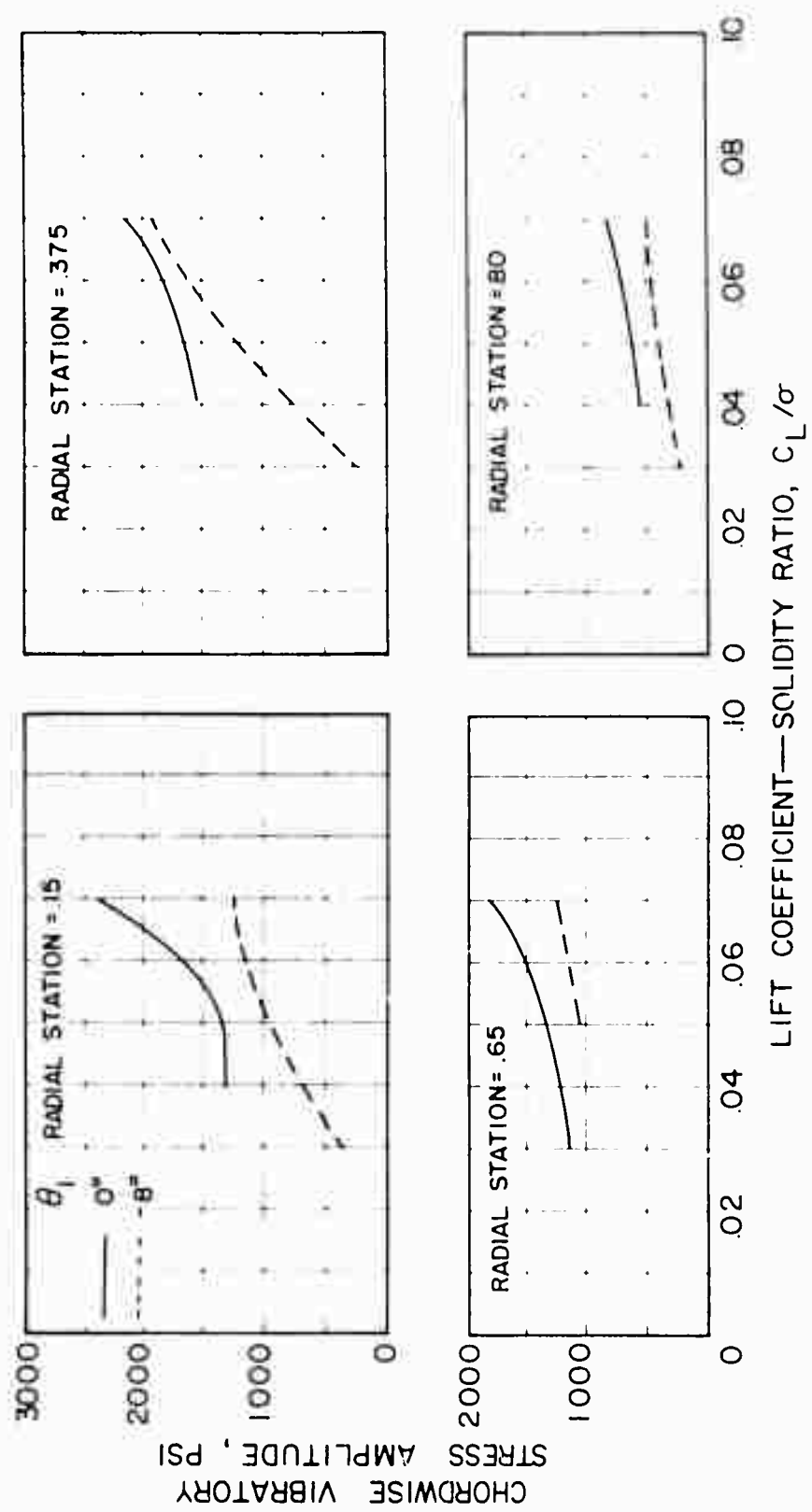
(c) $C_D/\sigma = -0.004$

Figure 71. Concluded

144
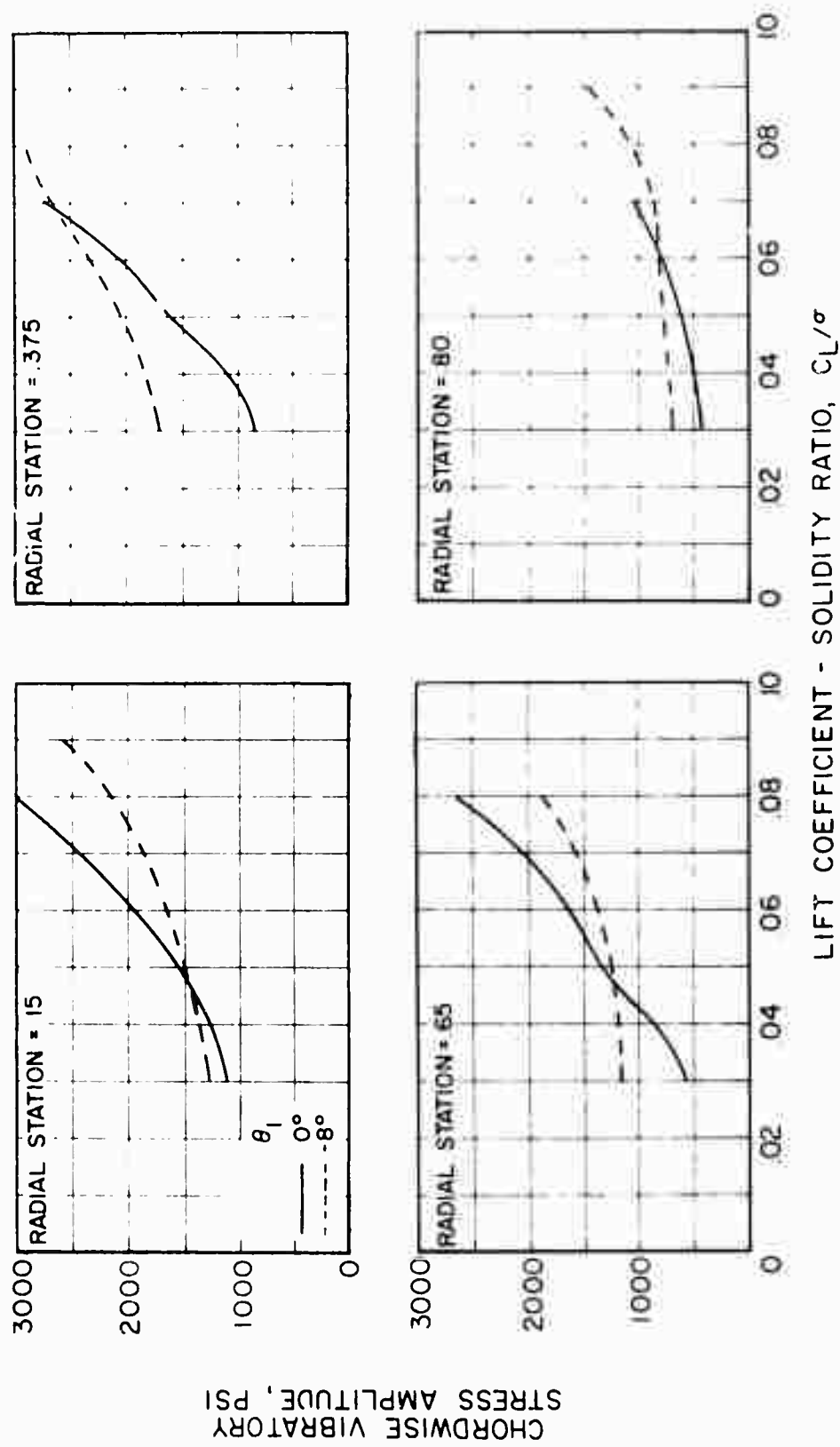
Figure 72. The Effect of Twist on Chordwise Vibratory Stress Amplitude as a Function of Lift at Two Values of Drag for Four Radial Stations, $V = 177$ Knots, $\mu = 0.46$, $M_{(1.0, 90)} = 0.82$.
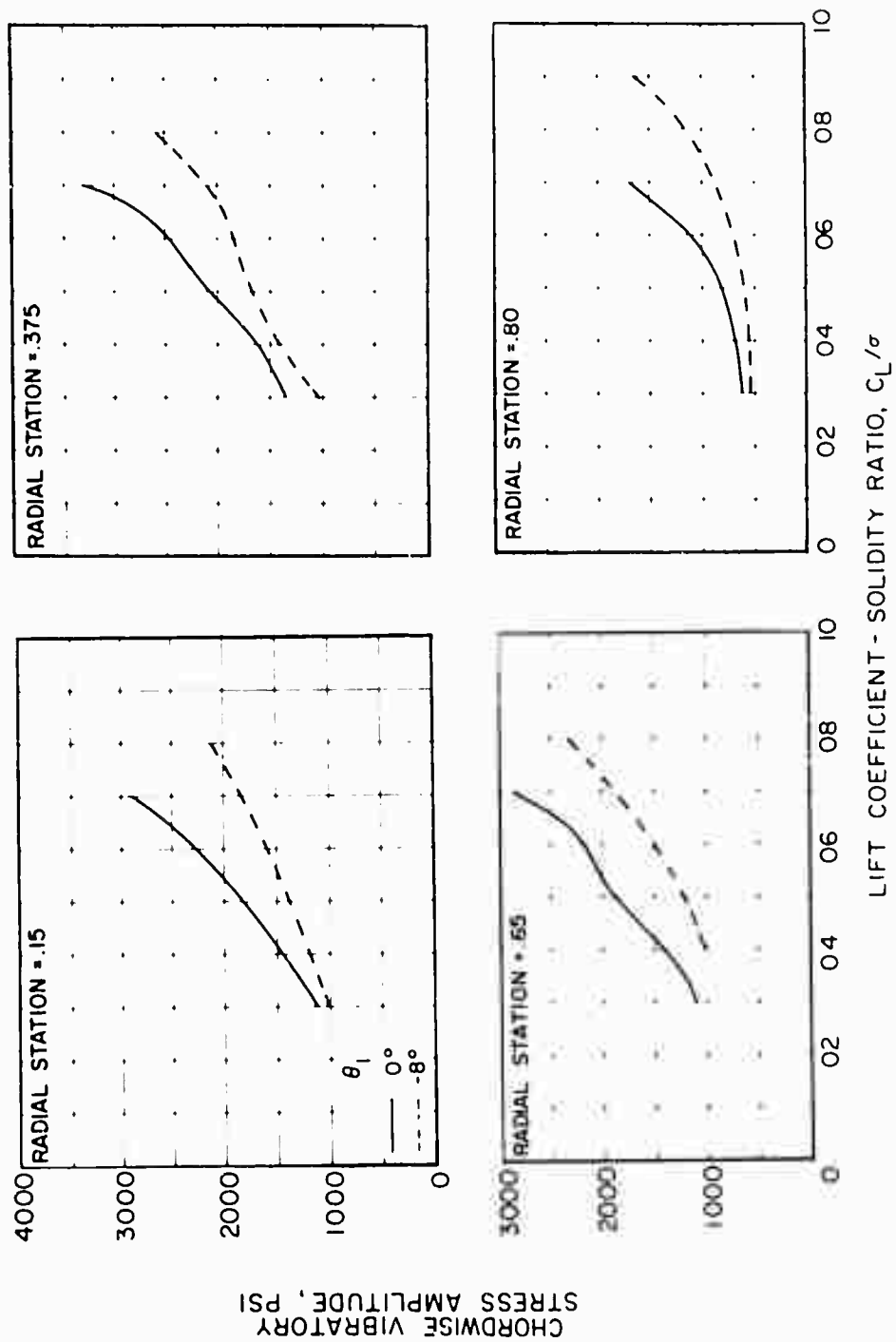
(b) $C_D, \sigma = 0$

Figure 72. Concluded.
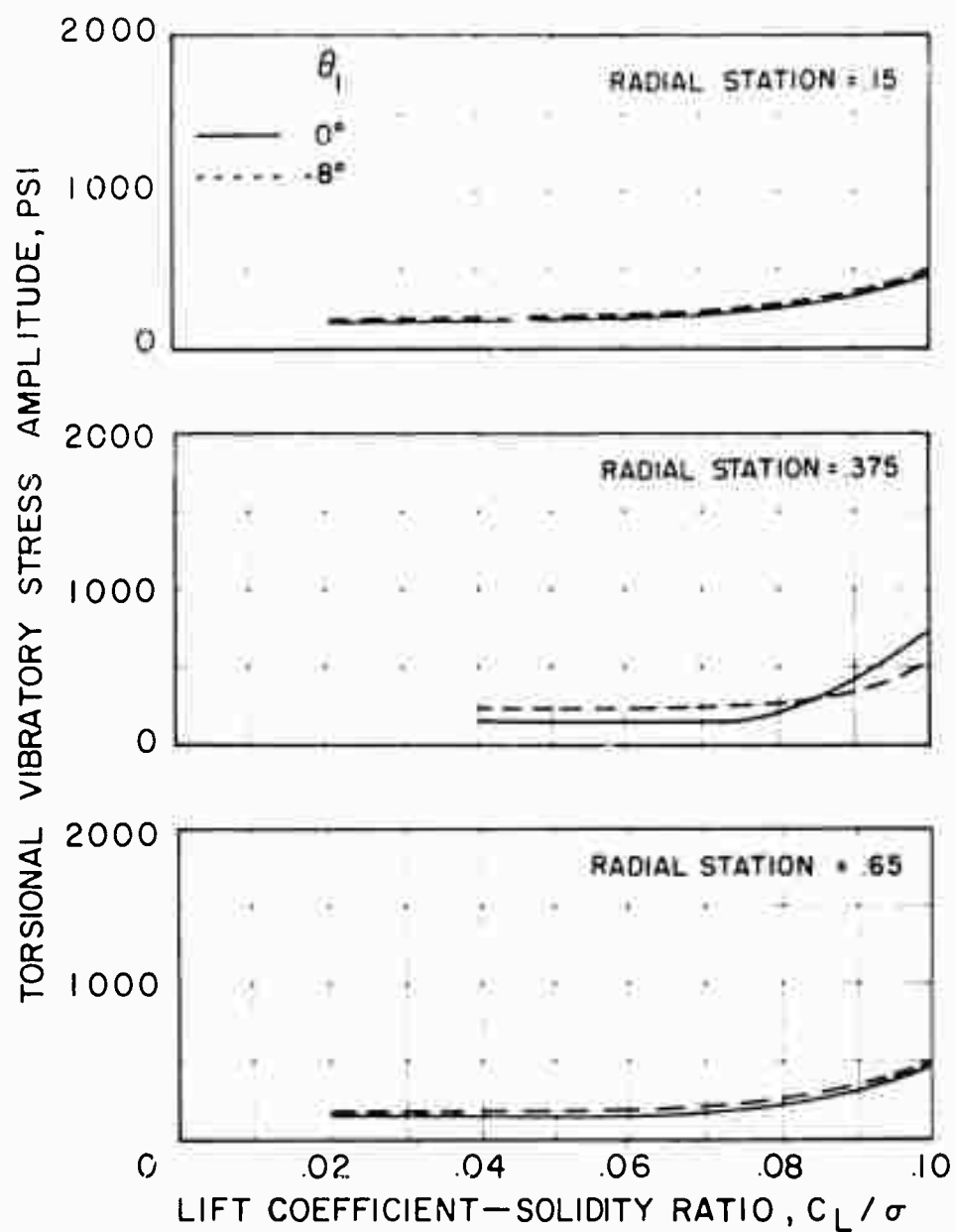
(a) $C_D \sigma = 0.004$

Figure 73. The Effect of Twist on Torsional Vibratory Stress Amplitude as a Function of Lift at Three Values of Drag for Three Radial Stations. $V = 117$ Knots, $\mu = 0.30$, $M_{(1.0, 90)} = 0.74$.

147
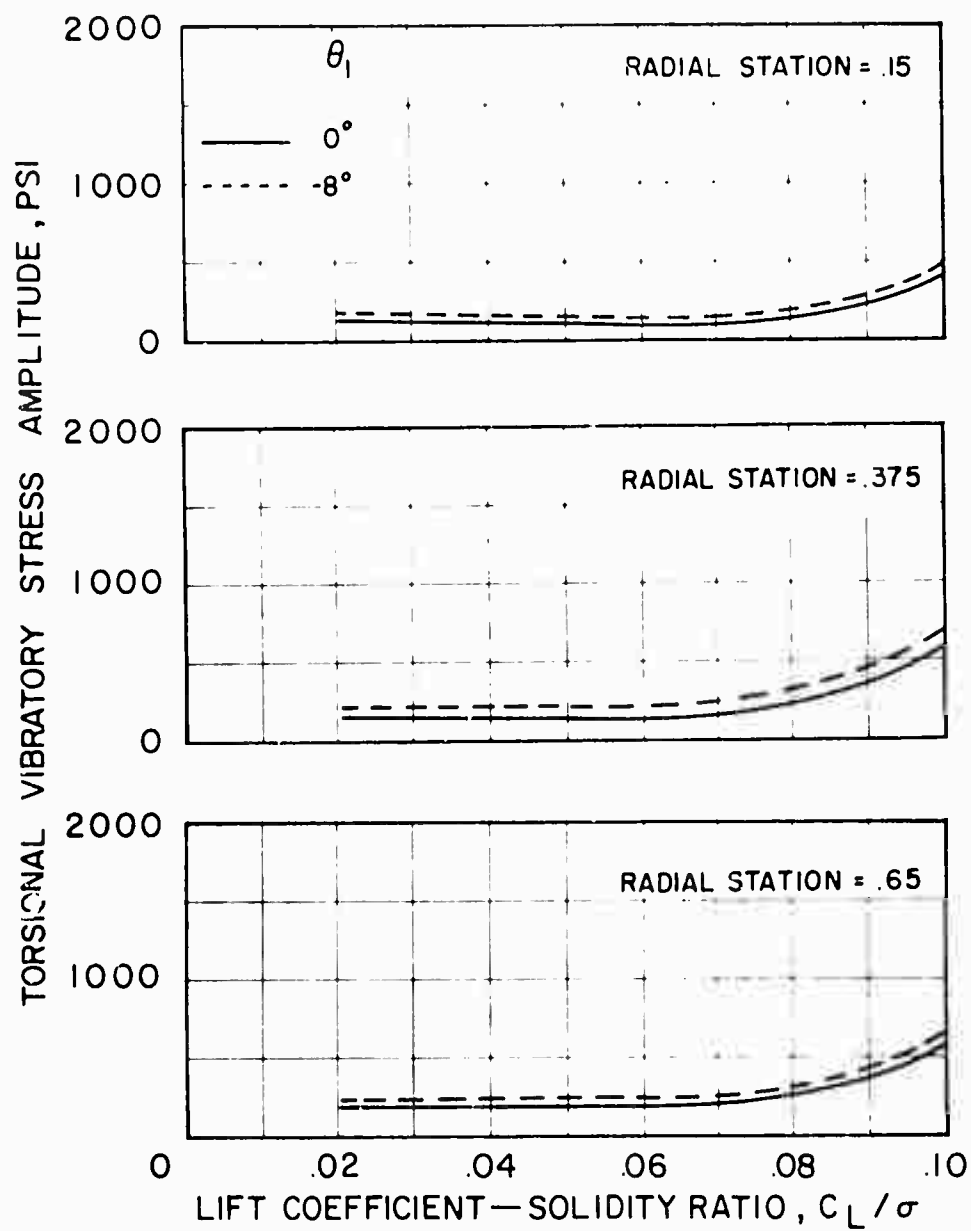
(b) $C_D/\sigma = 0$

Figure 73. Continued.

148
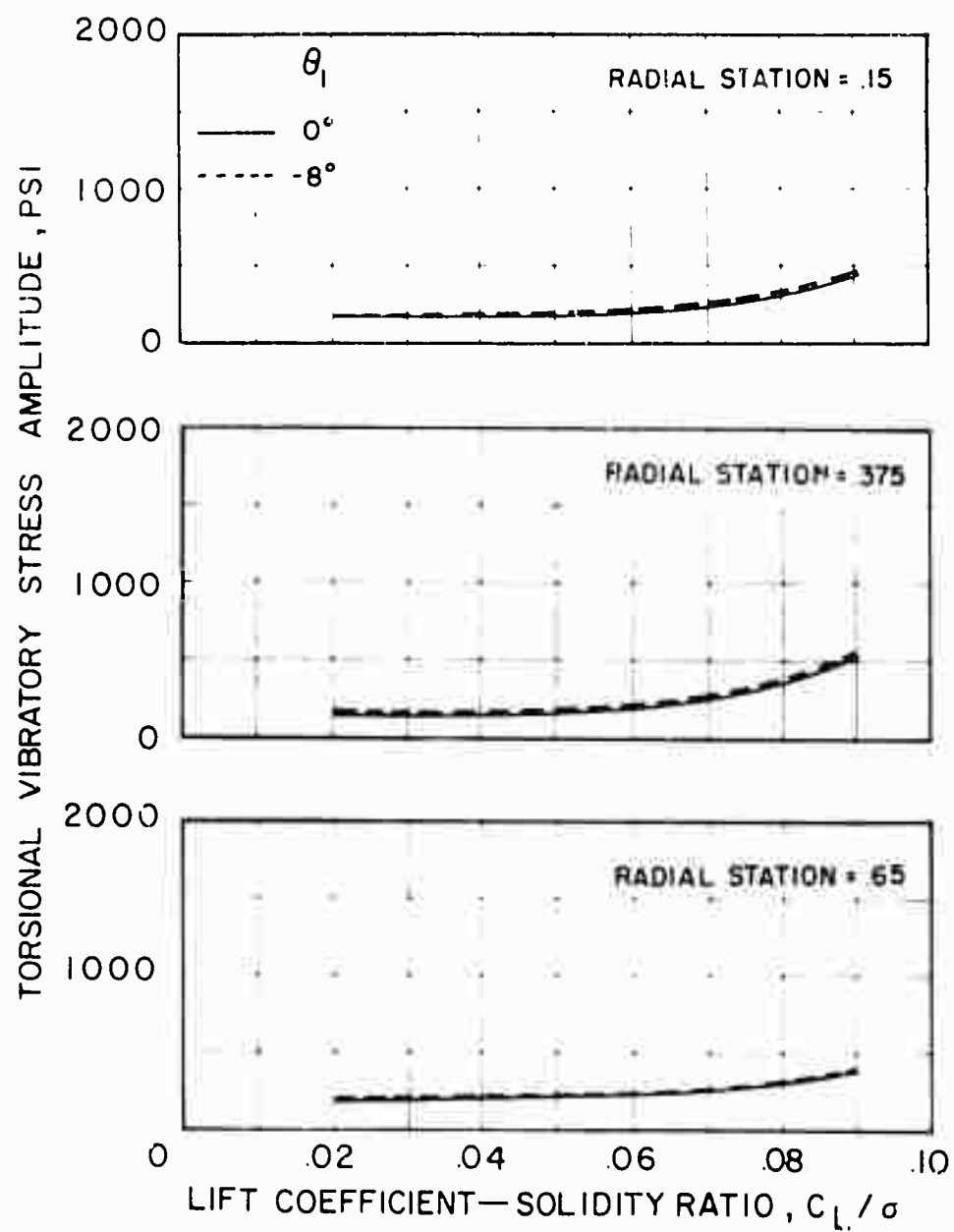
(c) $C_D/\sigma = -0.004$

Figure 73 - Concluded.
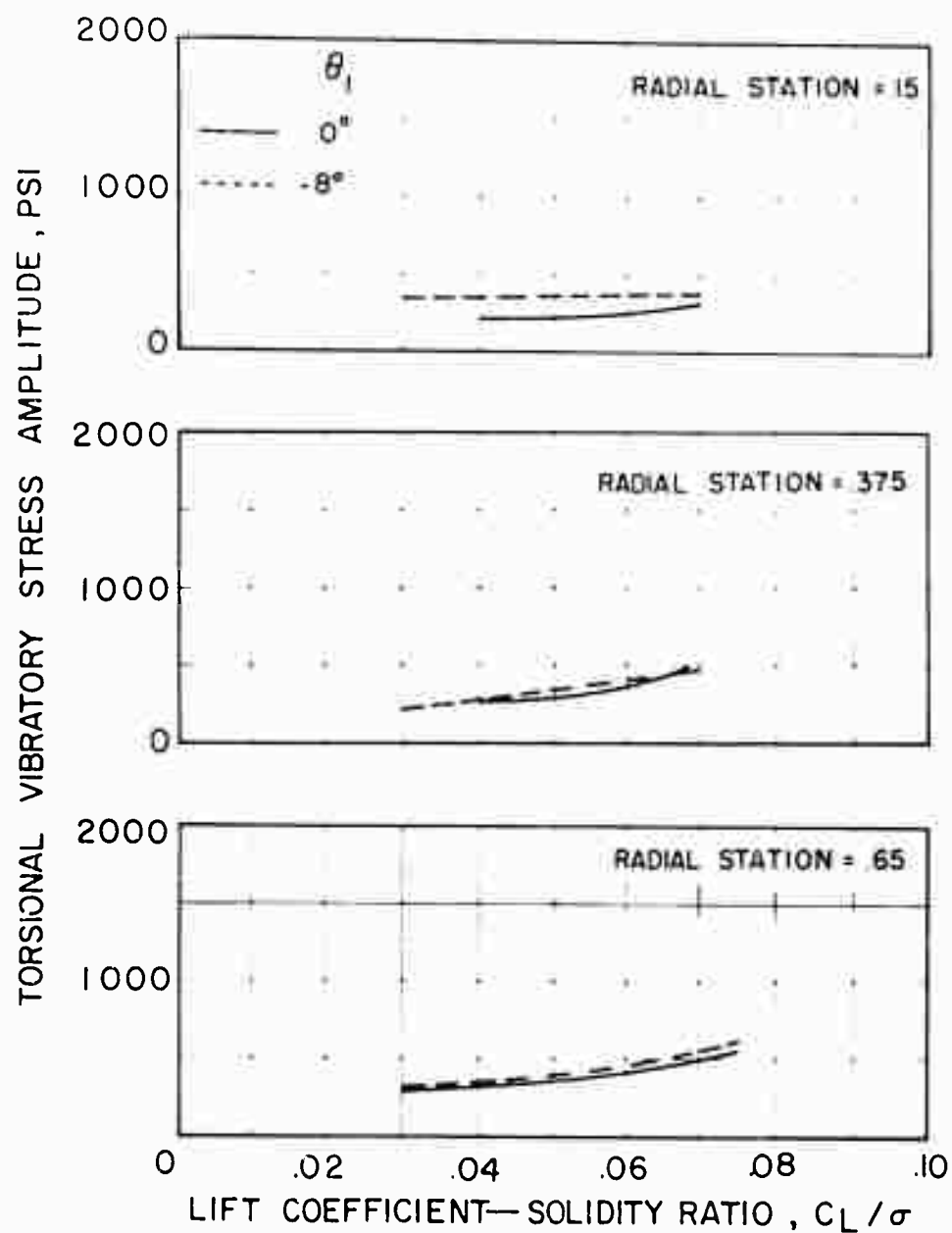
(a) $C_D/\sigma = 0.004$

Figure 74.   The Effect of Twist on Torsional Vibratory Stress
Amplitude as a Function of Lift at Three Values of
Drag for Three Radial Stations, $V = 163$ Knots,
$\mu = 0.40$, $M_{(1.0, 90)} = 0.82$.

150
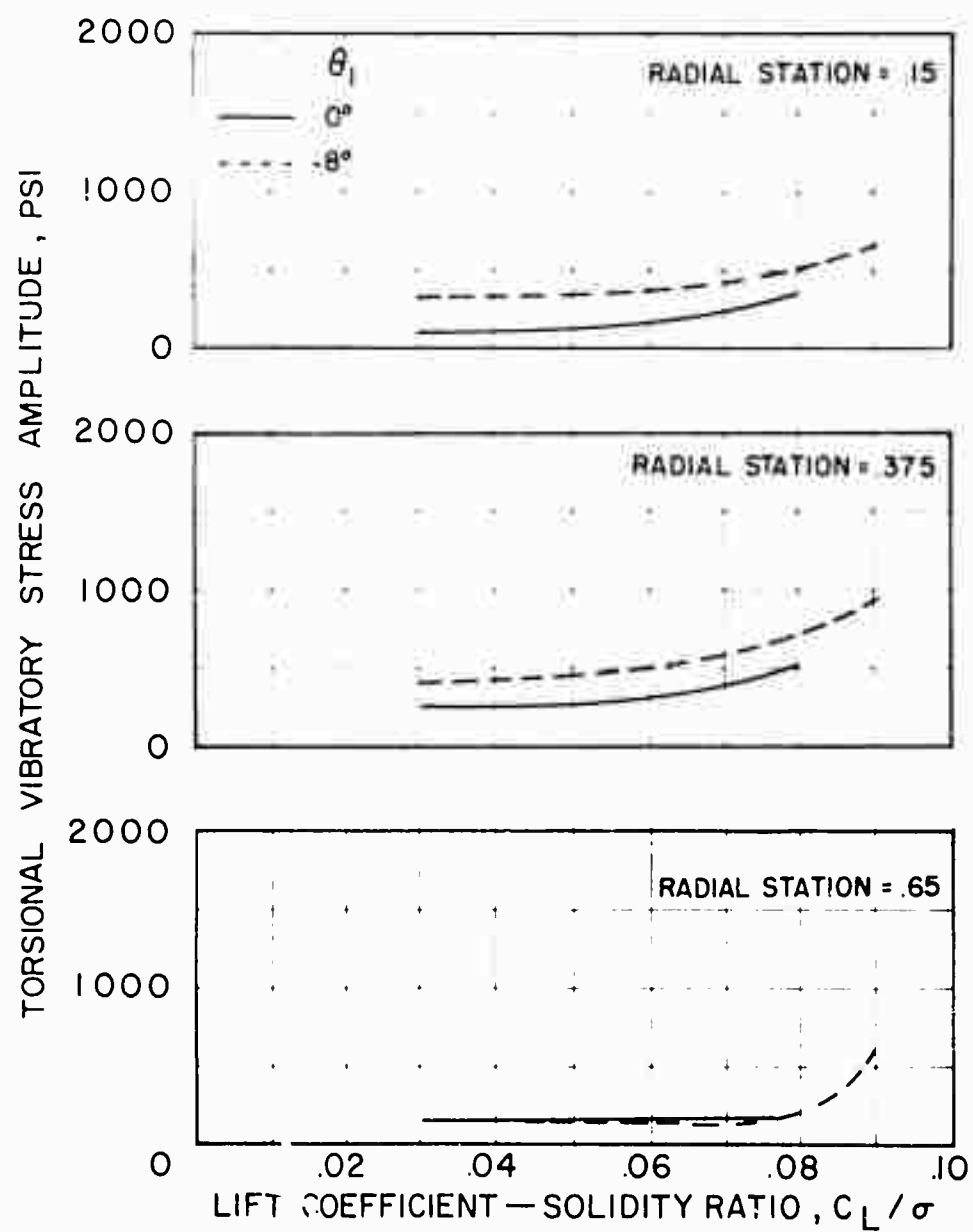
(b) $C_D \cdot \sigma = 0$

Figure 74. Continued.

151
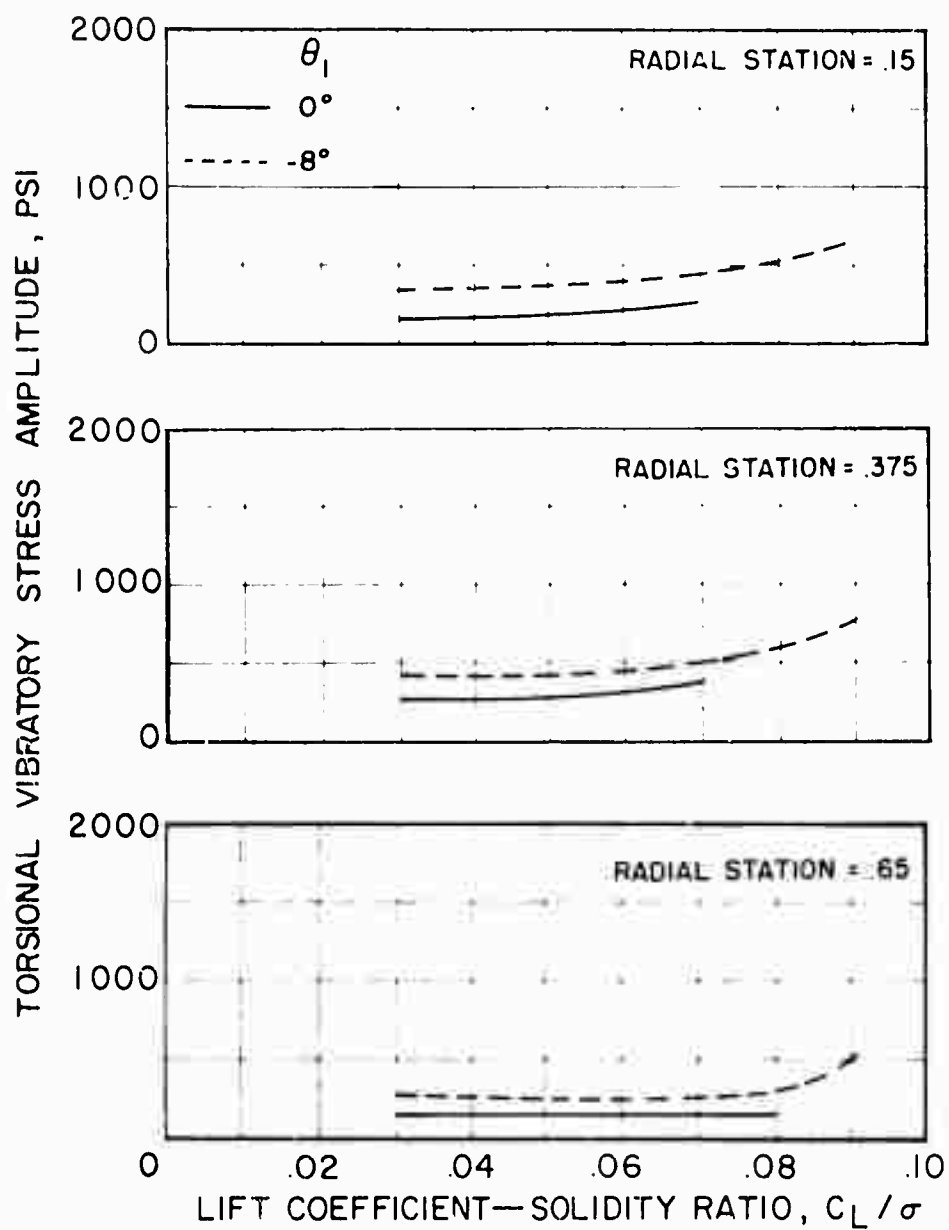
(c) $C_D/\sigma = -0.004$

Figure 74. Concluded.

152
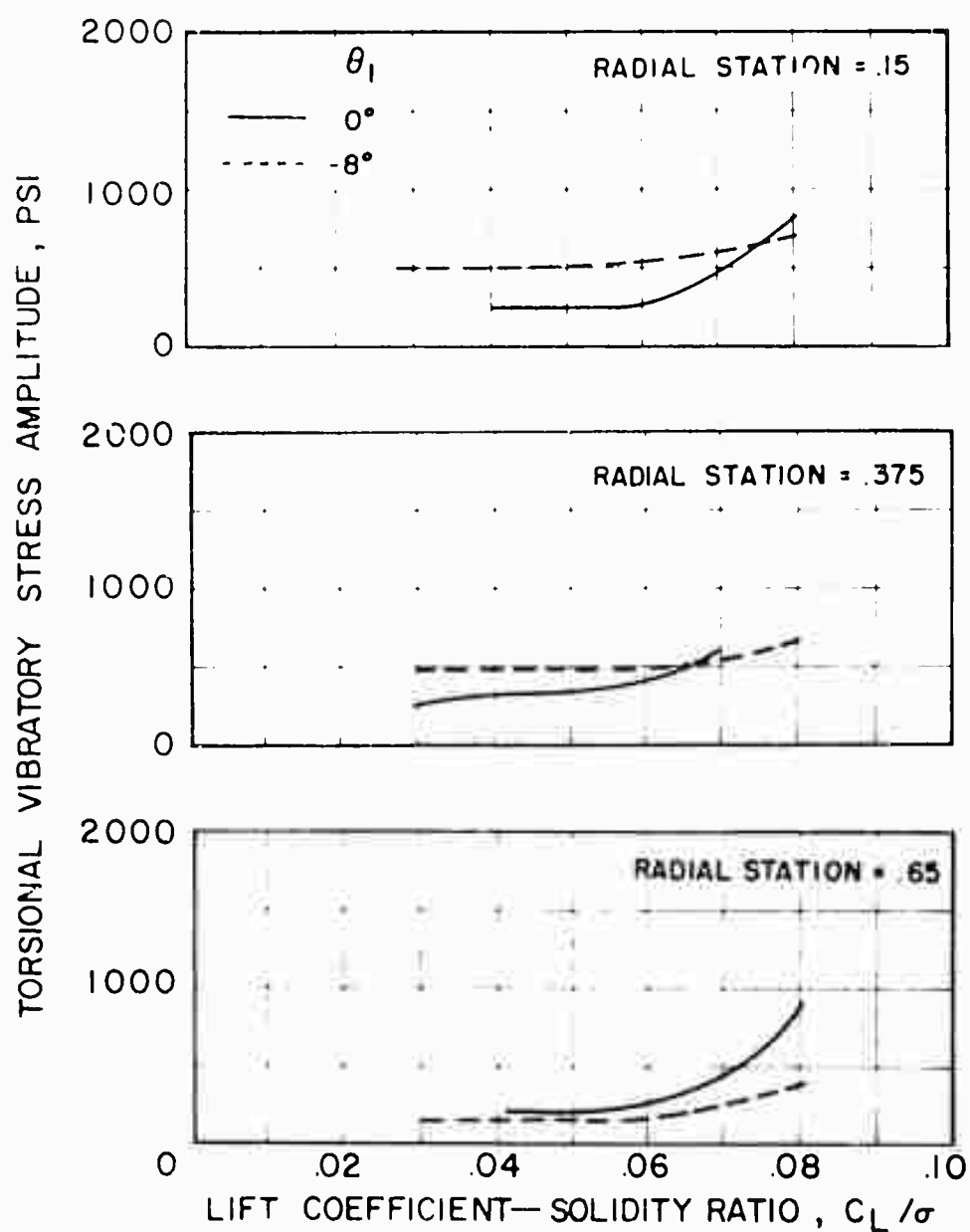
(a) $C_D, \sigma = 0.004$

Figure 75. The Effect of Twist on Torsional Vibratory Stress Amplitude as a Function of Lift at Two Values of Drag for Three Radial Stations, V = 177 Knots, $\mu = 0.46$, M(1.0, 90) = 0.82.

153
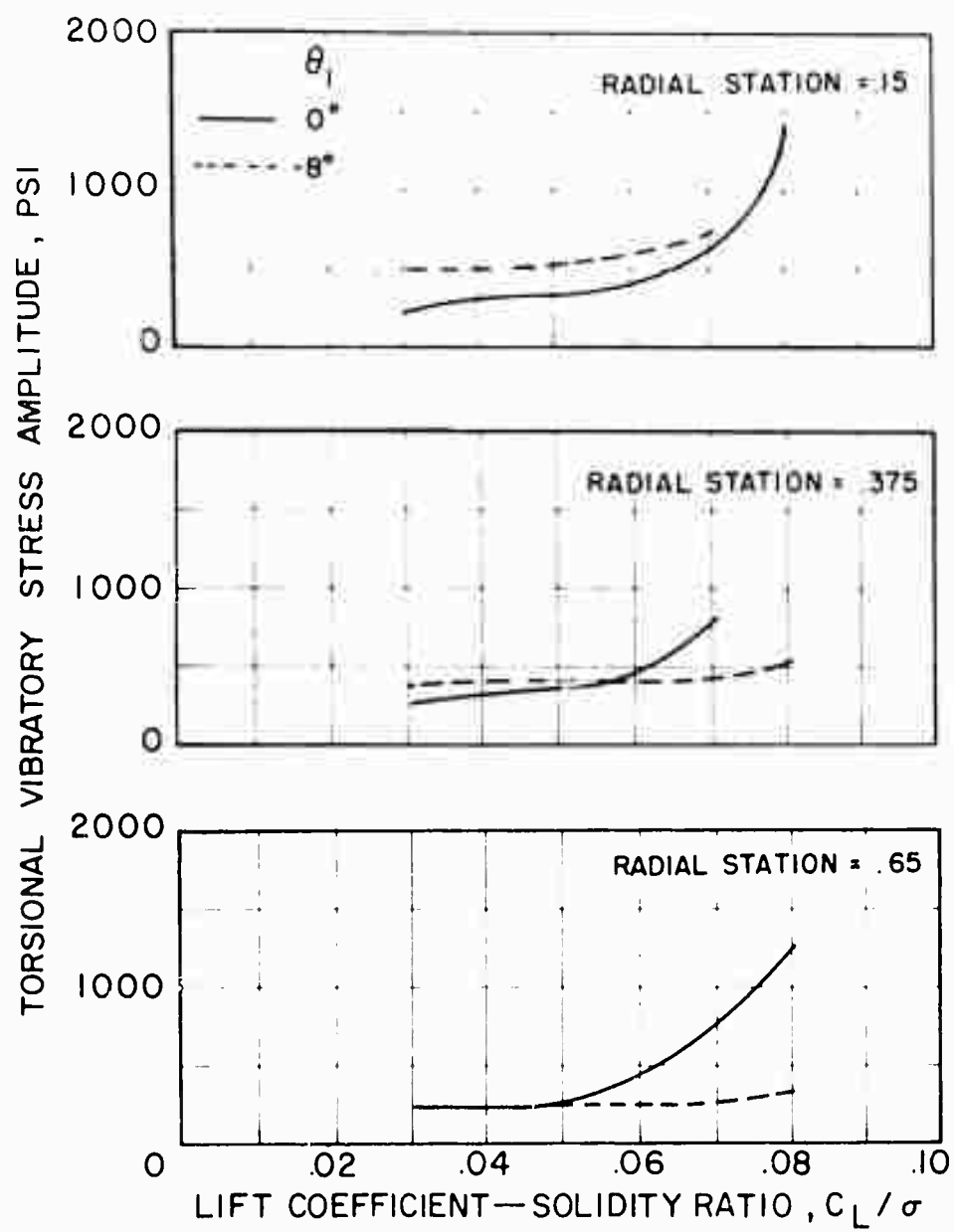
(b) $C_D/\sigma = 0$

Figure 75. Concluded.

154
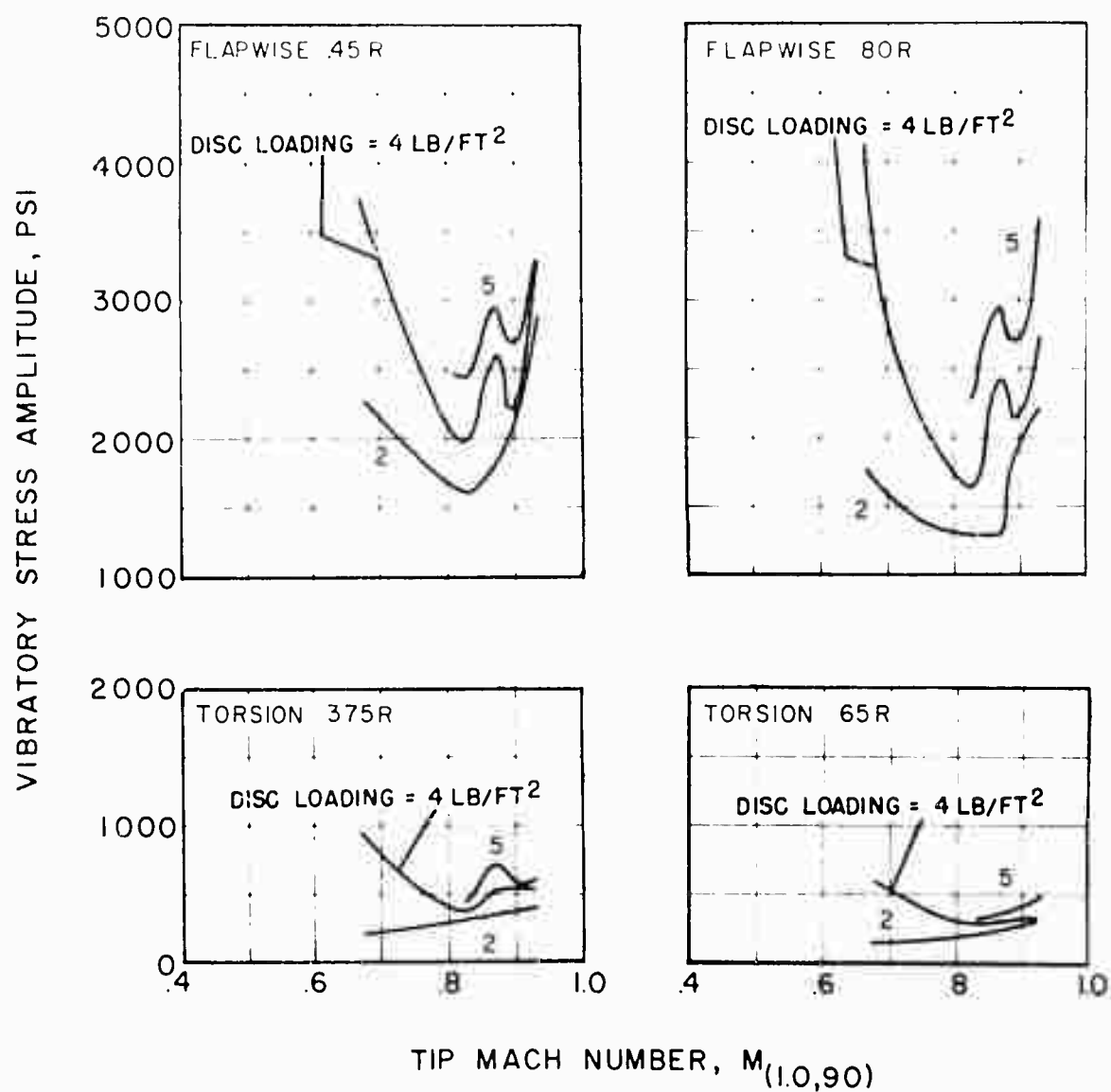
(a) $C_D \sigma = 0.004$

Figure 76.   The Effect of Advancing Tip Mach Number on
Flapwise, Chordwise, and Torsional Vibratory
Stress Amplitude at Constant Disc Loading for
Three Values of Drag Coefficient-Solidity Ratio,
$\mu \approx 0.40$, $\theta_1 = 0°$.

155
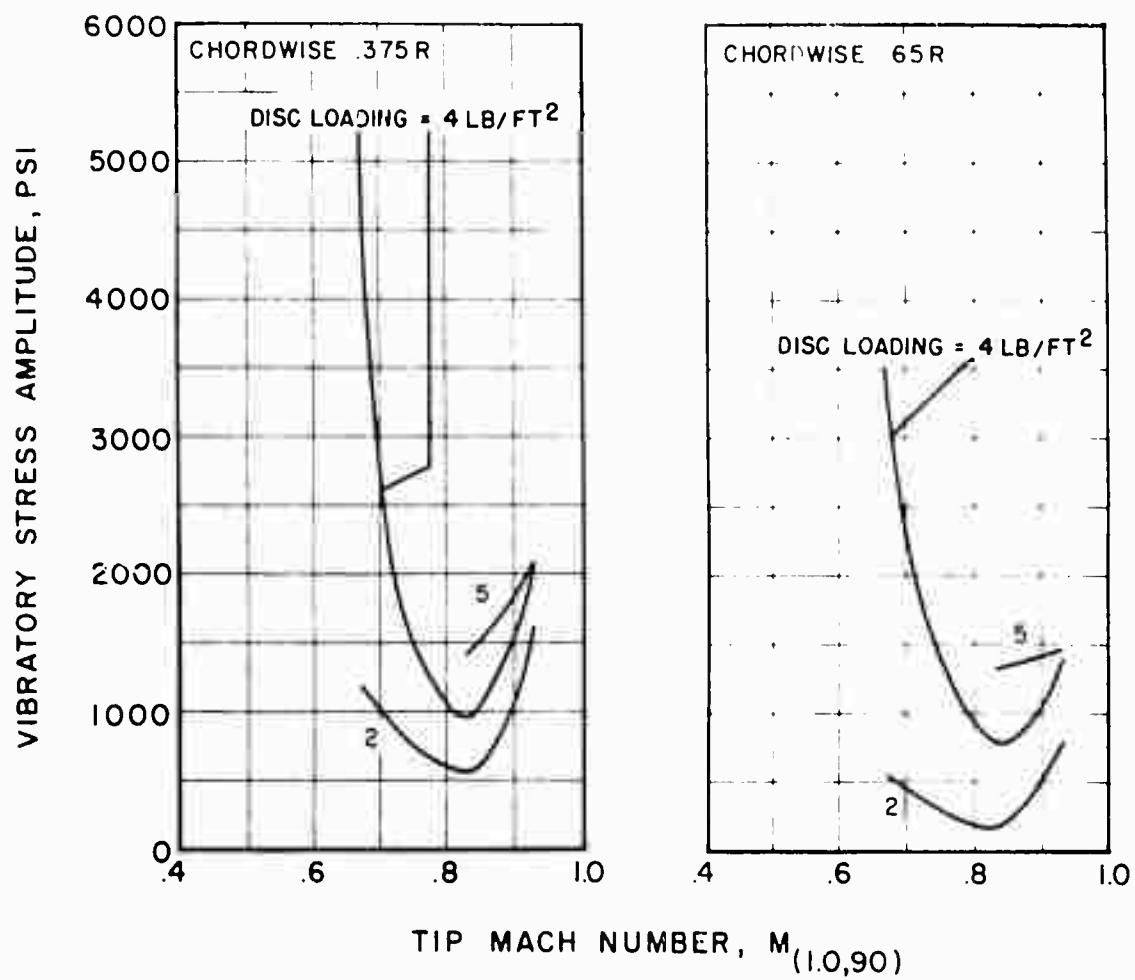
(a) $C_D/\sigma = 0.004$ Concluded.

Figure 76. Continued.

156
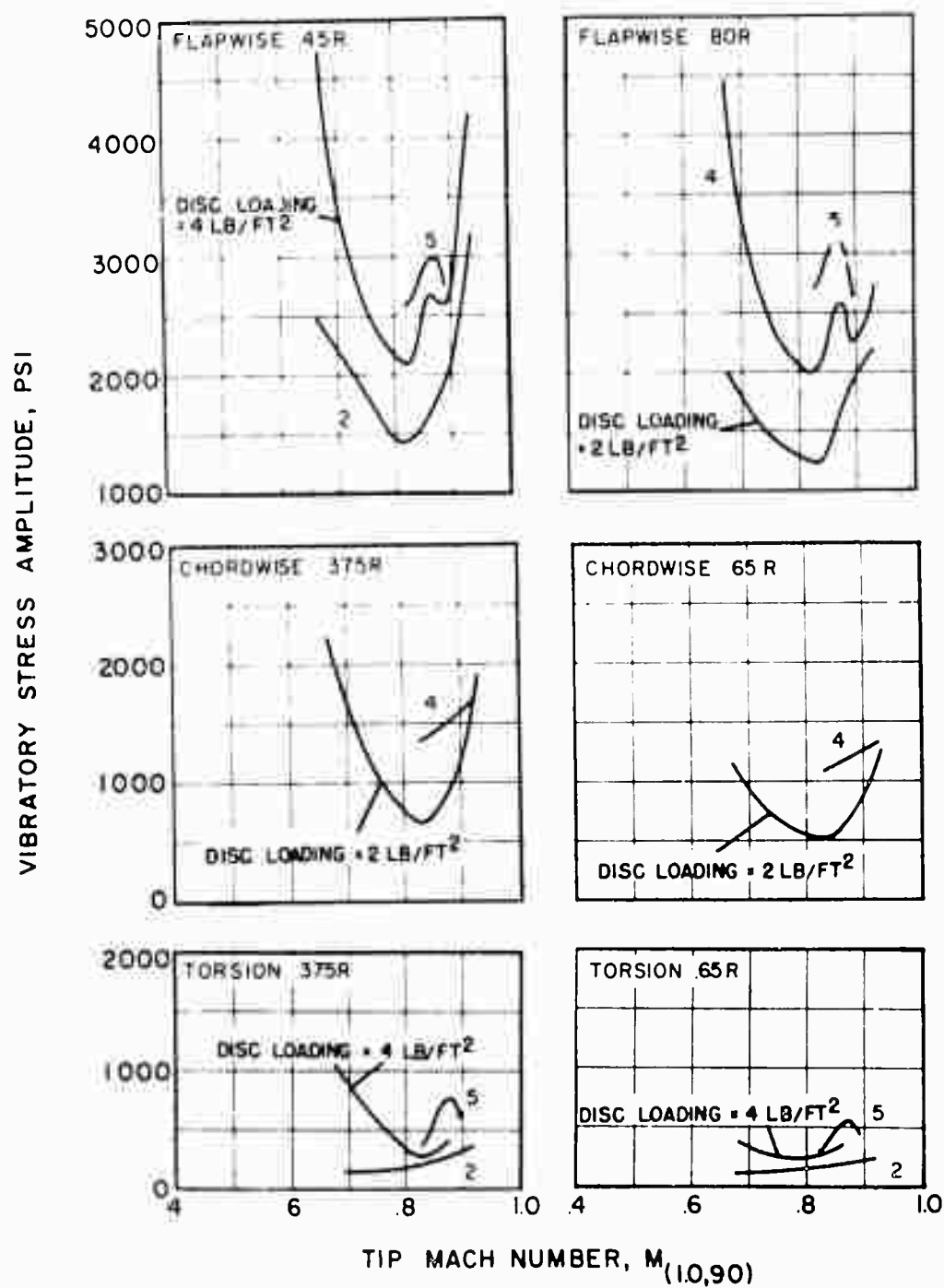
(b) $C_D/\sigma = 0$

Figure 76. Continued.

157
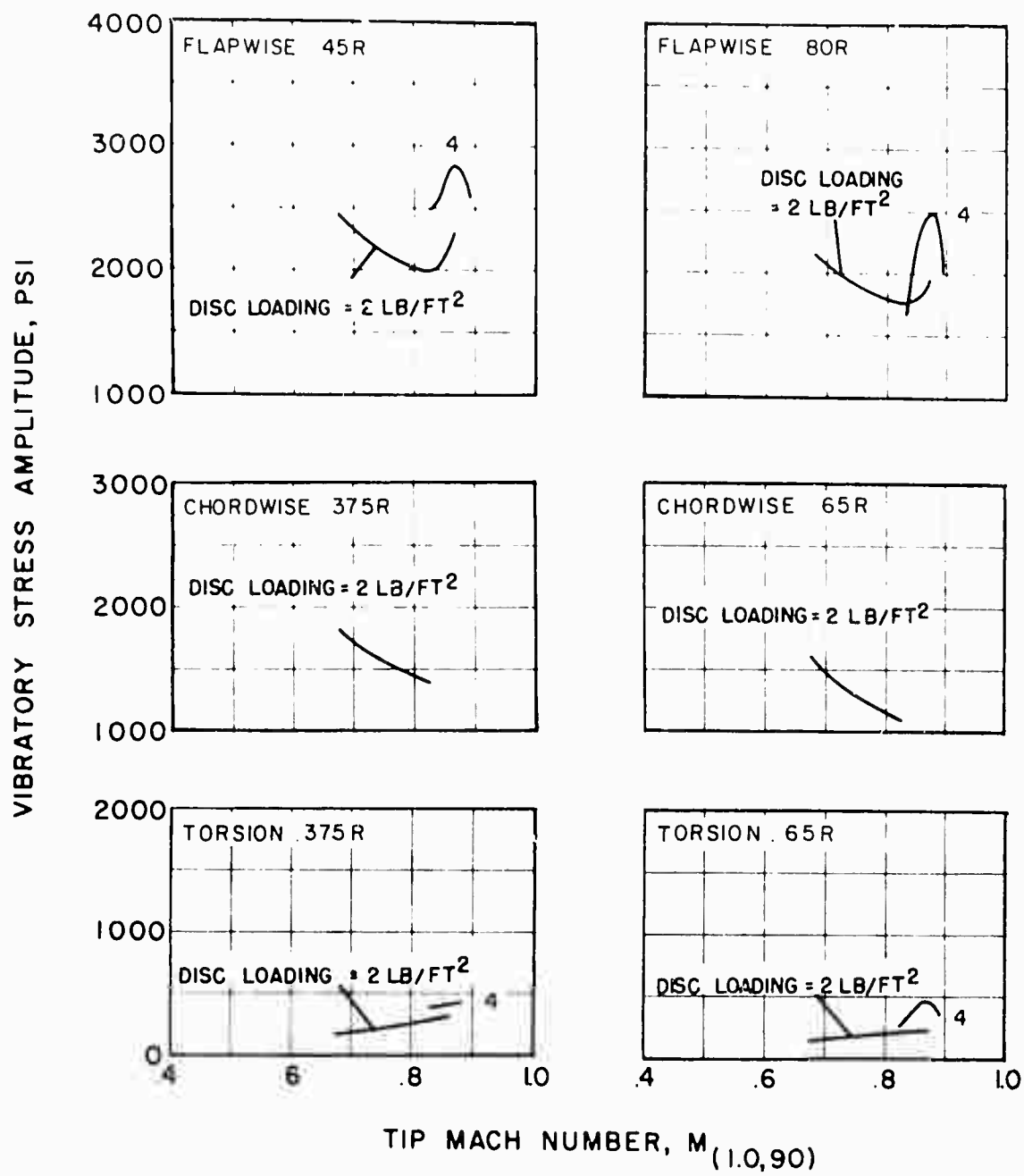
(c) $C_D/\sigma = -0.004$

Figure 76. Concluded.
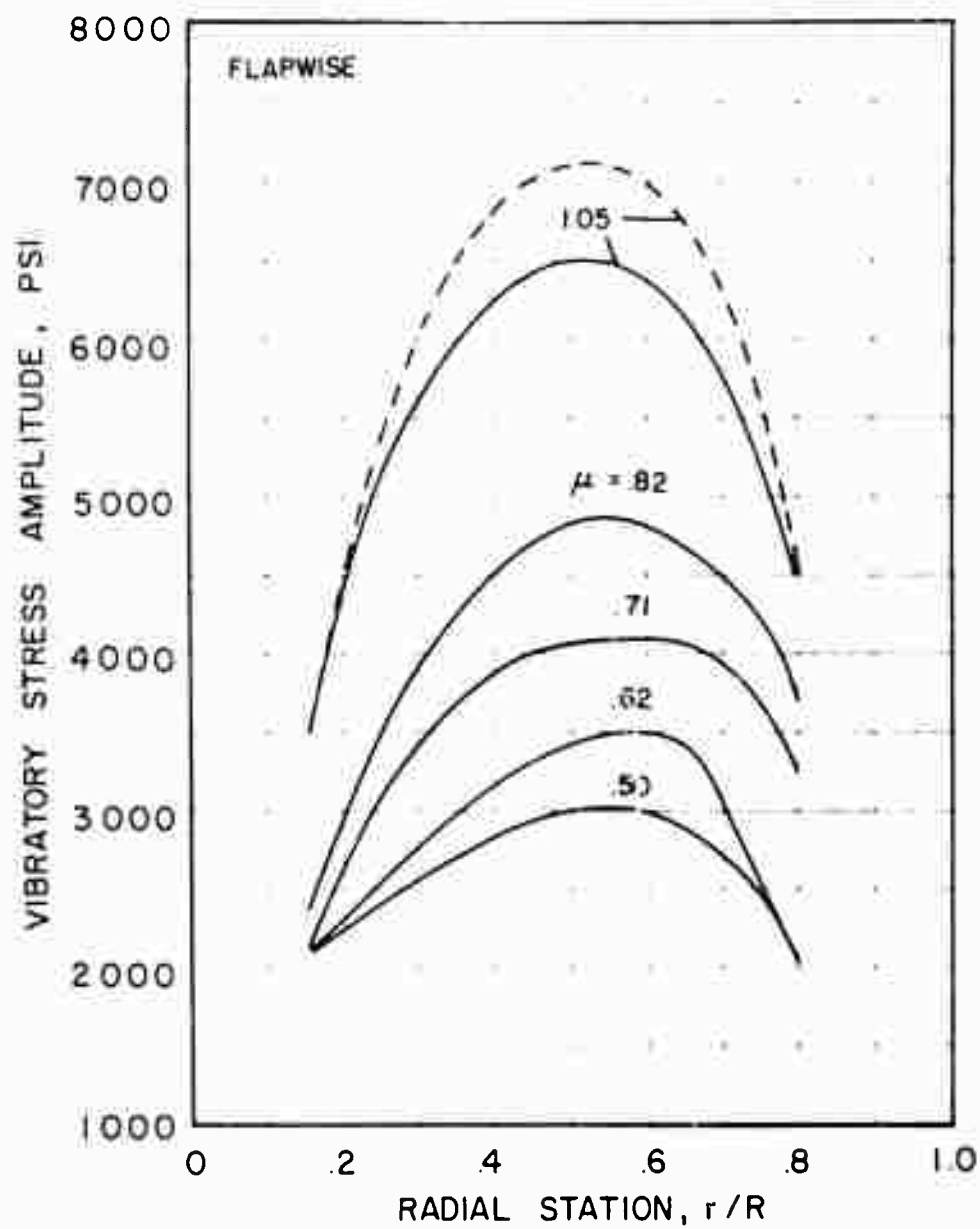
(a) Disc Loading = 0.85 LB/FT^2

Figure 77. The Effect of Advance Ratio on the Radial Distribution of Flapwise, Chordwise, and Torsional Vibratory Stress Amplitude for Two Disc Loadings, $V \approx 195$ Knots, $C_Q/\sigma = 0$, $\theta_1 = 0°$.

159
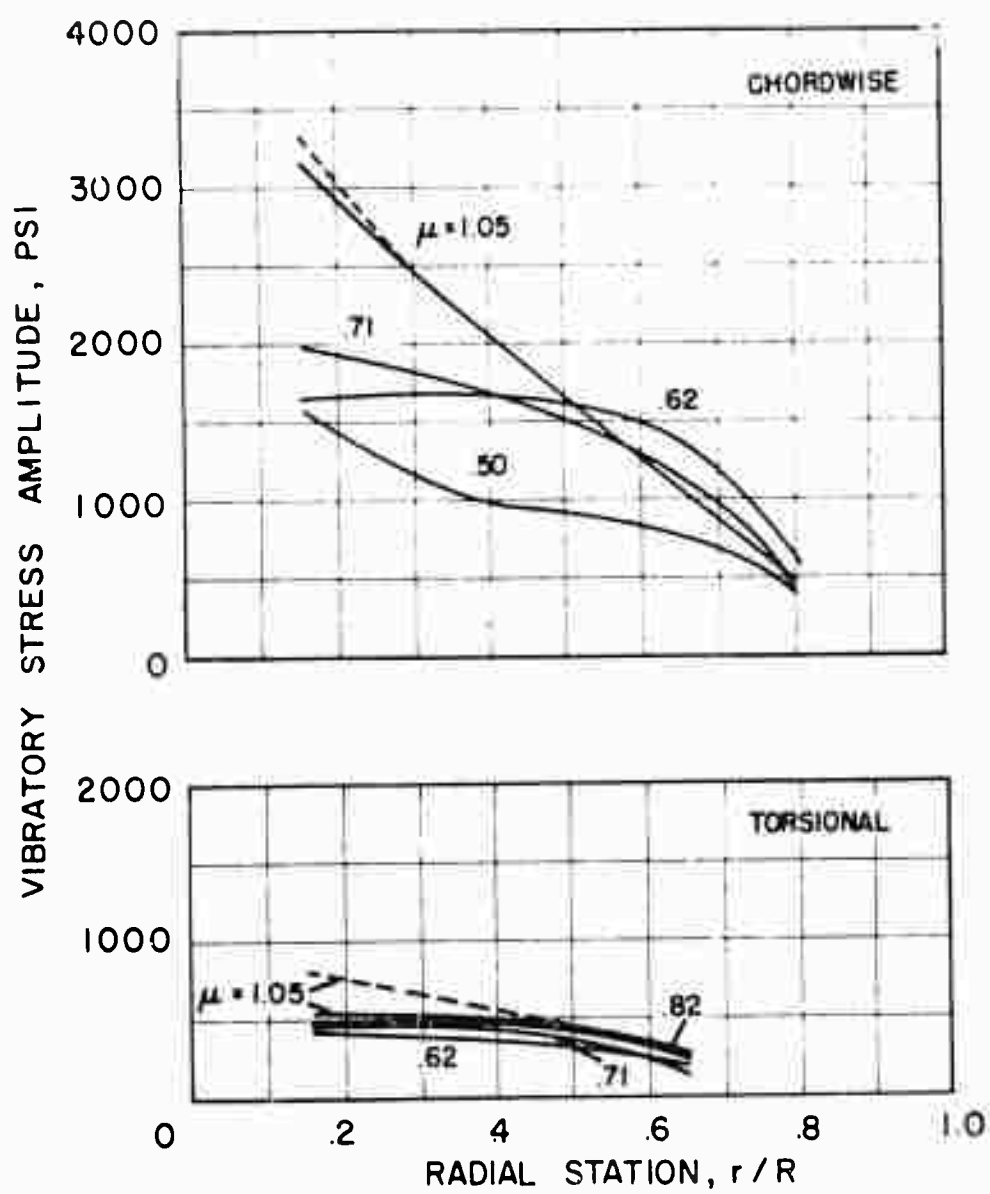
(a) Disc Loading = 0. 85 LB/FT^2 Concluded.

Figure 77. Continued.

160
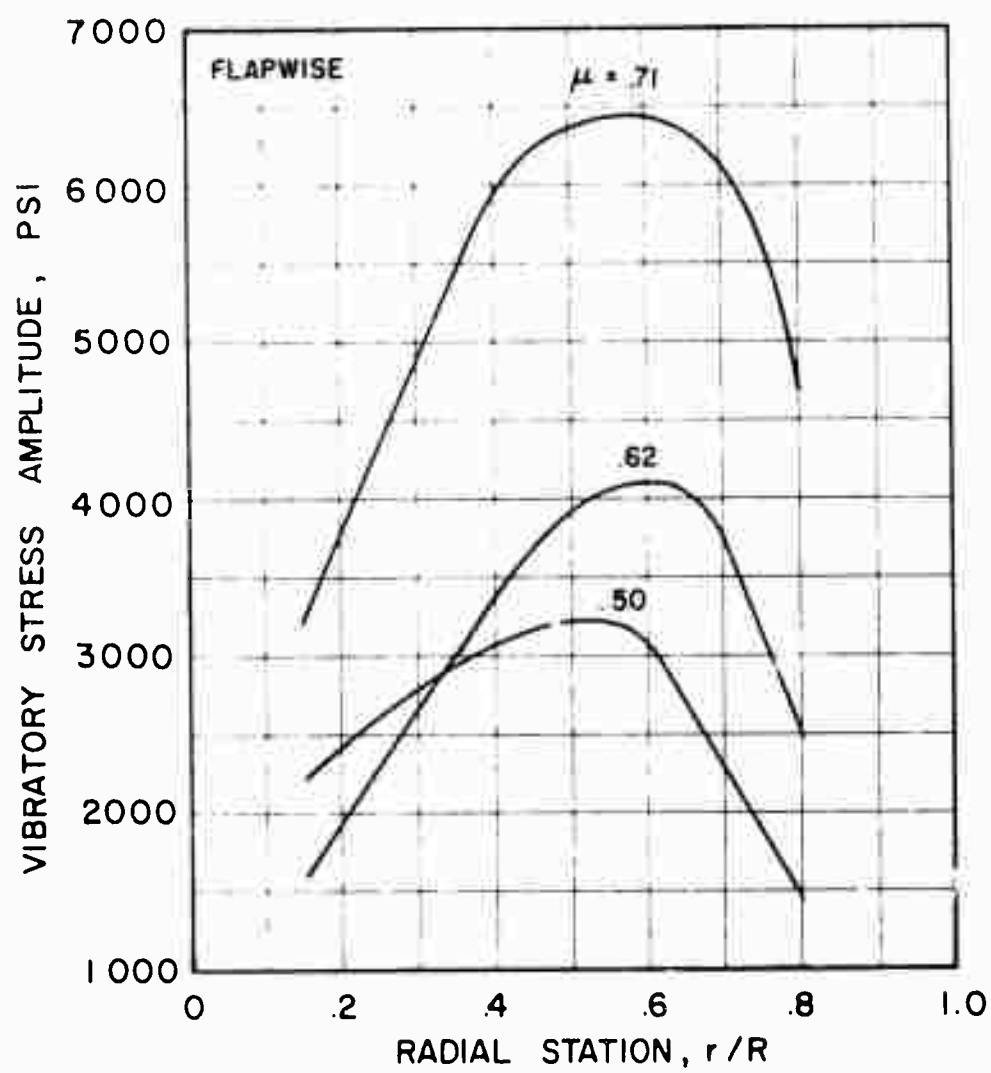
(b) Disc Loading = 1.5 LB/FT^2

Figure 77. Continued.

161
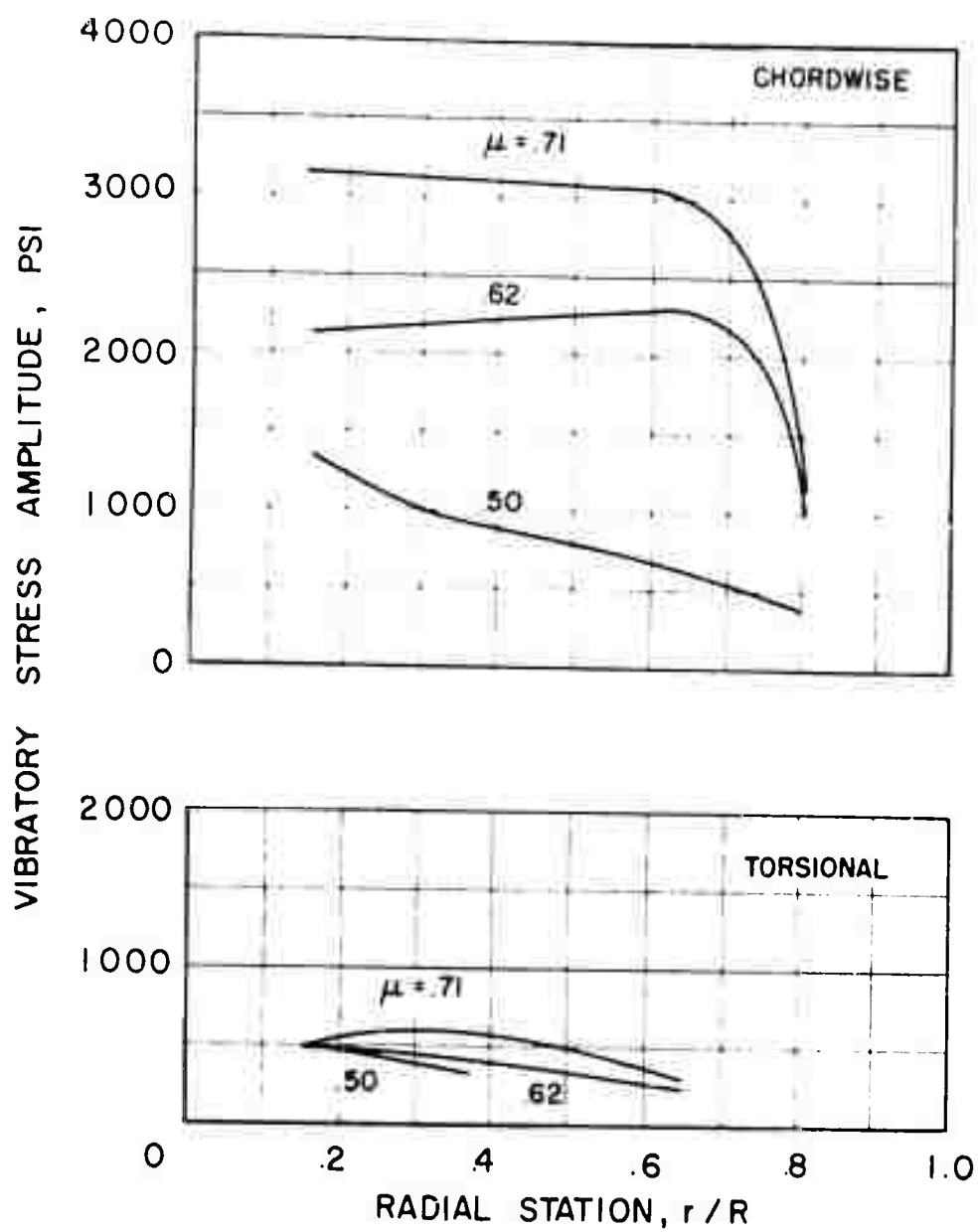
(b) Disc Loading = 1.5 LB, FT^2 Concluded.

Figure 77. Concluded.

162
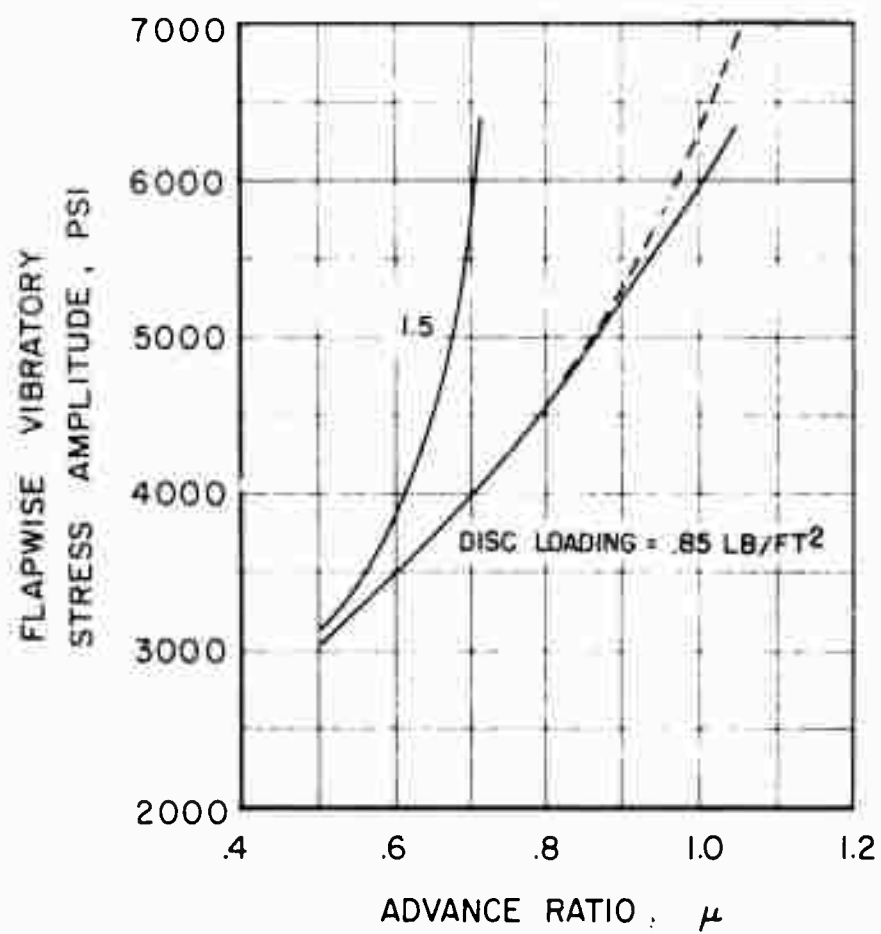
Figure 78. The Effect of Advance Ratio and Disc Loading on Flapwise Vibratory Stress Amplitude at 60% Radius, $V \approx 195$ Knots. $C_Q/\sigma = 0$, $\theta_1 = 0°$.
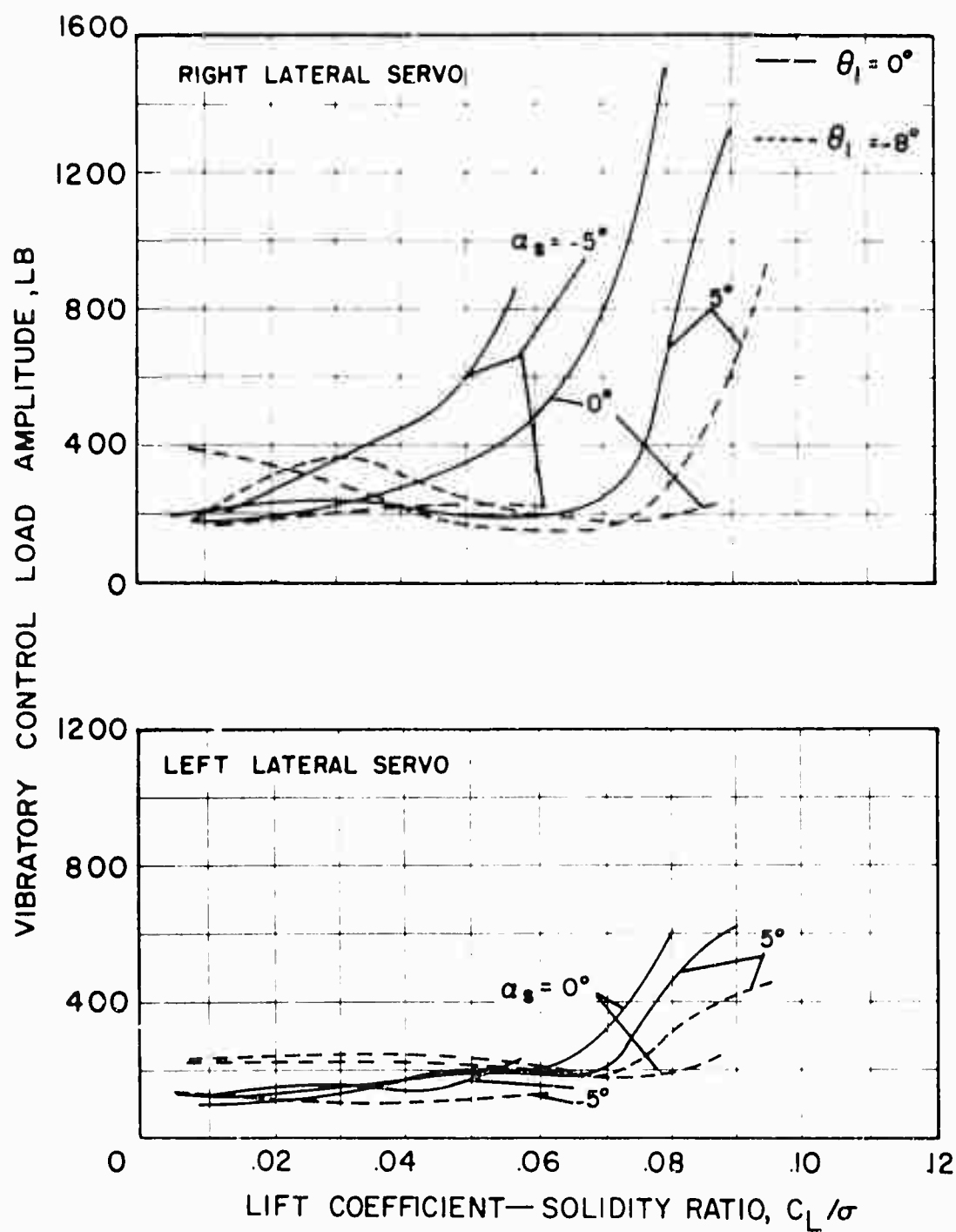
Figure 79. The Effect of Twist and Lift on Vibratory Control Load Amplitude at Constant Shaft Angle for One Rotating and Three Stationary Control Loads, $V = 177$ Knots, $\mu = 0.46$, $M_{(1.0, 90)} = 0.82$.

164
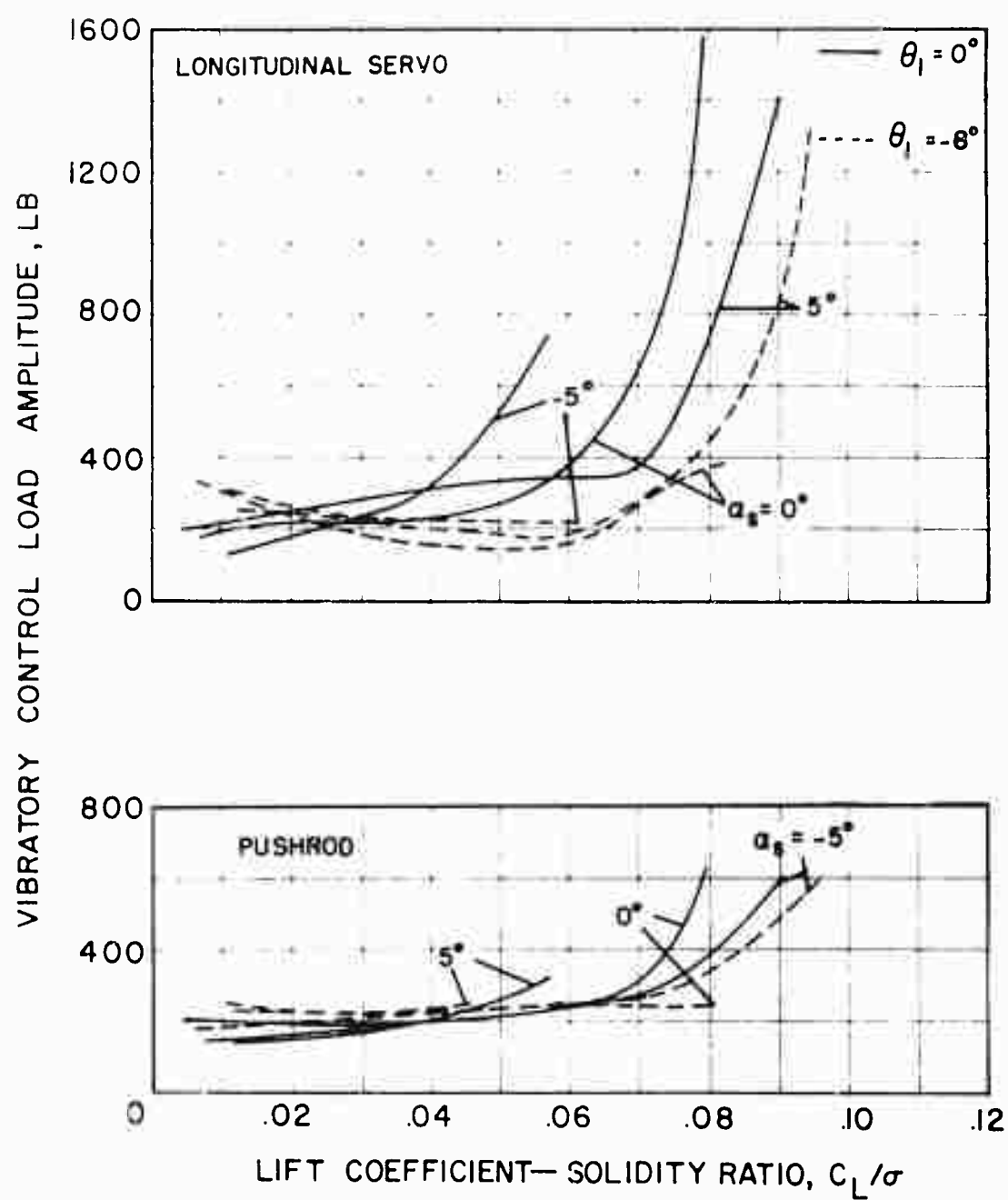
Figure 79. Concluded.

165
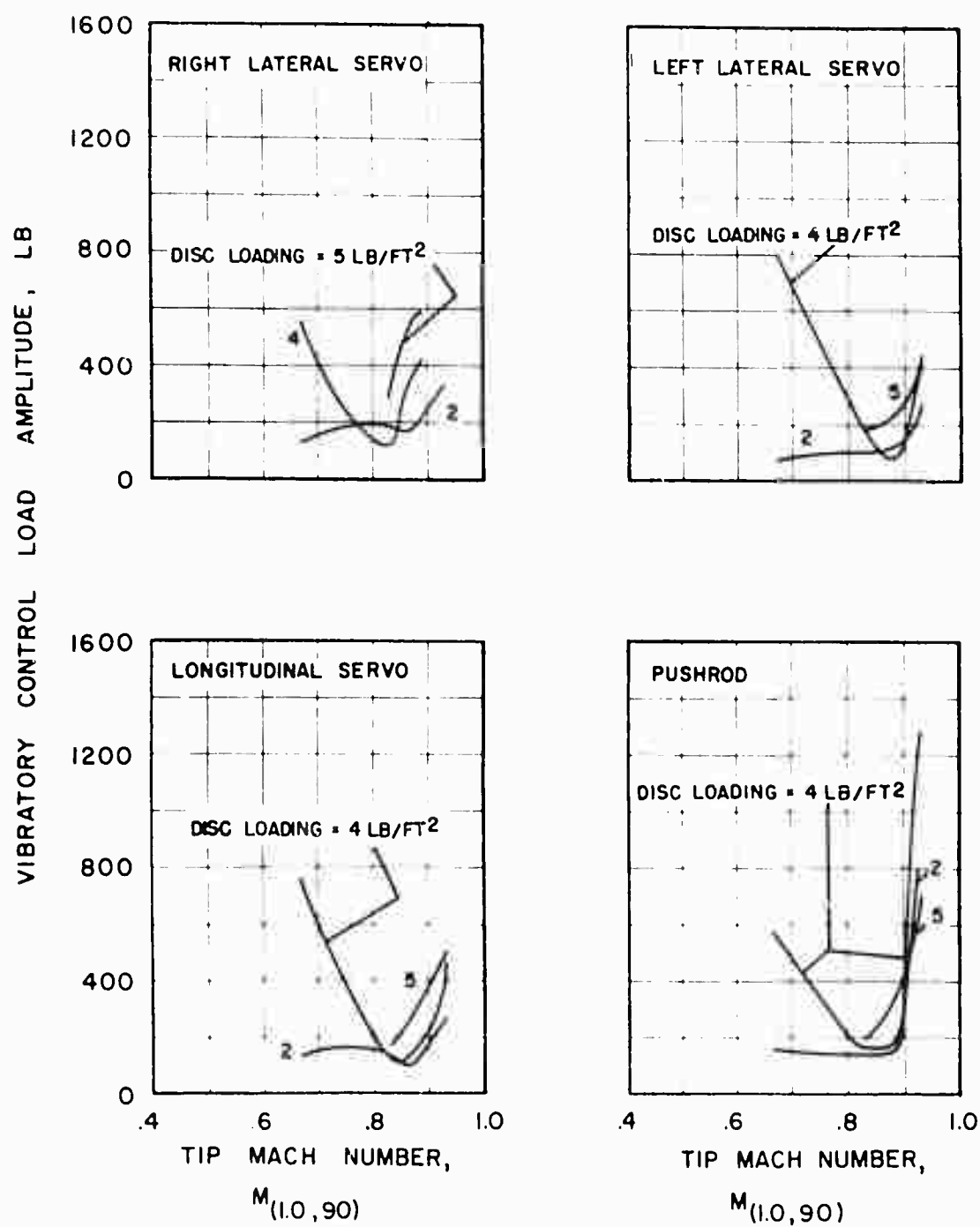
Figure 80. The Effect of Advancing Tip Mach Number on
Vibratory Control Load Amplitude at Constant
Disc Loading for One Rotating and Three Stationary
Control Loads, $\mu \approx 0.40$, $\theta_1 = 0°$, $\alpha_s = 0°$.

166
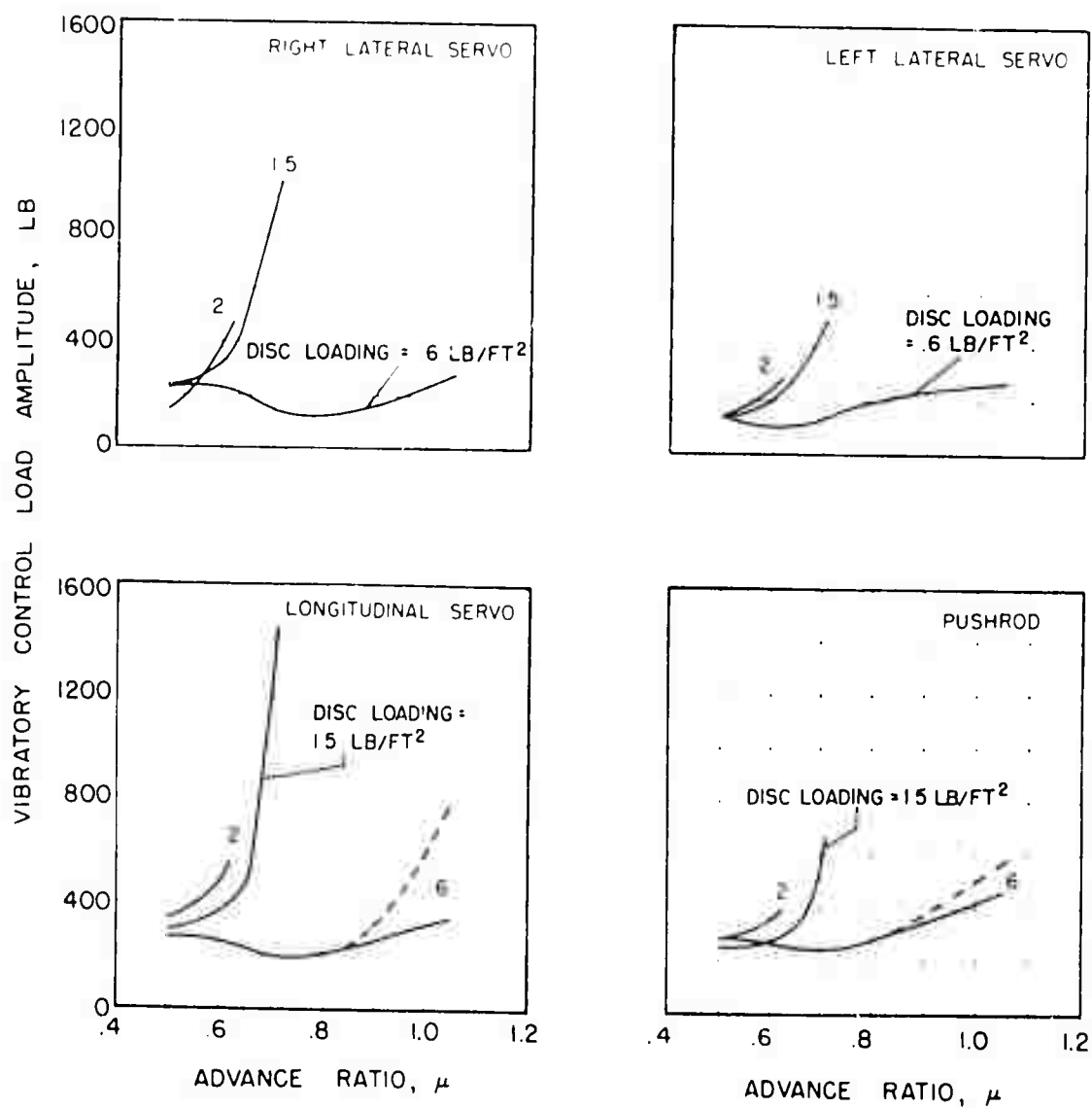
Figure 81. The Effect of Advance Ratio on Vibratory Control Load Amplitude at Constant Disc Loading for One Rotating and Three Stationary Control Loads, $V \approx 195$ Knots, $\theta_1 = 0°$, $\alpha_s = 5°$.

167

PRESENTATION OF MEASURED
BLADE VIBRATORY STRESS
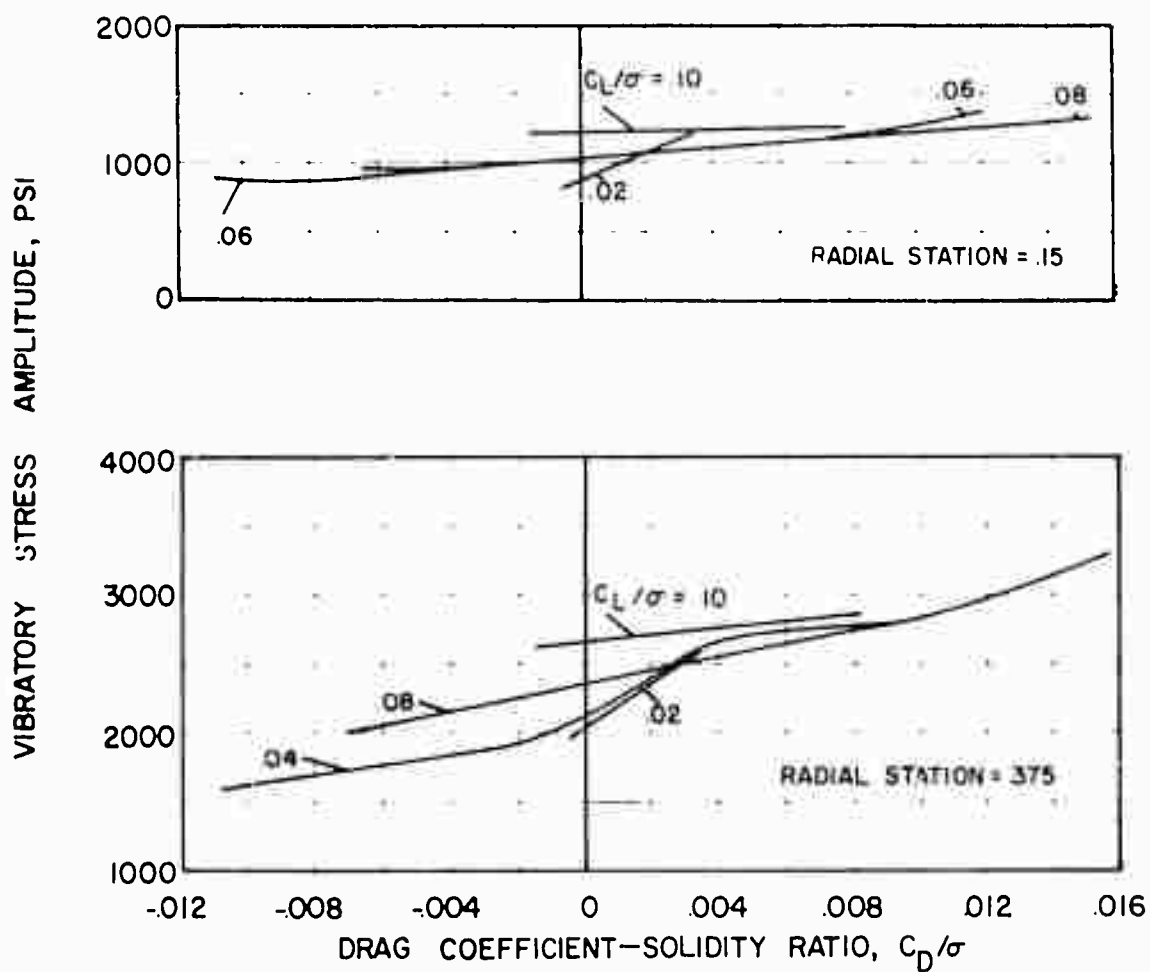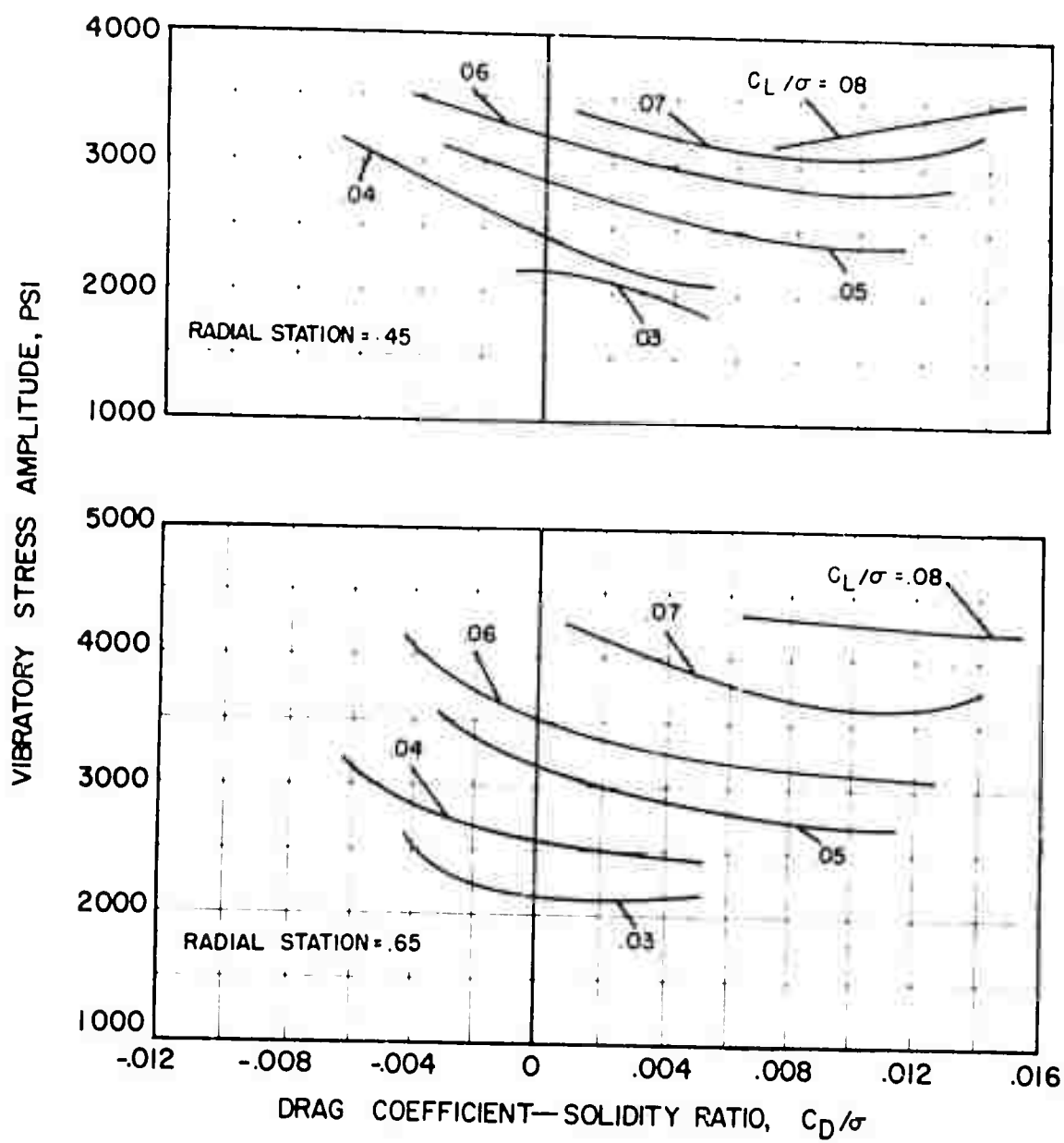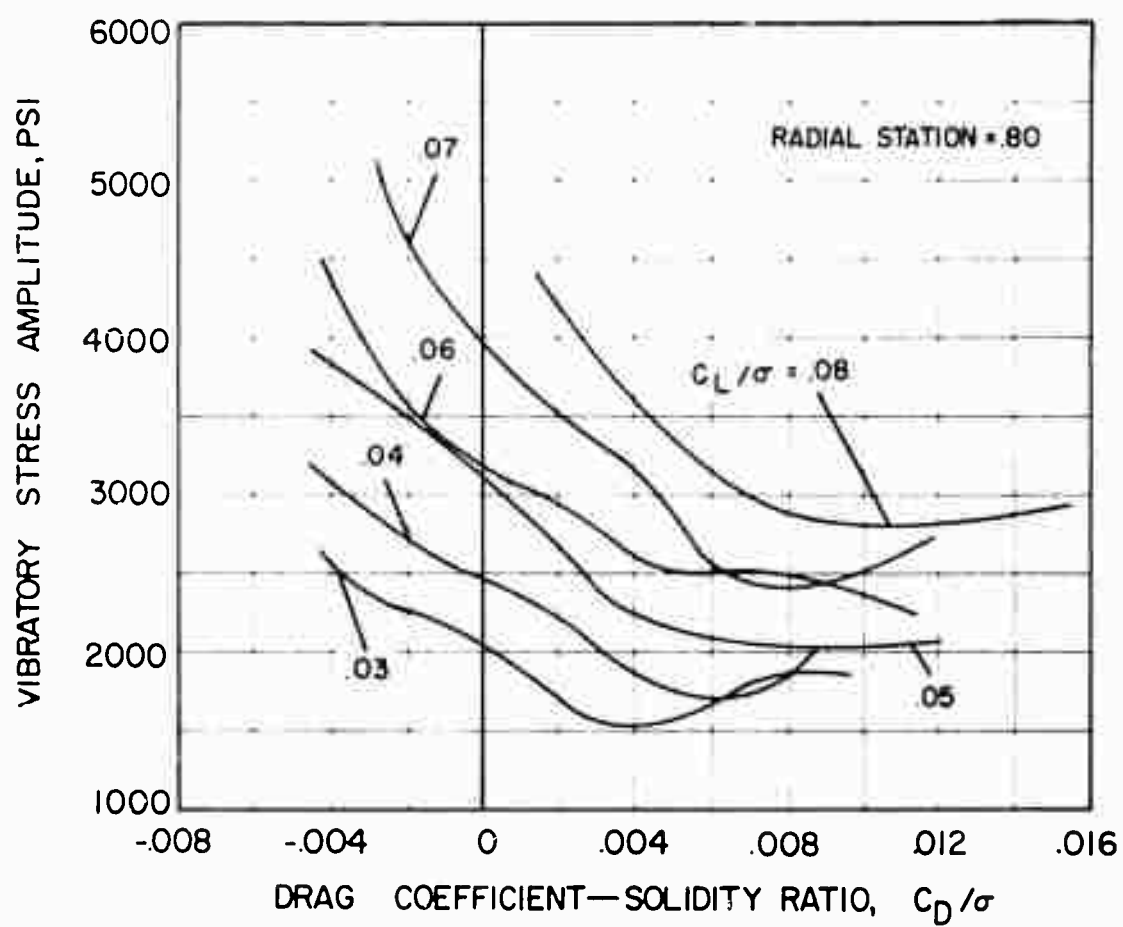

(a) Flapwise

Figure 82. The Effect of Drag on Flapwise, Chordwise and
Torsional Vibratory Stress Amplitude at Constant
Lift for Several Radial Stations, V = 117 Knots,
μ = 0.30, θ_1 = -8°, $M_{(1.0, 90)}$ = 0.74.
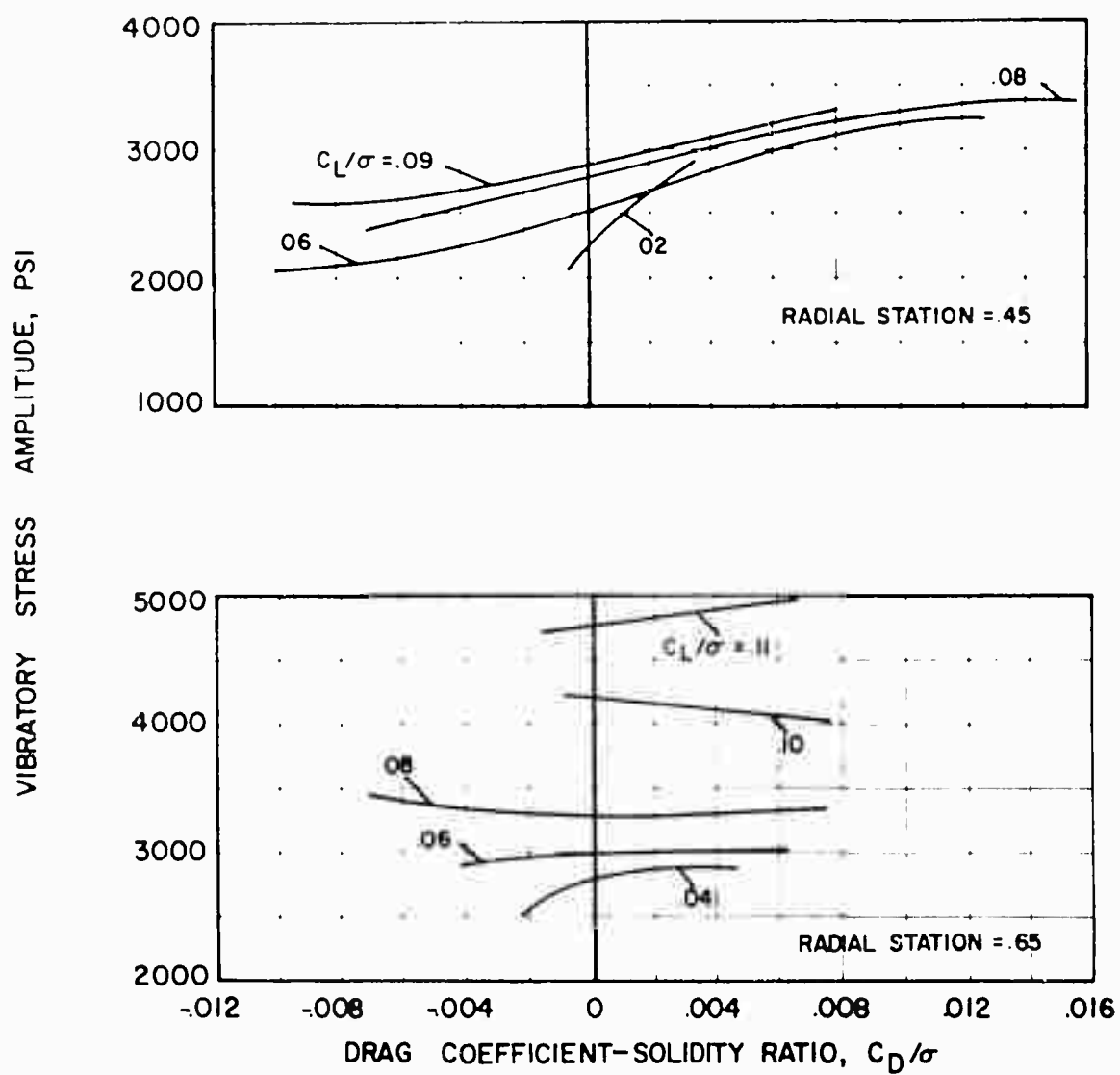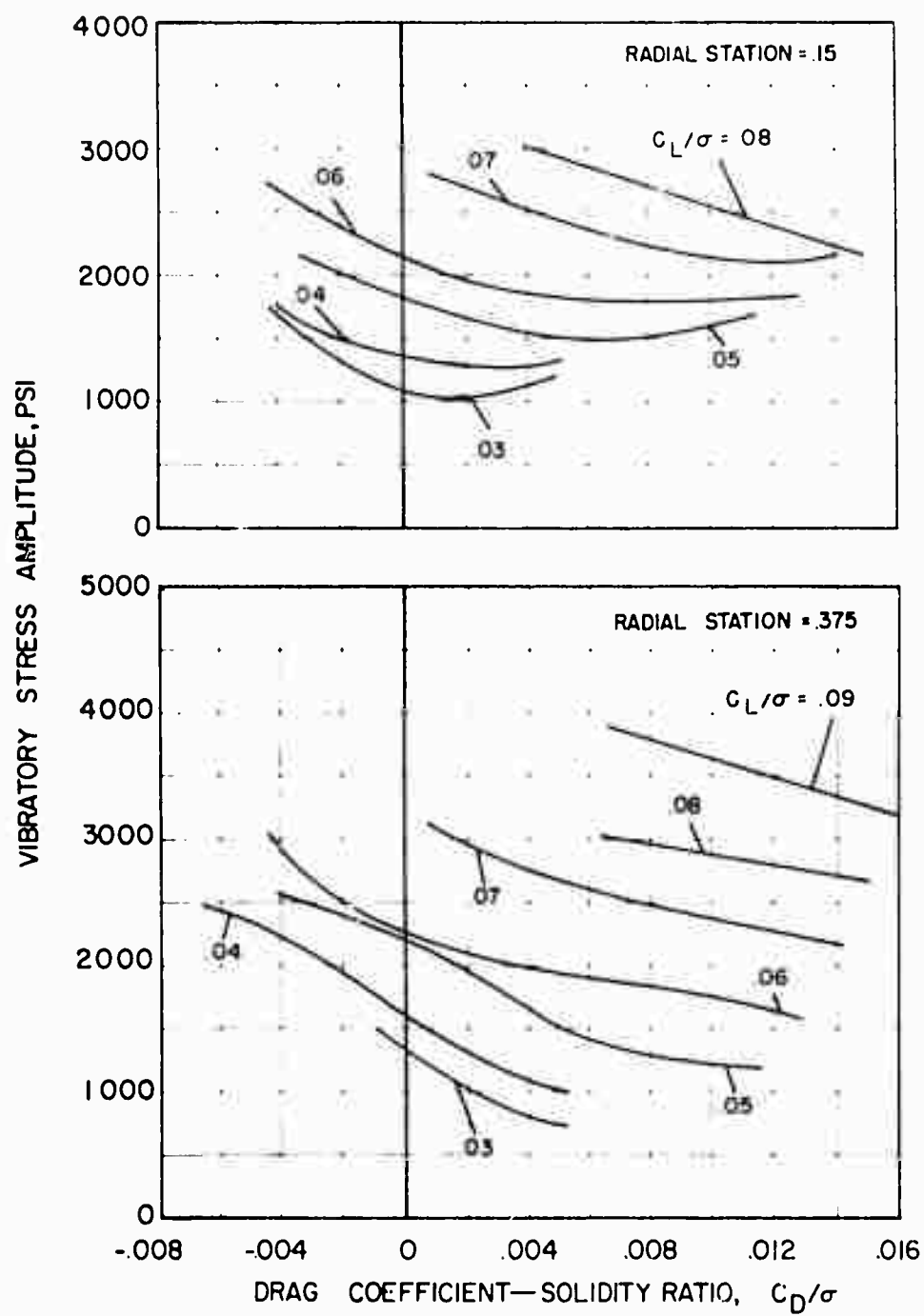
(a) Flapwise Continued
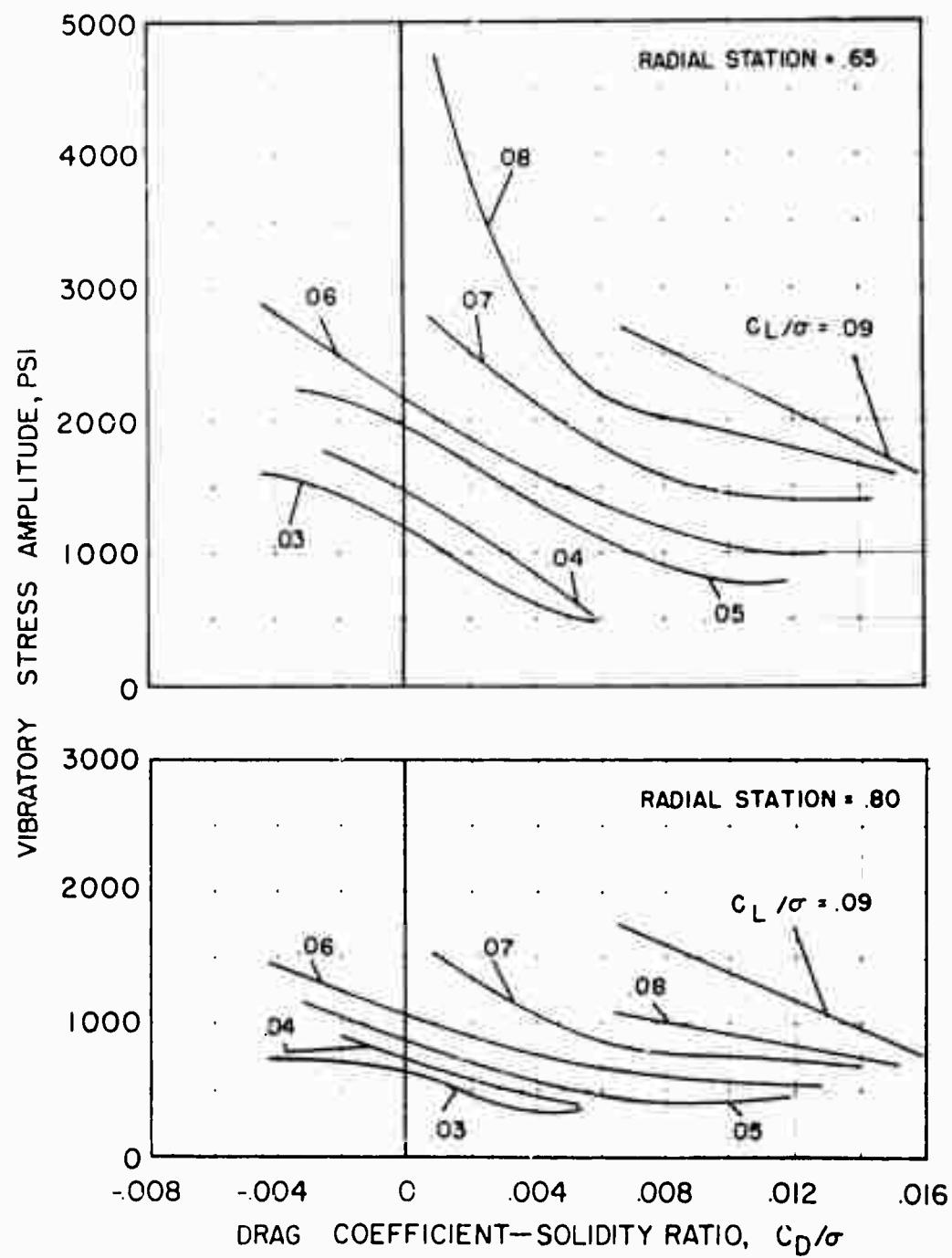
Figure 82. Continued.

169

(a) Flapwise Concluded

Figure 82. Continued.

170
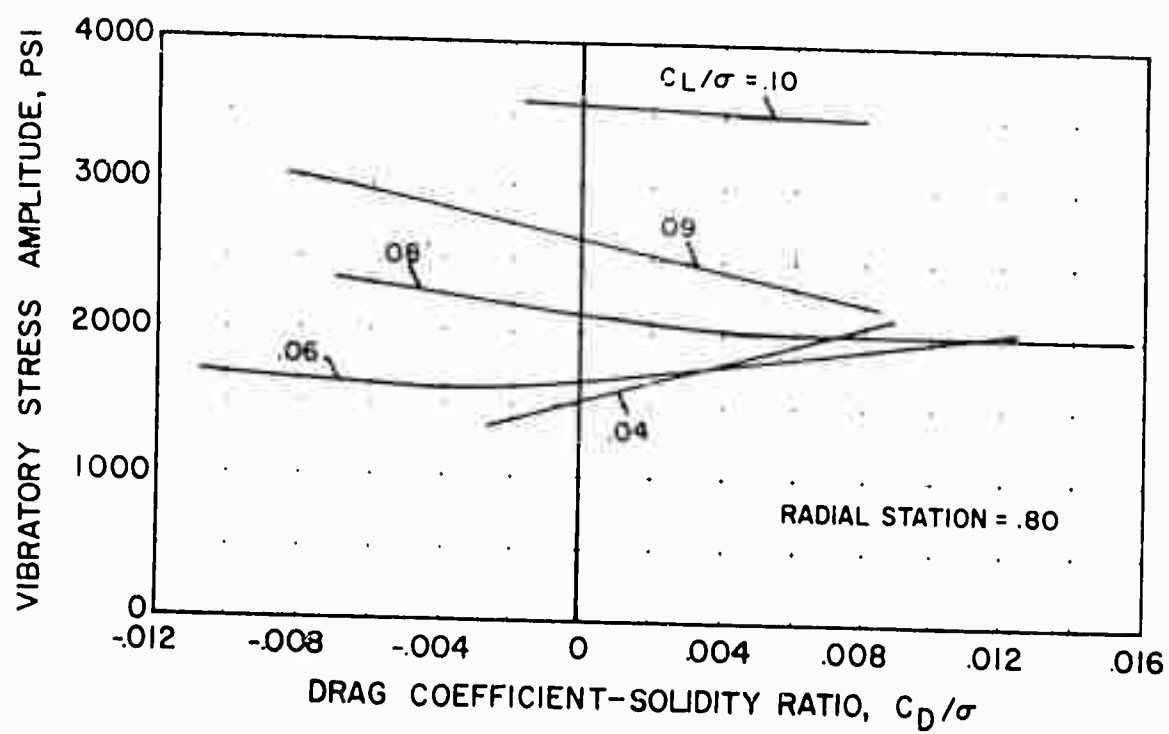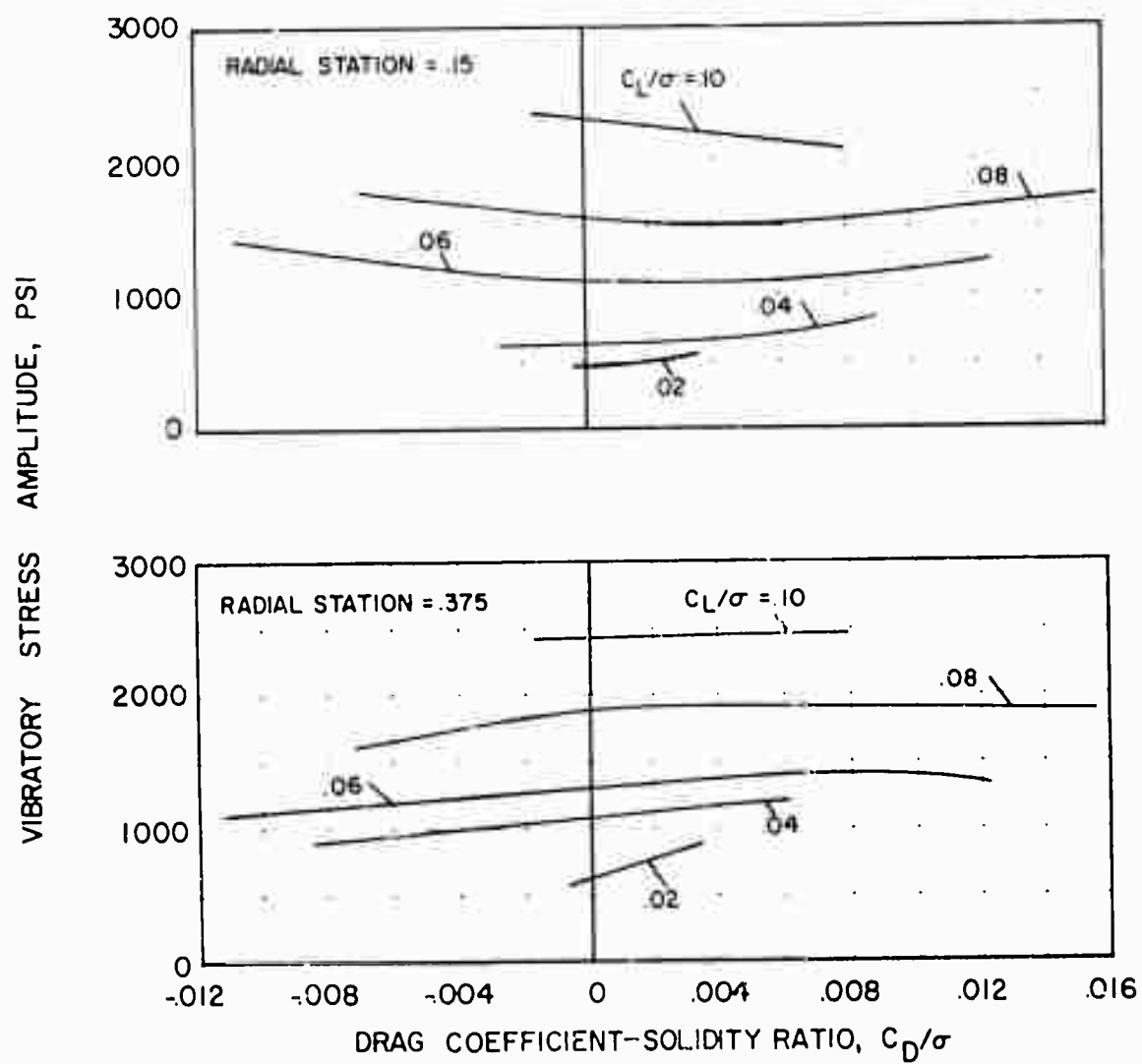
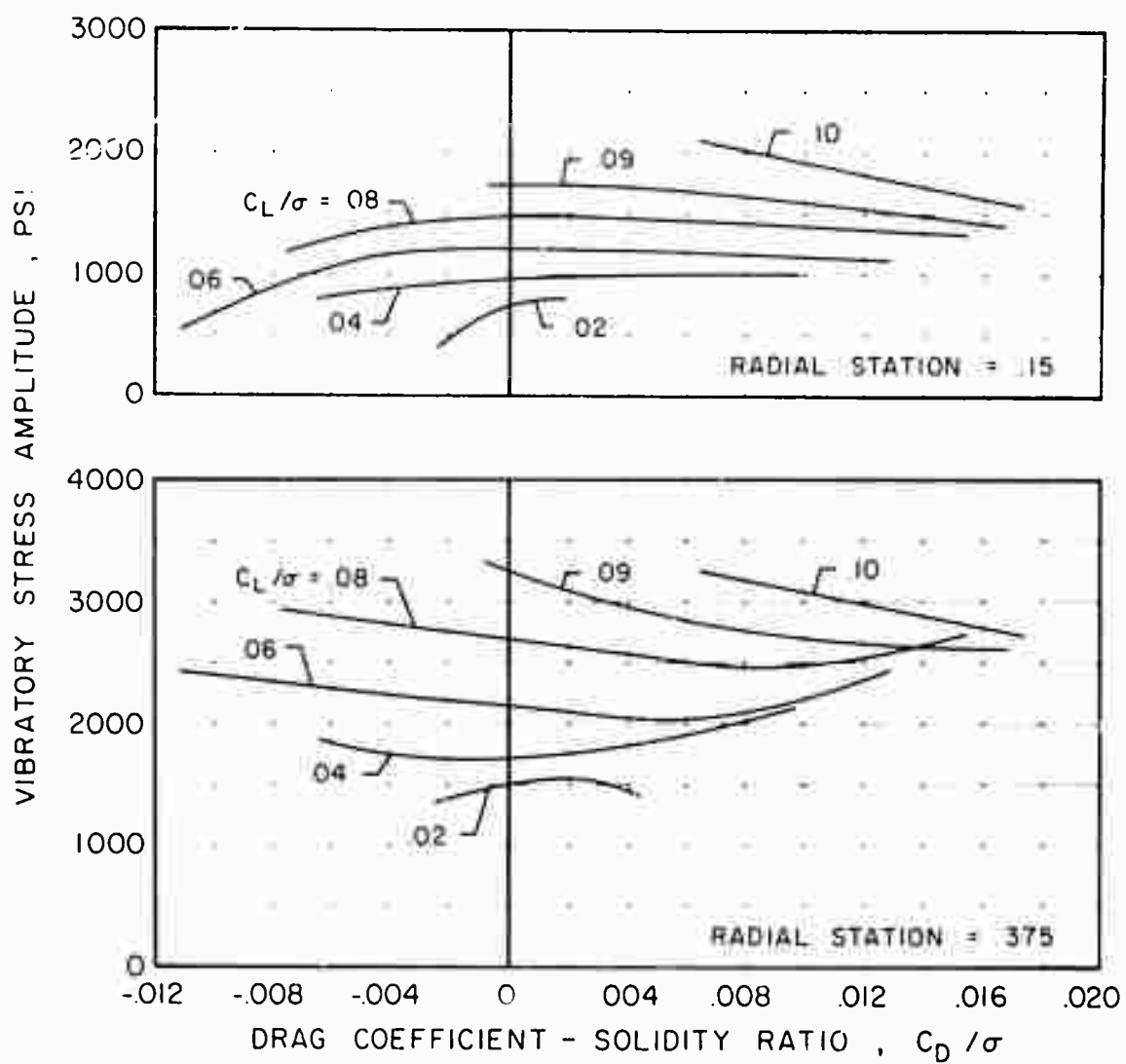(b) Chordwise

Figure 82. Continued

171

(b) Chordwise Concluded

Figure 82. Continued.

172
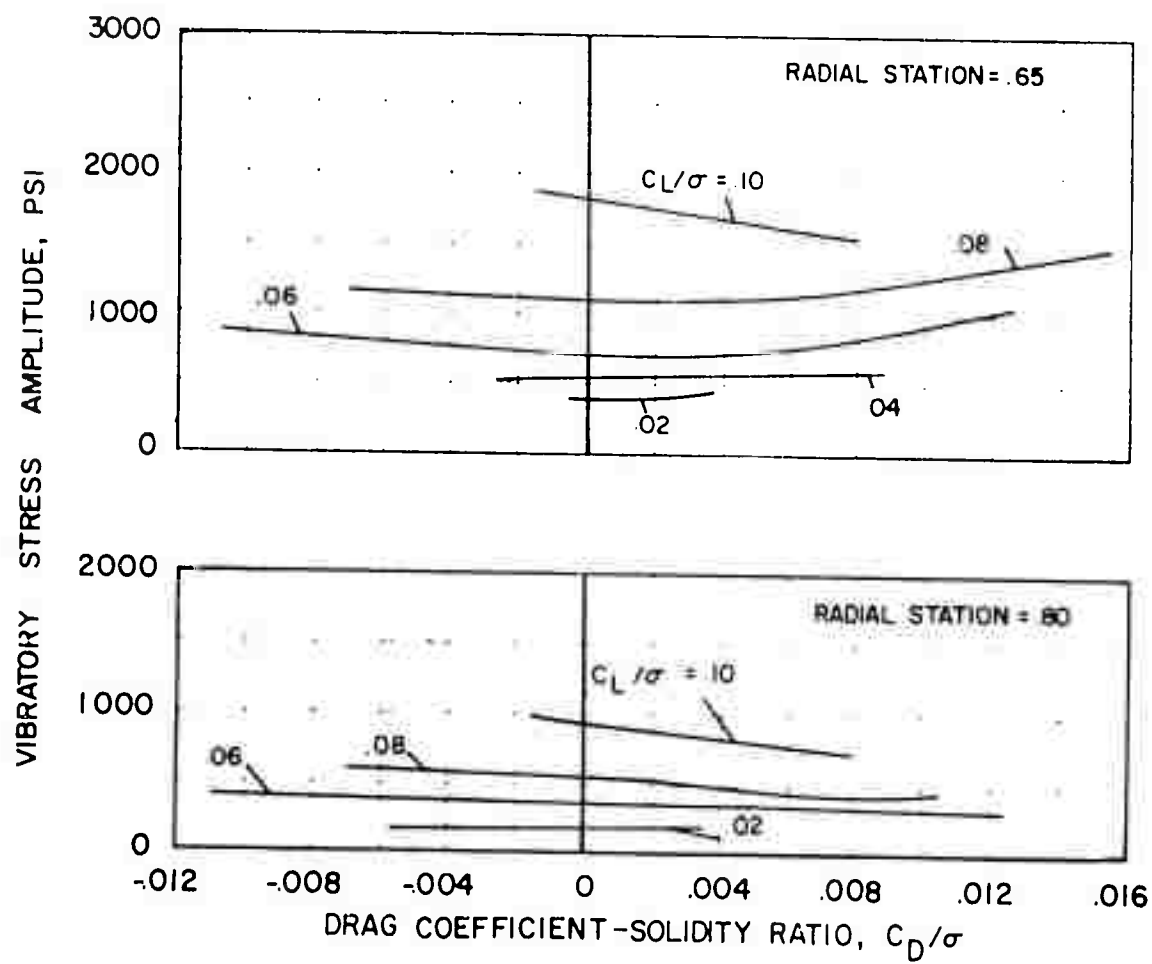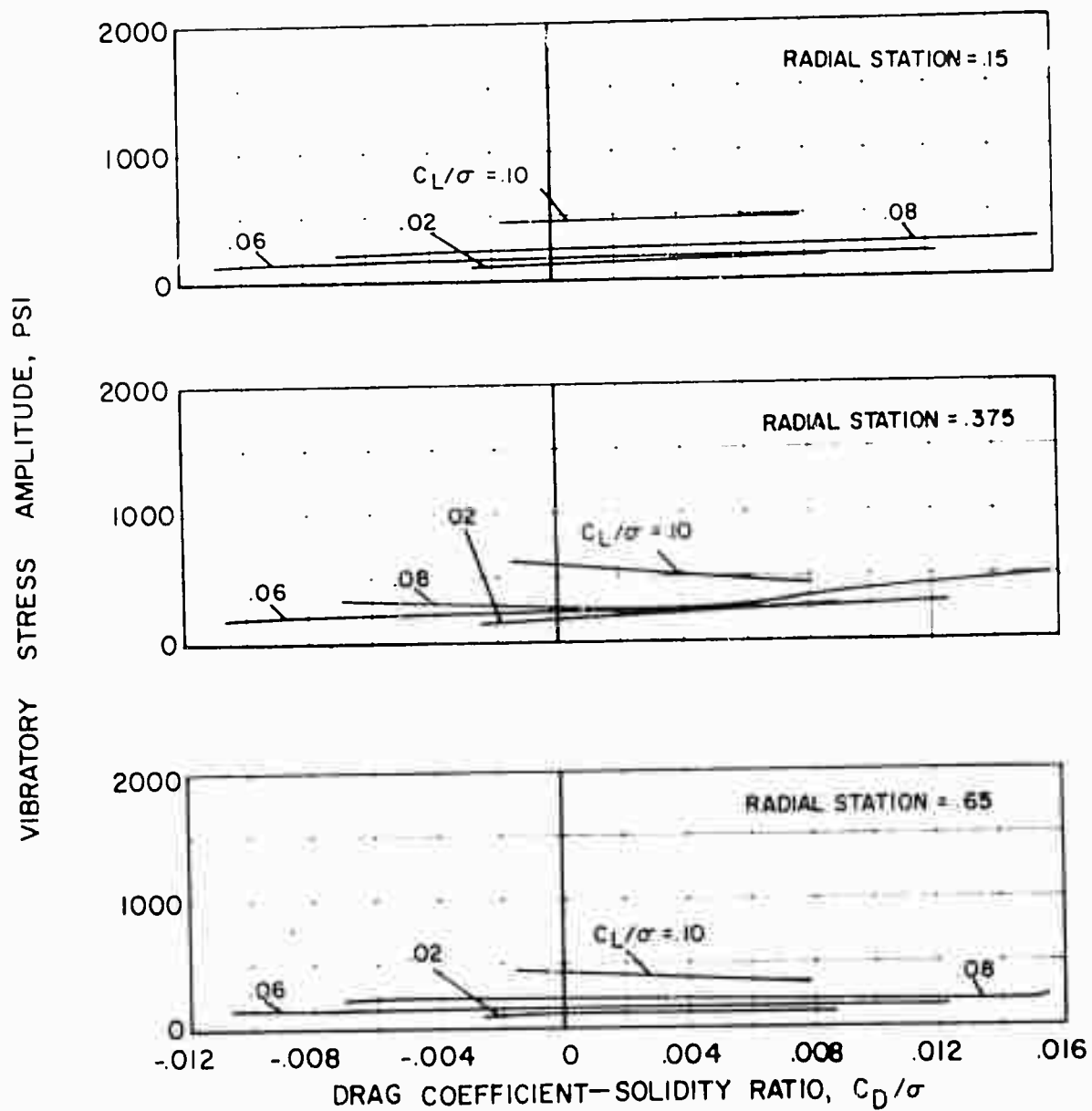
(c) Torsional

Figure 82. Concluded.
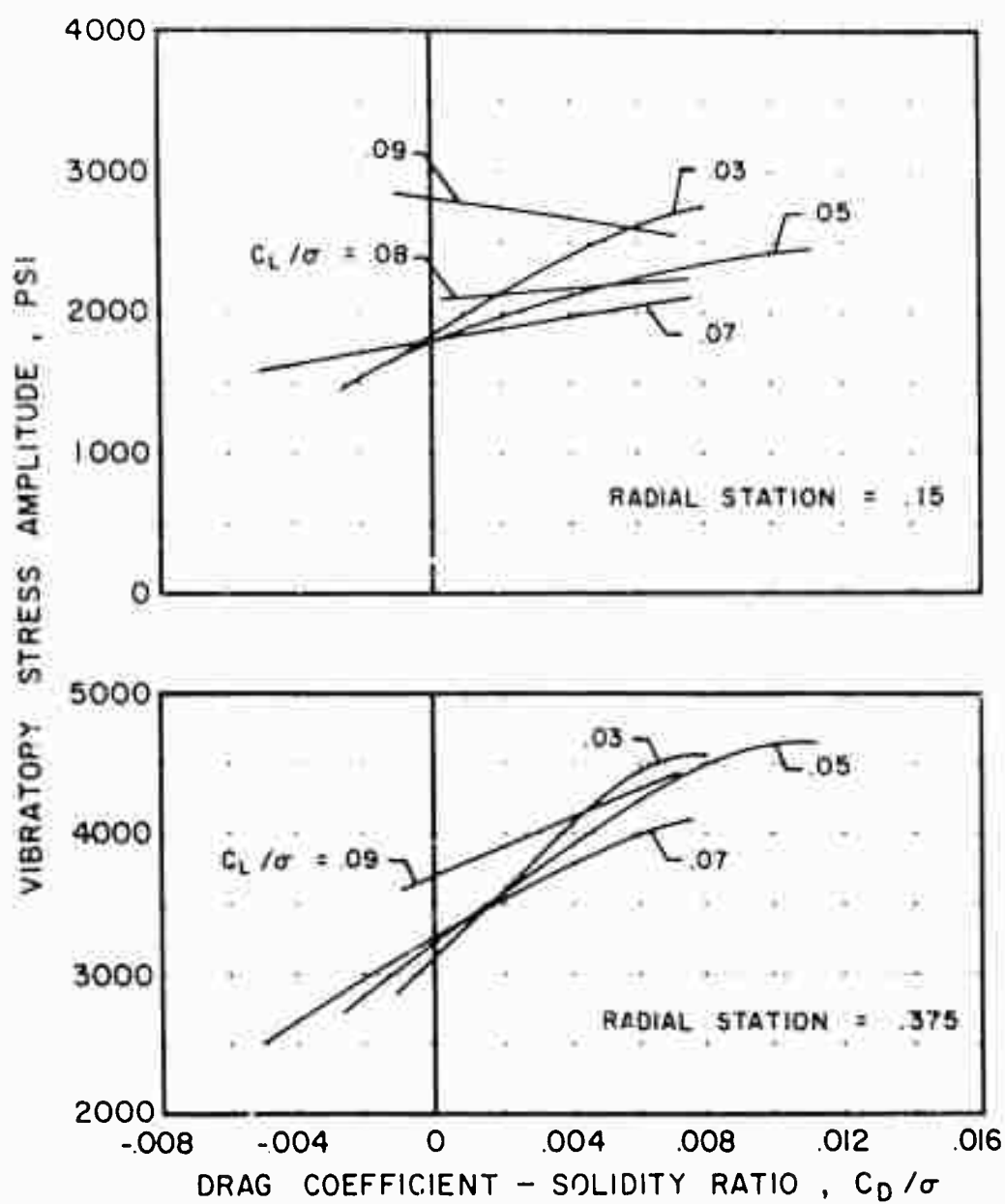
(a) Flapwise

Figure 83. The Effect of Drag on Flapwise, Chordwise and Torsional Vibratory Stress Amplitude at Constant Lift for Several Radial Stations, V = 163 Knots, μ = 0.40, θ_1 = -8°, M(1.0,90) = 0.82.

174
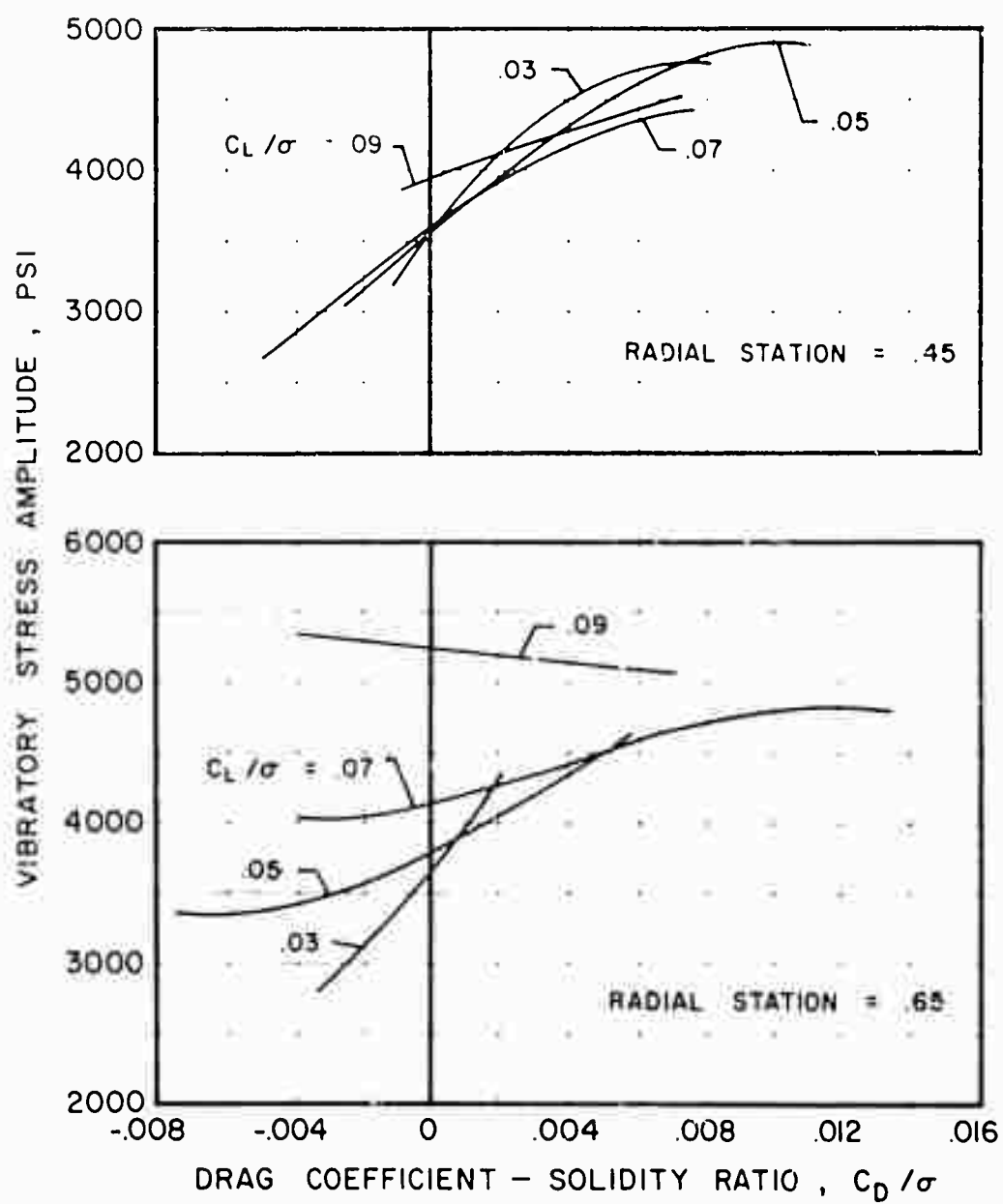
(a) Flapwise Continued

Figure 83. Continued.

175

(a) Flapwise Concluded

Figure 83. Continued.

176
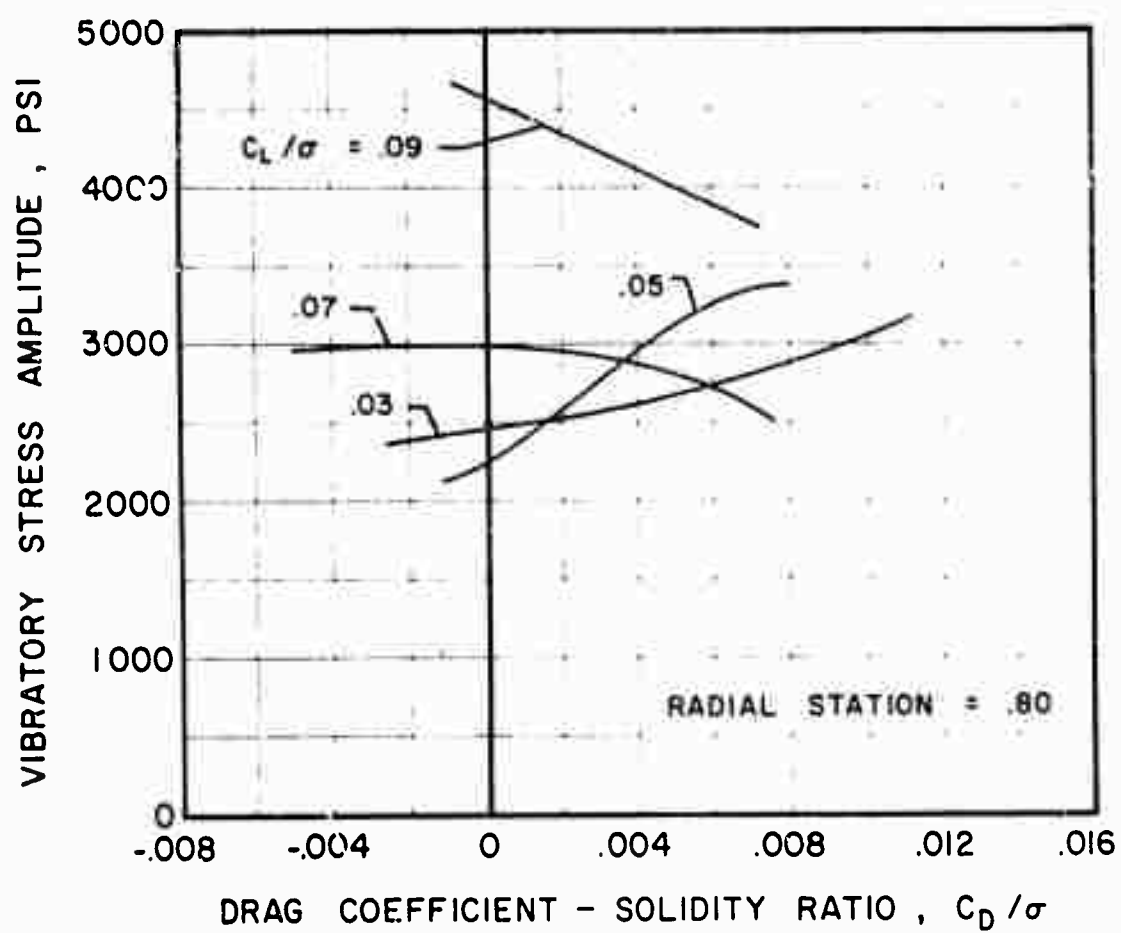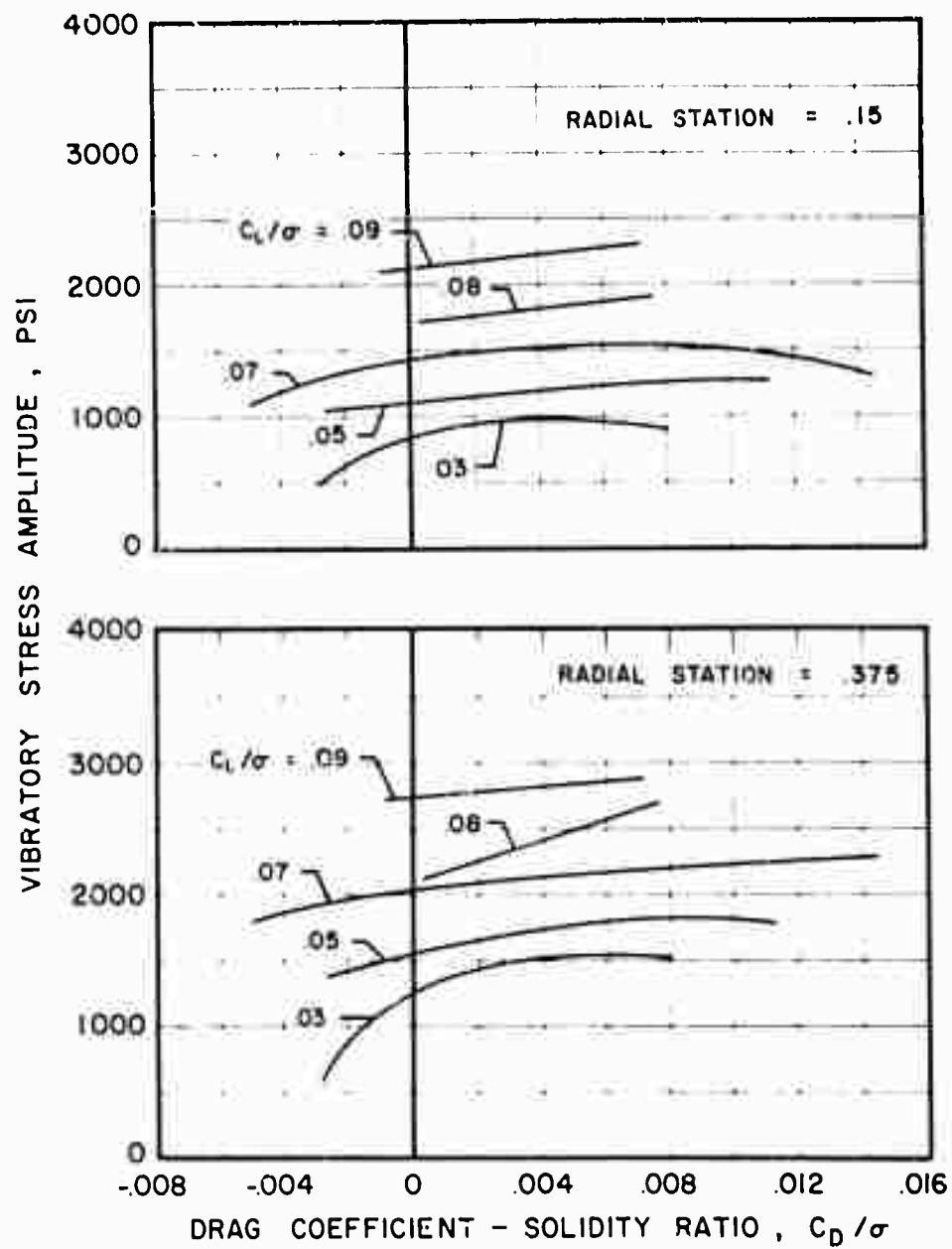
(b) Chordwise

Figure 83. Continued.

177

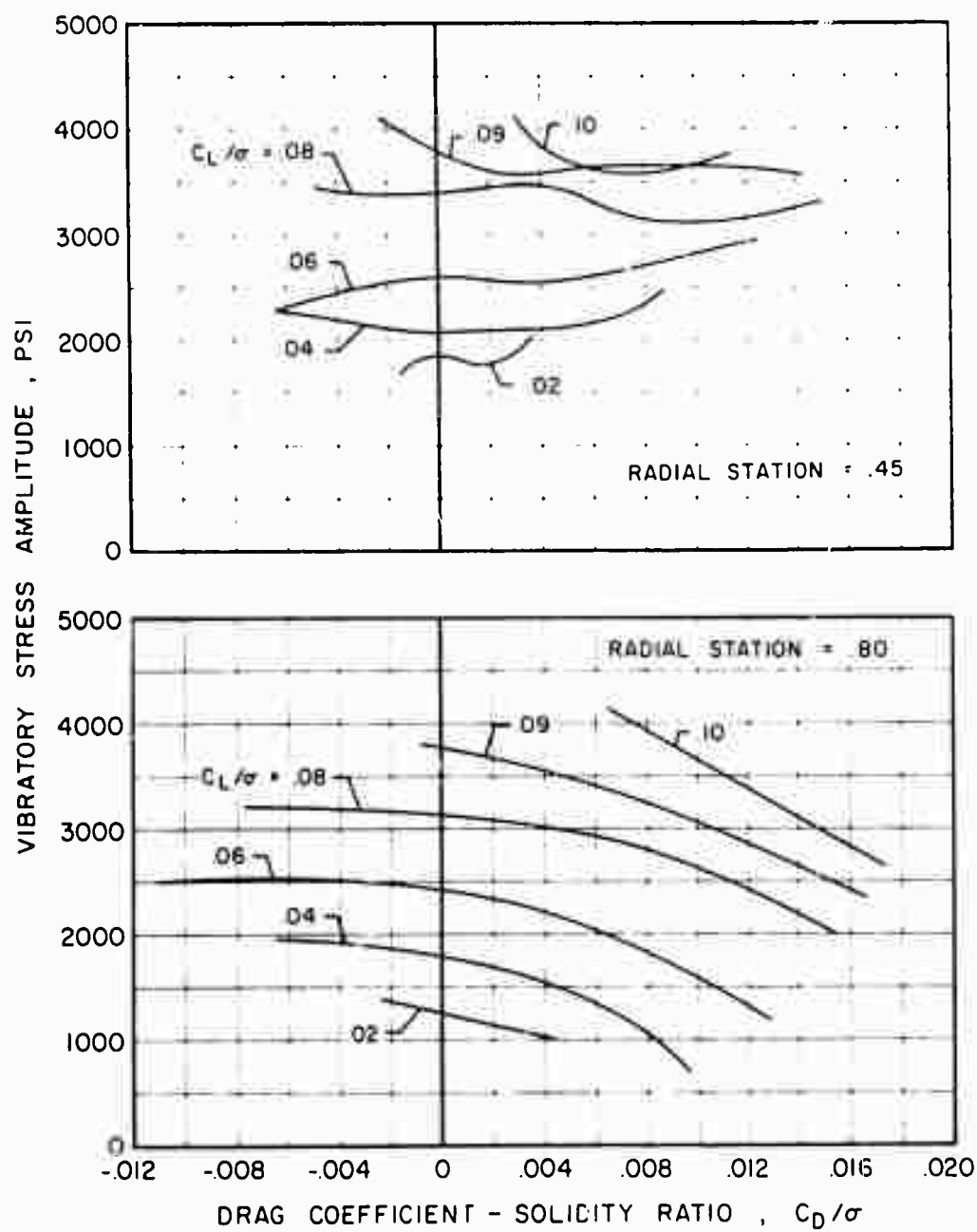(b) Chordwise Concluded

Figure 83. Continued.
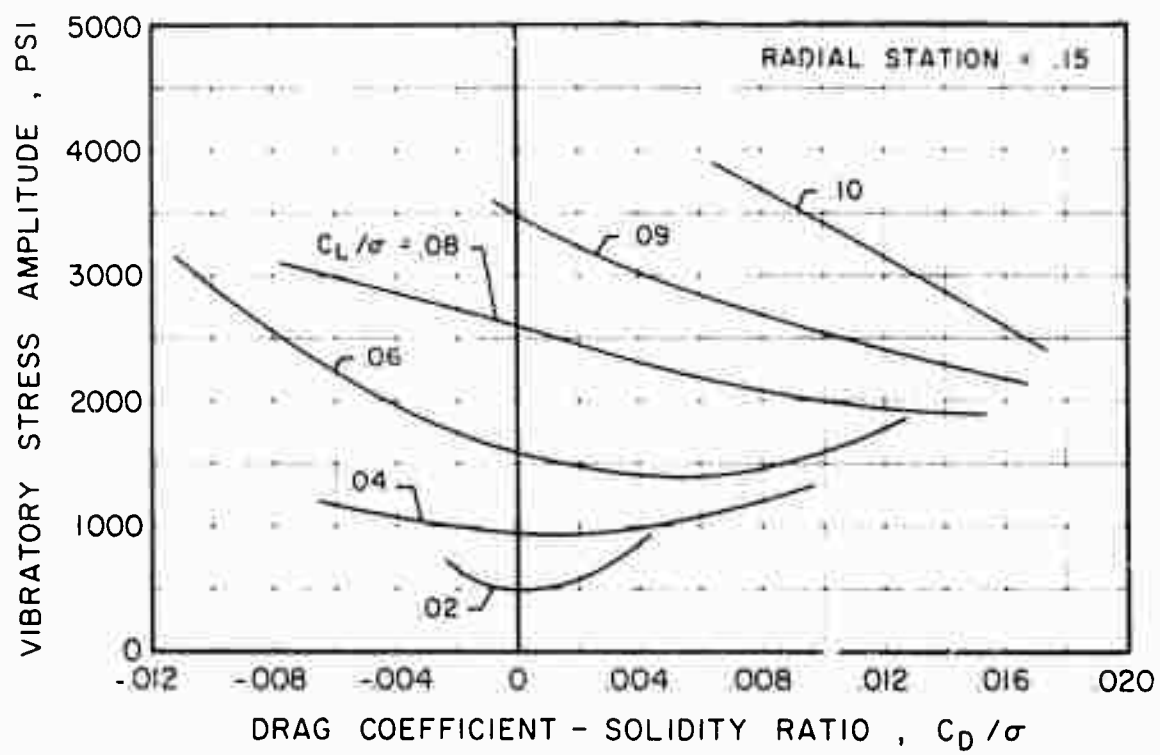
178
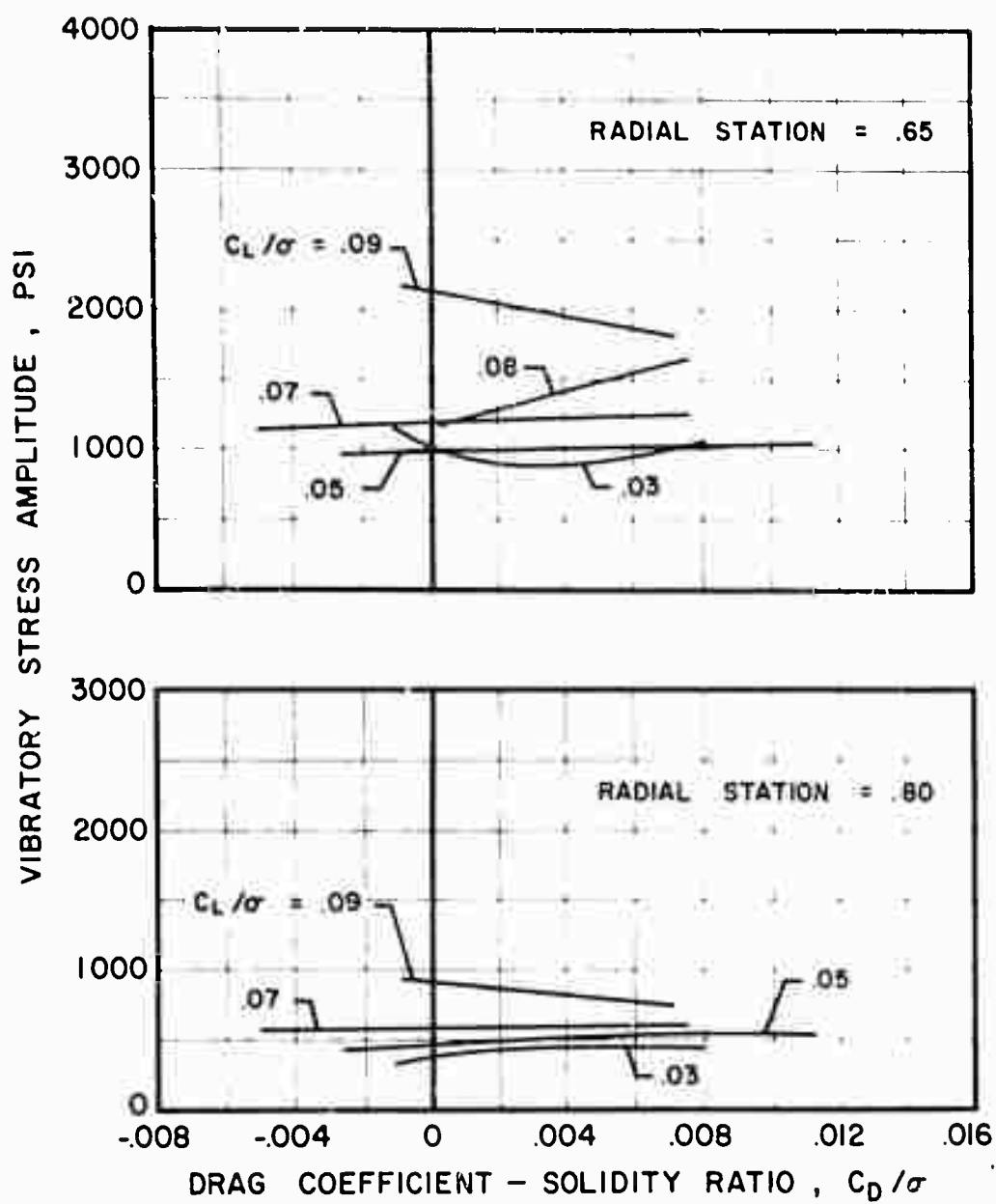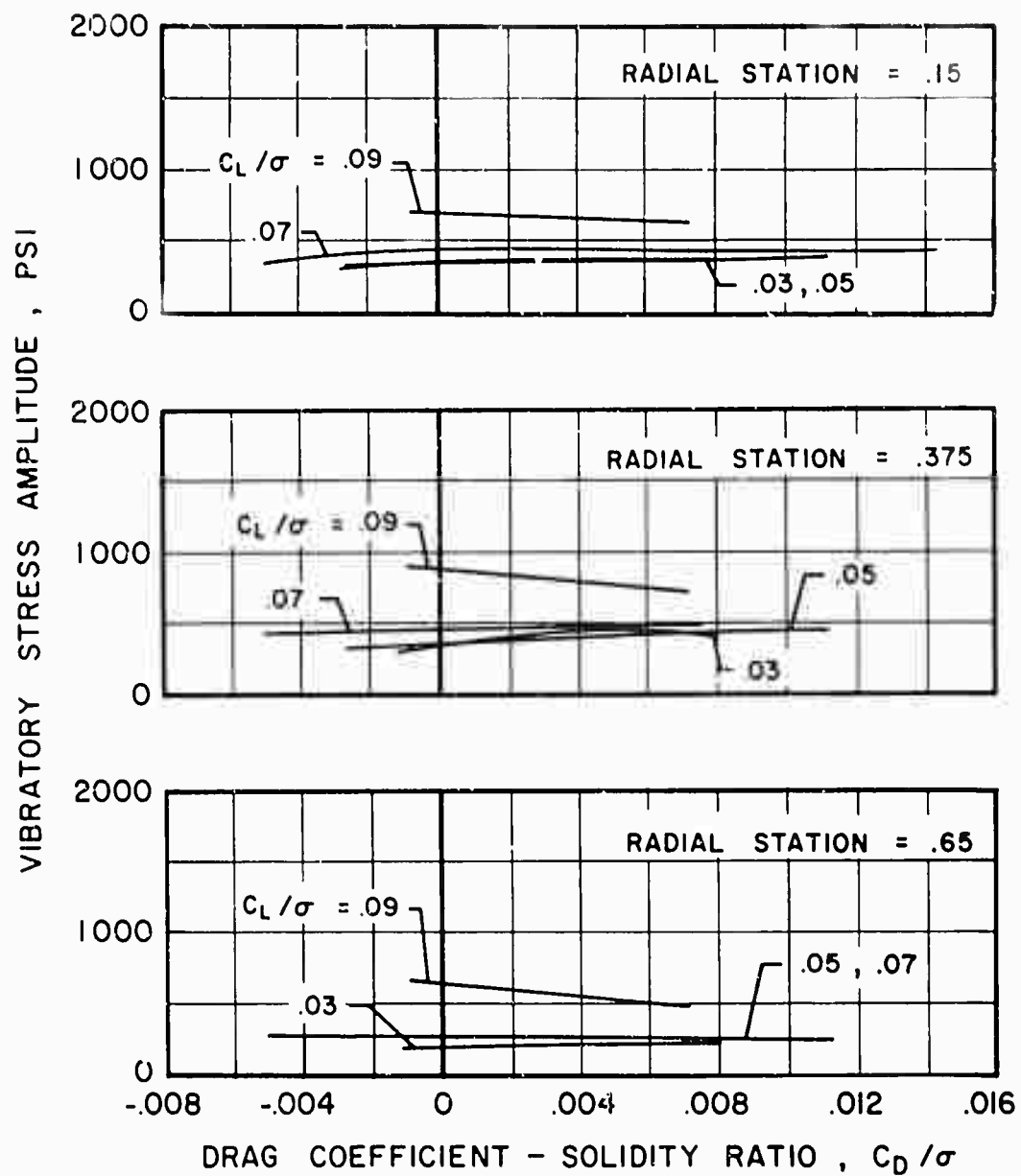
(c) Torsional

Figure 83.   Concluded.

179
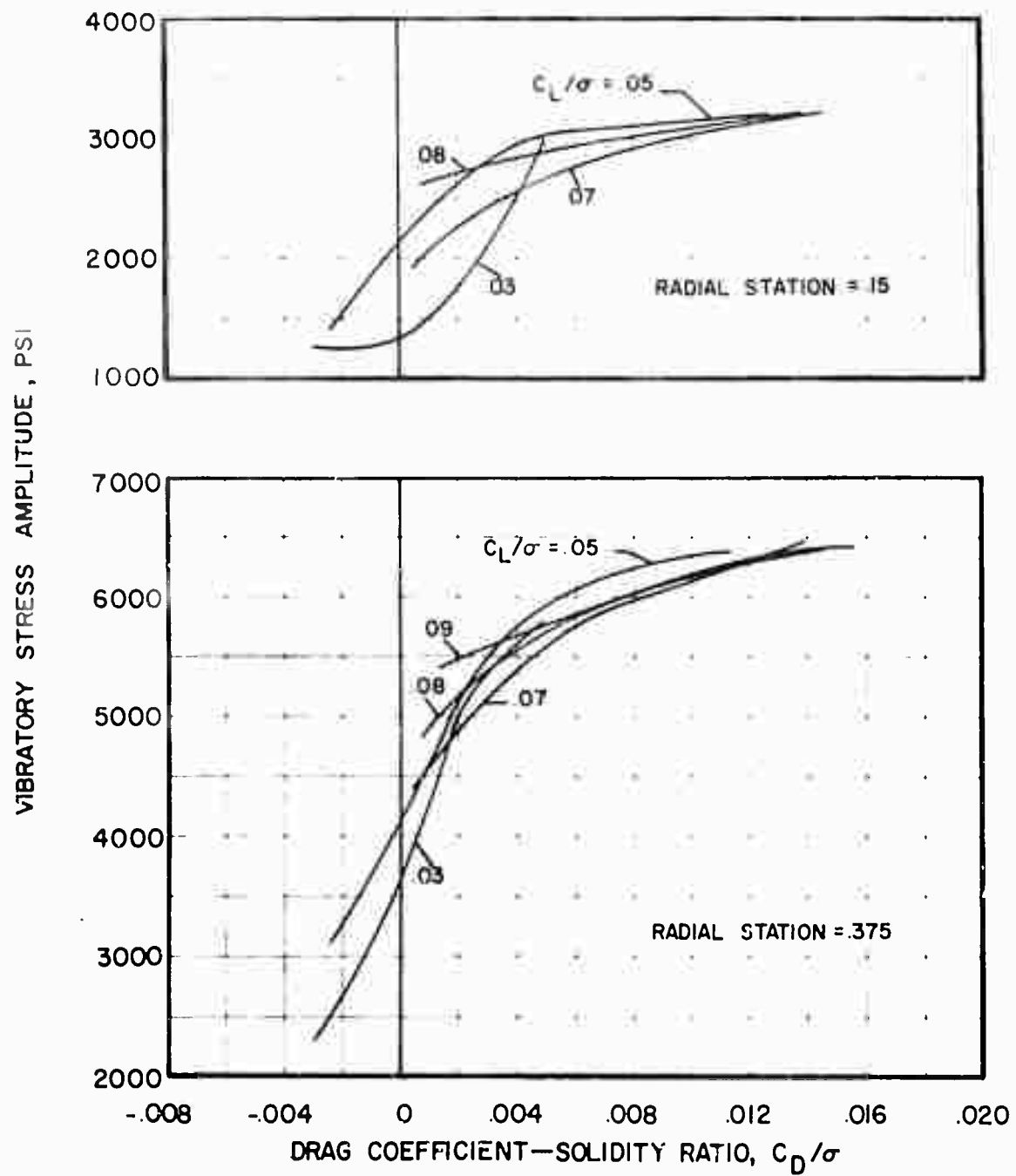
(a) Flapwise

Figure 84. The Effect of Drag on Flapwise, Chordwise and
Torsional Vibratory Stress Amplitude at Constant
Lift for Several Radial Stations, V = 177 Knots,
μ = 0.46, θ_1 = -8°, $M_{(1.0, 90)}$ = 0.82.

180
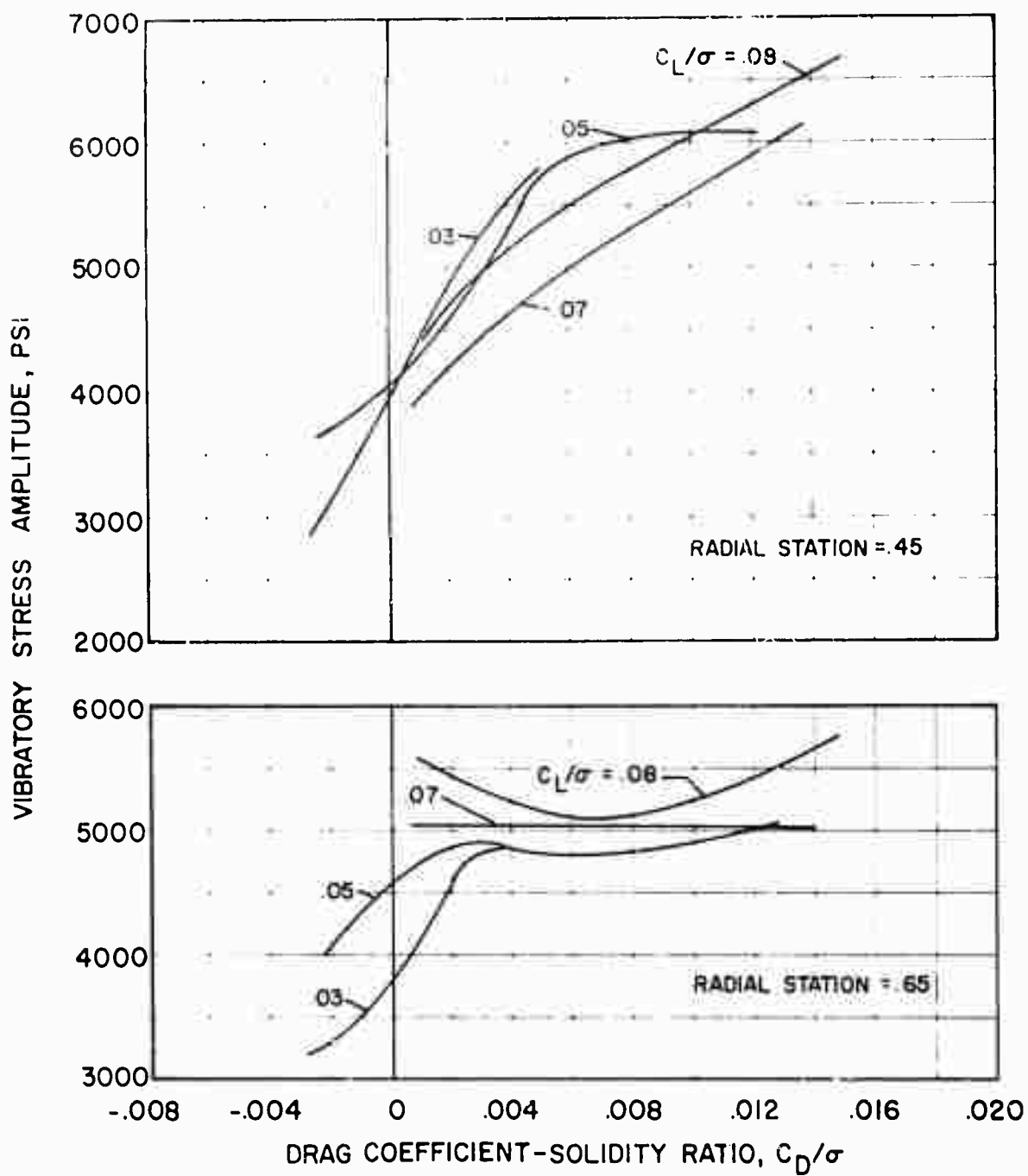
(a) Flapwise Continued

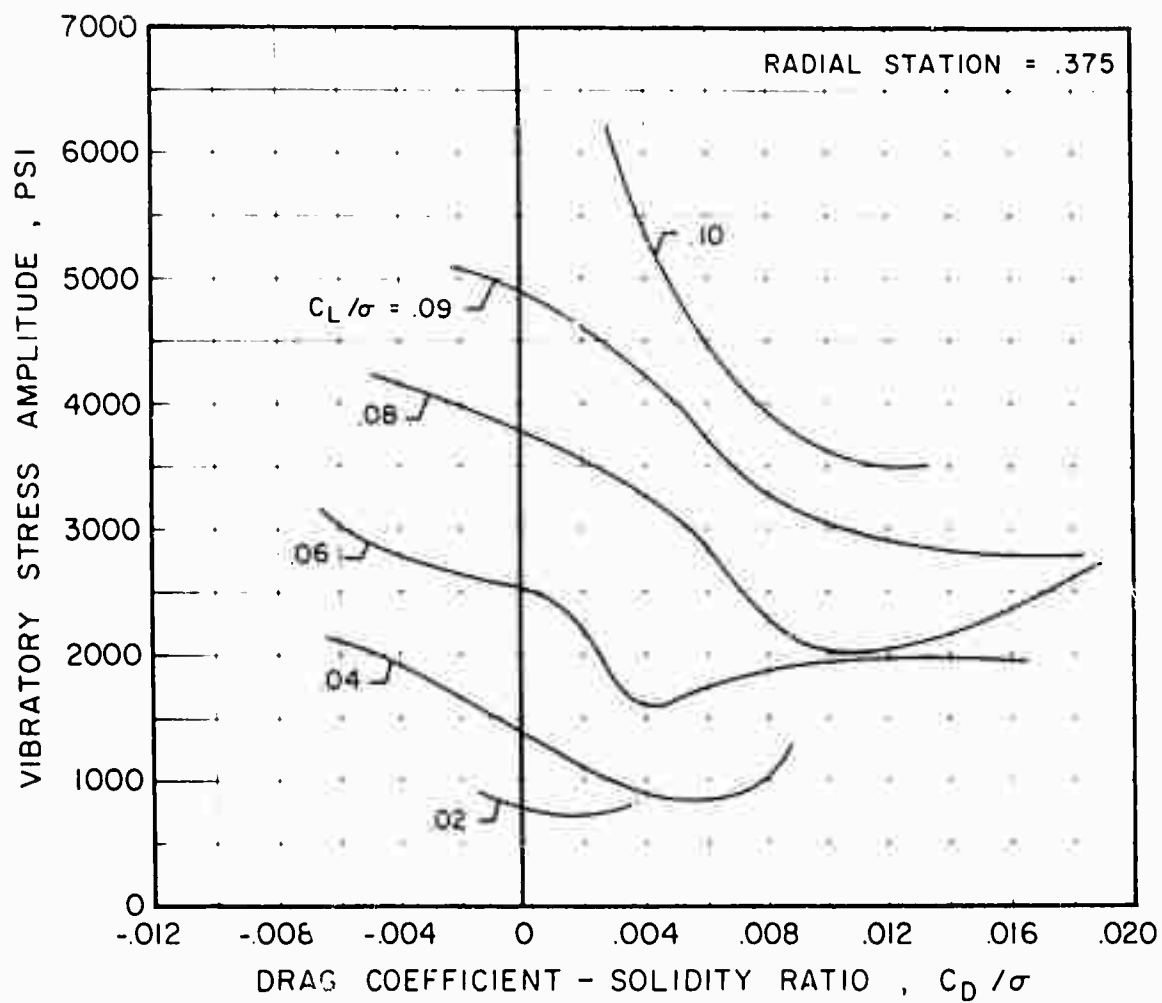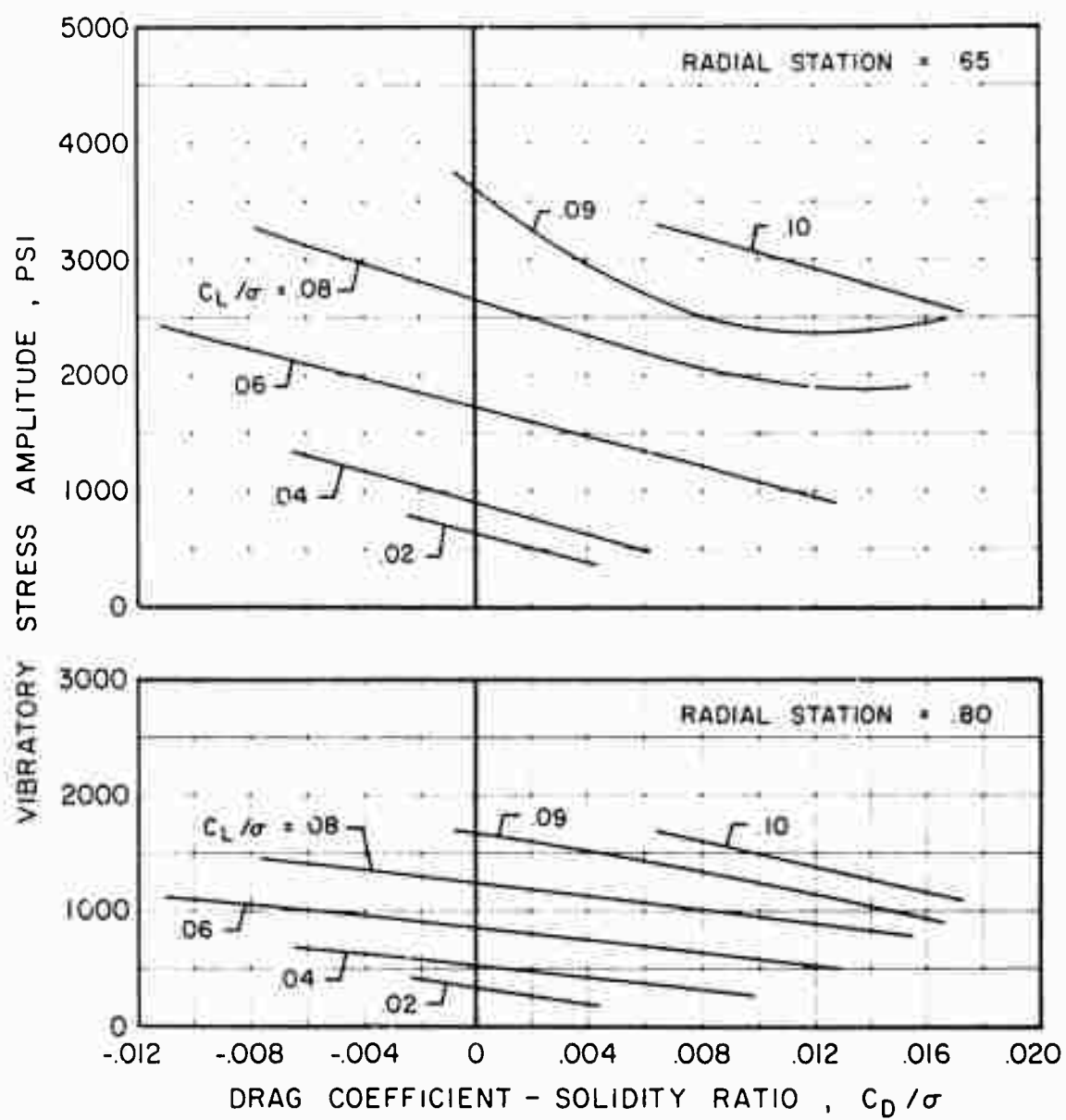Figure 84. Continued.

181

(a) Flapwise Concluded

Figure 84. Continued.

182
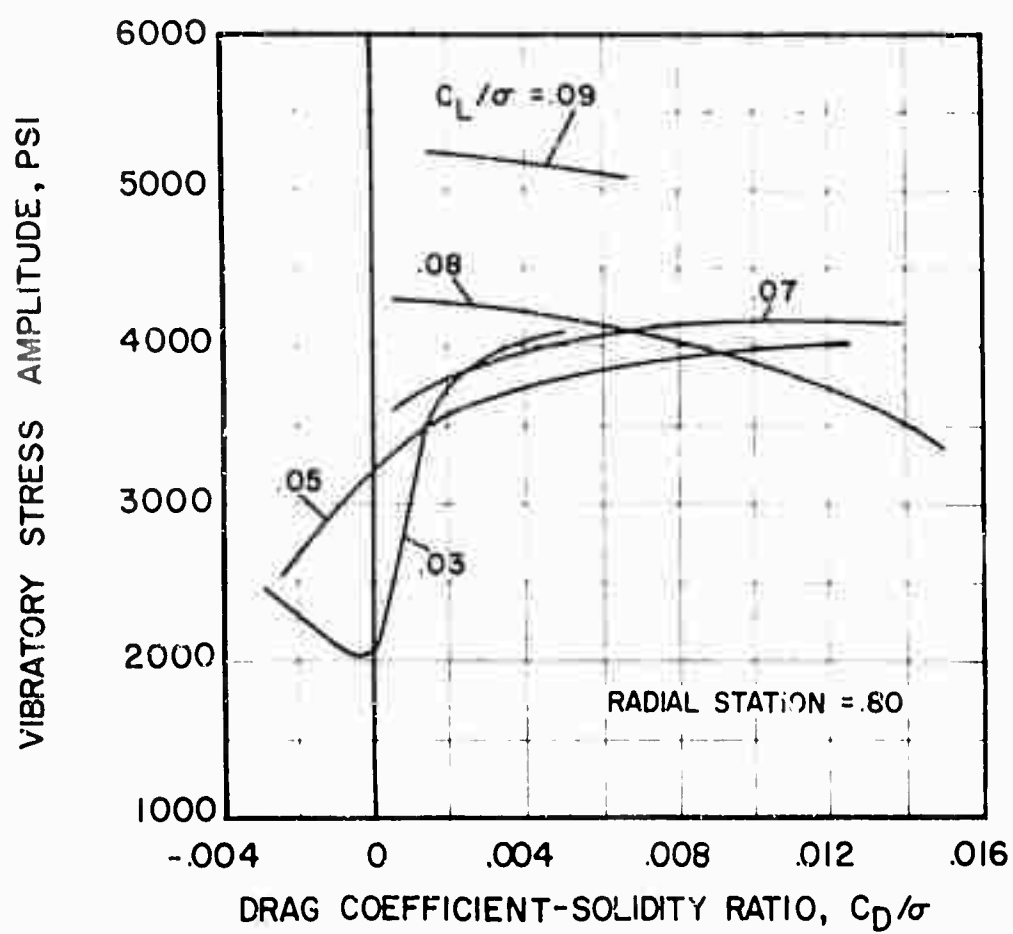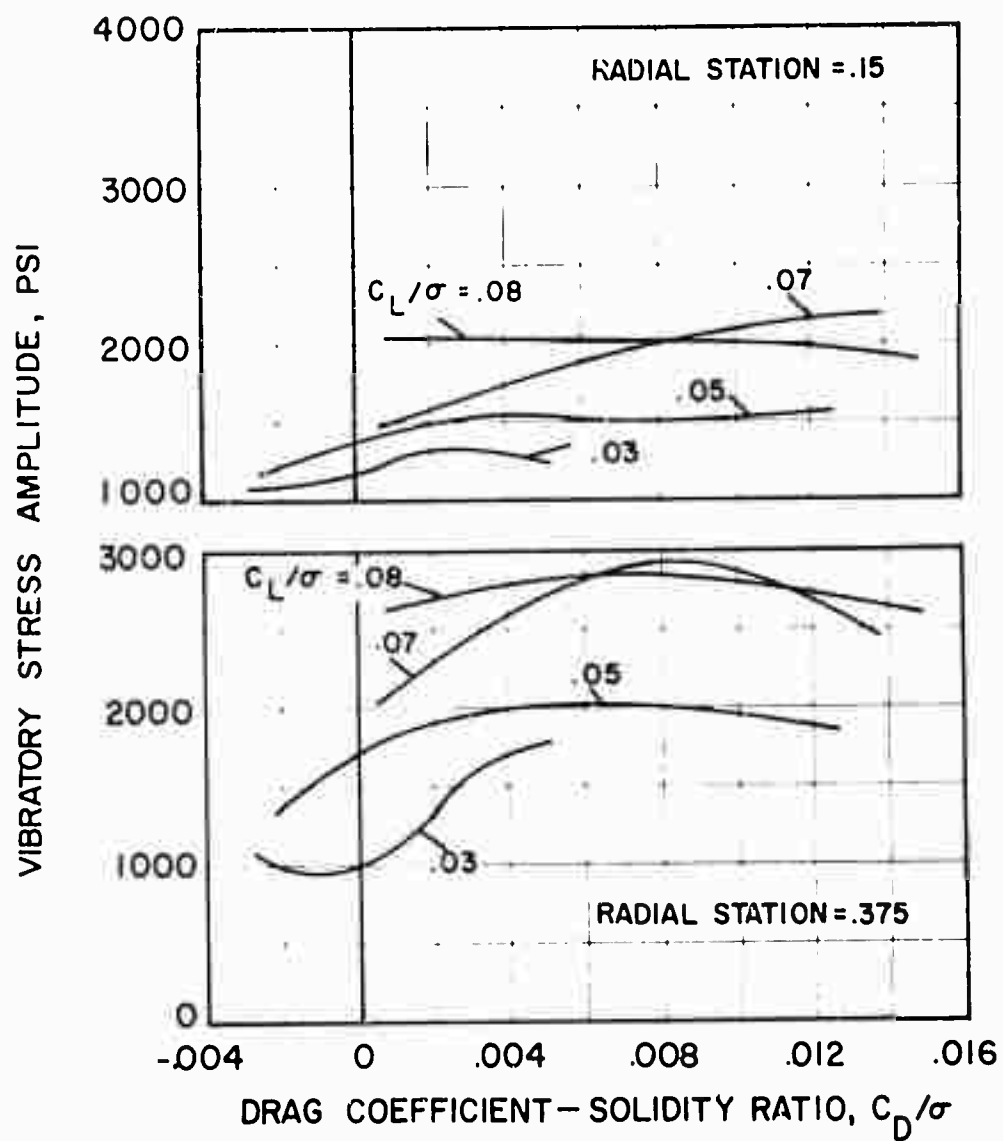
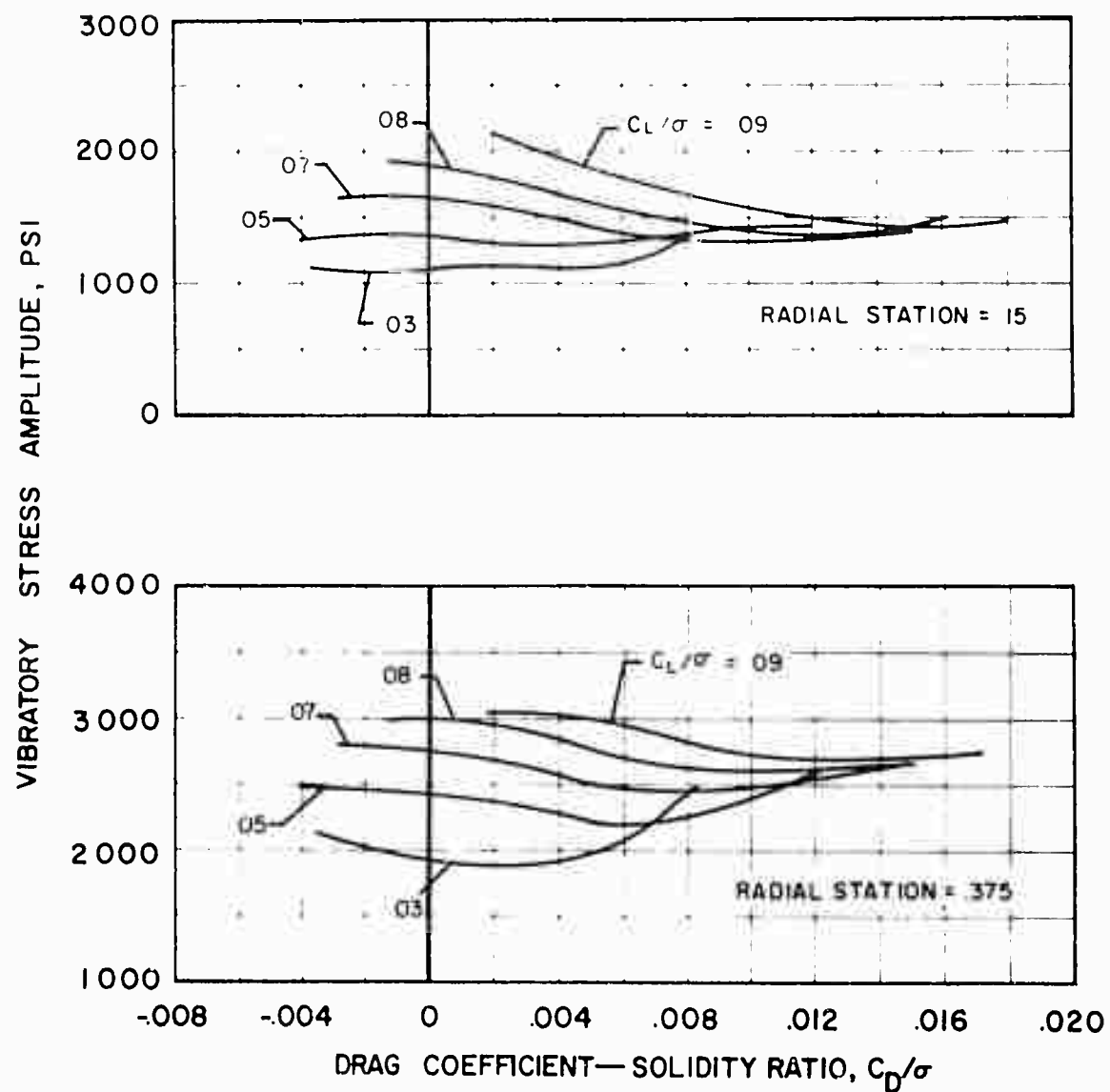(b) Chordwise

Figure 84. Continued.

183

(b) Chordwise Concluded

Figure 84. Continued.

184
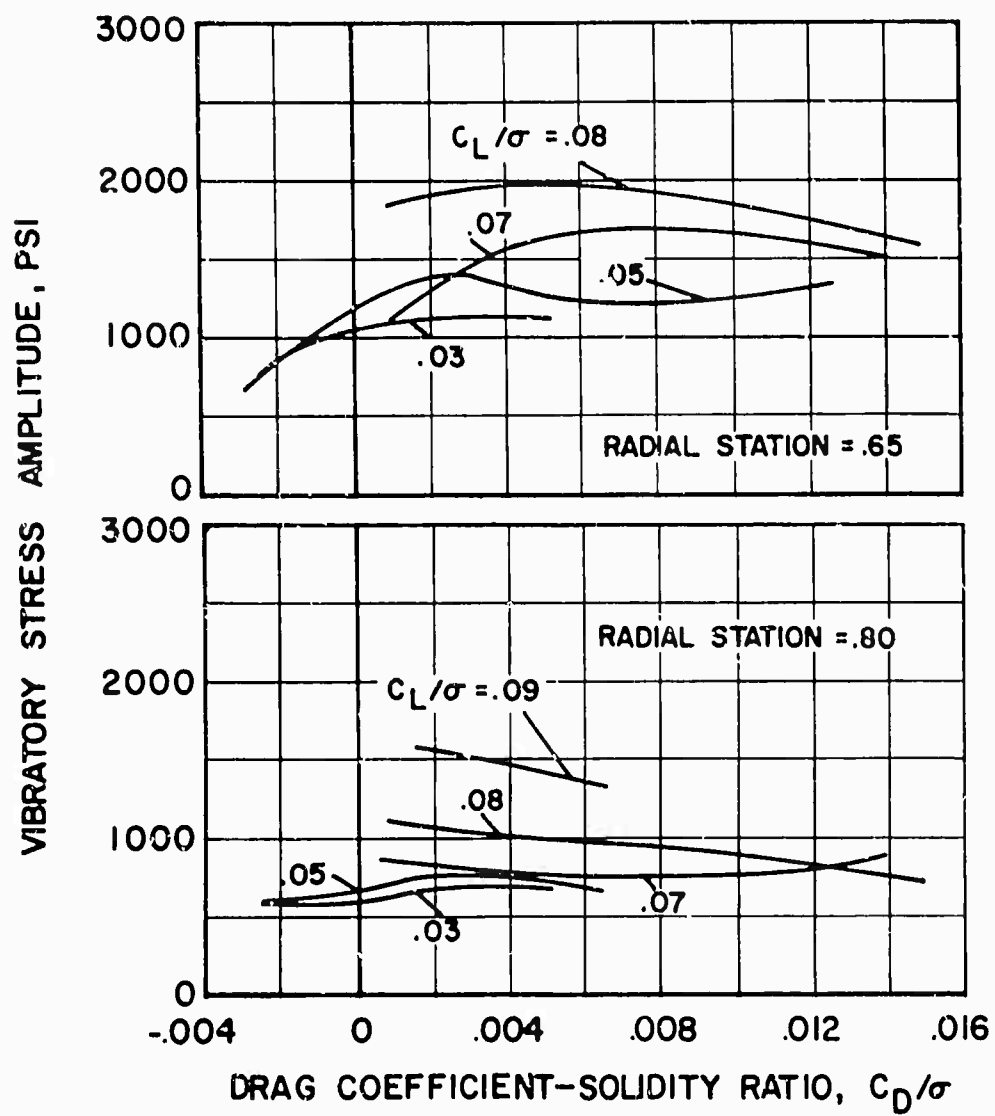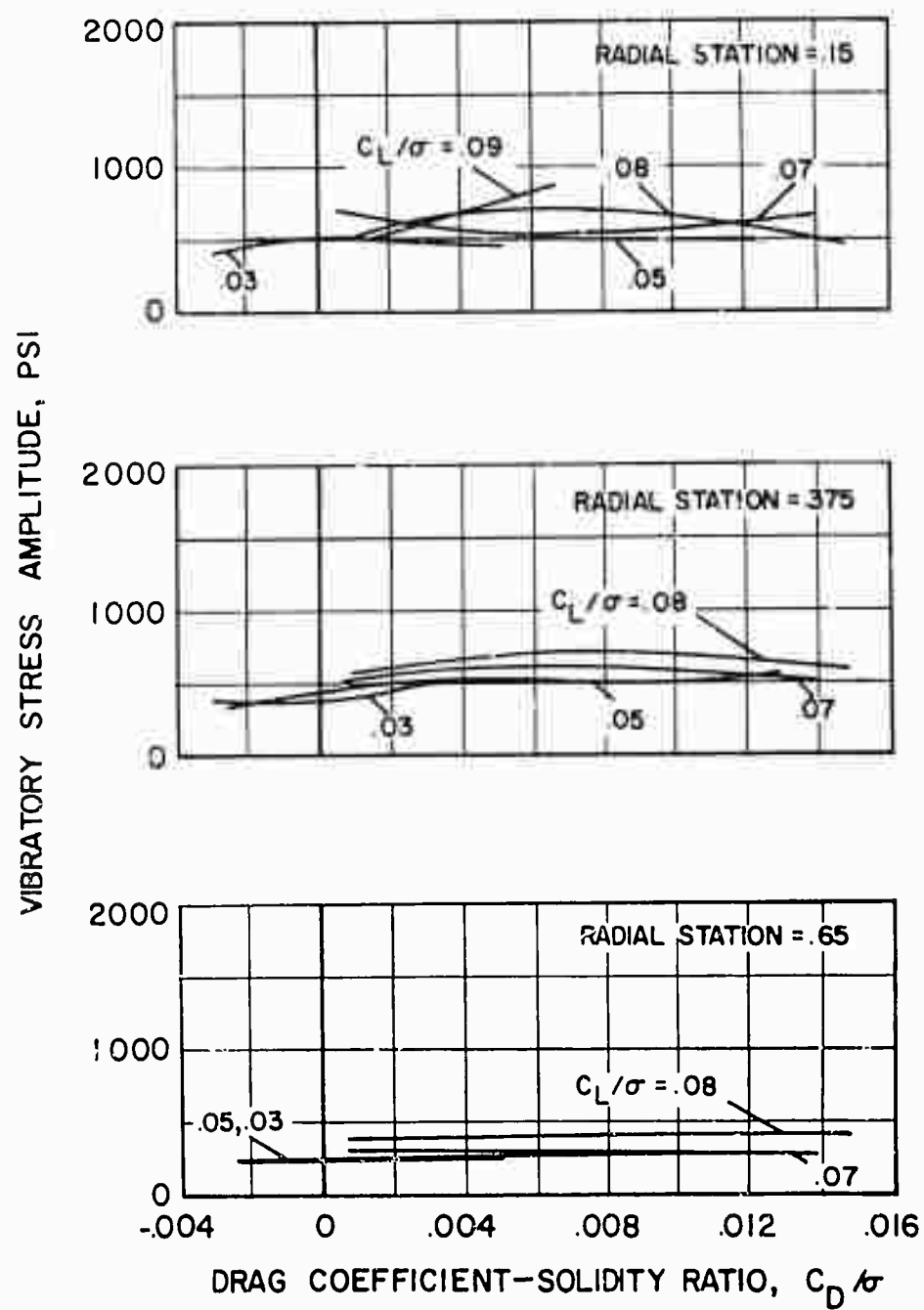
(c) Torsional

Figure 84 Concluded.
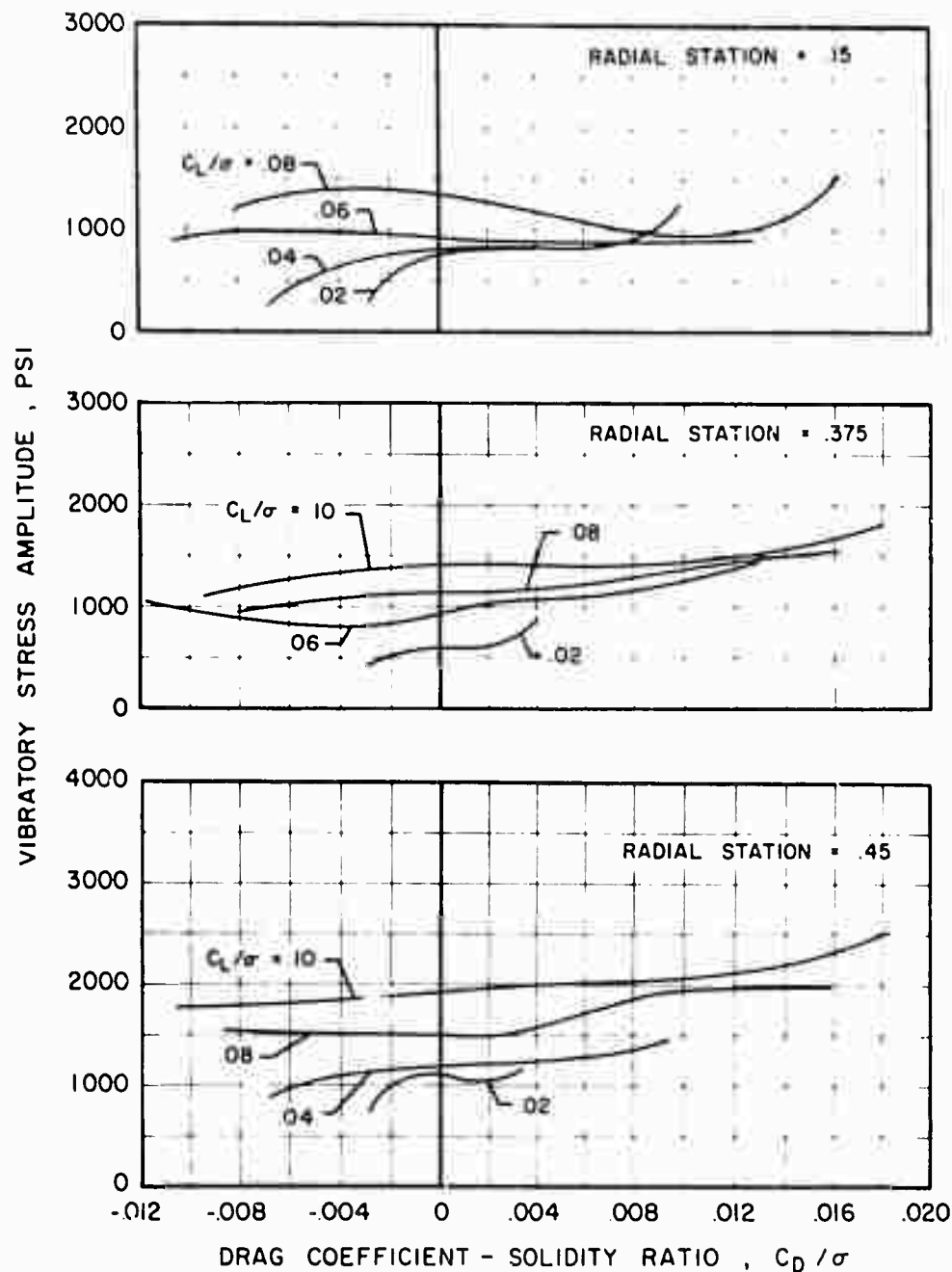
(a) Flapwise

Figure 85. The Effect of Drag on Flapwise, Chordwise and Torsional Vibratory Stress Amplitude at Constant Lift for Several Radial Stations, V = 116 Knots, μ = 0.30, θ_1 = 0°, $M_{(1.0, 90)}$ = 0.74.

186

(a) Flapwise Concluded

Figure 85. Continued.

187
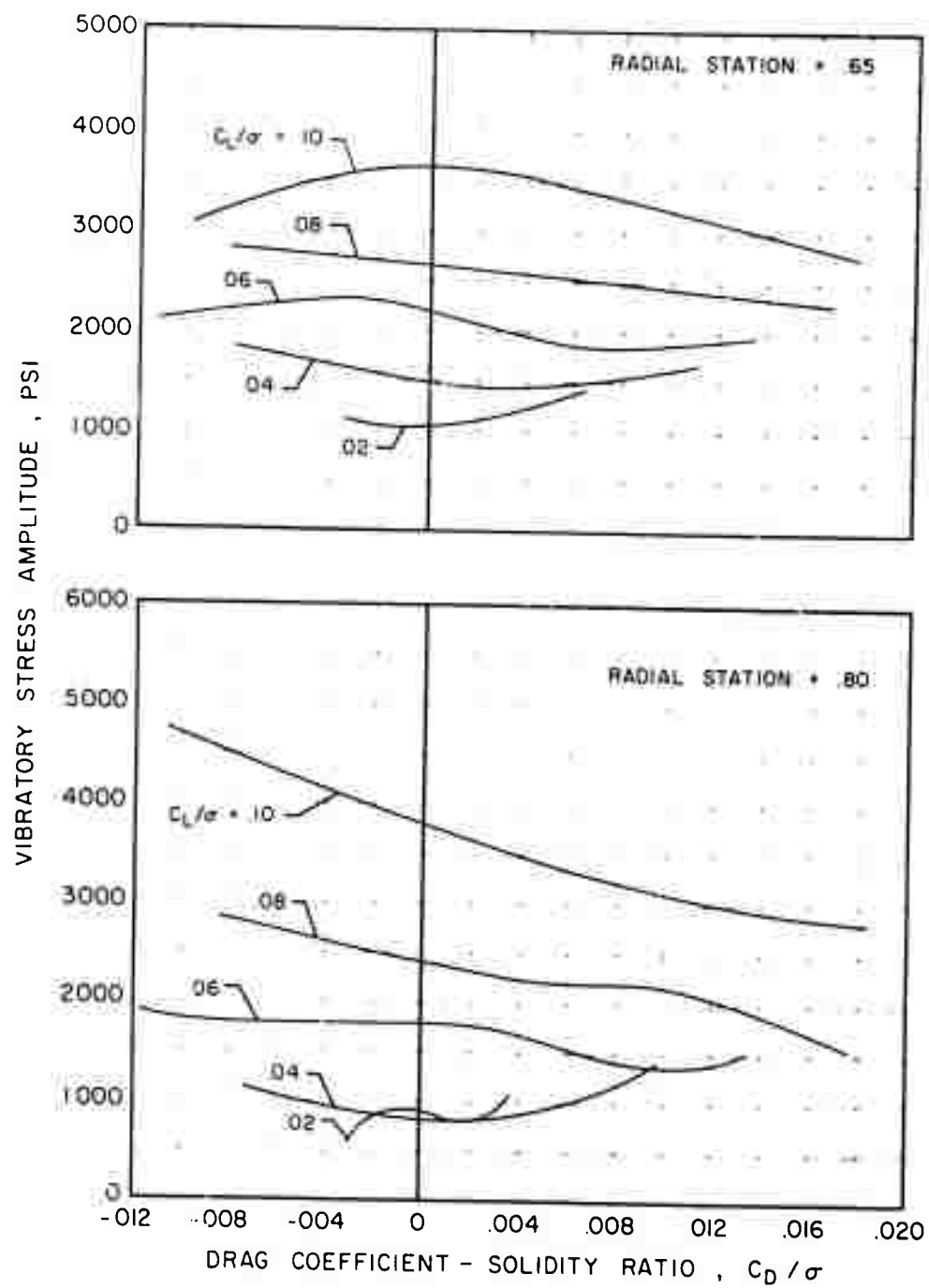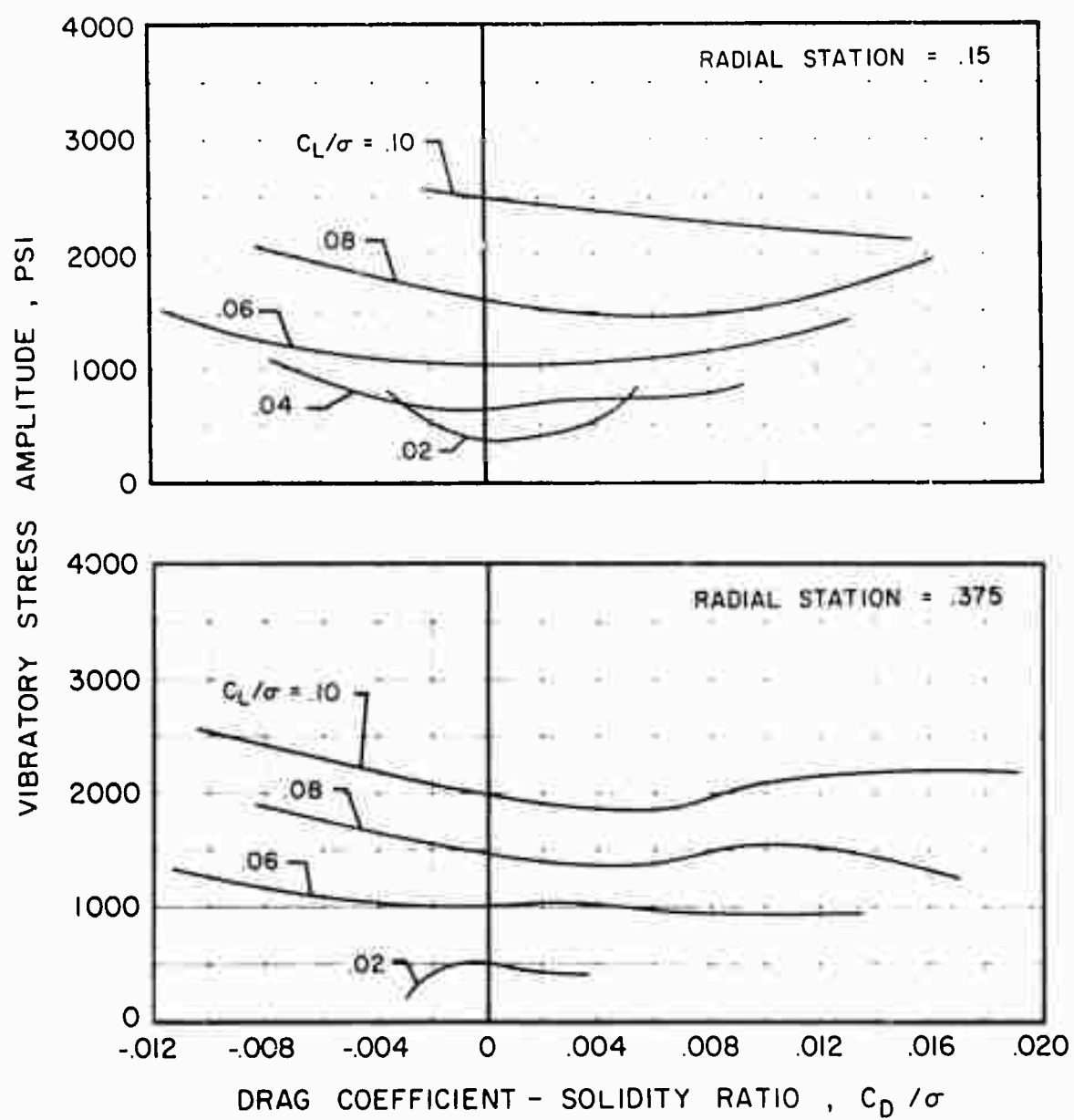
(b) Chordwise

Figure 85. Continued.

188

(b) Chordwise Concluded

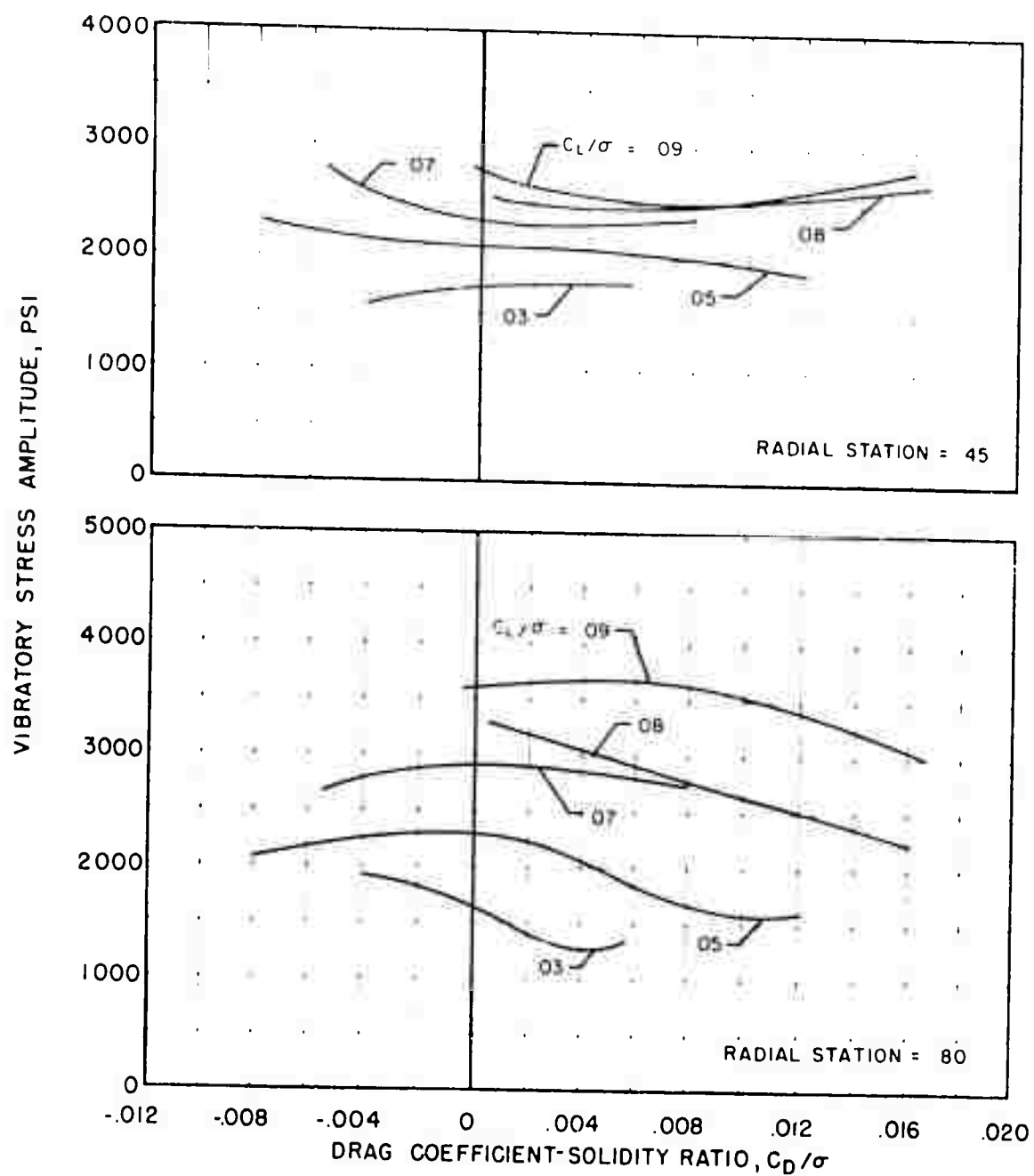Figure 85. Continued.

189
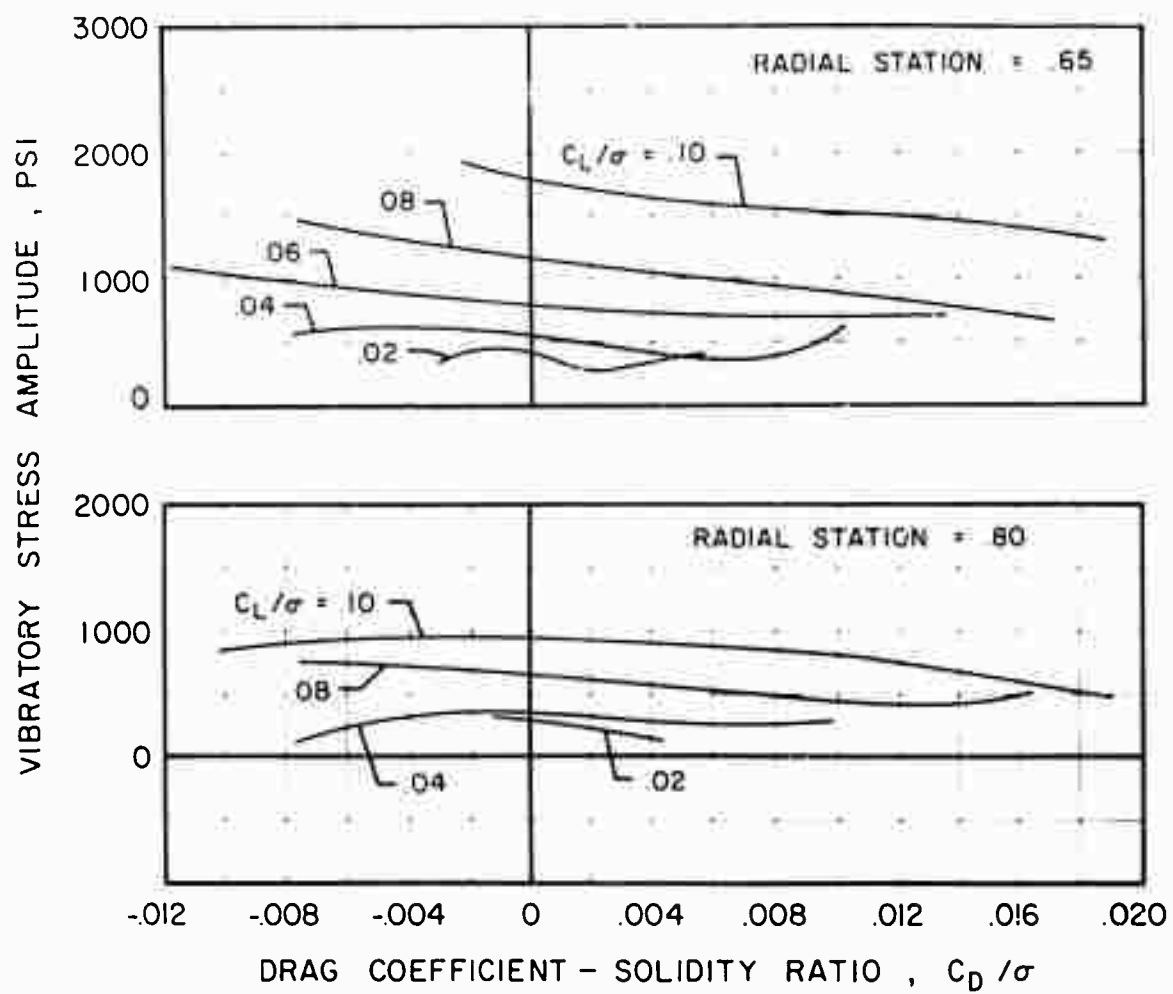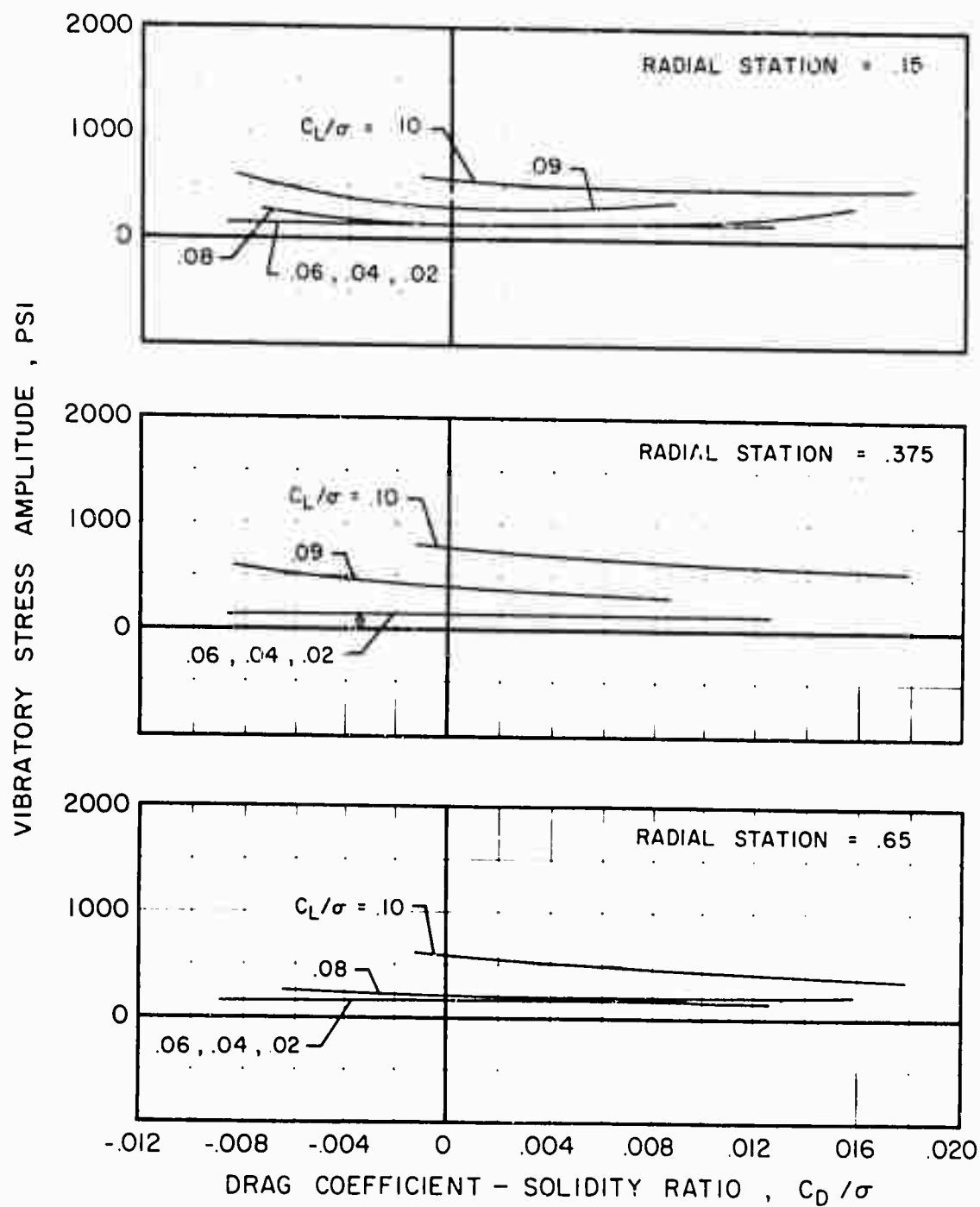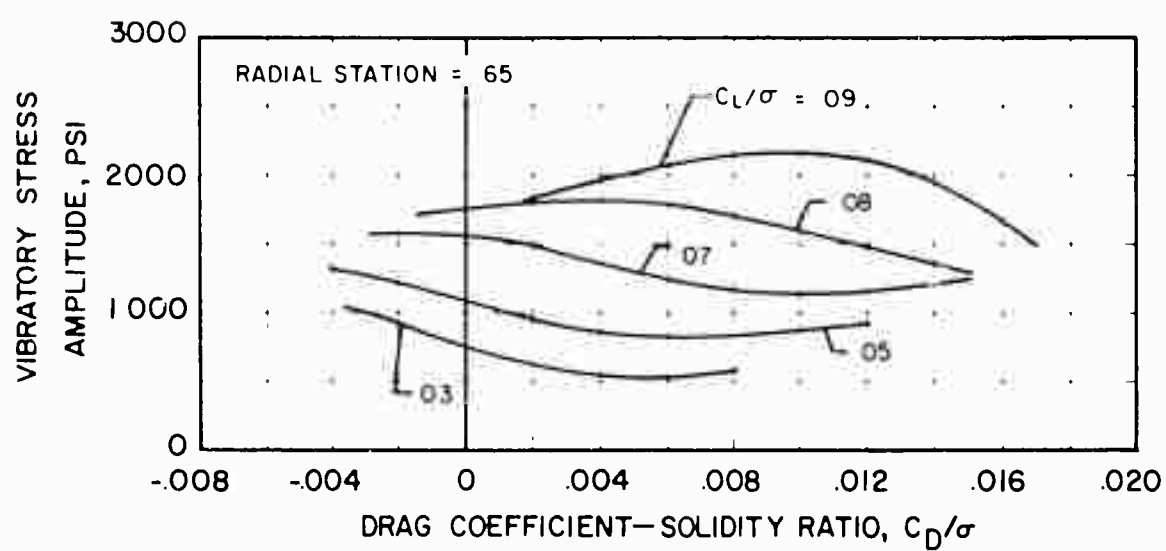
(c) Torsional

Figure 85. Concluded.

190
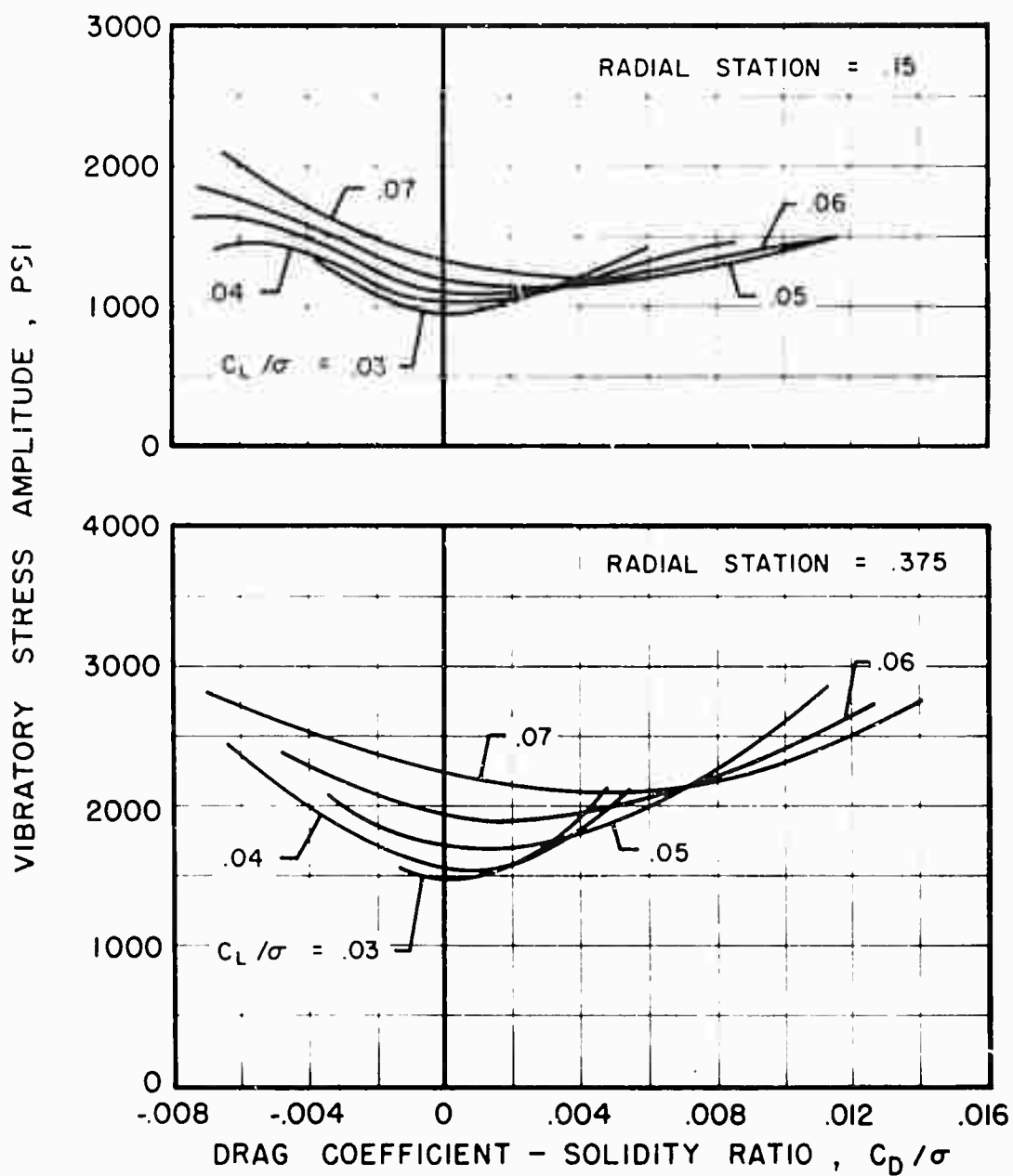
(a) Flapwise

Figure 86.   The Effect of Drag on Flapwise, Chordwise and
Torsional Vibratory Stress Amplitude at Constant
Lift for Several Radial Stations, V = 162 Knots,
μ = 0.40, θ_1 = 0°, M(1.0, 90) = 0.83.

191
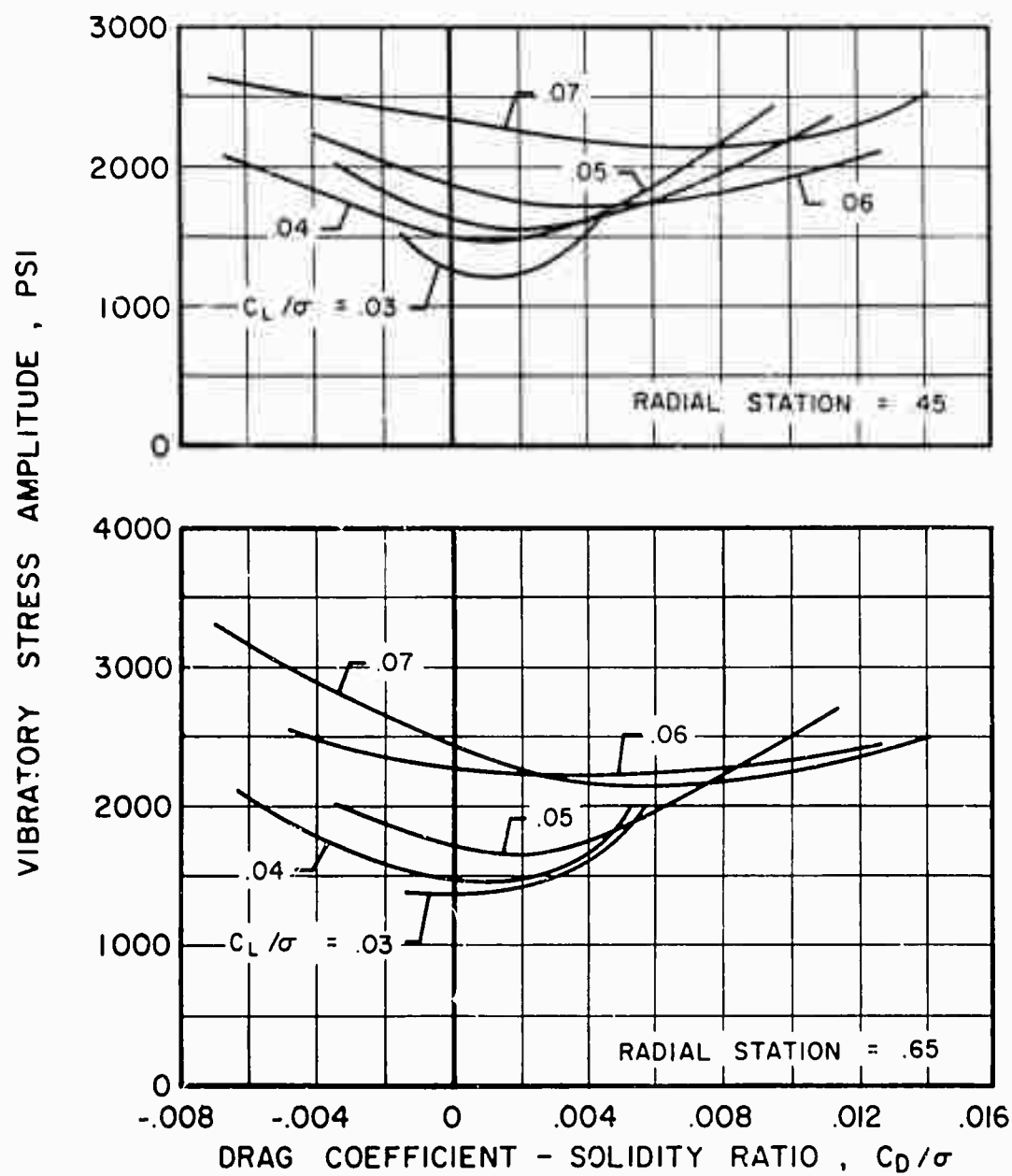
(a) Flapwise Continued

Figure 86. Continued.

192

(a) Flapwise Concluded

Figure 86. Continued.

193
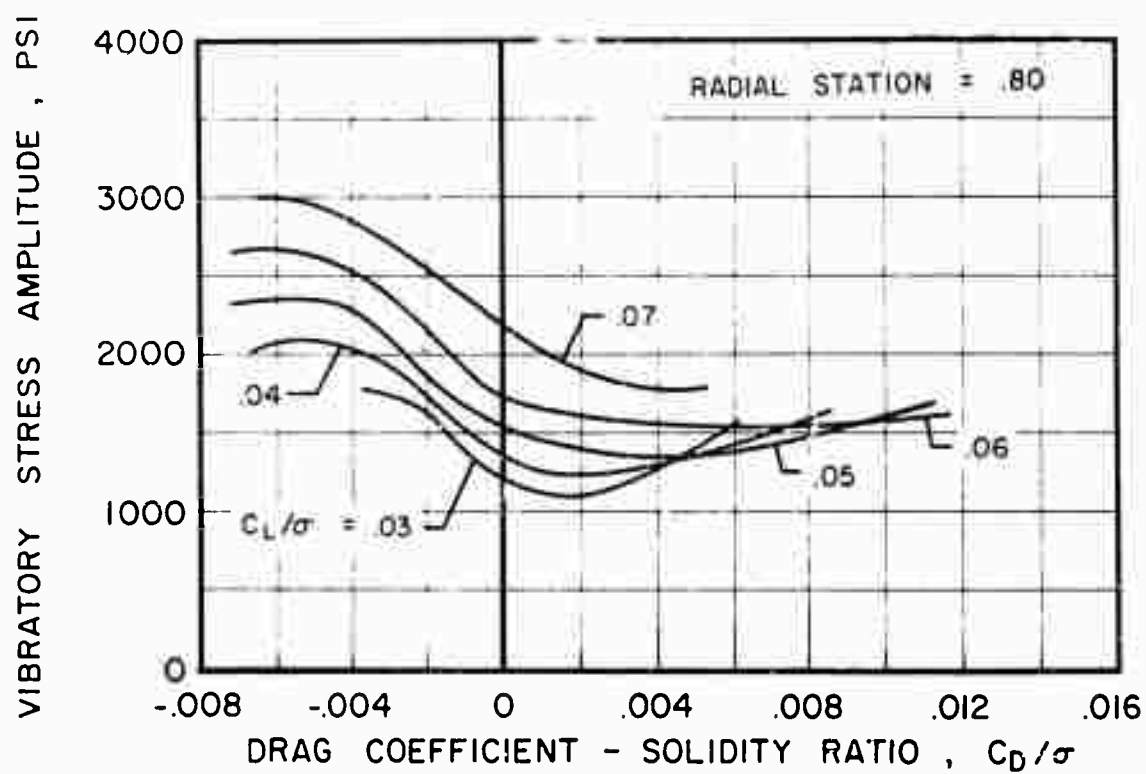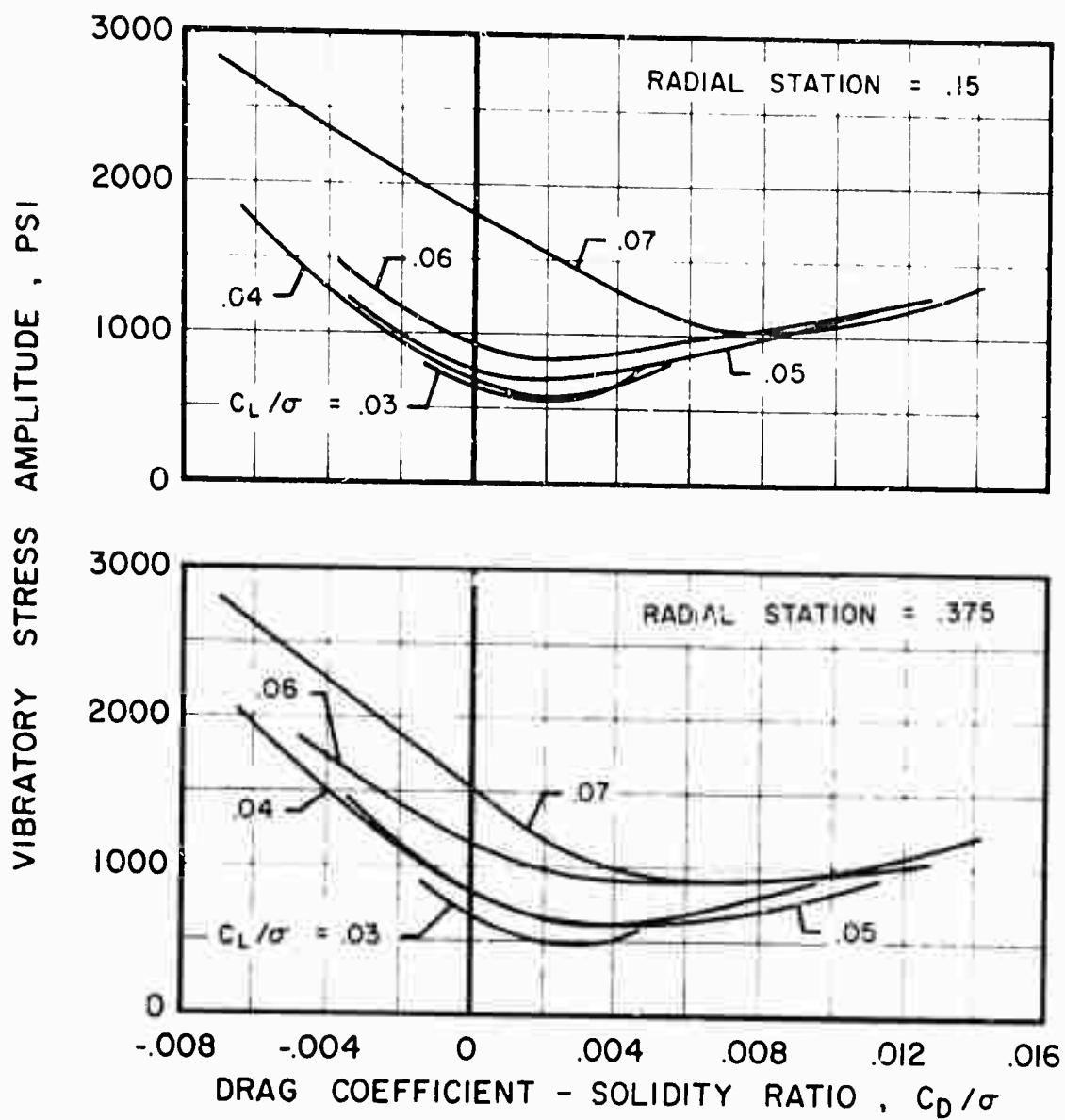
(b) Chordwise
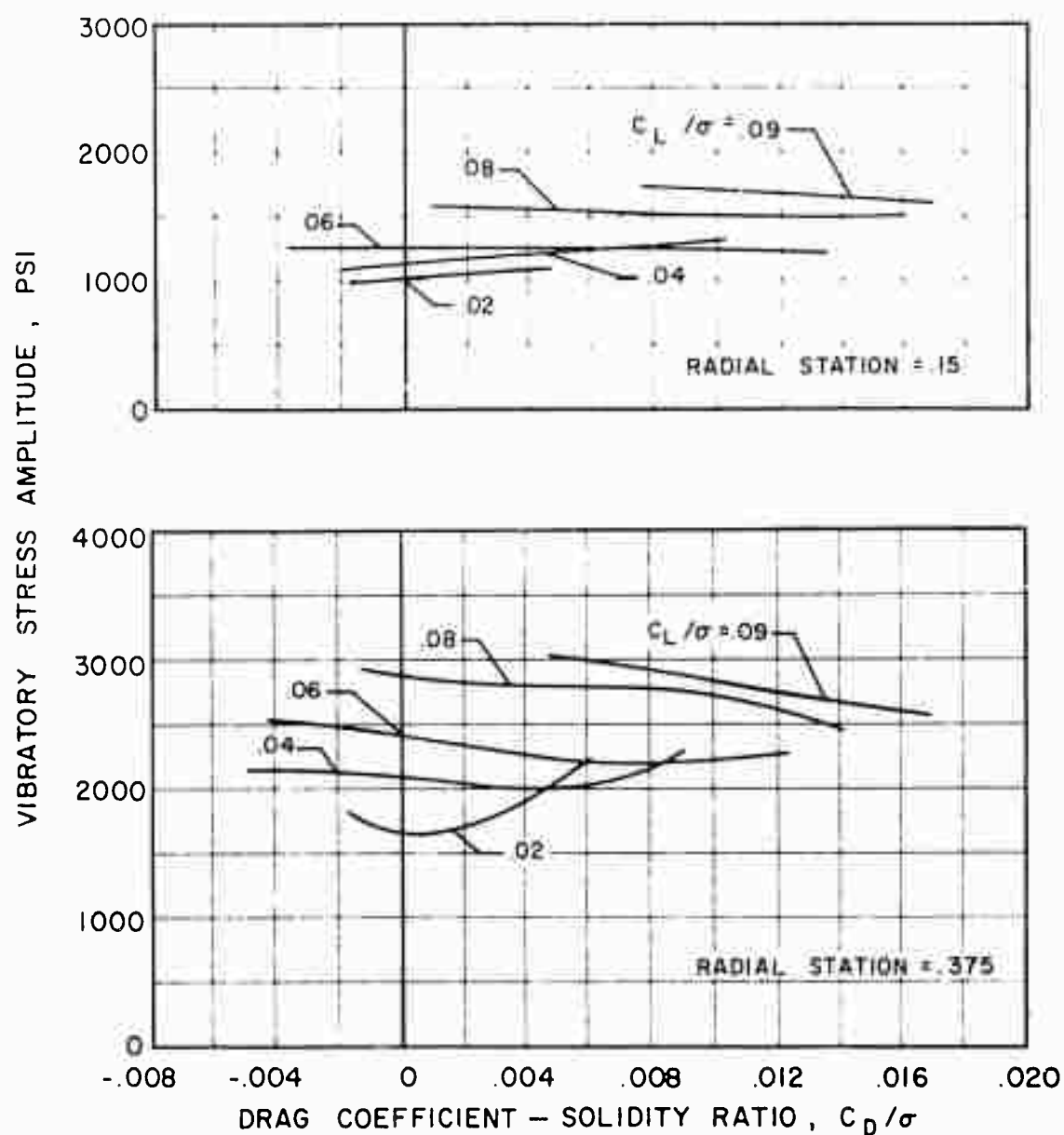
Figure 86. Continued.

194

(b) Chordwise Concluded
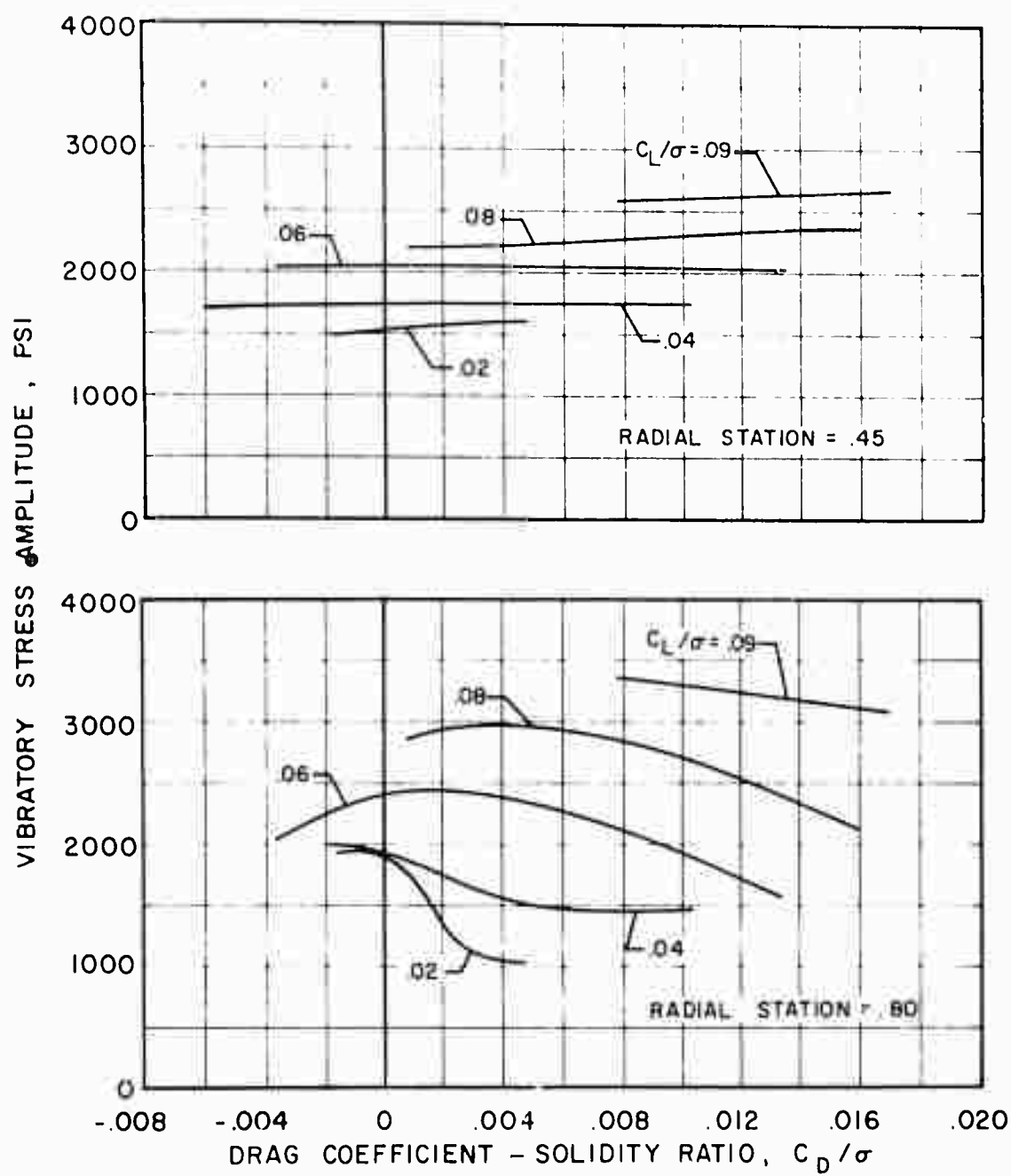
Figure 86. Continued.

195
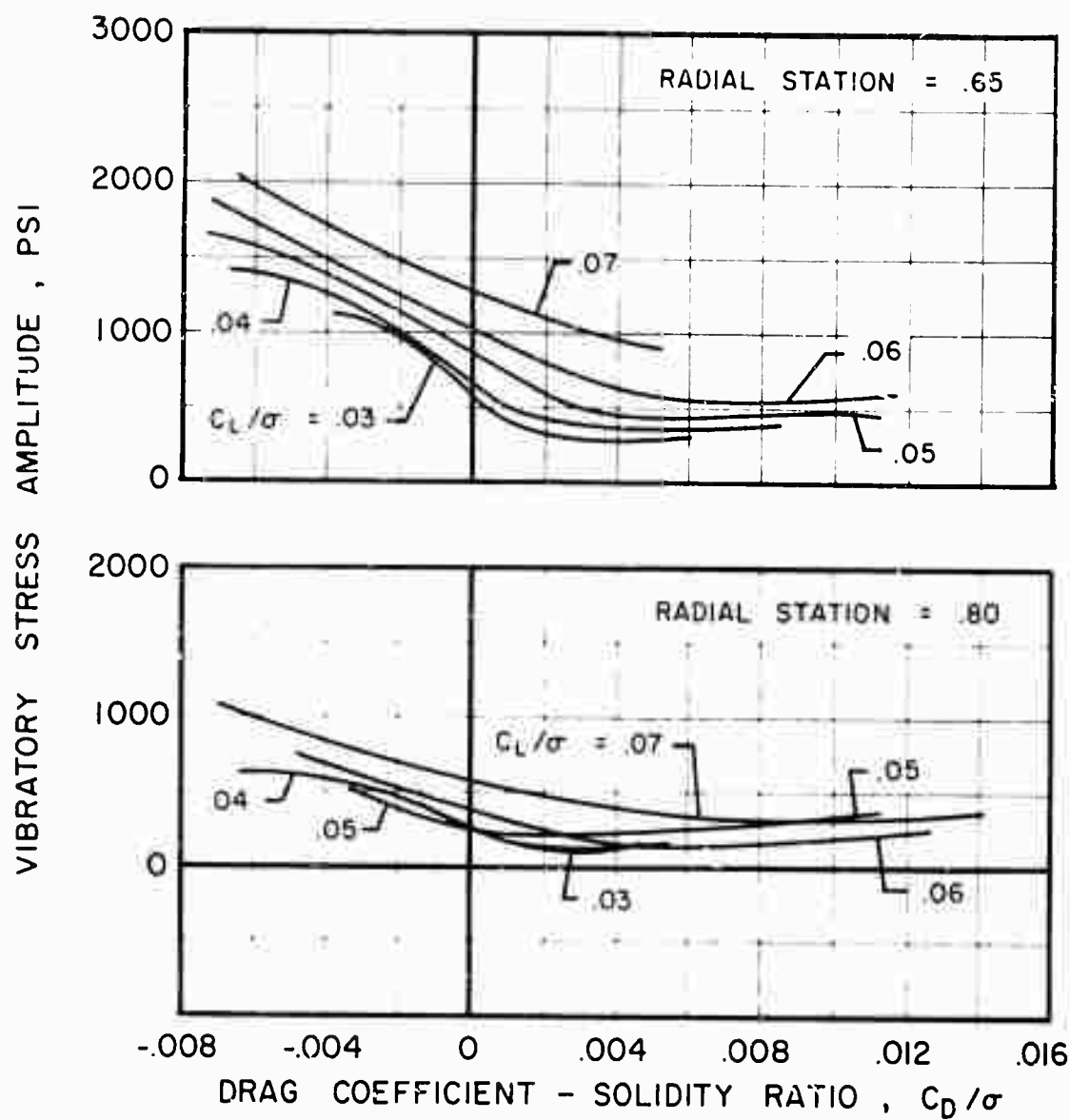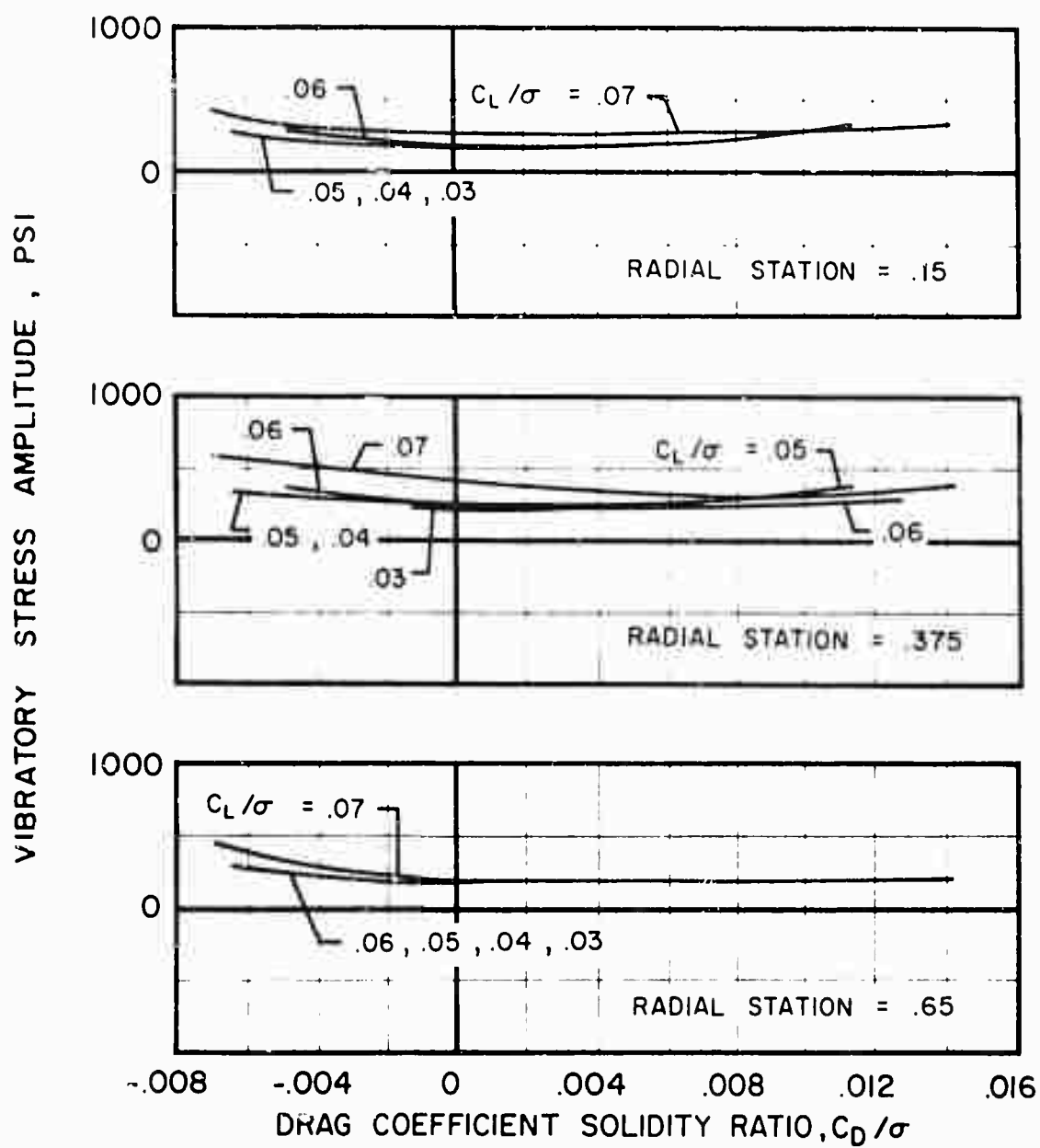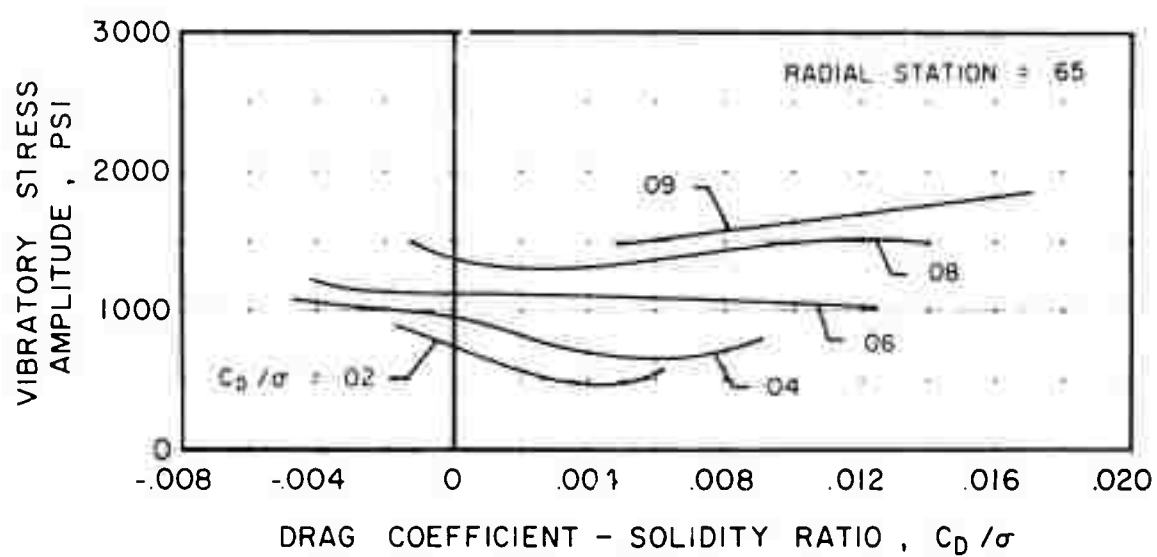
(c) Torsional

Figure 86. Concluded.

196
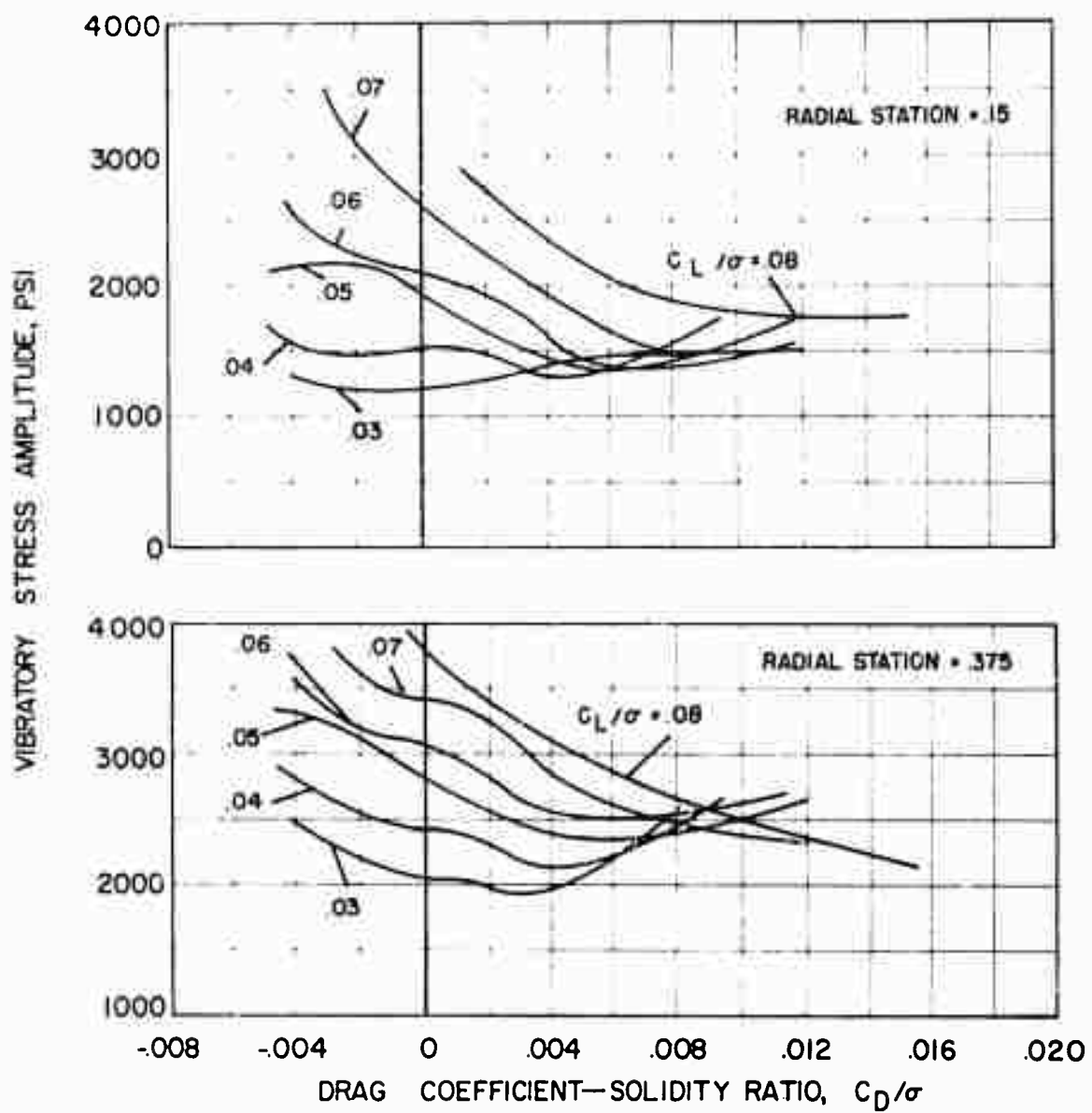
(a) Flapwise

Figure 87.   The Effect of Drag on Flapwise, Chordwise and
Torsional Vibratory Stress Amplitude at Constant
Lift for Several Radial Stations, V = 178 Knots,
μ = 0.46, θ_1 = 0°, $M_{(1.0, 90)}$ = 0.82.

197

(a) Flapwise Continued

Figure 87. Continued.

198

(a) Flapwise Concluded

Figure 87. Continued.

199

(b) Chordwise

Figure 87. Continued.

200

(b) Chordwise Concluded

Figure 87. Continued.

201
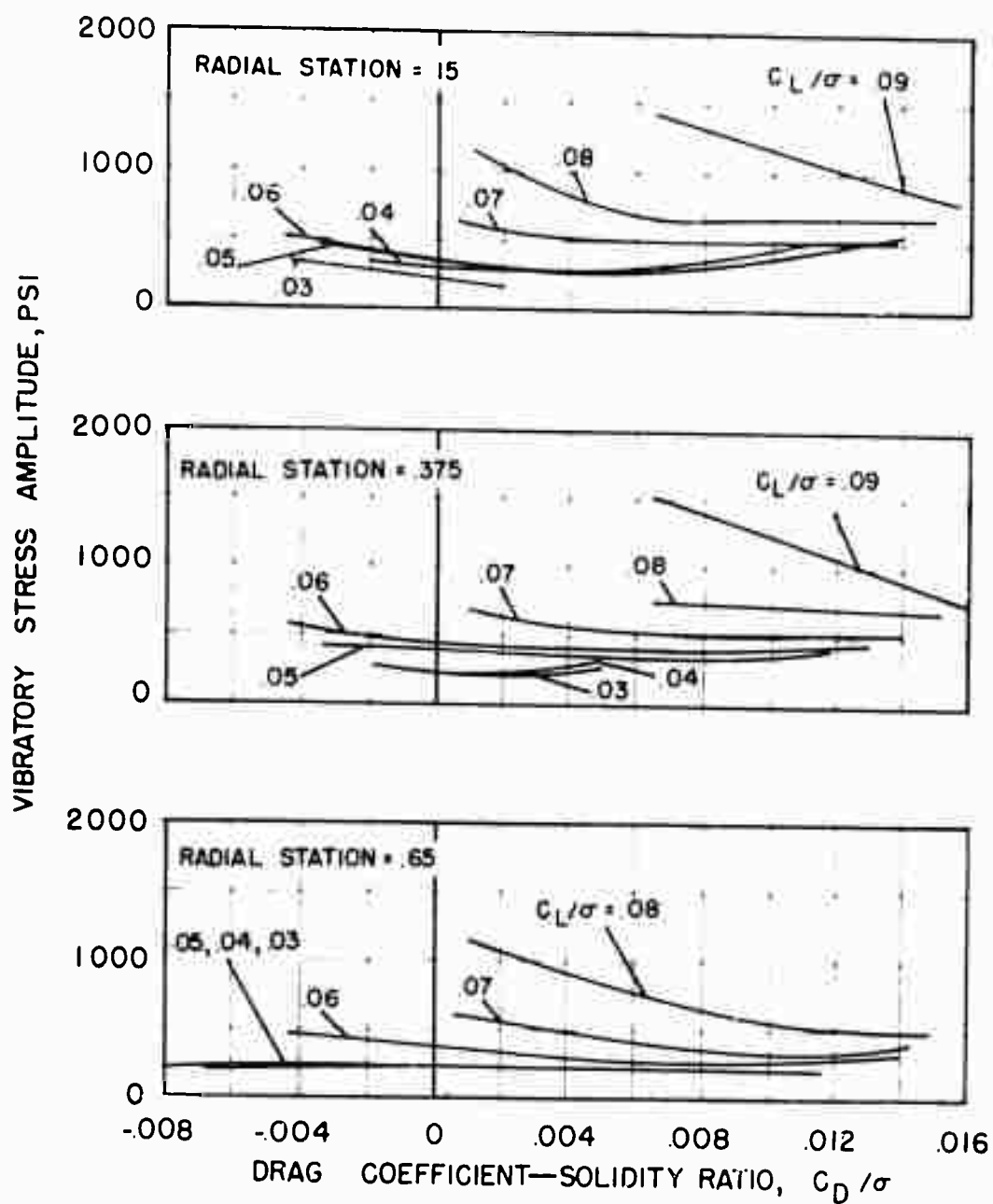
(c) Torsional

Figure 87. Concluded

202

(a) Flapwise

Figure 88. The Effect of Drag on Flapwise, Chordwise and Torsional Vibratory Stress Amplitude at Constant Lift for Several Radial Stations. $V = 132$ Knots, $\mu = 0.40$, $\theta_1 = 0°$, $M_{(1.0.90)} = 0.67$.

203

(a) Flapwise Concluded

Figure 88. Continued.

204

(b) Chordwise

Figure 88. Continued.

205

(b) Chordwise Continued

Figure 88. Continued.

206

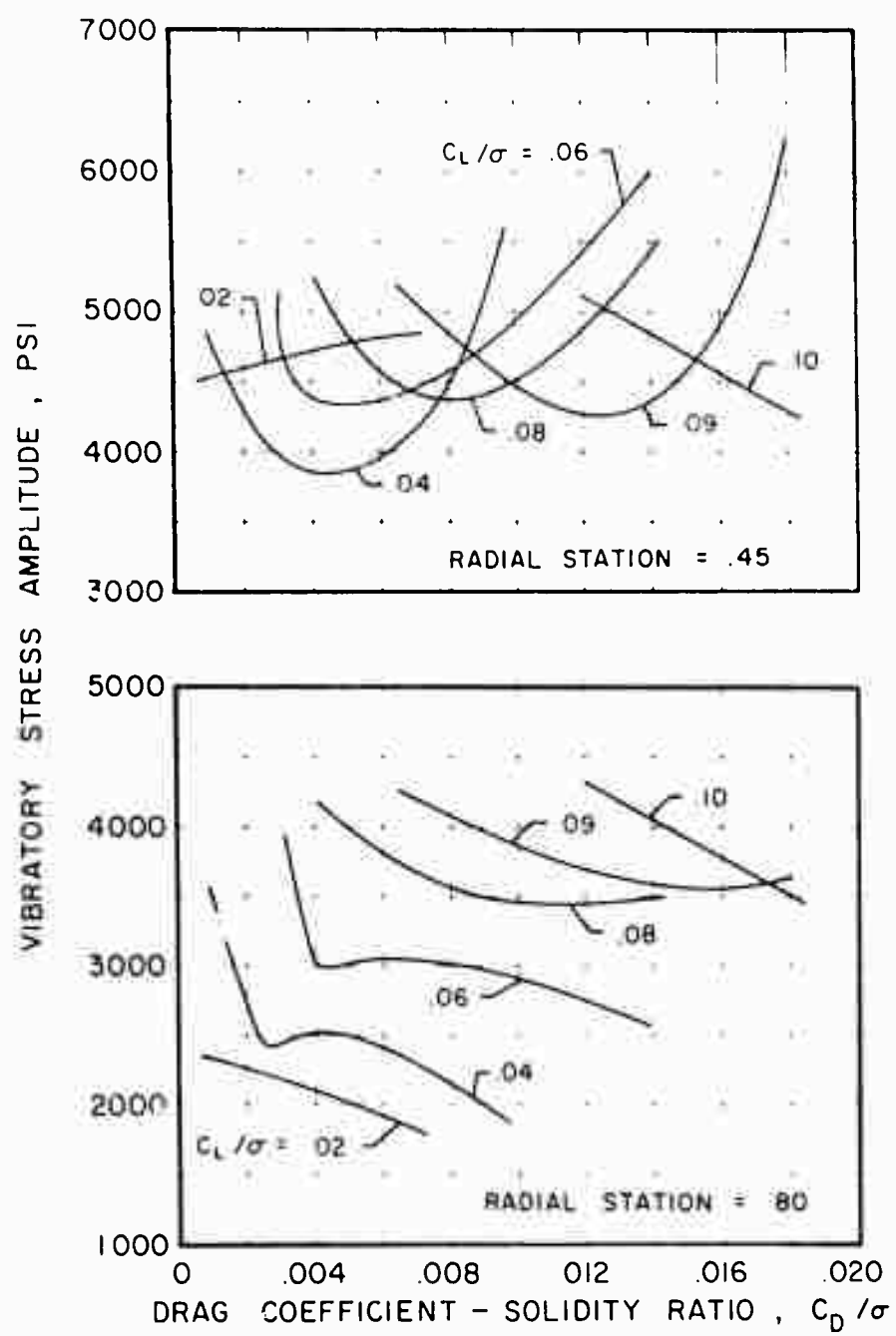(b) Chordwise Concluded

Figure 88. Continued.

207
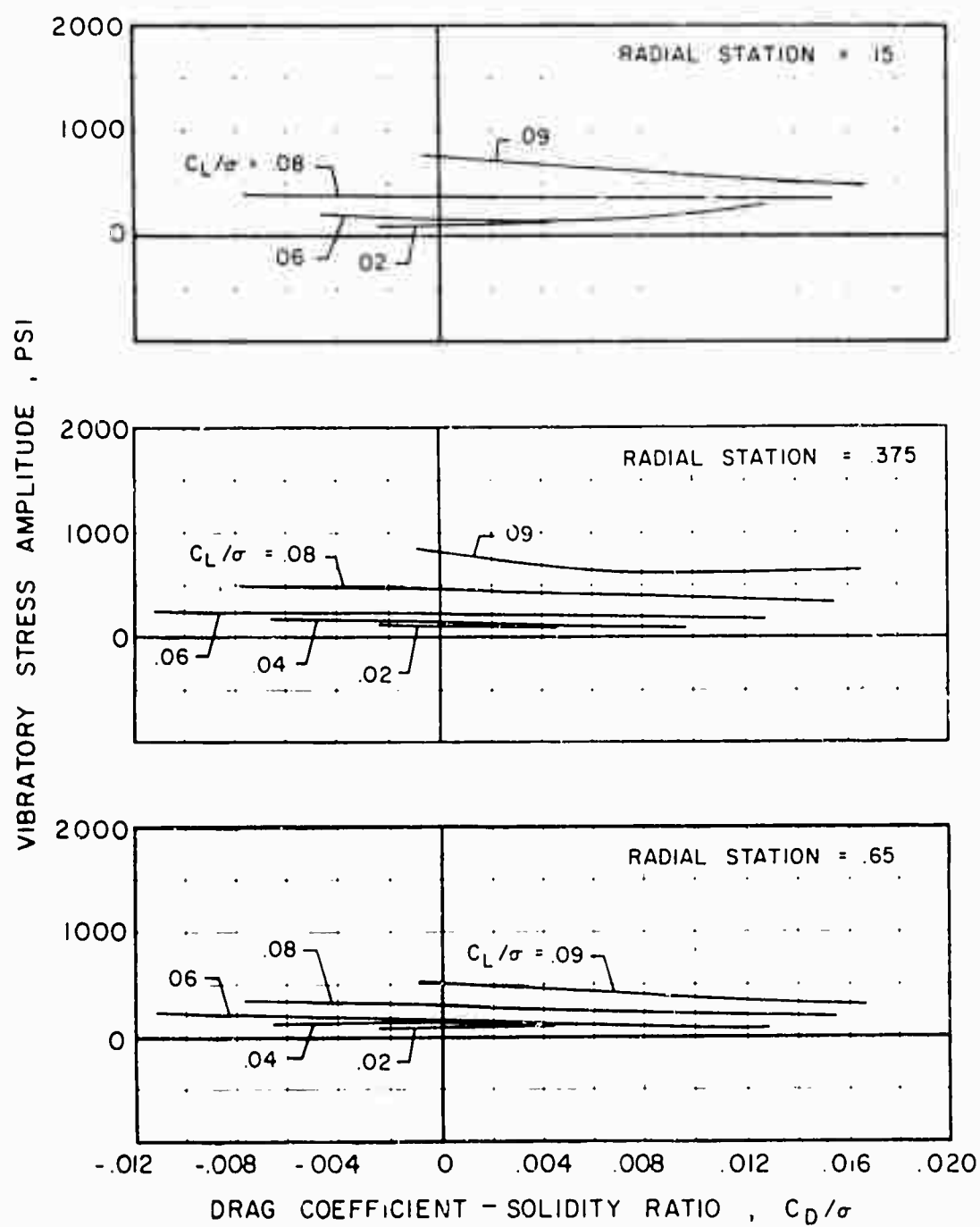
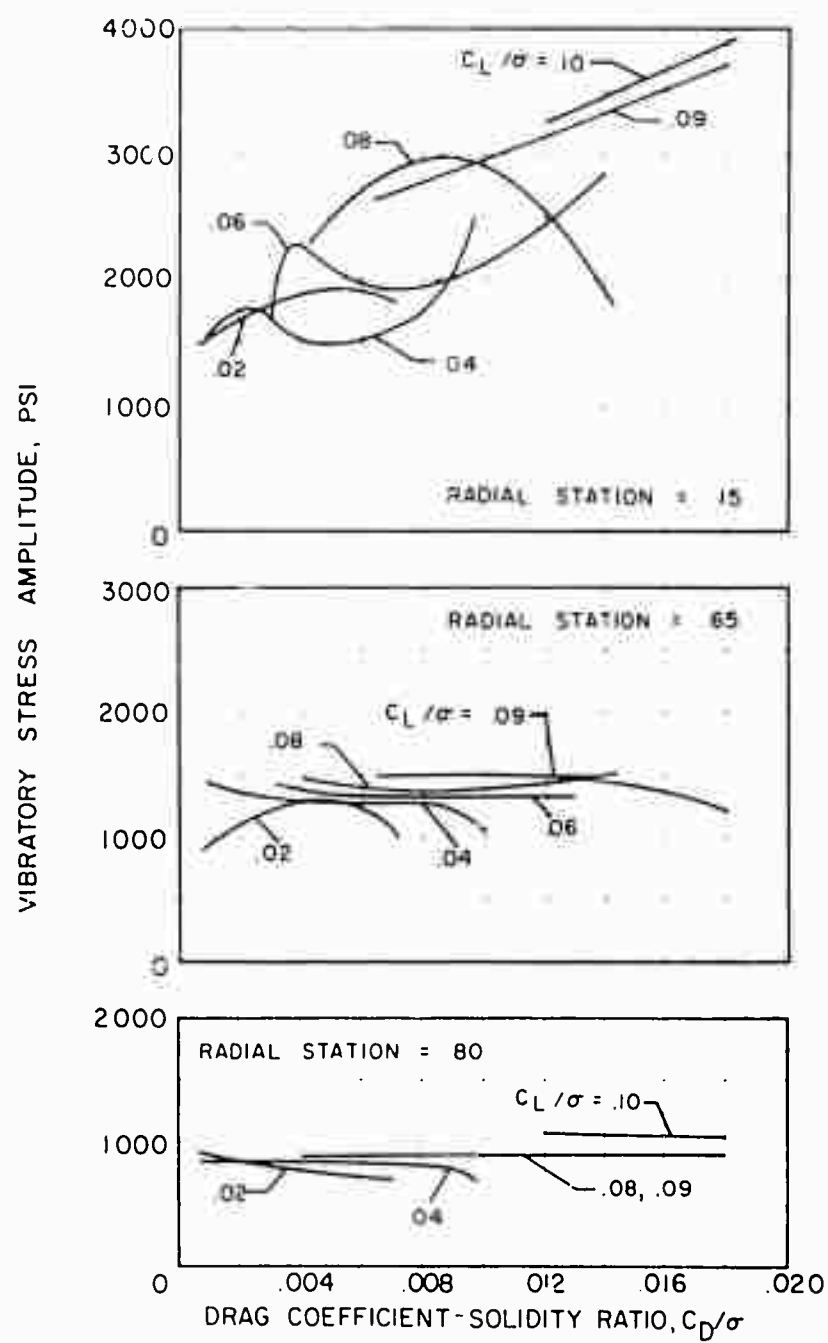(c) Torsional

Figure 88. Concluded.

208

(a) Flapwise

Figure 89. The Effect of Drag on Flapwise, Chordwise and Torsional Vibratory Stress Amplitude at Constant Lift for Several Radial Stations, V = 174 Knots, $\mu = 0.41$, $\theta_1 = 0°$, $M_{(1.0, 90)} = 0.87$.

209

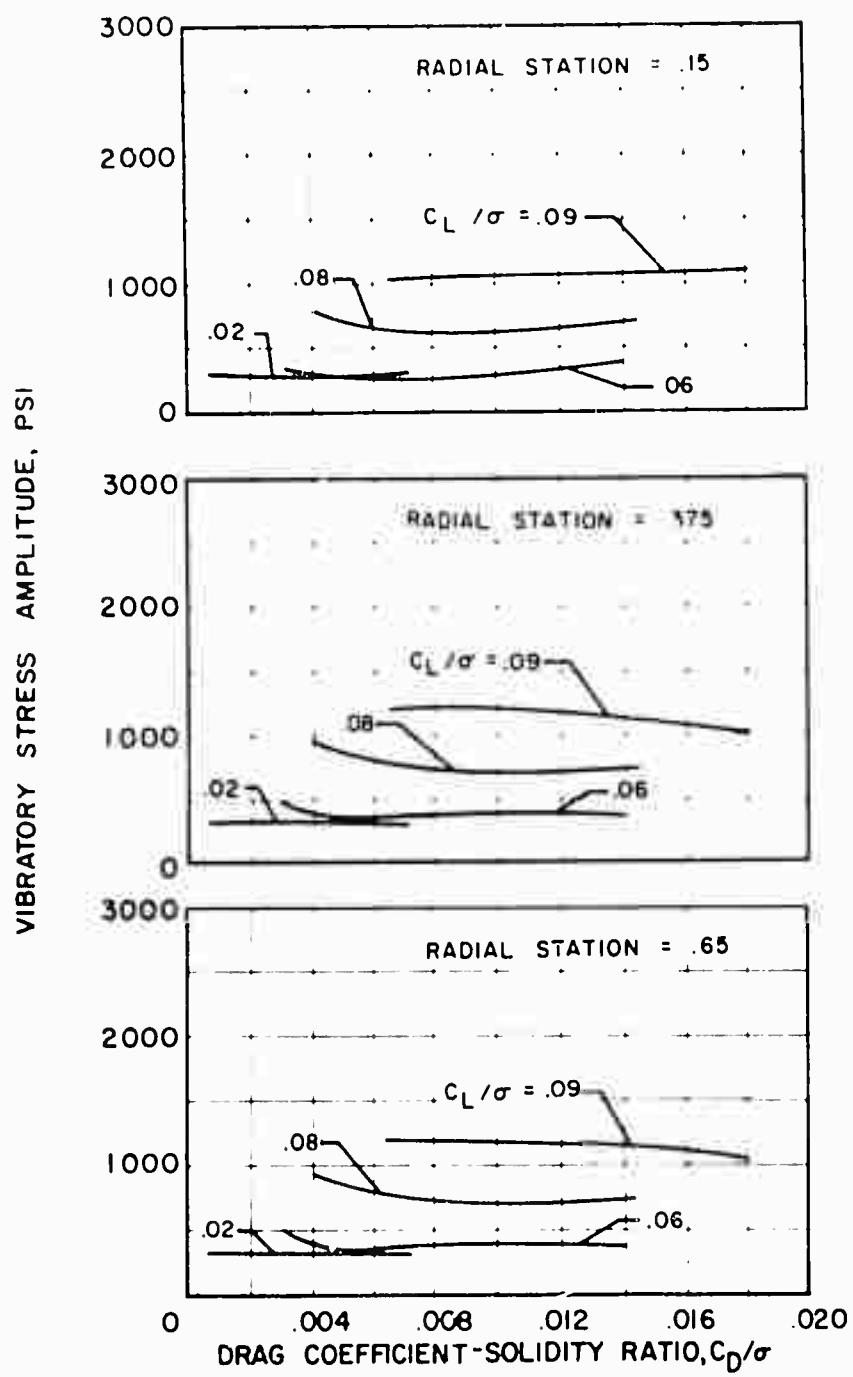(a) Flapwise Concluded
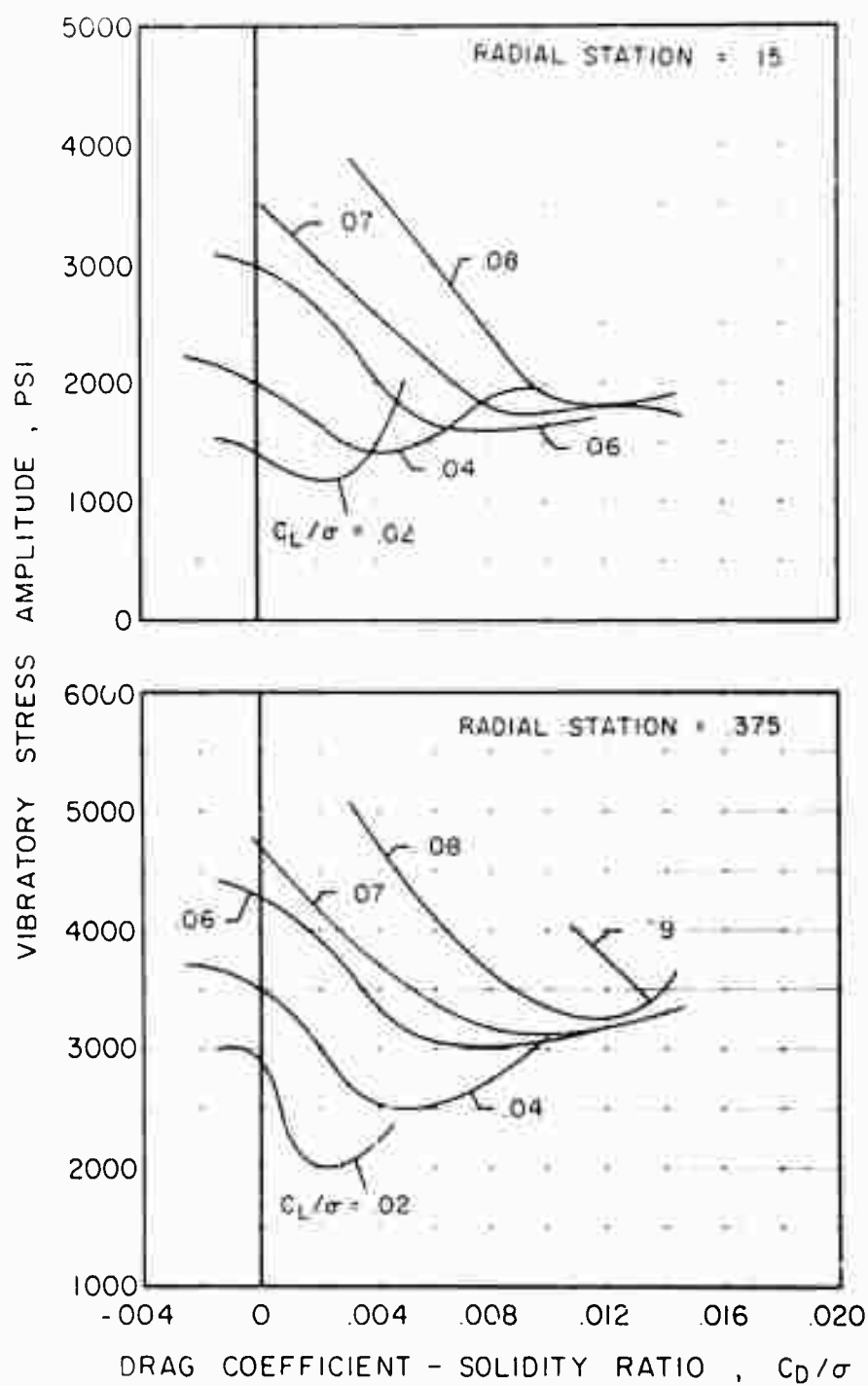
Figure 89. Continued.

210

(b) Chordwise

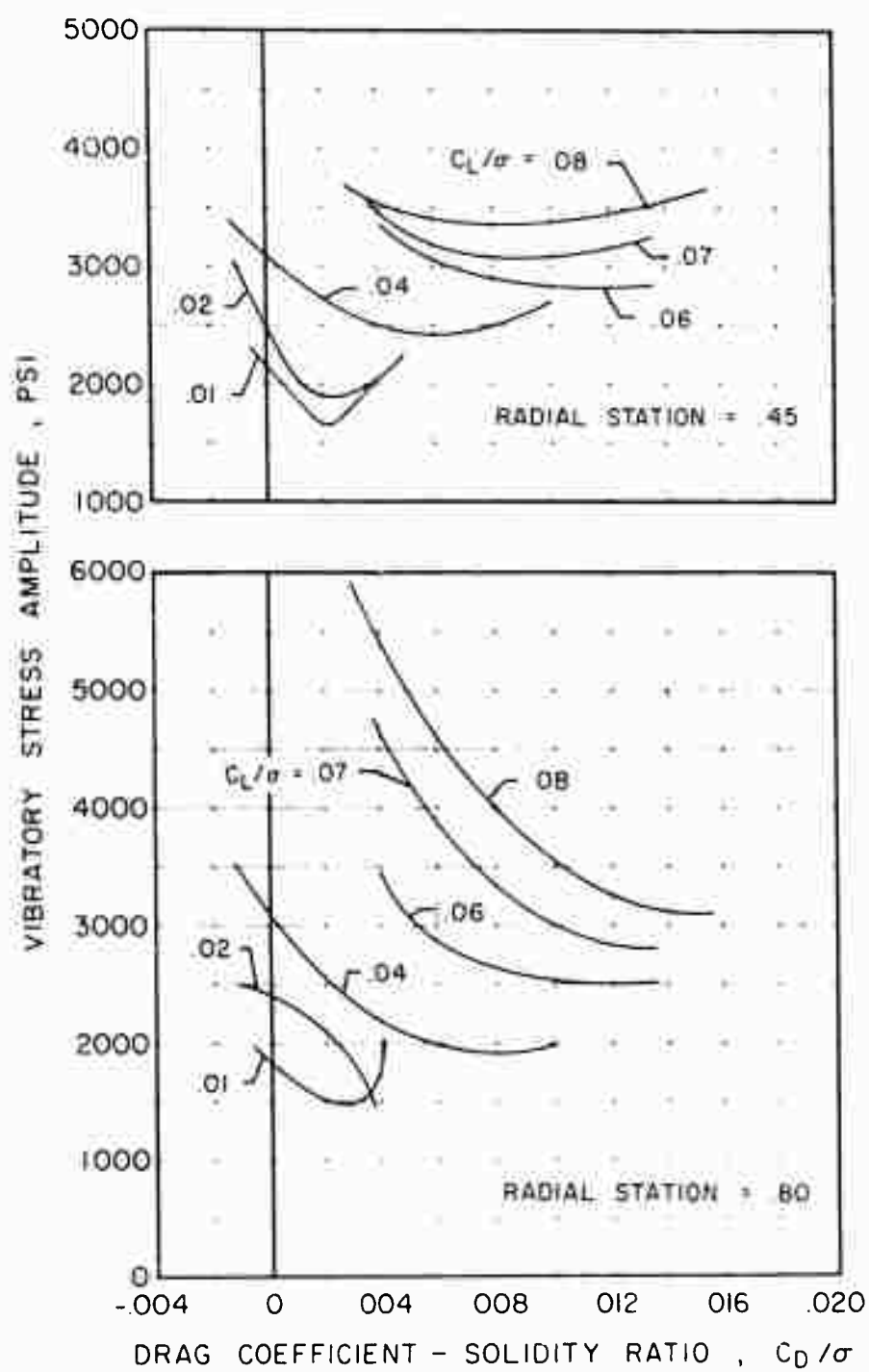Figure 89 Continued.

211
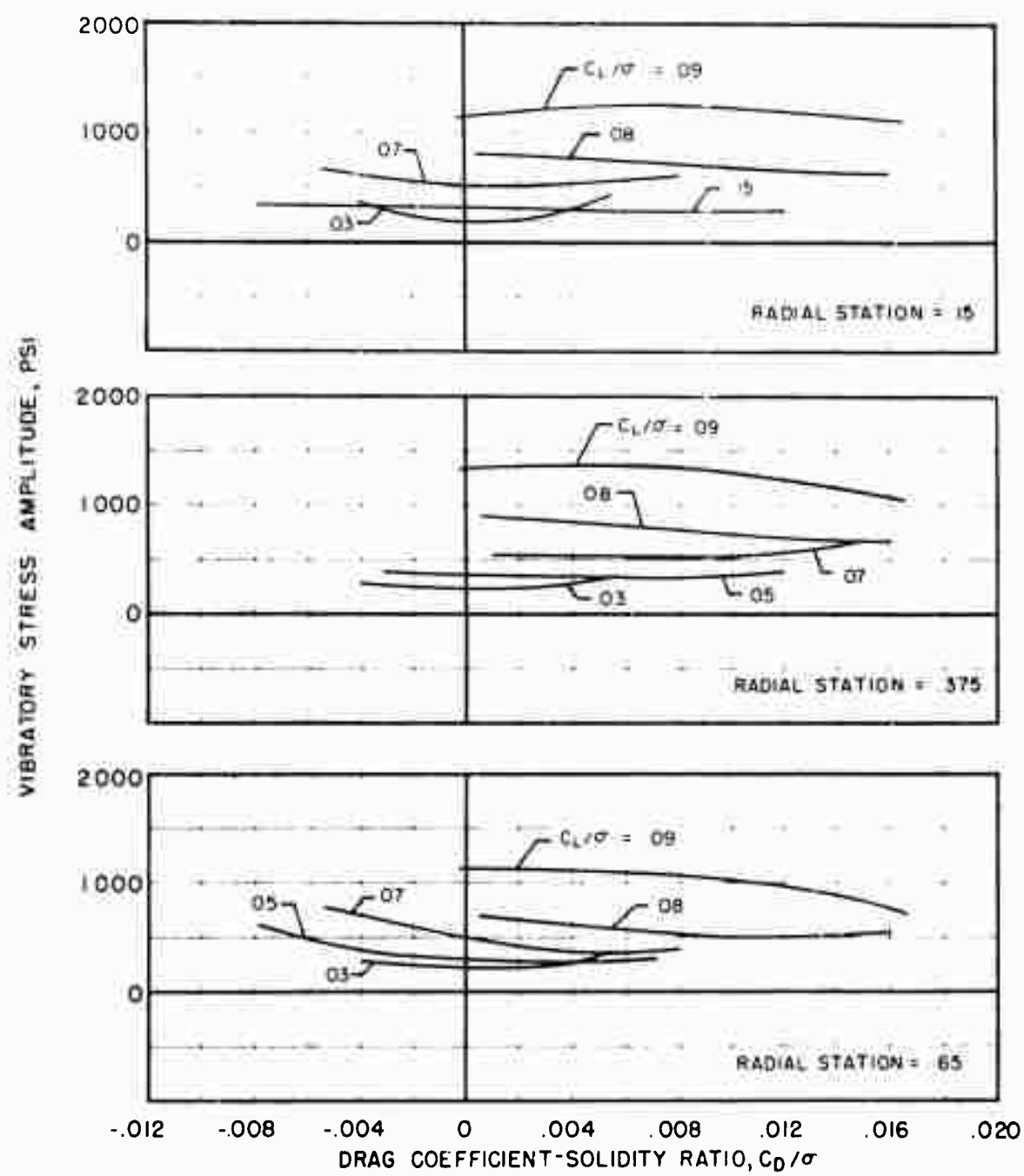
(c) Torsional

Figure 89. Concluded.

212

(a) Flapwise

Figure 90. The Effect of Drag on Flapwise, Chordwise and
Torsional Vibratory Stress Amplitude at Constant
Lift for Several Radial Stations, V = 175 Knots,
μ = 0.39, θ_1 = 0°, $M_{(1.0.90)}$ = 0.89.

213

(a) Flapwise Concluded

Figure 90. Continued.

214

(b) Chordwise

Figure 90. Continued.

215
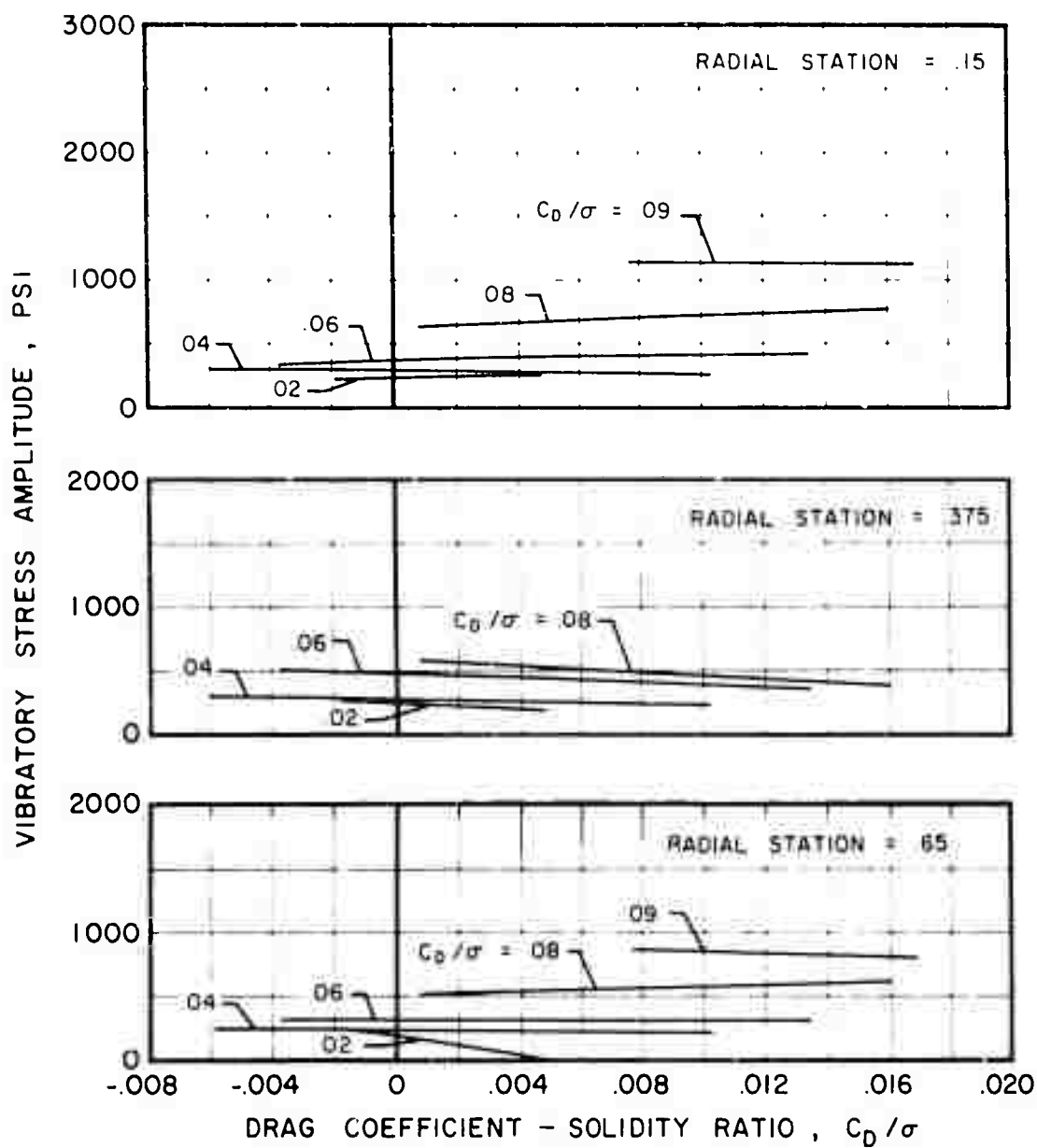
(c) Torsional

Figure 90. Concluded.

216
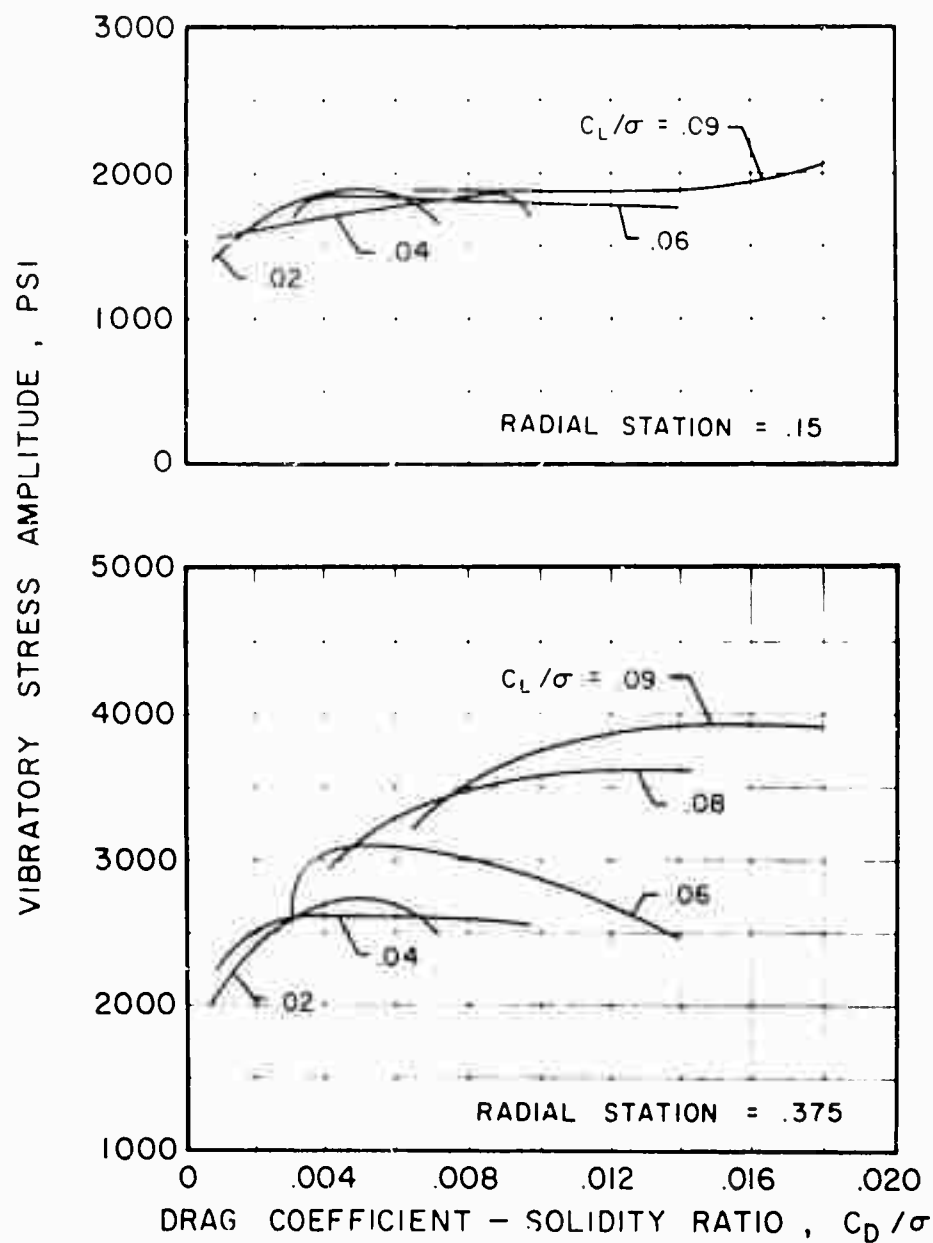
(a) Flapwise

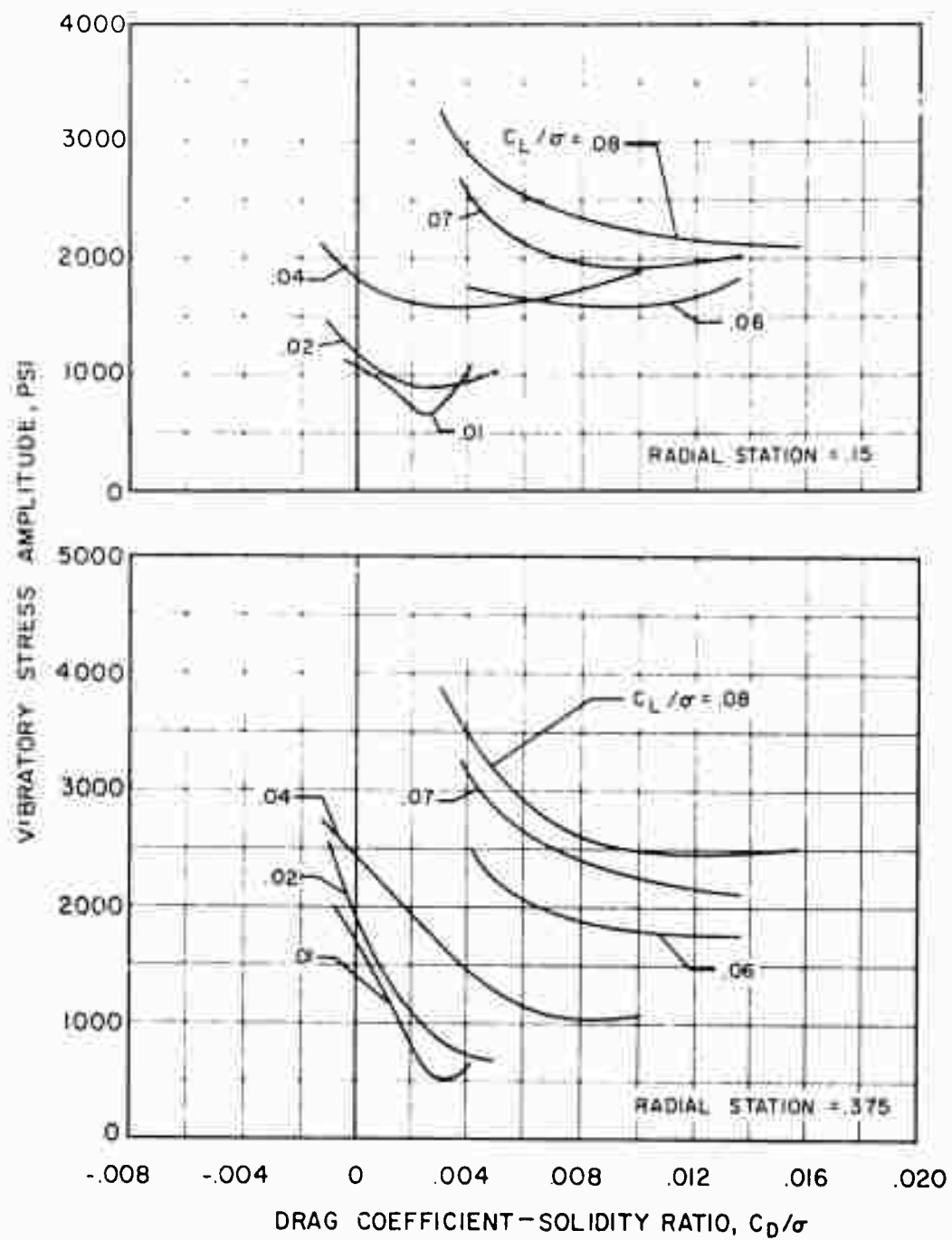Figure 91. The Effect of Drag on Flapwise, Chordwise and Torsional Vibratory Stress Amplitude at Constant Lift for Several Radial Stations, V = 180 Knots, μ = 0.39, θ_1 = 0°. $M_{(1.0, 90)}$ = 0.93.
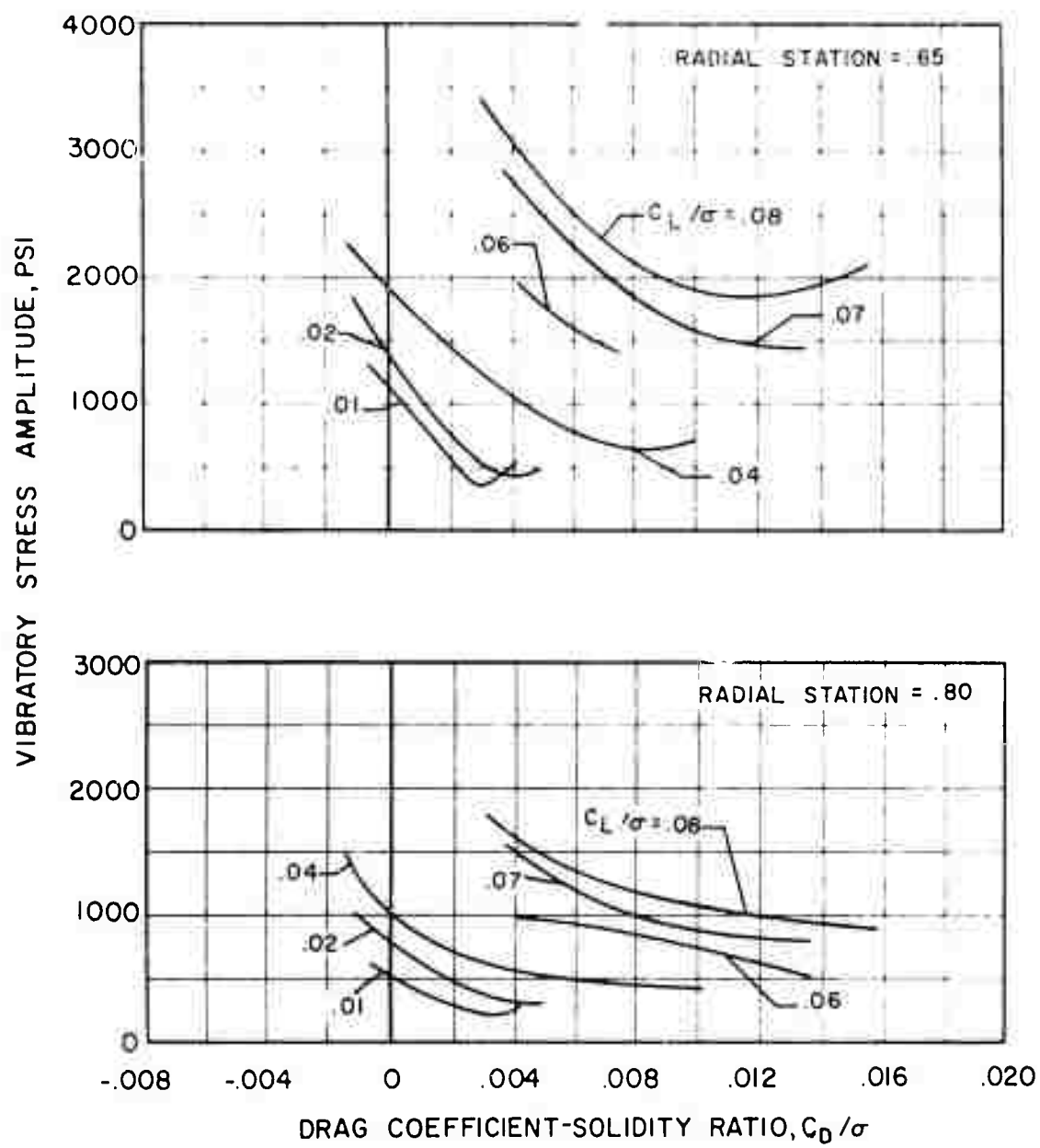
217

(a) Flapwise Concluded

Figure 91. Continued.

218

(b) Chordwise

Figure 91. Continued.

219

(c) Torsional

Figure 91. Concluded.

(a) Flapwise

Figure 92. The Effect of Drag on Flapwise, Chordwise and Torsional Vibratory Stress Amplitude at Constant Lift for Several Radial Stations, V = 194 Knots, μ = 0.50, θ_1 = 0°, $M_{(1.0, 90)}$ = 0.83.
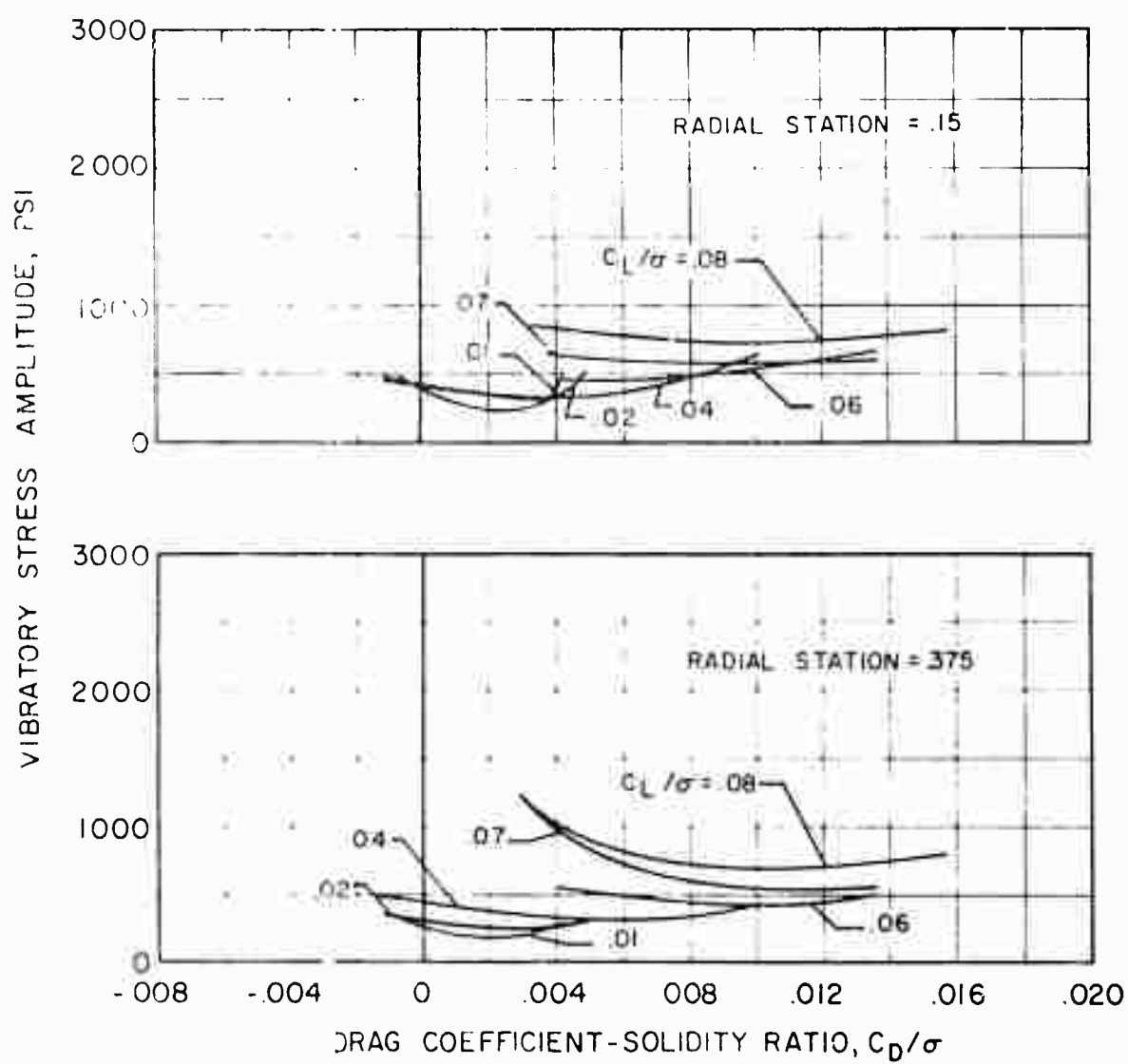
221

(a) Flapwise Concluded

Figure 92. Continued.

222

(b) Chordwise
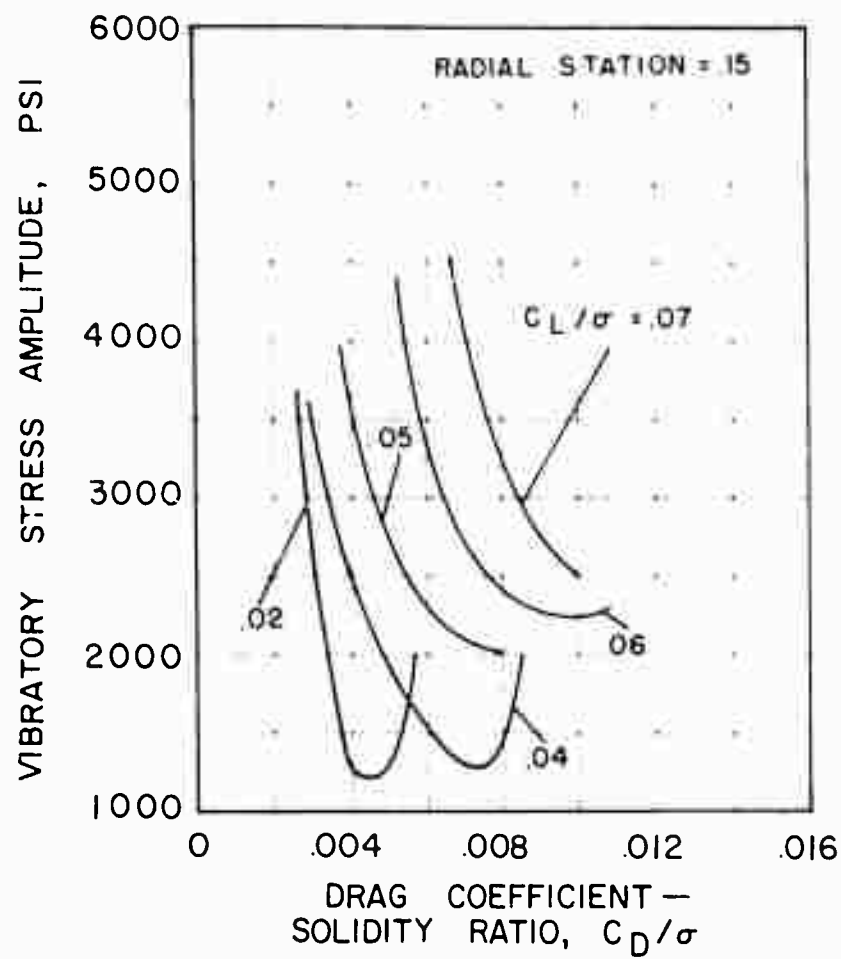
Figure 92. Continued.

223

(b) Chordwise Concluded

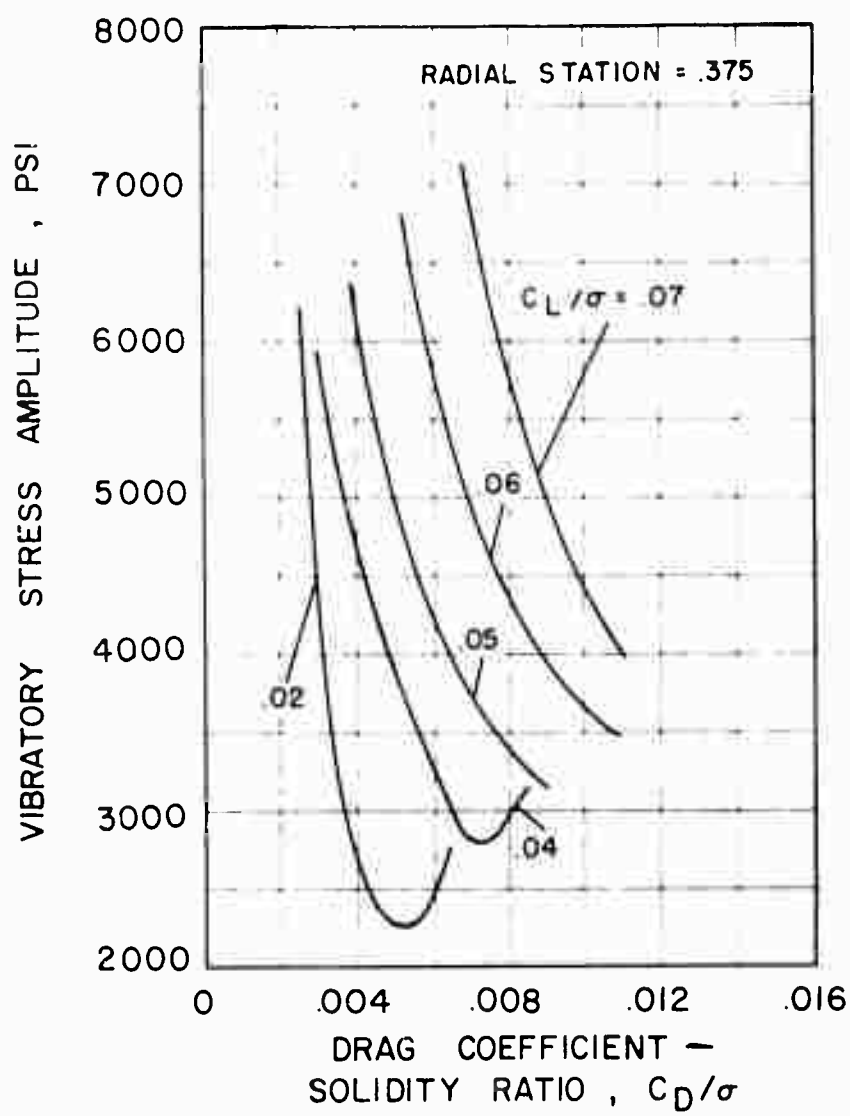Figure 92. Continued.
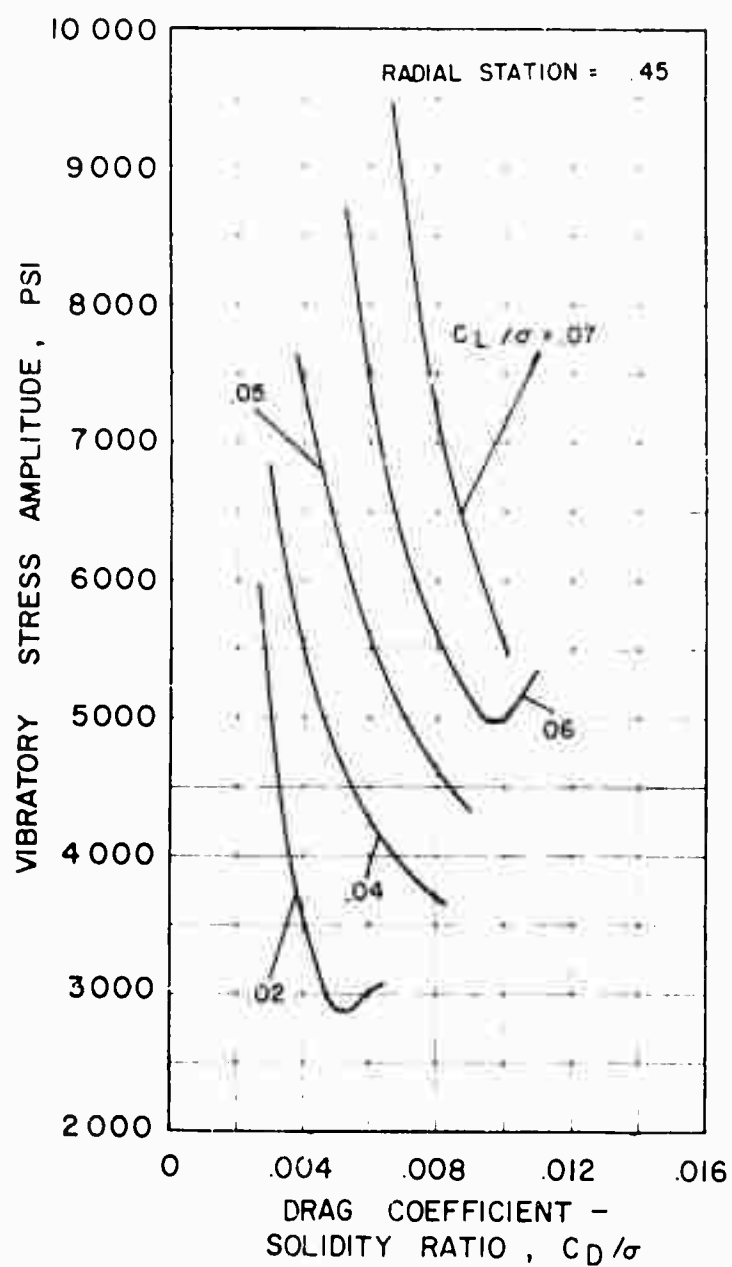
224

(c) Torsional

Figure 92. Concluded

(a) Flapwise

Figure 93. The Effect of Drag on Flapwise, Chordwise and Torsional Vibratory Stress Amplitude at Constant Lift for Several Radial Stations, $V = 194$ Knots, $\mu = 0.62$, $\theta_1 = 0°$, $M_{(1.0, 90)} = 0.73$.

226
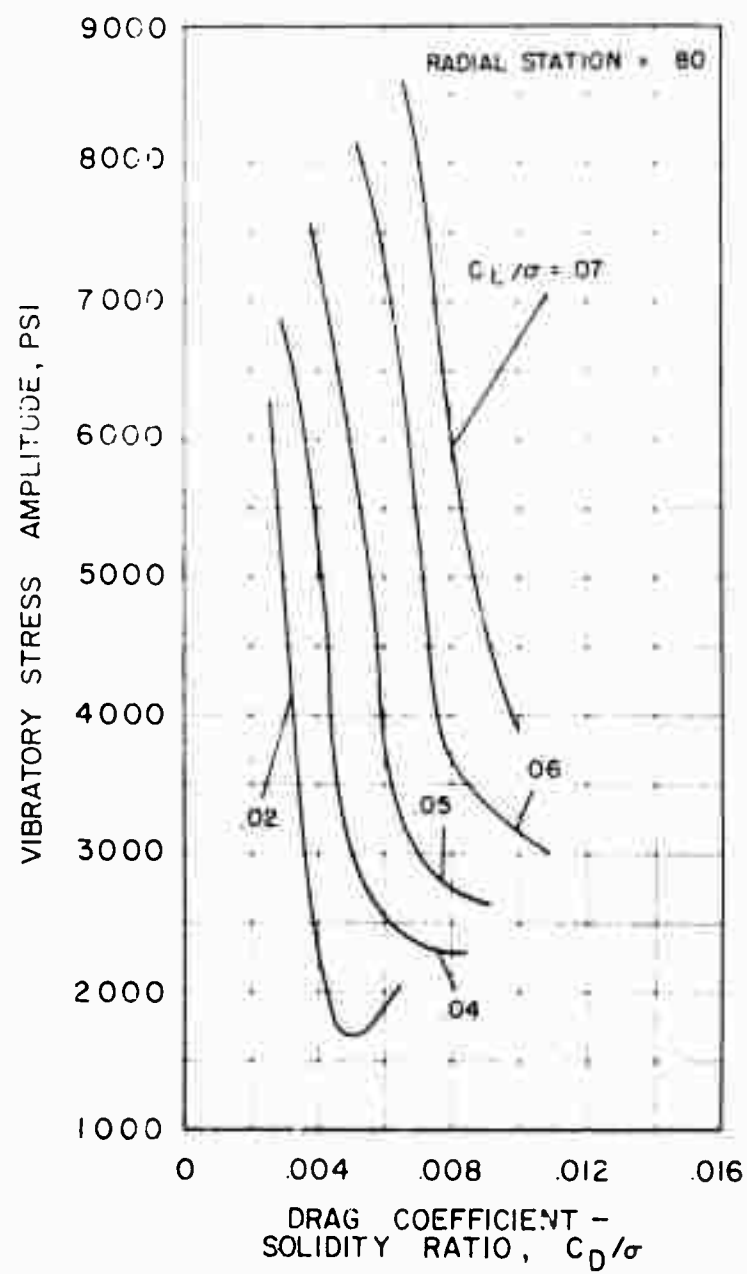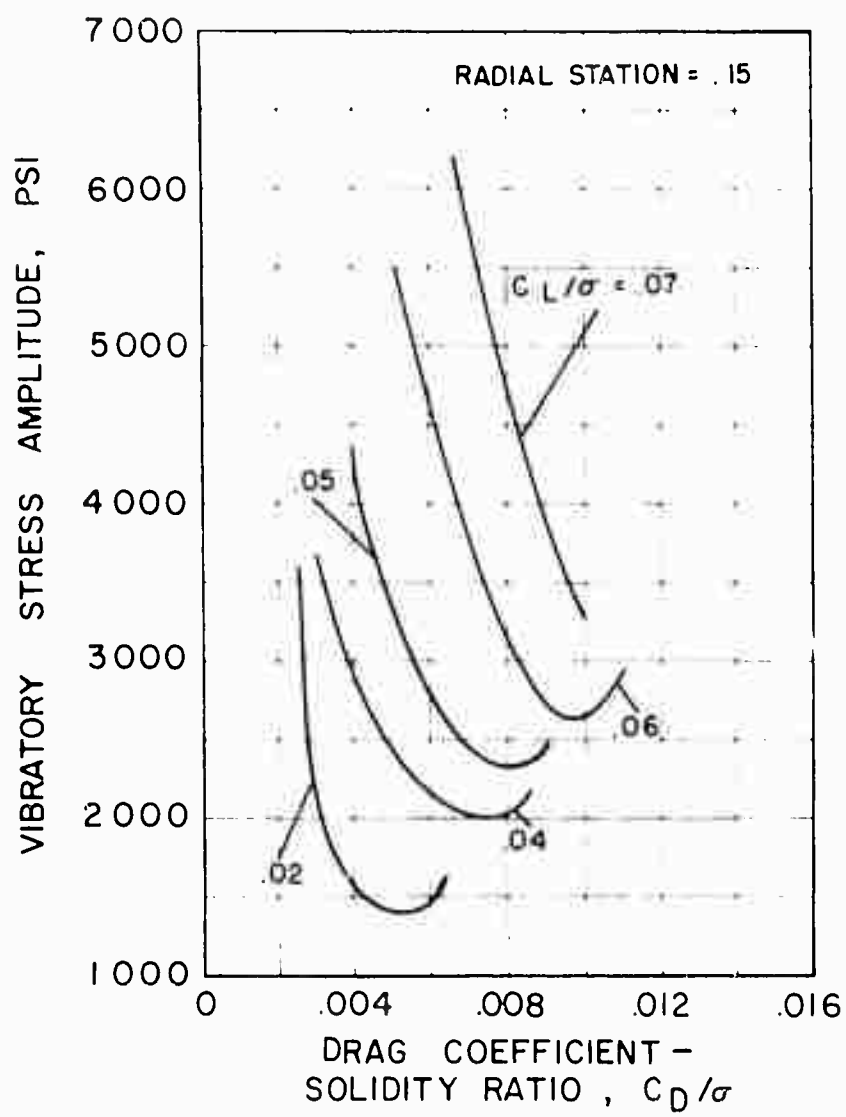
(a) Flapwise Continued

Figure 93. Continued

227

(a) Flapwise Continued

Figure 93. Continued.

228
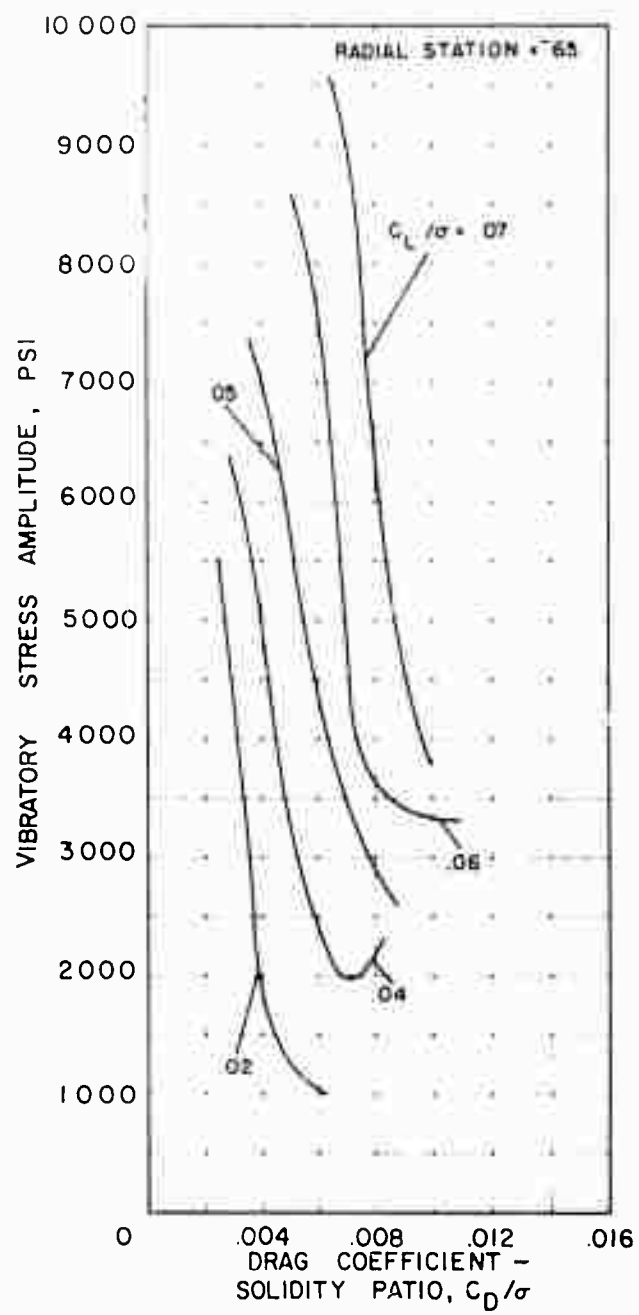
(a) Flapwise Concluded
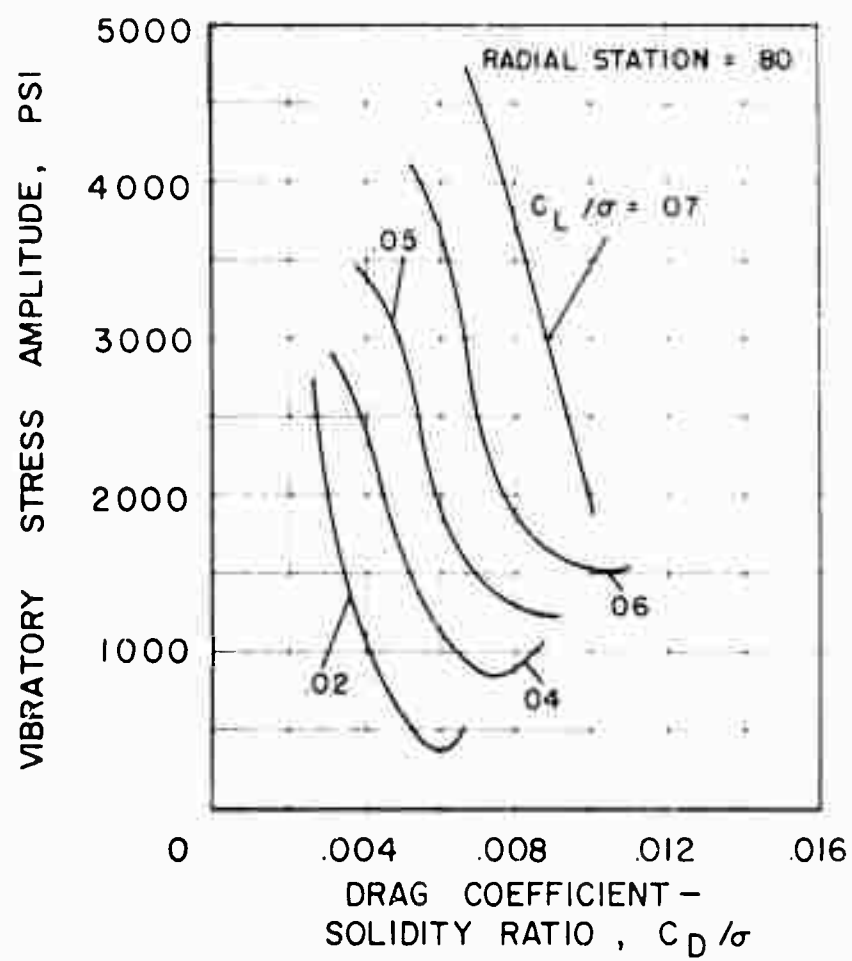
Figure 93. Continued.

229

(b) Chordwise

Figure 93.   Continued.

230

(b) Chordwise Continued

Figure 93. Continued.

231

(b) Chordwise Concluded

Figure 93.   Continued

232

(c) Torsional

Figure 93. Concluded.

(a) Flapwise

Figure 94.   The Effect of Rotor Angle of Attack on Flapwise,
Chordwise, and Torsional Vibratory Stress
Amplitude at Constant Lift for Several Radial
Stations, $V = 193$ Knots, $\mu = 0.71$, $\theta_1 = 0°$.
$M_{(1.0, 90)} = 0.68$.

234
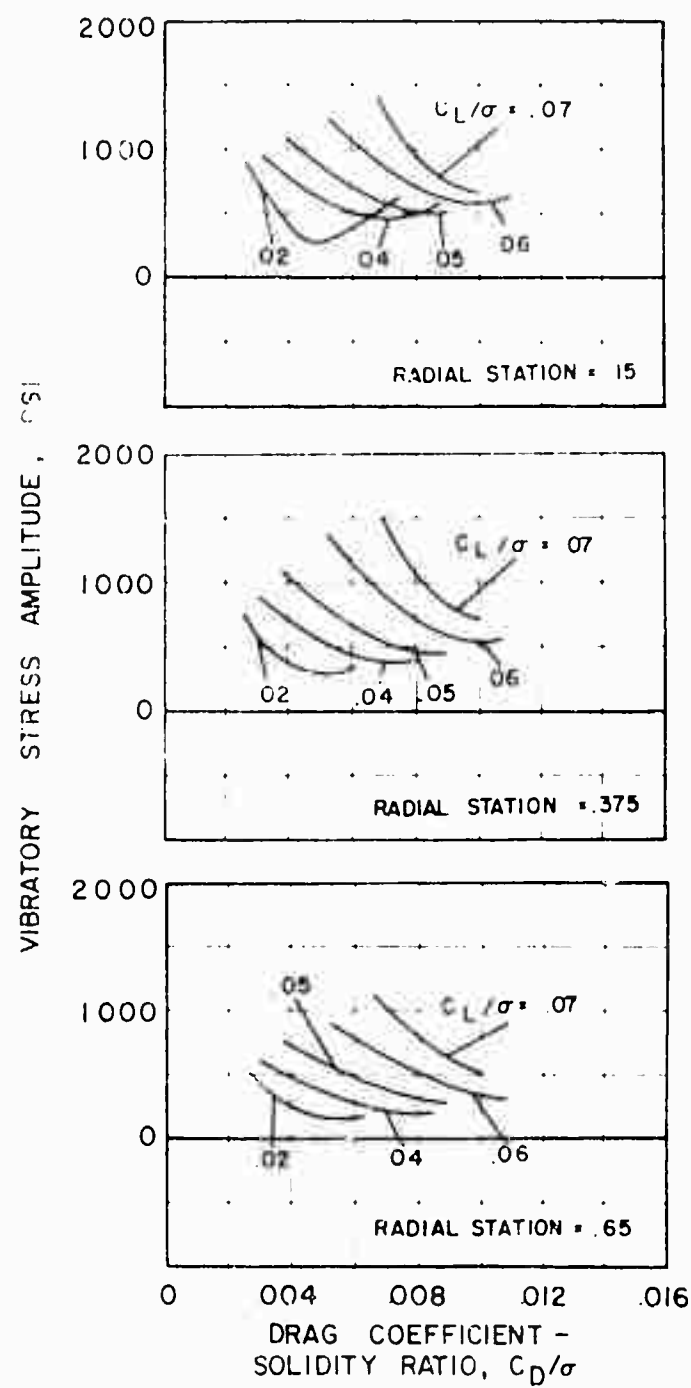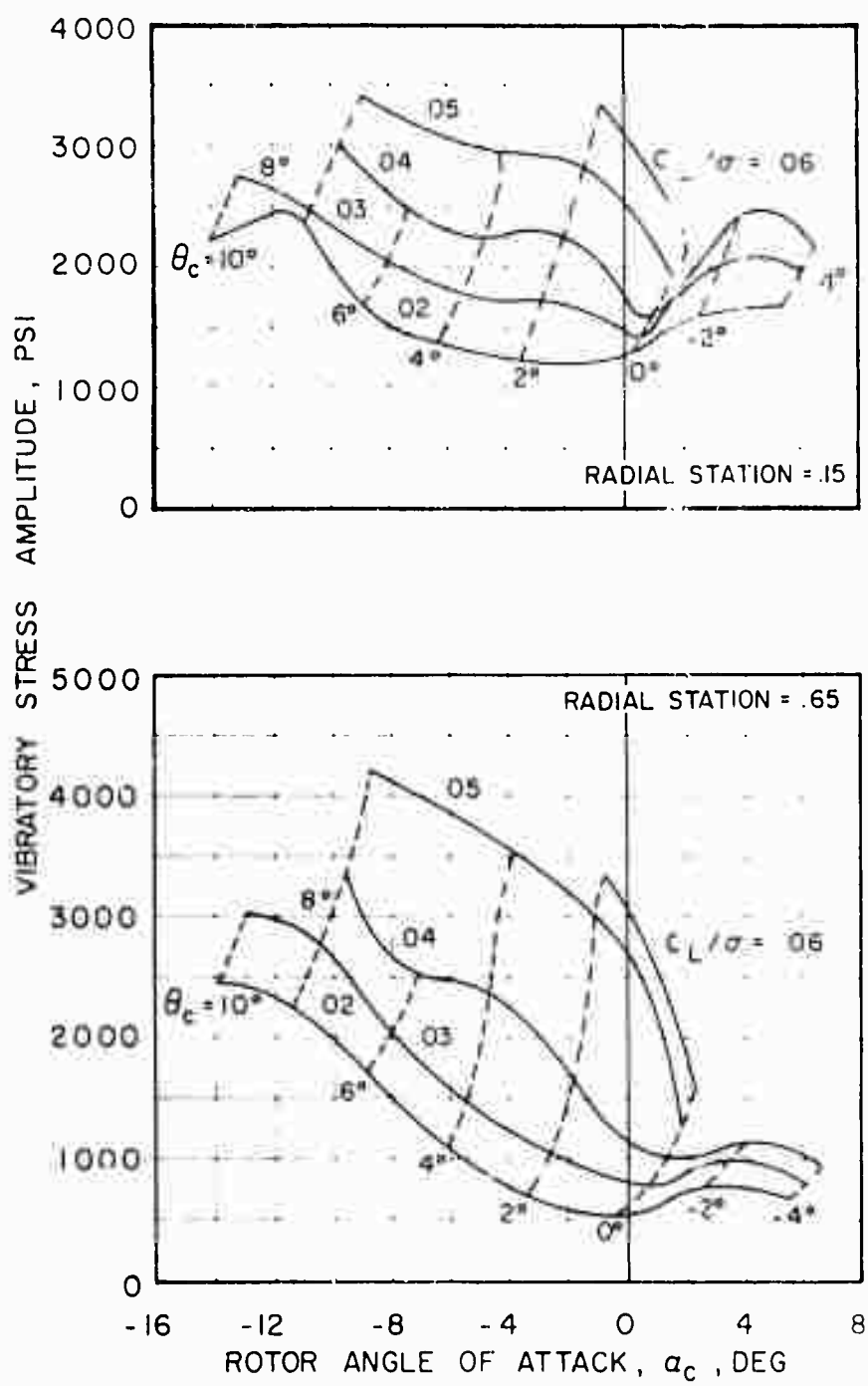
(a) Flapwise Concluded

Figure 94. Continued.

235

(b) Chordwise

Figure 94. Continued.

236

(b) Chordwise Concluded

Figure 94. Continued.

237

(c) Torsional

Figure 94. Concluded.

238

(a) Flapwise

Figure 95. The Effect of Rotor Angle of Attack on Flapwise, Chordwise, and Torsional Vibratory Stress Amplitude at Constant Lift for Several Radial Stations. $V = 195$ Knots, $\mu = 0.82$, $\theta_1 = 0°$, $M_{(1.0, 90)} = 0.62$.
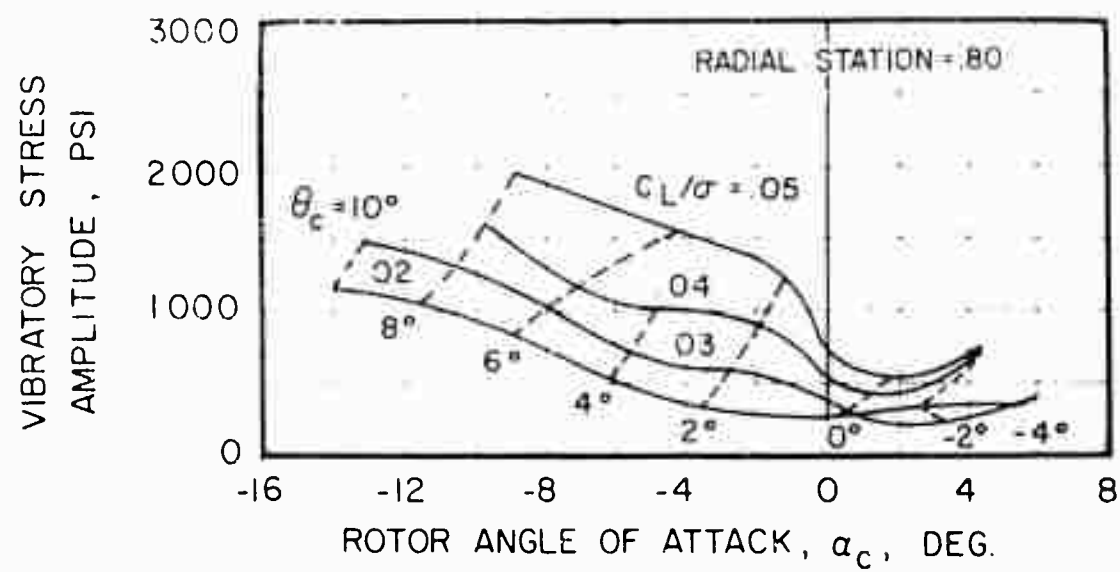
(a) Flapwise Concluded
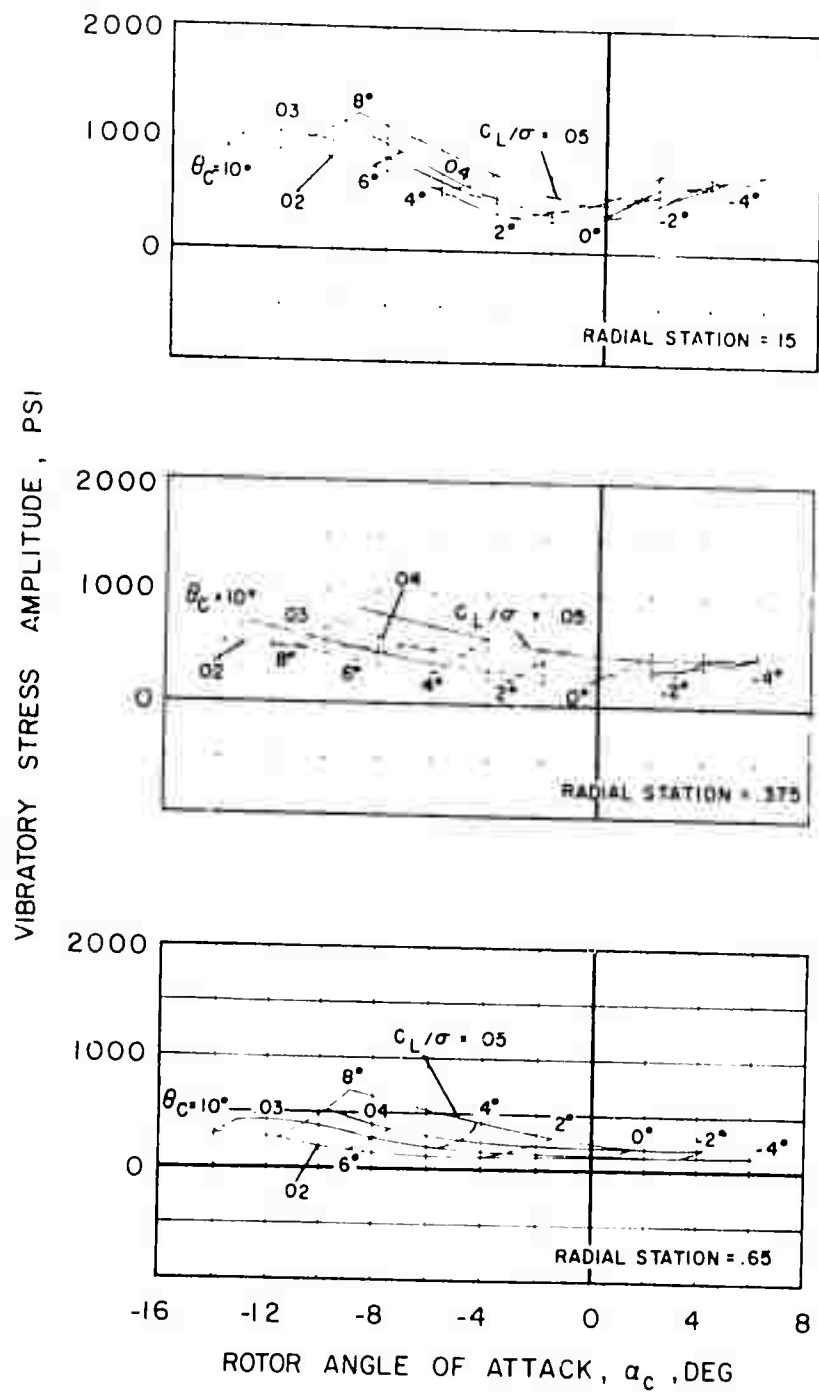
Figure 95. Continued.

240

(b) Chordwise

Figure 9: Continued
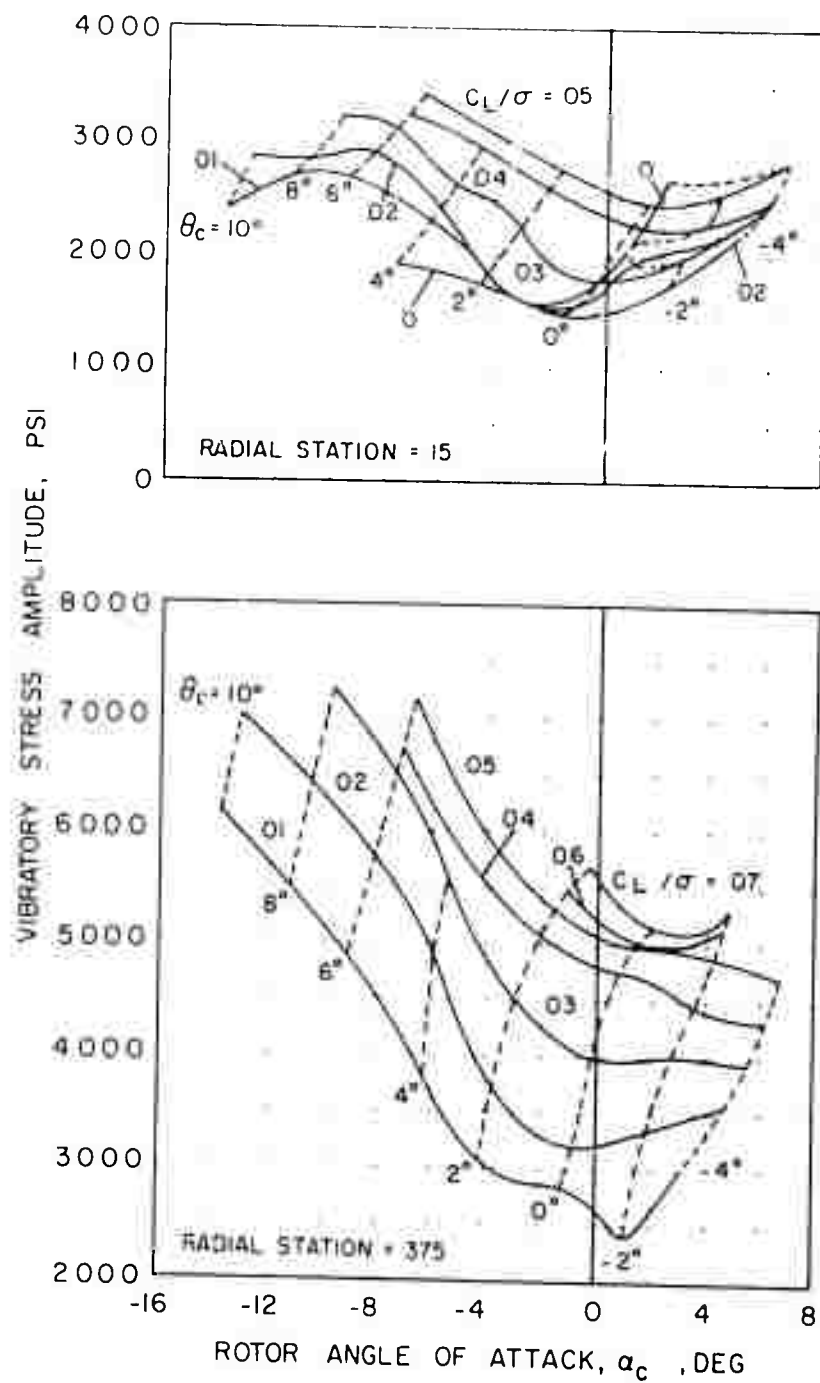
241

(b) Chordwise Concluded
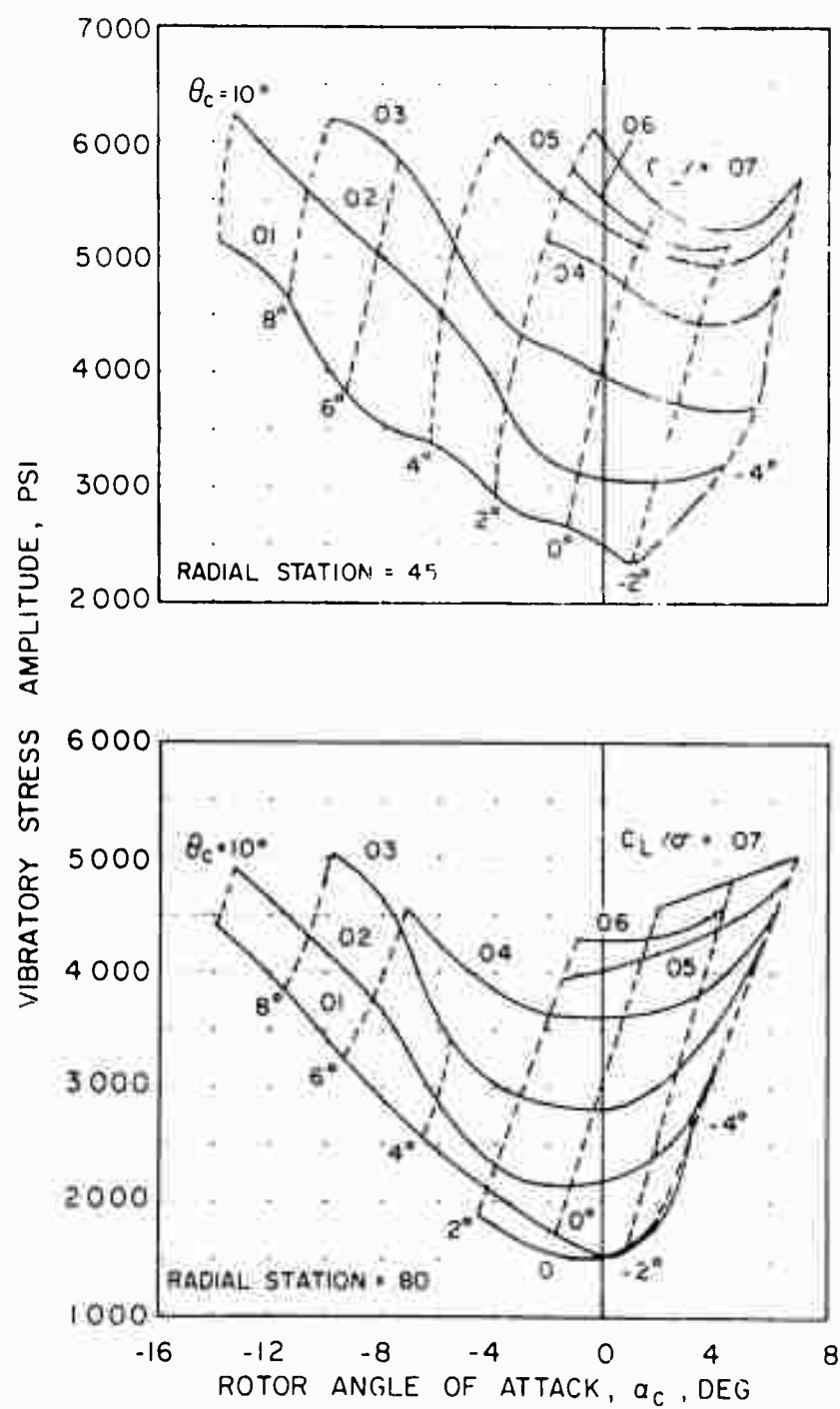
Figure 95. Continued.

242

(c) Torsional
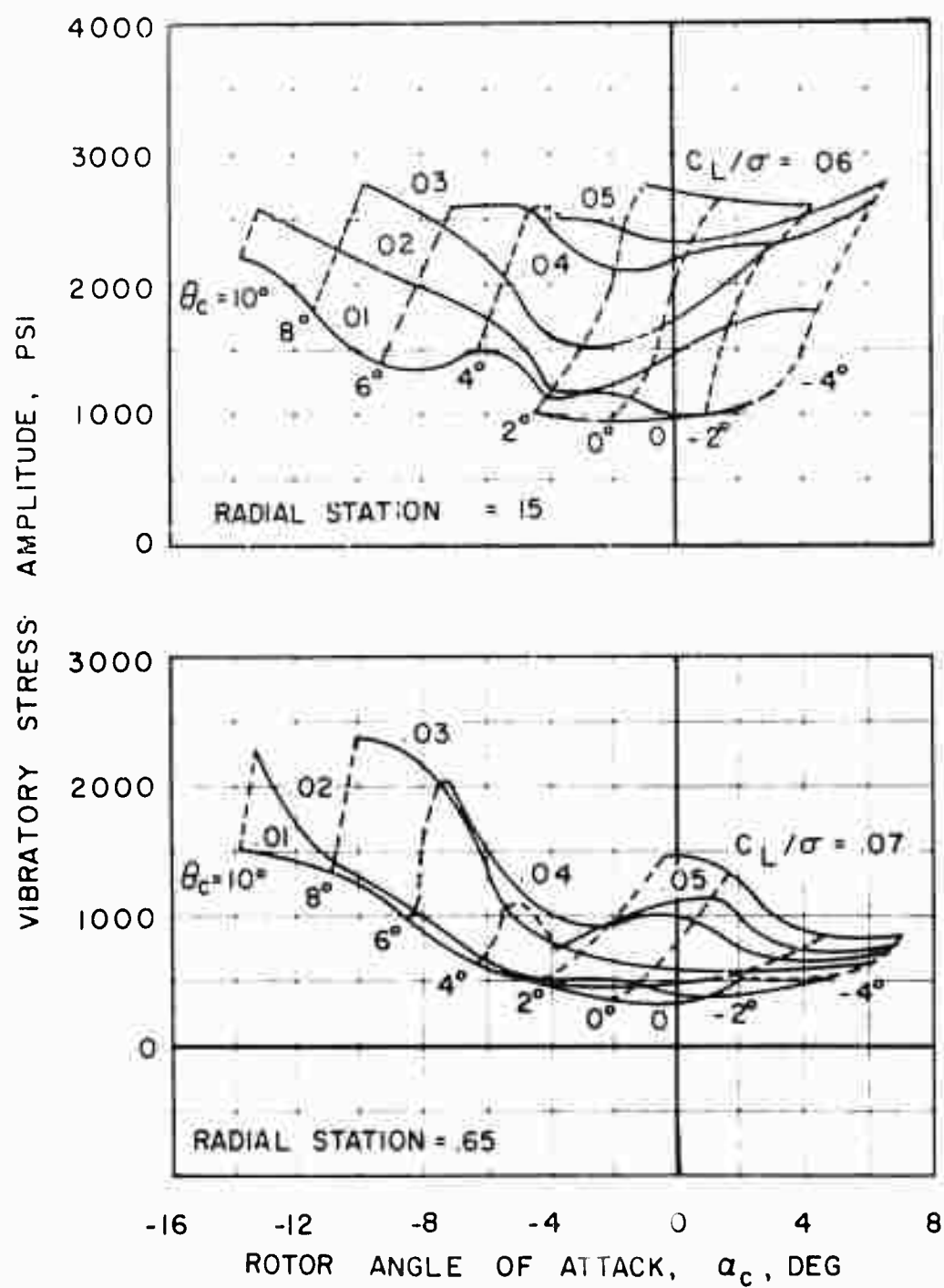
Figure 95. Concluded.

(a) Flapwise

Figure 96. The Effect of Rotor Angle of Attack on Flapwise, Chordwise, and Torsional Vibratory Stress Amplitude at Constant Lift for Several Radial Stations, V = 197 Knots, μ = 1.05, θ_1 = 0°, $M_{(1.0, 90)}$ = 0.54.

244

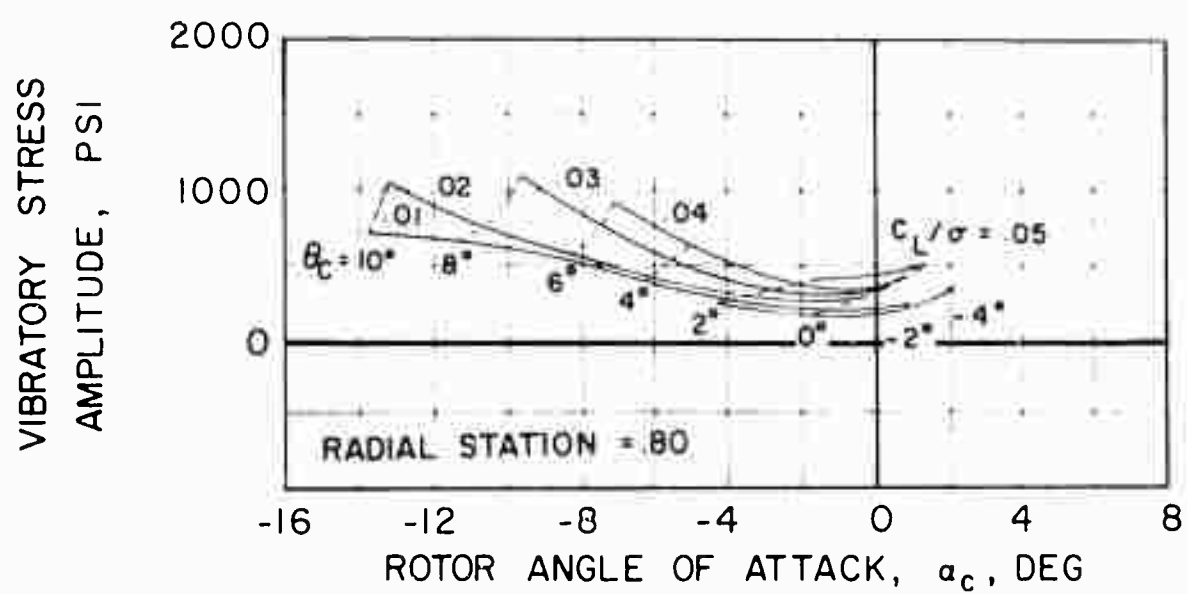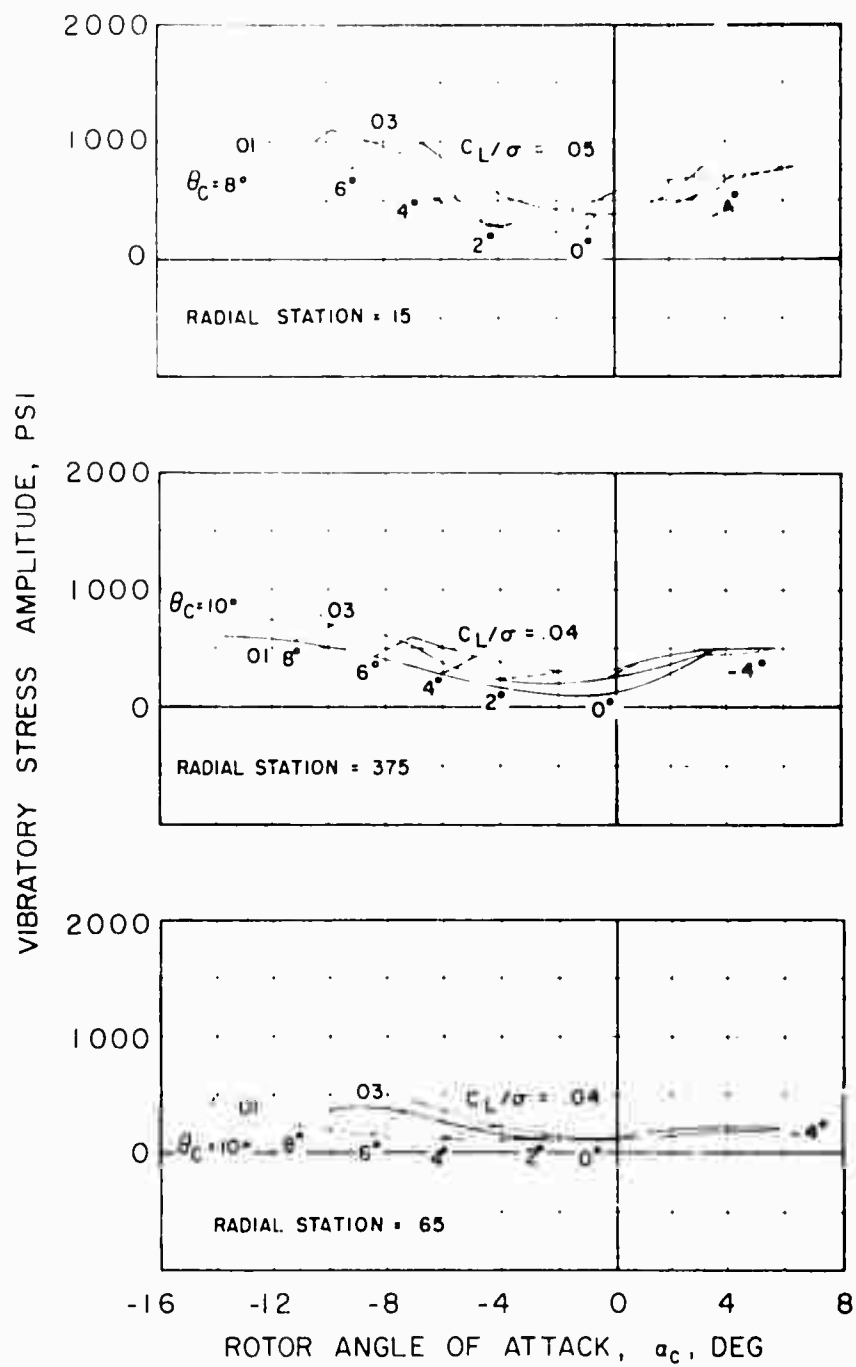(a) Flapwise Concluded
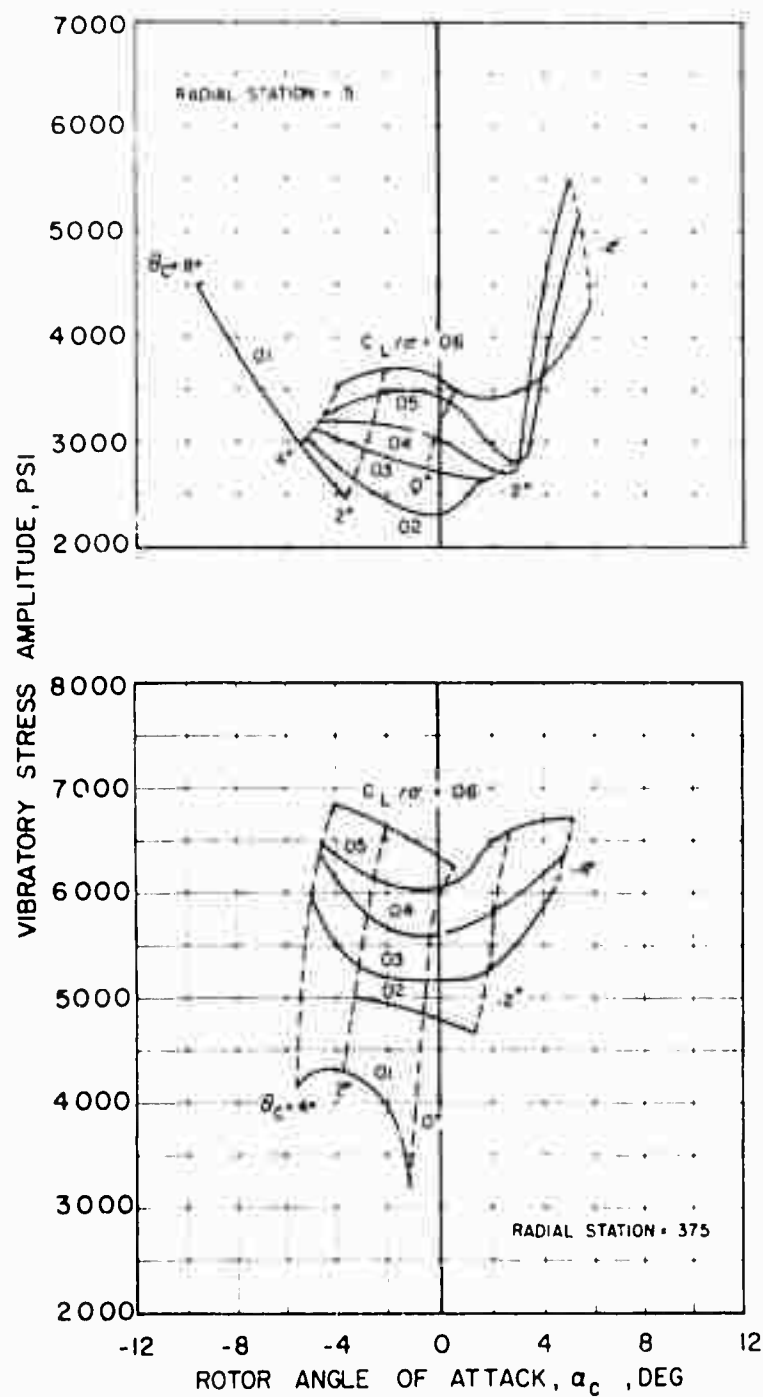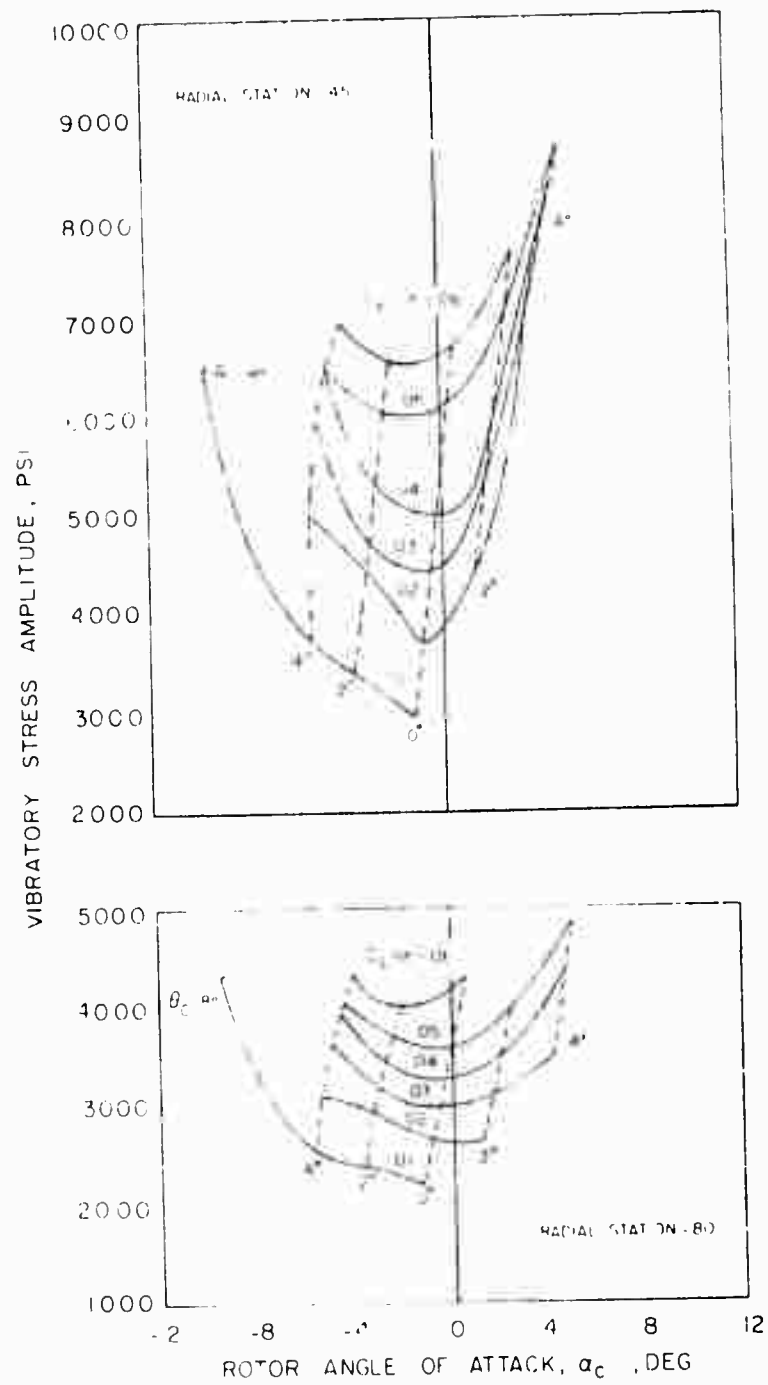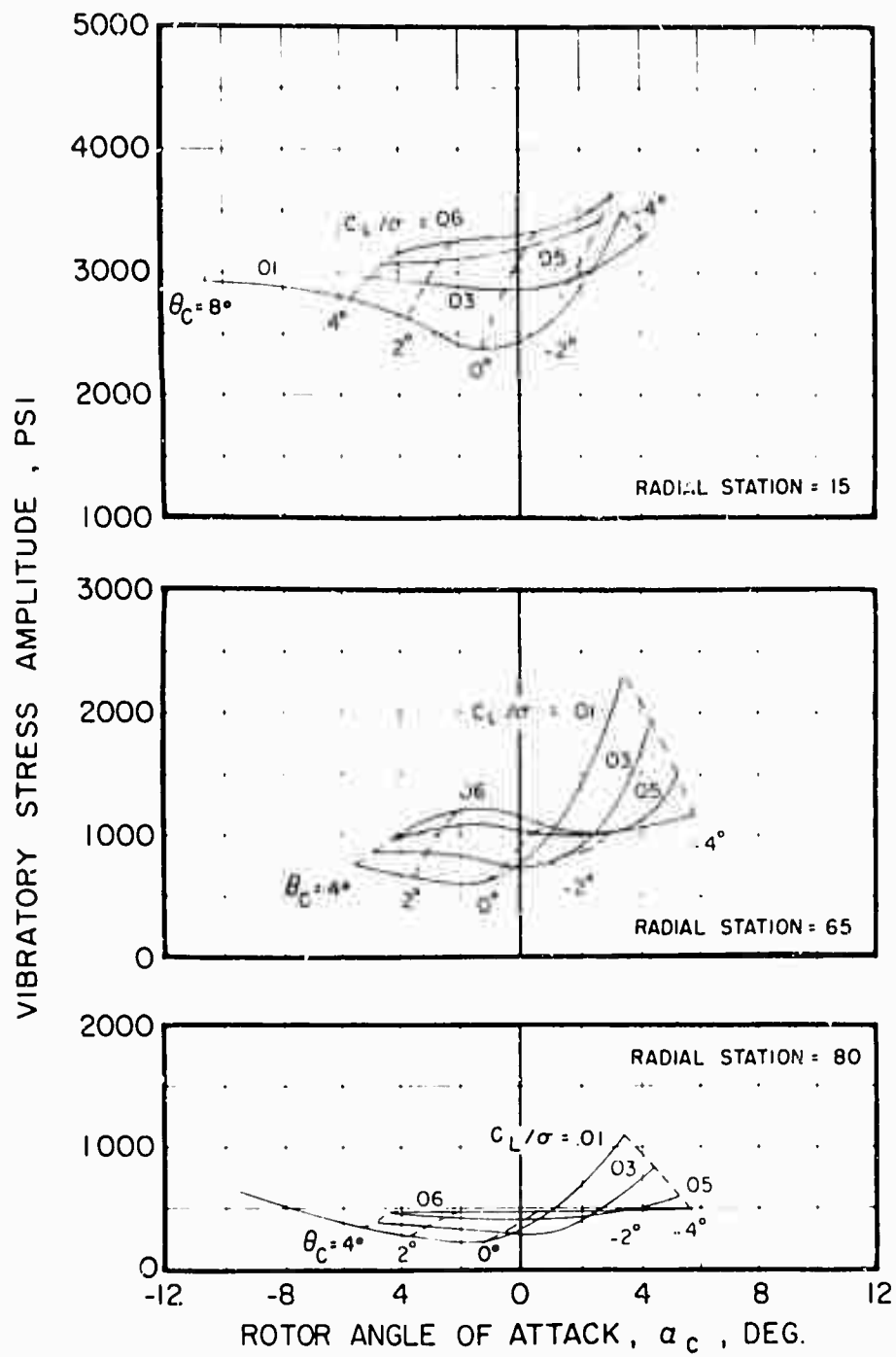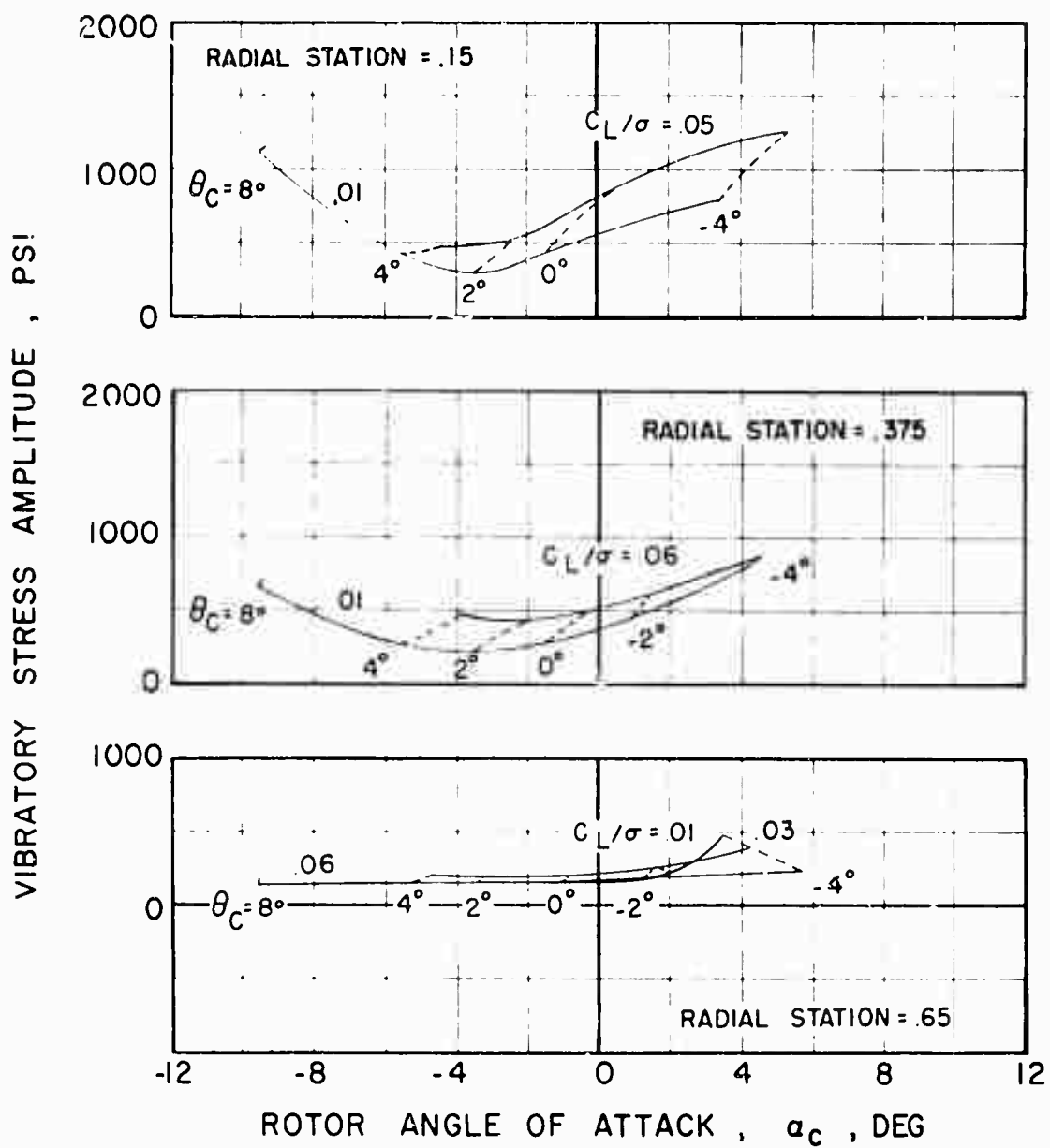
Figure 96. Continued.

(b) Chordwise

Figure 96. Continued.

246

(c) Torsional

Figure 96. Concluded.

247

DOCUMENT CONTROL DATA - R & D

(Security classification of title, body of abstract and indexing annotation must be entered when the overall report is classified)

1. ORIGINATING ACTIVITY *(Corporate author)*	2a. REPORT SECURITY CLASSIFICATION
Sikorsky Aircraft	UNCLASSIFIED
Division of United Aircraft Corporation	2b. GROUP
Stratford, Connecticut	

3. REPORT TITLE

AN EXPERIMENTAL STUDY OF THE PERFORMANCE AND STRUCTURAL LOADS
OF A FULL-SCALE ROTOR AT EXTREME OPERATING CONDITIONS

4. DESCRIPTIVE NOTES *(Type of report and inclusive dates)*

FINAL REPORT

5. AUTHOR(S) *(First name, middle initial, last name)*

Vincent M. Paglino
Andrew H. Logan

6. REPORT DATE	7a. TOTAL NO OF PAGES	7b. NO OF REFS
July 1968	250	16

8a. CONTRACT OR GRANT NO	9a. ORIGINATOR'S REPORT NUMBER(S)
DA 44-177-AMC-53(T)	
b. PROJECT NO	USSAAVLABS Technical Report 68-3
Task 1F125901A14604	
c.	9b. OTHER REPORT NO(S) *(Any other numbers that may be assigned this report)*
d.	SER-50505

10. DISTRIBUTION STATEMENT

This document has been approved for public release and sale; its
distribution is unlimited.

11. SUPPLEMENTARY NOTES	12. SPONSORING MILITARY ACTIVITY
	U. S. Army Aviation Materiel Laboratories
	Fort Eustis, Virginia

13. ABSTRACT

Two sets of strain-gage instrumented full-scale rotor blades were tested in the
NASA/Ames 40' x 80' Wind Tunnel. One blade set was a Sikorsky CH-34 rotor with
-8 degrees twist while the second set had zero twist. Advance ratios to 1.05 and tip
Mach numbers to 0.93 were tested over a wide range of collective pitch and shaft
angle. Effects of twist, Mach number, and advance ratio on performance and stress are
examined, as well as correlation of measured and predicted performance.

Negative twist blades improved performance in all propulsive for odes. The
zero twist blades had generally lower stresses with little or no performance penalty
when rotor lift and propulsive force requirements were decreased.

Predicted power rate of increase due to compressibility was somewhat greater than
measured in the rotor propulsive mode. Blade vibratory stress and control loads
increased sharply at high subsonic Mach numbers.

Reductions in power and disc loading optimized lift-drag at high advance ratios,
as predicted by theory, although drag calculations were low by 1 to 2 square feet of
parasite area. At high advance ratio, blade stress increased primarily in the flap-
wise mode.

The onset of stall is slower than predicted by theory and the inclusion of in-
duced, boundary layer, and unsteady effects could improve performance prediction.

DD FORM **1473** (PAGE 1)
1 NOV 65

S/N 0101-807-6801

Unclassified
Security Classification

14 KEY WORDS	LINK A		LINK B		LINK C	
	ROLE	WT	ROLE	WT	ROLE	WT
Helicopter						
Rotor						
Full-Scale						
Wind Tunnel Tests						
Performance						
Correlation						
Vibratory Stress						

DD FORM 1473 (BACK)
(PAGE 2)

Unclassified
Security Classification